UNIVERSITÀ DEGLI STUDI DI PERUGIA

Facoltá di Scienze Matematiche e Fisiche

Dottorato di Ricerca in Fisica - XV ciclo

Study of Cosmic Ray fluxes in Low Earth Orbit (LEO) observed with the AMS experiment

Tesi di Dottorato di

Gennaro Esposito

Gennaro.Esposito@pg.infn.it

Relatore : Prof. R. Battiston

Corelatore : Dott. E. Fiandrini

Coordinatore dottorato : Prof. P. Sodano

Ottobre 2002

Não sou nada.
Nunca serei nada.
Não posso querer ser nada.
A parte isso, tenho em mim todos os sonhos do mundo.

F. Pessoa

To my family

Table of Contents

Introduction

The principal sources of radiation in LEO are primary Cosmic Rays (CR), energetic protons and electrons trapped in the geomagnetic field making up the Earth's Radiation Belts (ERB), Solar Particles Events (SEP) produced during intense solar activity, albedo particles produced by the interaction of CR with the Earth's atmosphere and with a finite probability to become Quasi-Trapped in the geomagnetic field. The energy range of the sources is quite large as well as their density. As a consequence, different kinds of descriptions have to be used to address their physical properties. Only a fraction of the physical processes involved is well known actually, making the analysis of the radiation environment in LEO not only interesting for safety of human body and electronics equipment, but also a quite challenging task for the geophysics and astrophysics community.

In the first chapter, the reader is addressed to different aspects of the physics in LEO. Starting from the description of plasma fundamentals, the description of Earth's magnetosphere produced by interaction with solar wind is given. The focus of the chapter is on the Earth's plasmasphere were the radiation belts are created by the interactions with atmosphere by particles of solar and cosmic origin, together with the trapping effects produced by the Earth's magnetic field. Models and data comparisons are presented together with a brief description of the effect of radiation environment on human body and spacecraft electronics.

Cosmic ray physics near Earth is described in the second chapter: CR sources, composition and the modulation induced by the solar cycle are discussed. We also present the experimental situation for the main components of CR fluxes.

The Earth's magnetic field has a shielding effect on CR, limiting their possibility to interact with the atmosphere. The effect of the geomagnetic cutoff is described, showing how to separate CR in primary and undercutoff components. The undercutoff component remains trapped in the geomagnetic field. Details of the CR interaction with atmosphere and consequent production of secondary particles are also described. Some of those secondary particles can be captured by the Earth's magnetic field and become Quasi-Trapped. Model and data are also presented for this albedo population.

The AMS experiment has been approved to perform high energy physics research on board the International Space Station (ISS), starting from the year 2005 and running for three year. Using very a precise, large acceptance magnetic spectrometer, the experiment goals are the search of antimatter and dark matter signatures as well as high statistics measurements of CR spectra and composition. A prototype version of AMS flew on board of the Space Shuttle for ten days in 1998. The characteristics of this prototype are described in detail in chapter three. The data collected during the flight are analyzed with the purpose of selecting the undercutoff protons and leptons.

The fourth chapter describes the analysis of undercutoff particles. Tracing the particles in the geomagnetic field allows for the study of some peculiarities of the undercutoff particles. The use of the adiabatic invariant approach to the undercutoff particles allows for the construction of

flux maps in the appropriate magnetic description. Details of the striking features observed for protons and leptons in terms of equatorial pitch angle α_o and L shell parameter are given. The orbital coverage of AMS allows also for a clear separation for particles populations observed inside the South Atlantic Anomaly and outside of it. This brings to a clear distinction between particles Quasi-Trapped and Stably-Trapped in the Earth's magnetic field. Comparisons between QT and ST protons and leptons are given. We also present comparisons with other models and data of the same kind.

The AMS data offered the opportunity to analyze high energy particles collected with high accuracy at $400\,Km$ providing for the first time a complete observation of CR and geomagnetically trapped at this altitude. Understanding of the physics involved is the main task of this work.

Chapter 1

Radiation in Low Earth Orbit (LEO)

1.1 Introduction

When a satellite orbits close to the Earth it is said to be in Low Earth Orbit (LEO). Satellites in LEO cover the range of $320 \div 800\ Km$ of altitude, circling the Earth in almost 90 min with speed of $\sim 27.000\ Km/h$. The knowledge of the radiation environment in LEO is important not only from a scientific point of view but also for the applications, like the telecommunication systems. This chapter is focused on the definition and the explanation of the basic radiation physics involved in Low Earth Orbit.

We begin defining the basics of the plasma physics as a general framework and reference. Then, we discuss the peculiar characteristics of the space plasma physics focusing on particles reaching LEO. The description of the Earth's magnetosphere brings to the peculiarity of the Earth's magnetic field and the models currently used. To explain the standard techniques used to analyze the radiation belts we give a summary description of the adiabatic invariant approach with the limits of its application. Attention is paid to the description of the possible particle sources and losses in the belts describing static and dynamical models. Finally the description of how radiation affects human body and spacecraft subsystems is given and the way to parameterize its effects.

1.2 Plasma Physics

The stars as well as interplanetary and interstellar medium are made of ionized gas, the *plasma*. Plasma is believed to form the 99% of the matter of the universe. The region close to the Earth dominated by plasma is the magnetosphere. The features are intimately related to the plasma emitted by the Sun and its interaction with interplanetary magnetic field. Therefore plasma physics contributes to the understanding of our environment; we will start developing the basic ideas of this state of matter.

1.2.1 Plasma Fundamentals

A plasma is often referred to as the fourth state of matter. It can be defined as a quasi-neutral gas of charged and neutral particles which exhibits collective behaviour. One common configuration is a gas of particles heated to such a degree that most of its atoms are ionized into positively

charged ions and negatively charged electrons. The charge of the system over a large scale is still zero, but at small scales there are often collective effects that may result in local enhancements of either positive or negative charge. The typical scale size effects in a plasma is known as the Debye length, defined as the distance at which a single particle potential is shielded by the surrounding charged particles, or

$$\lambda_D = \sqrt{\frac{\epsilon_0 K T_e}{n_e^2}} \tag{1.1}$$

where T_e is the plasma temperature, n_e the particle density, K the Boltzman constant and ϵ_0 the vacuum dielectric permittivity. Another parameter is defined by the sphere with the Debye length as its radius, or the Debye sphere. If the number of particles contained within the Debye sphere is significantly larger than one, we can assume that we have a well defined plasma. For the typical parameters in space ($KT_e \approx 1eV, n_e \approx 1cm^{-3}$) we have Debye lengths are of $\sim 200m$. Since particle densities in this region are $\sim 1\, cm^{-3}$ we have much more particles in our Debye sphere than needed to define a reasonable plasma. In space, plasmas are everywhere, from outer layers of the sun, to the solar wind that blows out past the planets, to the plasma drifting in the Van Allen belts. Typical densities of these components are $1\, cm^{-3}$, with a temperature of $\approx 5\, KeV$ for protons, which corresponds to $2 \cdot 10^7\, K$.

1.2.2 Different Approaches for Plasma Description

What makes plasmas difficult to analyze is the fact that the densities fall in an intermediate range. Plasmas behave sometimes like fluids, and sometimes like a collection of individual particles [1]. There are three basic approaches to the theory of plasmas. The first one is the description in terms of *particle orbit theory* where each particle is considered individually, and the motion followed under the influence of the Lorentz force:

$$\mathbf{F} = \frac{\mathrm{d}\mathbf{p}}{\mathrm{dt}} = \mathrm{q}(\mathbf{E} + \mathbf{v} \times \mathbf{B}) \tag{1.2}$$

This approach is very valuable for gaining physical insight into plasma behaviour, and may be considered valid if the energy density of the electromagnetic fields exceeds energy density of the particles and no collisions occur between particles. It is not suitable however, for predictive calculations on real plasmas, e.g. for the macroscopic variables such as current density which both depends in a simple way on the individual particle trajectories, but cannot be obtained from orbit theory.

The second approach is the fluid description or *Magneto Hydro Dynamic (MHD)* approach, and is the most commonly used. It is a powerful approach to the study of macroscopic properties of plasmas. In this approach, we consider many-particles instead of a single-particle approach and the **E** and **B** fields are not prescribed but determined by the position and motion of the particles. Thus, the field equations and the equations of motion have to be solved simultaneously and self-consistently. While MHD describes many useful and important concepts, it is only a simple approach to plasma physics. In fact it describes the plasma as a fluid with all particles having the same speed, the bulk speed. The thermal motion of particles is neglected. The complete set of equations to solve involves the continuity equation and the Maxwell equations for the

$(\mathbf{E}, \mathbf{B})$ fields. MHD has the conservation laws enjoyed by fluid mechanics and electromagnetism, namely conservation of mass, momentum, energy and magnetic flux. The MHD approach can be used if the energy density of electromagnetic fields exceeds that of particles and collisions are present but we are only interested in the average properties of the plasma so that it can be seen as a fluid.

However, the fluid description relies on the most fundamental description, the third approach, the *kinetic theory*. This is a statistical treatment of a large ensemble of particles, from which macroscopic variables such as temperature and pressure can be derived by averaging over the particle distributions. Much of the basic physics of plasmas is formulated in a statistical way. To explain and predict the behaviour of such large ensembles of particles under the influence of external and inter-particle electric and magnetic fields, it is necessary to formulate a kinetic theory of plasmas. The fundamentals of this approach are described in great detail in [3]. The Klimotovich distribution is defined as the total number of particles in a given system, averaged over all similar systems having the same macroscopic properties. The result of this averaging is an equation describing the behaviour of a theoretical system in terms of a probability distribution. A system consisting of N distinct particles of a given specie is described by a set of N distinct points in phase space and with N very large it is convenient to describe the distribution of these points of a six-dimensional density function $F(\pi, \mathbf{q}, \mathrm{t})$ where $\pi, \mathbf{q}$ are respectively canonical momentum, position and t is time. In Hamiltonian mechanics the temporal evolution of F can be specified by Liouville theorem

$$\frac{dF}{dt} = \frac{\partial F}{\partial t} + \sum_{i}^{3} [\dot{\pi}_i \frac{\partial F}{\partial \pi_i} + \dot{q}_i \frac{\partial F}{\partial q_i}] = 0 \tag{1.3}$$

along any dynamical trajectory in phase space. The particle density is related to $F(\pi, \mathbf{q}, \mathrm{t})$ by:

$$n(\mathbf{r}, t) = \int_{-\infty}^{+\infty} f(\mathbf{r}, \mathbf{v}, \mathbf{t})\, d^3\, \mathbf{v} \tag{1.4}$$

Thermalization, i.e. equipartition of energy by collisions, will cause the system always to move towards a Maxwellian distribution, which is defined by one parameter only, the temperature T.

In plasmas, interactions are via long-range, weak Coulomb forces. A single particle moves in the average field due to the other charges. Relaxation due to Maxwellian distribution is slow, and many processes occur on a faster time scale than the relaxation process. Thus non Maxwellian distributions are often encountered when the kinetic theory is essential. However, for large scales slow phenomena, the fluid description is very effective.

Given an element of phase space $(\mathbf{r}, \mathbf{v})$ and assuming the conservation of particles by the Gauss theorem, the Vlasov equation may be derived:

$$\frac{\partial f}{\partial t} + \mathbf{v}\frac{\partial f}{\partial \mathbf{r}} + \frac{q}{m}(\mathbf{E} + \mathbf{v} \times \mathbf{B})\frac{\partial f}{\partial \mathbf{v}} = (\frac{\partial f}{\partial t})_{coll} \tag{1.5}$$

which is the starting point for much of plasma physics. In a fully ionized plasma, the $\mathbf{E}$ and $\mathbf{B}$ fields are determined by the rest of the plasma and depend on the f function. The Vlasov equation is the basic equation which prescribes the dynamics of *collisionless* plasmas: a conservation law in a seven-dimensional phase space. It is important to realize that this equation is

exact, no assumptions are made in its derivation. Solving the equation for the correct function with realistic magnetic and electric fields (external and self-generated fields) a complete solution to all the plasma behaviour, from wave modes to instabilities, will be obtained. However, in practice it is impossible to analytically solve the Vlasov equation in a general way for arbitrary fields, so other approximate methods must be used.

Typically, the most common parameters obtained from distribution functions are the velocity moments. In practice, the only moments used are $n = 0, 1, 2$ and sometimes 3. These moments are defined as *number density*, the *bulk velocity*, the *temperature* and the *heat flux* respectively. Also, note that the temperature and heat flux quantities are calculated in the rest frame of the plasma. The two latter quantities measure *internal energy* (temperature), and *internal energy flow* (heat flux), respectively. The Vlasov equation is in general non linear. Moreover, particles undergo micro-collisions, i.e. they are gradually deflected by large numbers of small deflections due to local Coulomb interactions which are treated by the term $(\partial f/\partial t)_{coll}$ and a suitable representation for the collision term has to be chosen.

The accumulation process of micro-collision brings to the procedure of the Fokker-Plank equation. In contrast to the Vlasov equation, the Fokker-Plank equation considers the short-range, local interactions between particles. Collisions arise from many small Coulomb interactions among charged particles, and the collision term has a mechanical analogy in the Boltzman motion of particles in a gas. Collisions are not deterministic but stochastic processes, thus for a given particle, even if the initial position and velocity are known, we cannot determine the future motion exactly. Only for an assembly of particles the collective behaviour can be determined using collision probabilities.

Given the probability $\psi(\mathbf{v}, \Delta\mathrm{v})$ that a particle, initially with velocity $\mathbf{v}$, acquires an increment velocity $\Delta\mathbf{v}$ in a time Δt, the phase space density $f(\mathbf{r}, \mathbf{v}, \mathrm{t})$ is a probability function too and can be written as:

$$f(\mathbf{r}, \mathbf{v}, t) = \int f(\mathbf{r}, \mathbf{v} - \Delta\mathbf{v}, t - \Delta t)\psi(\mathbf{v} - \Delta\mathbf{v}, \Delta\mathbf{v})\mathrm{d}(\Delta\mathbf{v}) \tag{1.6}$$

Then following [1] we can derive:

$$(\frac{\partial f}{\partial t})_{coll}\Delta t = -\frac{\partial f}{\partial \mathbf{v}}(f < \Delta\mathbf{v} >) + \frac{\partial^2}{2\partial \mathbf{v}^2}(f < \Delta\mathbf{v}^2 >) \tag{1.7}$$

where

$$< \Delta\mathbf{v} >= \int \psi\, \Delta\mathbf{v}\, d(\Delta\mathbf{v}) \qquad < \Delta\mathbf{v}^2 >= \int \psi\, \Delta\mathbf{v}\, d(\Delta\mathbf{v}^2) \tag{1.8}$$

The first term on the right side of eq. 1.7 describes the frictional forces slowing down fast particles and accelerating slow ones, while the second term is a diffusion in velocity space. The two terms operate in opposite directions, and are in balance for an equilibrium distribution.

1.3 Space Plasma Physics

Space plasma physics may be defined as the study of the physics of plasmas in space supported by direct measurement. It is concerned primarily with the processes involved in the flow of matter and energy through the solar system. It is closely related to magnetospheric, ionospheric,

cosmic ray physics, solar physics, planetary physics and astrophysics. Since different particle specie with different energies within a single species, behave very differently in the plasmas of the solar system, they cannot adequately be described through fluid approximation of MHD but, in general, the kinetic theory has to be used. The outer environment of the sun and planets contains very tenuous plasmas. The electron and ion number densities are typically only a few million per cubic meter, i.e. only a few per cubic centimeter. Space plasmas are in general *collisionless*, *neutral*, and *vast*. In fact in most applications, collisions with neutrals or other charged particles play no part in determining dynamics. Debye lengths are tens or hundreds of meters, with the result that the number of particles in a Debye sphere is some 10 billion or more. For the most part, boundaries play little role, since the size of the medium is very much greater than the Debye length. Space plasma physics begins at the Sun, and in particular at the outermost part of the Sun, the solar corona.

1.3.1 Plasma from the Sun and Magnetospheres

The closest and most intense source of plasma is the Sun. Our star is a strong emitter of particles ranging from few eV up to O(10 MeV) and determines the space environment at LEO. It is therefore worth summarize its features.

The solar corona streams out into space, and is visible during eclipses as giant streamers. The corona continuously expands into space forming a *solar wind* of protons, alpha particles and other solar constituents, along with a neutralizing sea of electrons. In the fig. 1.1 the pronounced latitudinal variation of the solar wind speed as measured in the Ulysses mission [9] is shown.

Thanks to the high temperature ($10^6\,^oK$), the solar corona is not gravitationally bound due to the high kinetic energy and therefore escapes to the interplanetary medium. The solar wind that emanates from the solar corona is source of both energy and plasma for the magnetosphere. The interplanetary gas is a supersonic plasma flowing out from the sun and interacting with the various planetary objects orbiting the sun. In addition their outer atmospheres are ionized by the solar ultraviolet radiation, creating a *ionosphere*. The dynamics of plasma in the ionosphere is dominated by the pressure gradients or hydro-magnetic forces created by collisional couplings to the neutral atmosphere. Since the kinetic energy density ($\epsilon_{kin} = 0.6\ erg\,cm^{-2}s^{-1}$) of the plasma is much higher than the magnetic field energy density ($\epsilon_{mag} = 0.01\ erg\,cm^{-2}s^{-1}$), the radially expanding solar wind carries away the magnetic flux. The 26-days solar rotation causes a distortion of the field lines, which assumes an Archimedean spiral configuration.

The solar wind continues the expansion until it interacts with the local interstellar magnetic field. Heliospheric boundary can be considered divided in three layers. First, we have the *termination shock*, where the gradual reduction of the speed of the wind comes to an abrupt end due to the passage from supersonic to subsonic speed due to interstellar background pressure ($\approx 10^{-13}\,Pa$). Then the *heliopause*, where the values of the interplanetary and interstellar magnetic fields are equal ($2.5 \cdot 10^{-10} T$). Finally the *bow shock*, a region of subsonic slow-down due to the interstellar wind. When the solar wind encounters an obstacle characteristics structures are formed around it. Most of the planets have inner magnetic fields capable of deviate the solar wind, creating a void in the heliosphere called a *magnetosphere*.

A magnetosphere is the region of space which is permeated by a magnetic field and in which the motion of the plasma is dominated by electromagnetic forces, rather than by hydrodynamic

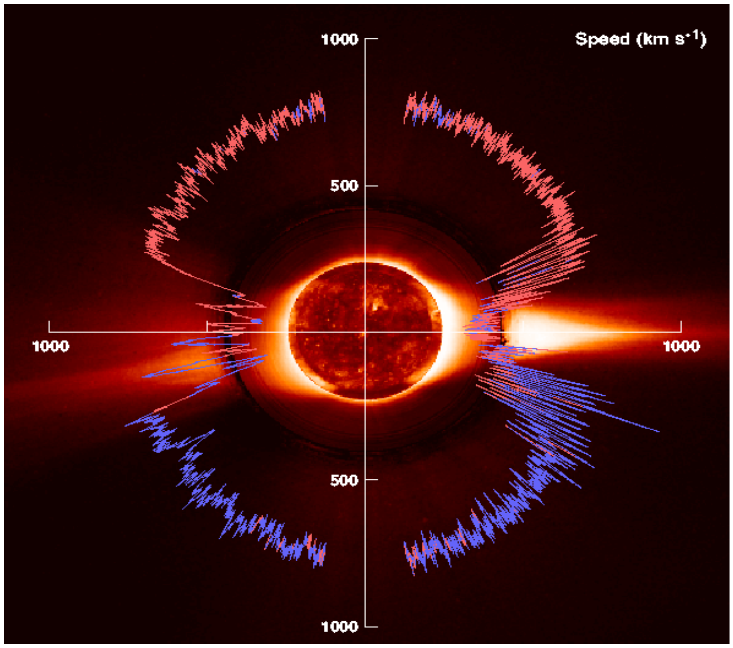

Figure 1.1: *Sun corona and polar plot of solar wind as function of the heliolongitude for the Ulysses mission [9]*

or pressure gradient forces. The magnetic field may be intrinsic to the object, such as a magnetic planet or it may be induced as that draped around Venus.

A planet in the solar system has the magnetic field grossly distorted by the solar wind, which flows past it at supersonic velocity. Thus instead of extending to infinity, the magnetic field of a planet is confined within a boundary called *magnetopause* the shape of which is determined by the interaction with the solar wind as shown in fig. 1.3. Since the wind is supersonic, there will be a *bow shock* standing off at some distance from the magnetopause. Between the bow shock and the magnetopause, there is a region of shocked plasma known as the *magnetosheath* in which the flow is subsonic and the temperature and entropy are higher than in the solar wind. Eddy currents are set up in the solar wind to cancel the planet's field ahead of the solar wind. The solar wind has only a limited ability to do this, though. A stand-off is established where the energy density of the solar wind matches a locally enhanced planetary magnetic energy density. A standing shock wave forms, broadening the velocity distribution in energy and direction to allow the heated solar wind to flow around the obstacle.

Magnetospheric plasmas are in general effectively collisionless, i.e. they have very long mean free paths, and therefore can be regarded as ideal conductors having very high electrical conductivities. In the limit of infinite conductivity, the magnetic field behaves as if it were frozen into the plasma. In this case the *frozen field* theorem holds, i.e. that there can be no relative motion between plasma and the magnetic lines of forces. Thus, the solar wind is deflected around the magnetopause or the ionopause of a non-magnetic object, because of a surface current generating a Lorentz force responsible for the deflection of the solar wind.

The ion flow outwards, approximately radially, at speeds ranging from 200 to 1000 Km/s, with typical energies of protons of $O(KeV)$. The electrons and ions do not travel together as a

composite fluid. Since the solar wind may be highly variable, it is common for faster winds from one region to catch up with slower winds forming regions of turbulence. The number densities are also highly variable around an average of $\sim 5 \cdot 10^6\, m^{-3}$, down to just 2% of this value. Ions and electrons experience electric fields set up by the solar wind. Acceleration by these fields in the presence of the interplanetary magnetic fields gives rise to a Lorentz force which causes the particles to move along curved paths.

The situation is different from the planet without strong magnetic field. The surface or atmosphere is continuously and directly bombarded by solar wind and cosmic rays, but even in this case a bow shock and magnetosheath are formed to allow the flow around the planet. One of the effects of the solar wind flowing past in the magnetosheath is a quasi-friction which creates eddies in the downstream part or tail of the magnetosphere. Since the plasma on both sides of the boundary, the magnetopause, are collisionless, the friction is effected through wave-particle interactions rather than direct particle-particle interactions. A flow of charged particles in the magnetic field of the magnetospheric tail sets up.

1.3.2 The Earth's Magnetosphere

The Earth's magnetosphere extends from the top of atmosphere up to $10R_e$ [1] toward the Sun and hundreds of R_e in the direction opposite from the Sun.

Its outer boundaries and dynamics depend on the solar wind conditions. The solar wind does not penetrate the geomagnetic field but compresses and confines the field around the Earth. The boundary is located where the external pressure of the flowing solar wind equals the internal pressure of the geomagnetic field together with a complex interconnection process between solar wind and magnetic field.

The existence of the solar wind is one of the reasons for which Earth's magnetosphere is not dipole like. The shape, as seen in fig. 1.2, is a sort of tapered cylinder, flattened on the dayside, with an exaggerated tail on the nightside. The solar wind pressure on the dayside causes the flattening and compression of the magnetosphere, while conversely the nightside magnetosphere is stretched out to great distances tailward. Typically, the dayside magnetopause boundary is at $\sim 10R_e$, while the nightside tail can stretch out to $200R_e$ or more. The distance of this dayside boundary, called *sub-solar point*, is directly related to the dynamic pressure of the solar wind varying from 4.5 to 20 R_e depending on the solar activity. The plasma within the magnetosphere is not homogeneous. Roughly speaking, when the magnetic field character (i.e. curvature, magnitude or topology) changes drastically, so does the plasma population contained therein. The inner magnetosphere consists of three partially overlapping regions.

We are concerned with regions in the center and just off-center of the middle magnetotail (10 to $30R_e$ tailward of the Earth). In this region there is a great deal of complex activity, and the nature of the plasma contained here can teach us much about the magnetospheric features. The fig. 1.3 shows a cutaway cross section of the Earth's magnetosphere with several important regions labelled. The Earth's bow shock, the point at which the solar wind, travelling at a supersonic velocity, slows down abruptly when it hits the Earth's magnetic field and forms a shock front (a familiar shock is produced by a supersonic airplane, commonly known as a sonic bang); behind the bow shock is the Earth's magnetopause. This is the actual boundary of

[1] $R_e = 1$ Earth radii $= 6371Km$ or $3957miles$

the Earth's magnetosphere. The Earth's magnetosheath is filled by solar wind plasma which crossed the bow shock. The kinetic energy is transformed in thermal energy passing through the shock front so that plasma is hot with respect to solar wind. The *plasma sheet* is a region that usually coincides with the minimum $|\mathbf{B}|$ region known as the *neutral sheet*. This is where the current sheet flows. Plasma in this region usually has densities of $\sim 0.1 \div 1.0\, cm^{-3}$, and ion temperatures $\sim 5\, KeV$ [5]. Plasma flows in this region are a combination of components perpendicular and parallel to the local magnetic field. The perpendicular flows contribute most to the Earthward flow at the center of the current sheet. Other perpendicular components also self-consistently generate the currents required to support the kinked magnetic field here. Typical current densities at the center of the current sheet are $\sim 3.5\ nA\, m^{-2}$ at midnight in quiet Sun periods, decreasing as we move away from the center of the current sheet and out to the flanks. As we move out of the plasma sheet, there is a boundary region known as the Plasma Sheet Boundary Layer (PSBL). This region is filled by fast parallel flows, both Earthward and tailward, with magnitudes of hundreds of Km/s. Densities here are usually $\sim 0.1\, cm^{-3}$. Thermal energies are close to flow energies, meaning that if we have a flow speed of about $400\, Km/s$, we would also have a temperature approximately of $1\, KeV$. The area between the magnetopause and the PSBL is called the *lobe region*. The lobes are the areas where the field lines are most stretched, and the particle densities are generally less than $0.1 cm^{-3}$. An important difference between the plasma sheet and the lobes is whether the field lines are normally closed or open and therefore directly connected to the solar wind. The difference between open and closed field lines is best answered by the process known as *reconnection*. Reconnection is a process where the frozen flux conditions are violated, allowing for plasma to diffuse across previously uncrossable flux tubes. With the increased flux density in the magnetotail lobes, the magnetic pressure is increased, causing the current sheet to become thinner and more intense. The lower energy O(eV) component is the dense and cold *plasmasphere* co-rotating with the Earth as shown in fig. 1.2. Most of the plasmaspheric plasma is of ionospheric origin. The temperature is low (below $1\, eV$) but due to the high energy densities, the plasmasphere has significant effects on radio wave propagation. The outer boundary of the plasmasphere, the *plasmapause* is characterized by a rapid plasma density drop from as much as $1000\, cm^{-3}$ down to below $1 cm^{-3}$. However, the location and the shape of the plasmapause are strongly dependent on solar magnetic activity. During prolonged quiescence, the plasmapause reaches equatorial distances beyond $8R_e$ and gradually vanishes, but during strong magnetic activity it is compressed down to $3R_e$. Finally there is the *Ring Current (RC)* system, arising from the motion of low energy charged particles in the nearly dipolar magnetic field of the Earth. As the gradient and the curvature of the field make positively charged ions drift westward and electrons eastward, the net effect is a westward current. Because of the energy density of the energetic ions has a maximum in the range $20 - 300\, KeV$, they are the primary carriers of the enhanced RC during magnetic activity. The main ion species are H nuclei of solar wind origin and O nuclei of ionospheric origin.

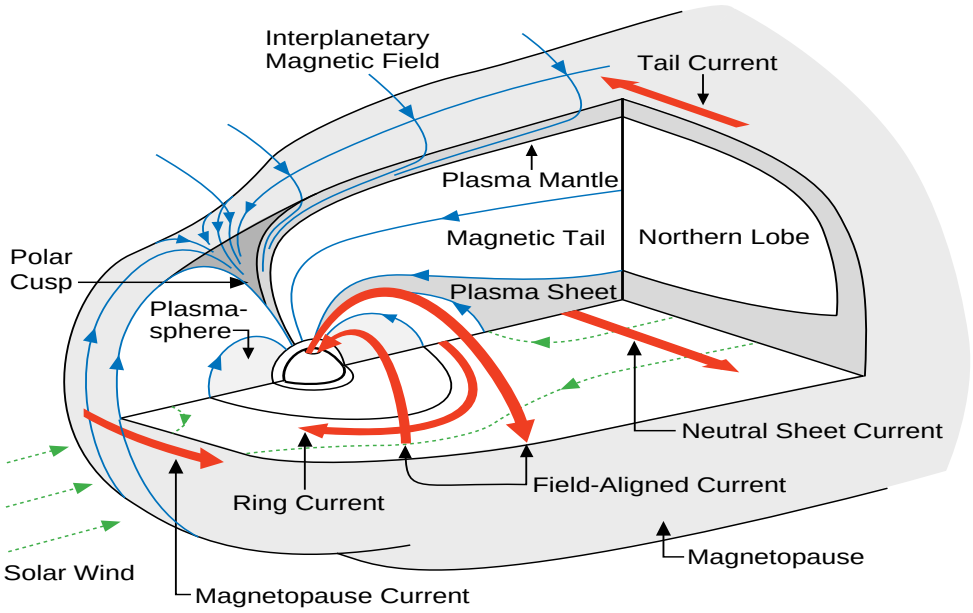

Figure 1.2: *Sketch of the Earth's magnetosphere with plasma regions and currents system [2]*

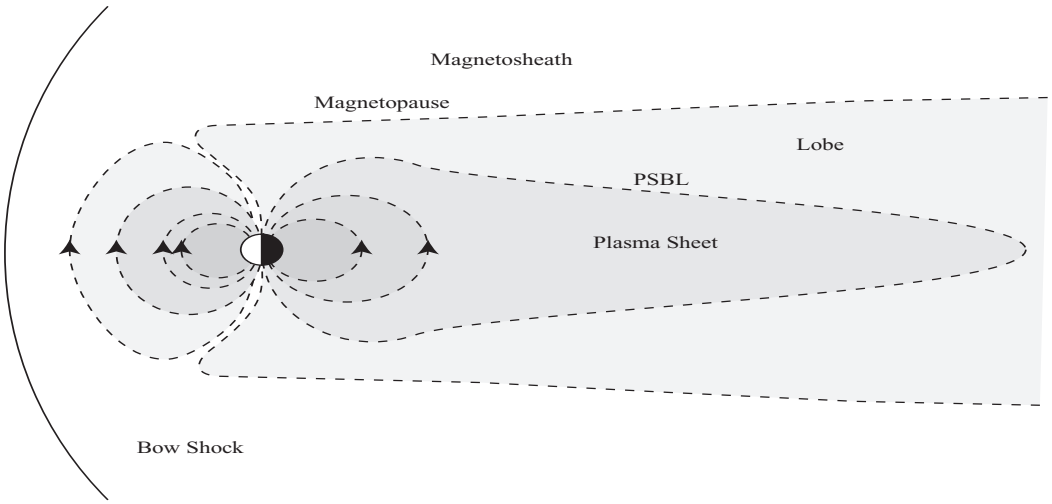

Figure 1.3: *Cutaway diagram of the magnetosphere with plasma regions and currents system [4]*

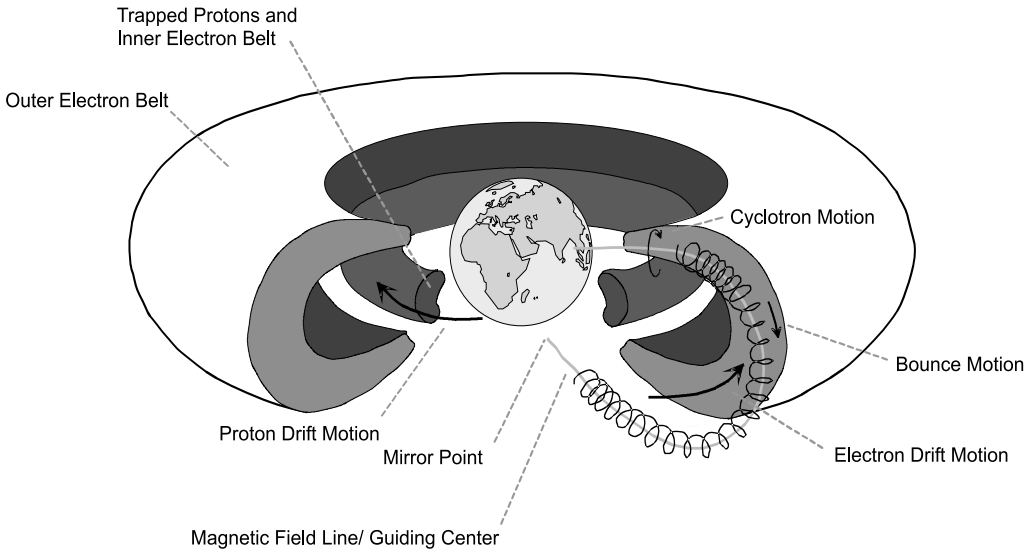

Figure 1.4: *A schematic view of the Earth's radiation belts [37]*

1.4 Earth's Radiation Belts

Very early in the history of spacecraft exploration of the environment of the Earth, it was discovered that the magnetosphere contains populations of energetic particles [10]. The study of the morphology, composition and energy budget of these belts was the main topic of research during the first decades of the world-wide space program. A *radiation belt* is an interior feature of a magnetosphere and comprises populations of energetic, electrically charged particles (electron, protons and heavier atomic ions) stably trapped by the magnetic field in a wide energy range, from eV up to O(GeV). Depending on their energy and location, these particles are conventionally divided in classes as shown in fig. 1.14. The radiation belts are embedded in the plasmasphere. To give an explanation of their features, we need to go further in the description of the Earth's magnetic field and the physics of a single particle in a magnetic field using the adiabatic invariant approach.

1.4.1 Magnetic Field Models of the Magnetosphere

The magnetic field vector around the Earth has been measured with many satellites in different positions. The field is quite well known up to few R_e but large uncertainties are present for large distances, due to the lack of measurements and highly variable conditions of the solar wind. The Earth's magnetic field is conventionally separated into *internal field*, produced by the Earth's dynamo and into *external field* produced by the currents circulating in the magnetosphere (see fig.1.3).

The Inner Earth's Magnetic Field The inner Earth's magnetic field is produced by the interior Earth's dynamo, due to electric currents flowing in the Earth's core. This field alone,

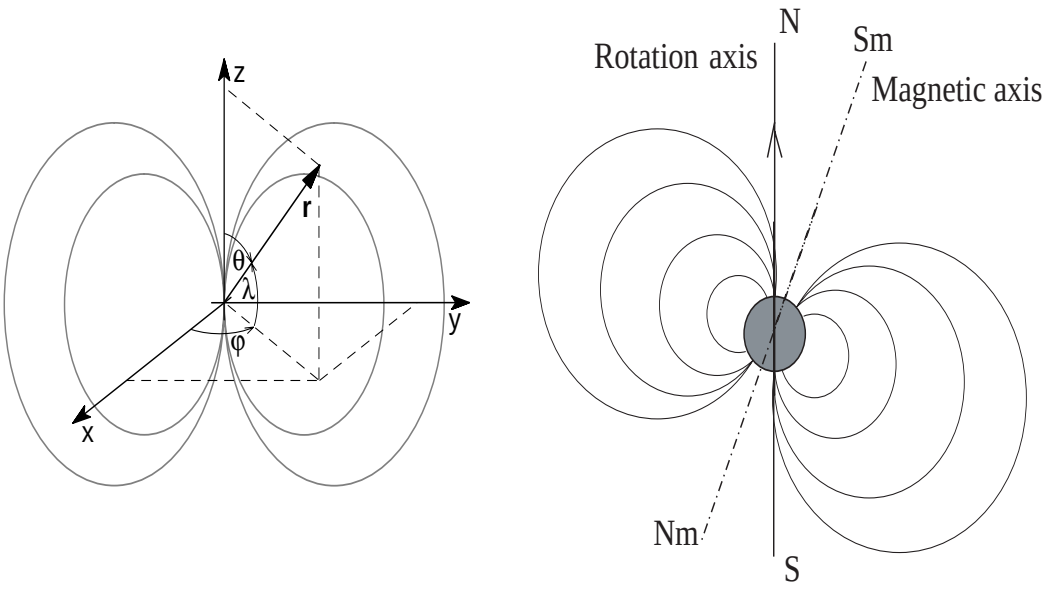

Figure 1.5: *On the left panel the coordinate system for a dipole field, on the right panel the Earth's magnetic field with magnetic axis inclination*

would be similar to a simple dipolar field. The Earth has a crust and a mantle surrounding a liquid metallic core which in turn encloses a metal core with 16% of the planet consisting of core and 84% of mantle.

The convection of hot conducting material across the magnetic field induces electric currents reinforcing the magnetic field itself. This is a self-exciting dynamo which produce the main part of a steady field. A dynamo is a conductor driven in a magnetic field such that it acts to sustain the field. A primary current produces the dipole-like field, a secondary current near the core-mantle boundary produces the local dipoles which give the multipole nature of the field. Other sources of geomagnetic field are crystal rocks which retains permanent magnetism, which is weak $O(10^{-4})$ and localized usually $\sim 400\,Km$ beneath surface.

Secular variations of the field have been observed on a time scale of centuries, with the field becoming weaker. Moreover, there are geological evidences, the reason of which is unclear, that the polarity of the geomagnetic field reverses at irregular intervals of the order of half million of years, while the secular variation is of the order of $0.15 \cdot 10^{-5}\,G/year$ and the westward drifting similar to precession with an approximately period of 5000 *years*.

To first order, the Earth can be described as a sphere uniformly magnetized along its dipole axis, as shown in the left panel of fig. 1.5, with the mean North-South direction opposite with respect to the geographic poles. The intersection of this axis with the Earth's surface are the magnetic North pole at $78.3^o\,S\;111^o\,E$ in the Antartica, and the South pole at $78.3^o\,N\;69^o\,W$ in Greenland. Both positions are $\sim 800\,Km$ away from the geographic poles. The magnetic dipole axis is inclined by 11.3^o with respect the rotation axis and is shifted by $\sim 400 Km$ in the direction of western Pacific. The typical magnetic field intensity on the surface of the Earth is $\approx 0.3\,G$ at geomagnetic equator and $\approx 0.6\,G$ at poles, while the typical resolution for a measurements is

$10^{-5}\ G = 1\ nT$. The dipole moment of the Earth is $M_o \simeq 8 \cdot 10^{25}\ Gcm^3$.

The geomagnetic coordinate system is oriented along the magnetic dipole axis, while a perpendicular plane intersecting the Earth's center, defines the equatorial plane, as shown in the right panel of fig. 1.5.

Under the steady state conditions with no currents present in the magnetosphere in the region of interest, a scalar potential $\psi(\mathbf{r})$ can be used to define the dipolar field as $\mathbf{B}(\mathbf{r}) = -\nabla\psi(\mathbf{r})$ with

$$\psi(\mathbf{r}) = -\frac{\mu_o}{4\pi}\frac{M_o \sin\varphi}{r^2} \tag{1.9}$$

the magnetic field follow as

$$\mathbf{B}(\mathbf{r}) = \frac{\mu_o}{4\pi}\frac{M_o}{r^3}(-2\sin\lambda_m \cdot \mathbf{e_r} + \cos\lambda_m \cdot \mathbf{e_{\lambda_m}}) \tag{1.10}$$

with no dependence on φ_m because of the cylindrical symmetry of the dipole field. The field density falls off with distance as

$$B = \sqrt{B_r^2 + B_{\lambda_m}^2} = \frac{\mu_o}{4\pi}\frac{M_o}{r^3}\sqrt{1 + 3\sin^2\lambda_m} \tag{1.11}$$

with the equatorial field at the Earth's surface $B_o = \mu_o M_o / 4\pi R_e^3 = 0.311\ G$. The strength at poles ($\lambda_m = 90^o$) is twice than at the equator ($\lambda_m = 0^o$). The equation of a field line can be inferred from eq. 1.10 taking the ratio between the radial and transverse components $r\, d\lambda_m/dr = 1/2 \tan\lambda_m$ giving $r = R_o \cos^2\lambda_m$, R_o being the equatorial distance of the field line from the dipole axis and corresponding also to the largest distance of a field line from it; R_o completely determines the field line and can be used as independent parameter. Moreover, the field line intersects the Earth's surface at $\cos\lambda_{mo} = R_o^{-0.5}$.

The dipole approximation is precise at level of 30% at distances $2 \div 5\ R_e$. Nevertheless, it contains most of the relevant features of the Earth's magnetic field. Furthermore, the dipolar relations provide the basis for the proper formulation of the particle motion in the magnetic field based on adiabatic invariants, as described in the following section. The dipolar relations formally holds even in presence of non-dipolar axial symmetric fields.

The ideal dipolar structures are distorted by irregularities in the Earth's dynamo and a more correct expression for the geomagnetic field is the multipole expansion in spherical coordinate of the scalar potential:

$$\psi(r) = \sum_{n=1}^{\infty}\frac{R_e}{r^{n+1}}\sum_{m}^{n}[g_n^m \cos(m\varphi) + h_n^m \sin(m\varphi)]P_n^m(\cos\theta) \tag{1.12}$$

The g_n^m and h_n^m are normalization coefficients and $P_n^m(\cos\theta)$ are the Legendre polynomials, n gives the order of the multipole expansion and $n = 1$ corresponds to the dipole field. The coefficients are determined from fit to the measured magnetic field values, and have to be adjusted for the change in time of the magnetic field, with an accuracy of $\leq 0.1\%$ close to the Earth's surface. The fields measurements come from worldwide, long-lasting campaigns since 1945 and upgraded every 5 years in a compilation of the best fit for the multipole expansion. The results are published by the International Association of Geomagnetism and Aeronomy (IAGA) [11]

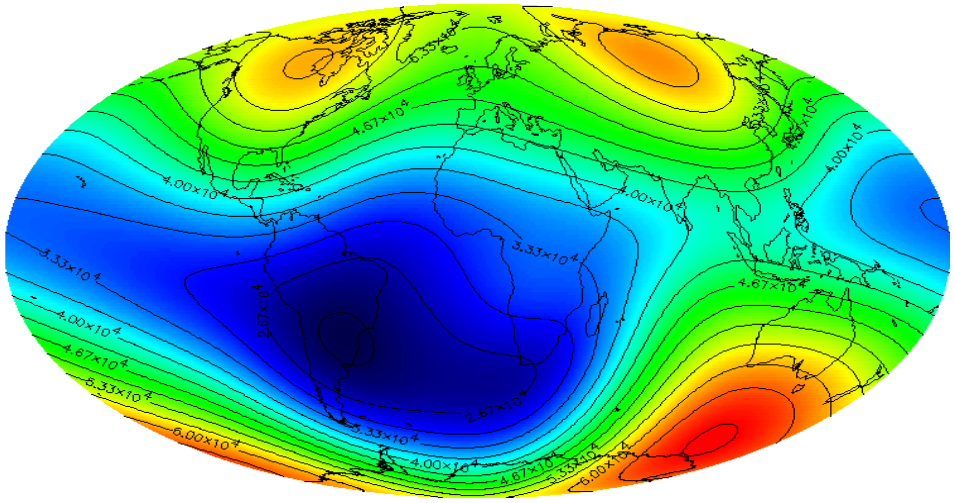

Figure 1.6: *Total magnetic field map on the Earth's surface based on IGRF1995 for the 1998 epoch in [nT] [11]*

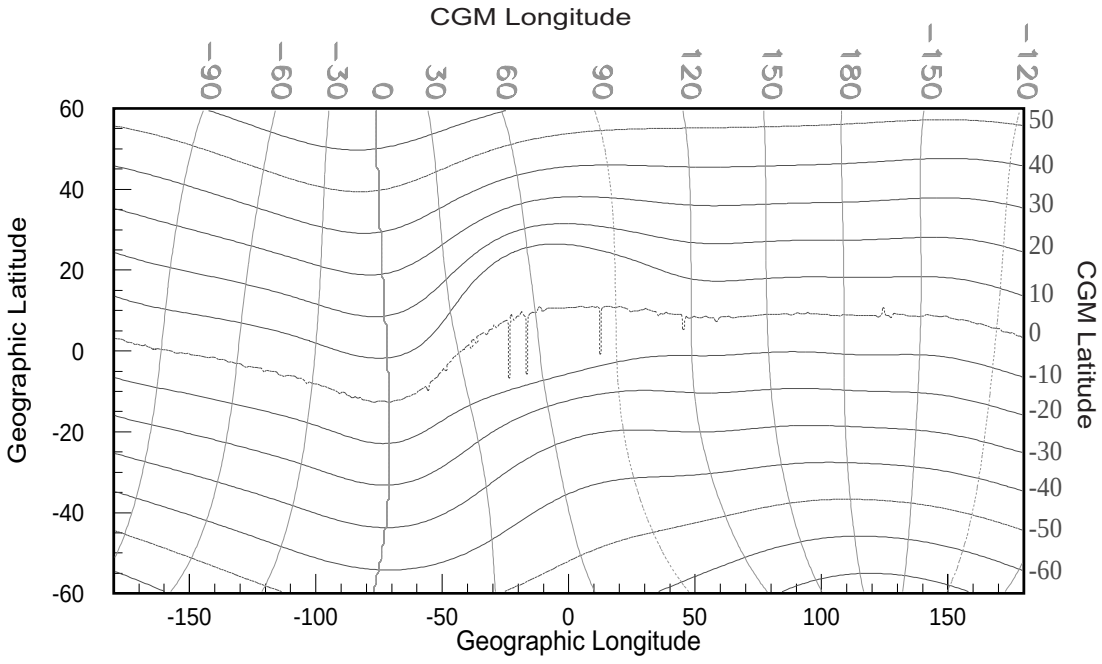

Figure 1.7: *Contour of the CGM coordinates versus geographic coordinates*

as International Geomagnetic Reference Field (IGRF), shown in fig. 1.6. The *IGRF* has order up to 10 degree (120 coefficients) for the main field and up to 8 degree (80 coefficients) for the secular variation. Using a multipole expansion, we cannot simply refer to the geomagnetical coordinate defined before. Using a realistic magnetic field, [12] developed a system called Correct GeoMagnetic Coordinate (CGMC). By definition, the CGM coordinates of a point in space are computed by tracing the IGRF magnetic field line through the specified point to the dipole geomagnetic equator, then returning to the same altitude along the dipole field line and assigning the obtained dipole latitude and longitude $(\lambda_{cgm}, \varphi_{cgm})$ as the CGM coordinates to the starting point. In some cases, near equator region, the magnetic field lines may not reach the dipole equator and the standard definition of the CGM coordinates may be ill posed and some correction must be applied [12]. The relation between geographical and CGCM coordinates are shown in fig. 1.7.

The External Field Even in absence of irregularities in the inner field, the dipolar structure is distorted by the solar wind because the wind pressure compresses the Earth's magnetic field. The solar wind plasma fuels the complex system of currents circulating in the magnetosphere, which are the sources of the external component of the magnetic field. The solar wind impinging on the dayside of the magnetosphere distorts the Earth's magnetic field into a shape different from a simple dipole. In the dayside, the magnetosphere is compressed by the solar wind pressure, causing an increase in flux density. Some of the flux from the dayside is diverted to the nightside through convection processes and as we move away from the dayside, the field is stretched in the anti-sunward direction, forming a long magnetic tail. This tail can stretch out to $200R_e$ or more behind the Earth (for comparison the Moon is at $\sim 60R_e$), as seen in fig. 1.8. The modelling region for the external field extends from low altitudes up to the distant geotail. The external magnetic field is much less stable than the internal one, and the factors contributing to the external field variations are not completely understood. The most important perturbating factor is the solar activity, which can be highly variable, causing strong magnetic disturbances with possible particle injection and acceleration in the magnetosphere.

The strength of magnetic disturbances can be parameterized using different magnetic indices based on ground observations. A widely used method is to consider magnetic observation from low-latitude stations and calculate the deviation of the magnetic north component from a smoothed average behaviour. This determines the so-called D_{st} index. When the D_{st} reaches a value below $-30 \div -40\ nT$, the disturbances qualifies as an intermediate storm. With the D_{st} below $-100\ nT$ we have an intense storm. There are also several other magnetic activity indices (K_p, A_p, etc) which give different weighting to the various current systems in the magnetosphere. A magnetic storm can be characterized by a strong world-wide suppression of the magnetic north component which lasts from several hours to days.

The representation of the external field is based on the modular principle, according to which, the external part of the total field $\mathbf{B_e}$ is represented as the sum of contributions from all the major magnetospheric current systems. The Tsyganenko model [13] is a semiempirical best-fit representation for the external magnetic field, based on a large number of satellite observations. It does not include the IGRF model for the inner dipole part of the geomagnetic field. The model includes the contributions from the external magnetospheric sources: ring

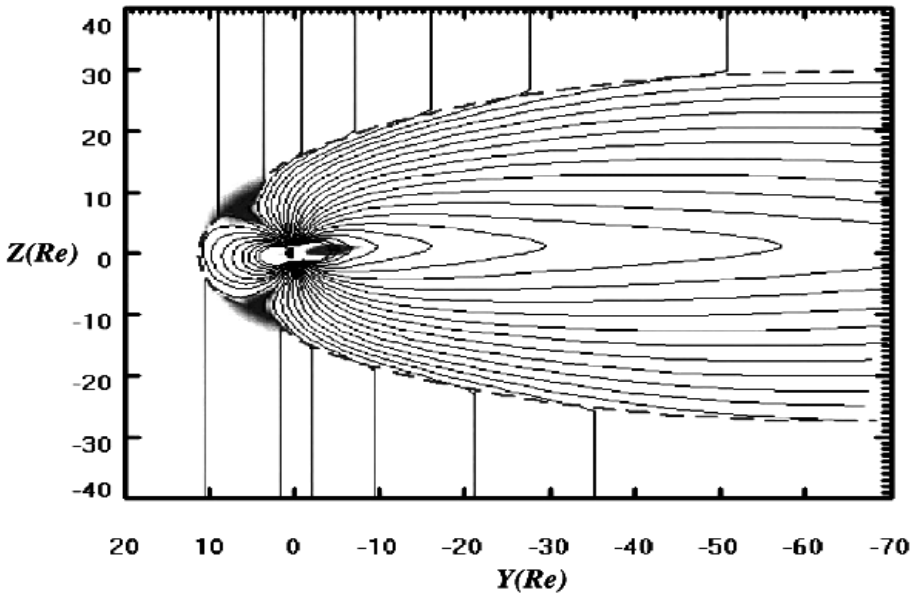

Figure 1.8: *The noon-midnight projection of the Tsyganenko model field line for the solar wind conditions of June 13, 1998 [13]*

current, magnetotail current system, magnetopause currents and large scale system of field aligned currents, schematically shown in fig. 1.2:

$$\mathbf{B_e} = \mathbf{B_{mp}} + \mathbf{B_{rc}} + \mathbf{B_t} + \mathbf{B_r} + \mathbf{B_{int}} \tag{1.13}$$

The term $\mathbf{B_{mp}}$ represents the field responsible for confining the field of all internal magnetospheric sources within the model boundary. The magnetopause shape can be determined solving the equation: $p = B^2/8\pi = 2n\,m\,v^2\cos\Psi$, where n is the number density of the solar wind particles, v the speed, m the mass and Ψ the angle between the velocity and the normal to the boundary of the magnetopause. This equation from the MHD express the pressure balance between the solar wind and the magnetic field pressure. The shape of the cavity is not known, and in the Tsyganenko model is described by an half ellipsoid sunward from the lunar distance, smoothly continued by a cylinder down to the far tail. The only control parameter is the solar wind pressure p_{dyn}.

The ring current term $\mathbf{B_{rc}}$ is based on a simple vector potential representation for an axially symmetric field, corresponding to a spread-out close to the equatorial distribution of the electric current. The D_{st} and the p_{dyn} are used to parameterize the data dependence. The tail current term $\mathbf{B_t}$ is different because of the larger spatial extent compared to $\mathbf{B_{rc}}$, and hence in addition of its shielding field, it removes from the model all the contributions from the part of the current flowing outside the magnetopause, replacing it with the contribution from the tail closure current flowing on the magnetopause itself. A complex dependence based on the p_{dyn} and magnetopause geometry is used for the $\mathbf{B_t}$ data dependence.

The $\mathbf{B_r}$ and $\mathbf{B_{int}}$ refers to the region 1 and 2 of Birkeland current systems and to the Interplanetary Magnetic Field (IMF), the details of which can be found in [13]. As a whole to

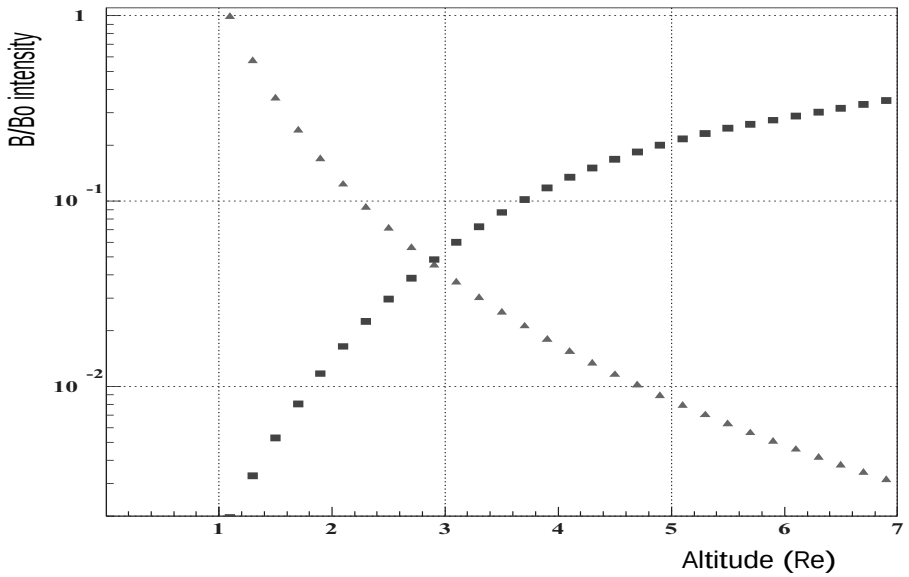

Figure 1.9: *Magnetic field intensity contributions relative to the value at the Earth surface and coming from the IGRF field model (triangles) and the Tsyganenko model (squares).*

control the model one has to use the D_{st} index from the storm activity, the p_{dyn} solar wind pressure and the IMF. As a comparison we have evaluated the internal and external field using IGRF95 and the Tsyganenko model as function of the radial distance from the Earth center. The result in fig. 1.9 shows as the external field becomes important for distance above 3 R_e.

1.4.2 Particle Motion in a Magnetic Field

The movement of a charged particle with charge q and mass m in a electromagnetic field is described by the Lorentz equation of motion:

$$\mathbf{F} = \frac{d\mathbf{p}}{dt} = q(\mathbf{E} + \mathbf{v} \times \mathbf{B}) \tag{1.14}$$

This equation describes the force exerted on a charged particle at position $\mathbf{r}$ by external electric and magnetic fields, $\mathbf{E}$ and $\mathbf{B}$. For particles in non-idealized magnetic fields, it is usually impossible to solve this equation analytically to get the full solution, and trajectories can be very complicated [6]. Under the assumption that the radius of gyration of the particle is small compared to the field gradient scales and the electric field term is small with respect to the magnetic term, the particle movement can be described by the so called *guiding center* approximation, which lead to the adiabatic approach for particle motion [7]. These approximations are common in plasma physics, and are useful in describing the orbits of many particles in space environments, such as the ring current particles moving in the near Earth's field.

Any mechanical system with periodic motion has adiabatic invariants associated to the period given by the action-angle integrals of the Hamilton-Jacobi formalism, defined as

$$J_i = \oint \mathbf{p_i} \cdot \mathbf{dq_i} \tag{1.15}$$

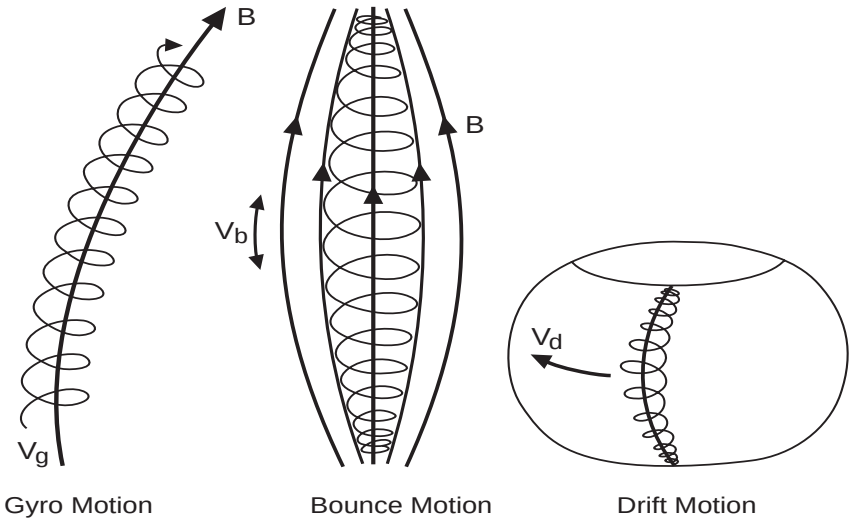

Figure 1.10: *Motion of a gyration ion in a magnetic field. On the left the gyration about a straight line. In the middle the converging magnetic field. On the right the gradient and curvature drift*

where the integrand is the canonical momentum of the particle $\mathbf{p}_i$ and $\mathbf{q}_i$ the generalized coordinate.

The motion and trapping of particles in the geomagnetic field is described by the theory of adiabatic motion of charged particles in a magnetic field. The particle trajectory is expressed as $\mathbf{r}=\mathbf{R}+\boldsymbol{\rho}$, where $\mathbf{R}$ denotes the trajectory of the center of gyration, the *guiding center*, and $\boldsymbol{\rho}$, the position of the particle with respect with the guiding center. As a result, it turns out that the motion can be expressed as motion along field lines and a drift motion perpendicular to the magnetic field line. It was found by Alfven that the motion of such a particle can be described with full relativistic generality by three invariants or first integrals of motion. The term adiabatic is used in the sense that the invariance is valid only if some parameter vary slowly in either time or space with respect to the motion scales. As a consequence, the motion of a particle in the magnetic field will have three modes.

The first mode of motion is the *gyration* of the particle around a magnetic field line. The angle α between the particle speed $\mathbf{v}$ and the magnetic field $\mathbf{B}$ is called *pitch angle*. The radius of gyration is defined as:

$$\rho = \frac{m_o \gamma v_\perp}{qB} = \frac{m_o \gamma v \sin\alpha}{qB} = \frac{p_\perp}{qB} \tag{1.16}$$

where γ is the Lorentz factor, and m_o the particle rest mass. The time scale is the gyroperiod, defined as:

$$\tau_g = \frac{2\pi m_o \gamma}{qB} \tag{1.17}$$

which for example close to the Earth for a $100\,MeV$ electron is $\sim 0.1\ ms$ while the gyroradius is $1\ Km$.

If the magnetic field variation is small during a Larmor period or within a gyroradius, i.e.

$$|\frac{\nabla B}{B}| \ll \frac{1}{\rho} \quad or \quad \frac{dB}{dt} \ll \frac{B}{\tau_g} \tag{1.18}$$

it can be easily shown that the first adiabatic integral of motion leads to the conservation of the magnetic moment μ of the particles:

$$\mu = \frac{p_\perp^2}{2m_o B} = \frac{p^2 \sin^2 \alpha}{2m_o B} = const \tag{1.19}$$

where p is the particle momentum. Since the energy is conserved, we may define the mirror ratio $B/B_m = \sin^2 \alpha$. As the particle moves into converging field region, α increases to 90^o where the particle reverses its motion and travels back along the field line in the direction from which it came (*mirror points*). The maximum value of the magnetic field magnitude felt by the particle is attained at the turning point where $B = B_m$ and $\sin \alpha = 1$.

The parallel component of the momentum can be written as:

$$p_\parallel = p \cos \alpha = p\sqrt{1 - \frac{B}{B_m}} \tag{1.20}$$

A particle can move along a field line until the magnetic field becomes equal to the maximum field. It will then turn and move back towards weaker field regions. On closed field lines, the particle will bounce between two mirror points denoted as m_1 and m_2.

The pitch angle is minimum at the magnetic equator during each bouncing and becomes 90^o at mirror points in the northern and southern hemispheres, as the particle penetrates into stronger magnetic field regions. When the Earth's equatorial magnetic field B_o is used as a reference, the particle's pitch angle anywhere along the field line is determined by the equatorial pitch angle, and the following relation holds: $\sin^2 \alpha = \sin^2 \alpha_o B/B_o$. The period of the bounce motion is given by:

$$\tau_b = 2 \int_{m_1}^{m_2} \frac{ds}{v_\parallel} = \frac{2}{v} \int_{m_1}^{m_2} \frac{ds}{\sqrt{1 - \frac{B(s)}{B_m}}} \tag{1.21}$$

where s is the arc length over a field line between the equator to the mirror points. A useful approximation holding for a dipole is:

$$\tau_b \approx \frac{R_o}{\sqrt{E_k/m_o}}(3.7 - 1.6 \sin \alpha_o) \tag{1.22}$$

which become respectively for protons and electrons:

$$(\tau_b)_p \approx \frac{2.41 R_o}{\sqrt{E_k}}(3.7 - 1.6 \sin \alpha_o) \tag{1.23}$$

$$(\tau_b)_e \approx \frac{5.62 \cdot 10^{-2} R_o}{\sqrt{E_k}}(3.7 - 1.6 \sin \alpha_o) \tag{1.24}$$

expressed in seconds while energies are expressed in MeV.

The periodic motion along the field line between mirror points is associated with the second adiabatic invariant of particle motion. If the field variations are small during a particle bounce

Period [s]	$E_p = 1000\ MeV$		$E_e = 100\ MeV$	
$\tau_{\mathbf{g}}$	10^{-1}	10	10^{-3}	3.10^{-2}
$\tau_{\mathbf{b}}$	0.08	0.16	0.01	0.03
$\tau_{\mathbf{d}}$	3	1	3.10^{1}	10^{1}
$R_o = L$	1.5	4.5	1.5	4.5

Table 1.1: *Typical gyration τ_g, bouncing τ_b and drifting τ_d periods for trapped protons and electrons*

period, i.e. $Bdt/dB \ll \tau_b$, a second adiabatic invariant can be obtained from the action integral associated with the bouncing. In terms of canonical momentum and conjugate coordinates, the second invariant or first integral of the motion can be written:

$$J_2 = \oint p_{\|} ds = 2p \int_{m_1}^{m_2} \sqrt{1 - \frac{B(s)}{B_m}}\, ds = 2pI \tag{1.25}$$

where I depends solely on the field geometry. If the time scales variations of the field over a bouncing are small with τ_b then J_2 is an adiabatic invariant i.e. $dJ_2/dt \simeq 0$.

A particle experiences a force associated with field gradients and inhomogeneity. The gradient drift is caused by a Lorentz force perpendicular to $\mathbf{B}$ and in the direction of the gradient normal to the field, $\nabla_\perp$, and is given by:

$$\mathbf{v_{dm}} = \frac{m\mathbf{v}_\perp^2 \mathbf{B} \times \nabla \mathbf{B}}{2qB^3} \tag{1.26}$$

The guiding center motion along the field line causes a centrifugal force due to field line curvature which yields to a drift velocity

$$\mathbf{v_{dc}} = \frac{m\mathbf{v}_\|^\mathbf{2} \mathbf{B} \times \nabla \mathbf{B}}{qB^3} \tag{1.27}$$

Note that drift speed depends both on energy and charge, therefore electrons and protons will drift in opposite directions. The slow longitudinal drift is westward for $q > 0$ and eastward for $q < 0$ particles, with the drift velocity proportional to the particles kinetic energy. This generates a current, known as ring current, and plays an important role in planetary physics.

The overall drift velocity is then $\mathbf{v_d} = \mathbf{v_{dm}} + \mathbf{v_{dc}}$. The bounce averaged drift period can be approximated for a dipole field as

$$\tau_d = \frac{q\pi B_o R_o^2}{3E_k(0.35 + 0.15 \sin \alpha_o)} \tag{1.28}$$

which becomes both for protons and electrons:

$$(\tau_d)_p = (\tau_d)_e \approx \frac{1.05}{E_k R_o (1 + 0.43 \sin \alpha_o)} \tag{1.29}$$

expressed in hours with E_k in MeV.

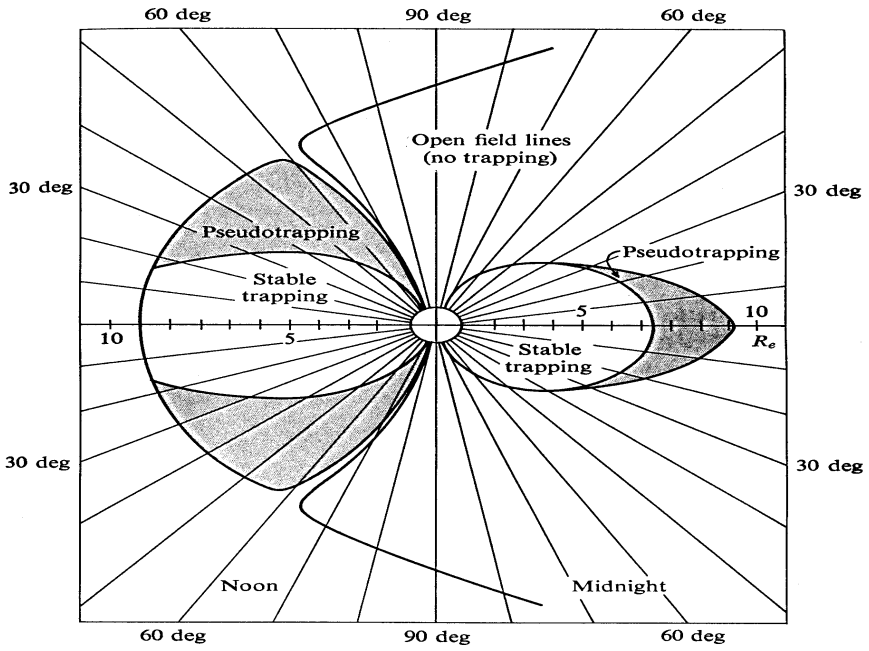

Figure 1.11: *Location of Stably and Quasi Stably trapping region in the Earth's equatorial plane [15].*

If $Bdt/dB \ll \tau_d$ the third action integral:

$$J_3 = \frac{q}{c} \oint \mathbf{A} \cdot \mathbf{ds} = \frac{q}{c} \Phi \tag{1.30}$$

where Φ is the magnetic flux through the surface, is constant. The magnetic flux is conserved in absence of forces or if the magnetic field does not vary significantly during a particle drift period. In fig. 1.11 the regions of stable trapping are shown. The trapping conditions depend on the possibility to complete the drift, and the theoretical boundary of stable trapping is a surface which separates open and closed field lines around the Earth.

A special coordinate system may be defined using the adiabatic invariants to describe the motion of a charged particle trapped in the Earth's magnetic field [14], because all the particles with the same invariants will move in the same way in the magnetic field.

Therefore, they provide naturally a coordinate system where particles in geomagnetic equivalent positions have the same coordinates, irrespective from the geographical position. As a consequence a particle will move following segments of field lines such that the three invariants are conserved.

The set of field line segments defines a surface in space called *drift shell* as shown in fig. 1.12. The value of the magnetic field B and the integral invariant I (eq. 1.25) can be obtained for any observational point in space using models of the Earth's magnetic field. More easily readable coordinates can be derived from the adiabatic invariants. All the particles with the same μ, will mirror at the same B_m or equivalently α_o. Therefore, the conservation of the first invariant implies that B_m and α_o are also constant and they can be used as invariant in place of μ.

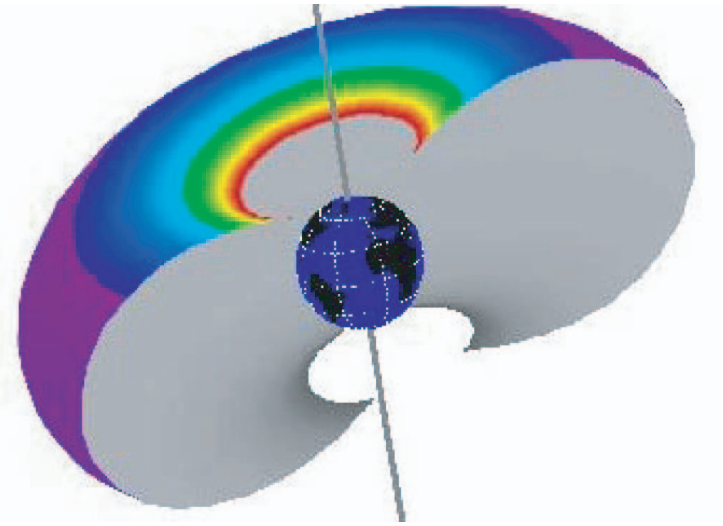

Figure 1.12: *Closed drift shell example typical for the Van Allen belt produced with SPENVIS [26].*

For the second invariant following the dipolar field analogy in which the equatorial radius R_o completely determines the drift shell once B_m or α_o are fixed.

The following relation holds for a dipole field:

$$\frac{R_o^3 B_m}{M_d} = f_d(\frac{I_d^3 B_m}{M_d}) \tag{1.31}$$

where f_d is a known function for the dipolar case [14]. Dealing with the real magnetic field an equivalent conventional equatorial radius can be defined using the relation:

$$\frac{L^3 B_m}{M_o} = f_d(\frac{I^3 B_m}{M_o}) \tag{1.32}$$

which depends on the invariants I and B_m of the real field. L is called *L-shell parameter* and through such convention we can use the dipolar relations even for a distorted field. The position of a particle can be defined by the magnetic field and a parameter L which identifies the drift shell on which the particle is moving.

Another set coordinates used in mapping particles in the geomagnetic field are the *invariant coordinates* R_m and Λ_m which give a representation equivalent to a polar coordinate mapping defined through:

$$R_m = L\cos^2\Lambda_m \tag{1.33}$$

$$B = \frac{M_o}{R_m^3\sqrt{1+3\sin^2\Lambda_m}} \tag{1.34}$$

This system is widely used as coordinate system to describe processes involving particles mirroring at very low latitudes. To be noticed that $R_m = 1$ does not correspond to the Earth's surface due to the effect of higher order terms in the multipole expansion of the magnetic field.

Since the magnetic gradient drift is perpendicular to both $\mathbf{B}$ and $\nabla_\perp B$, it follows that for a particle trapped in the equatorial plane, the drift trajectory will be along a surface of constant

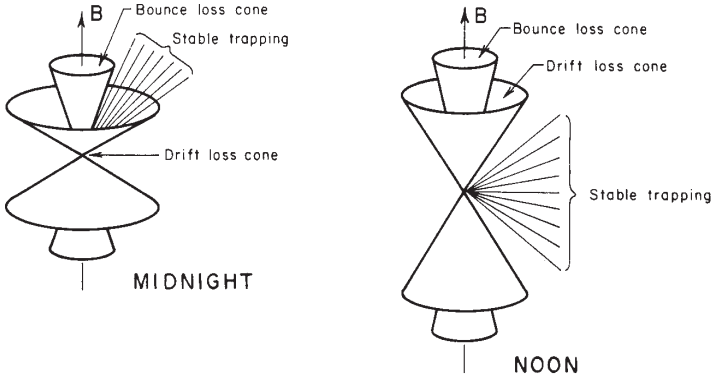

Figure 1.13: *Particles inside the loss cone are lost in the dense atmosphere [15]*

B. The parameters B_m and L, are sufficient to identify the position of a particle in a static or slow varying field having dipole symmetry. In a field with axial symmetry, particles would simply drift around in circles.

It turns out that for a particle to be trapped, the mirror points must lie well above the dense atmosphere and the drift surface must contain only closed field lines.

Since the solar wind compresses the magnetosphere, a given value of the magnetic field will lie closer to the planet on the night-side with respect to the day-side. If a drift shell for a particle is closed at all longitudes, then the particle is said to be stably trapped. If the particles of the radiation belts are able to gyrate, bounce and drift while conserving all the invariants, they will remain trapped indefinitely in the magnetosphere.

A major sink for particles on drift shells is the interaction with the atmosphere if mirror points are below atmospheric limit. There is an equatorial pitch angle on every field line for which the associated mirror point will be low enough in the dense atmosphere so that the particle will undergo to collisions with the atmospheric particles and will be removed. This range of pitch angle defines a cone known as the *loss cone* as shown in fig. 1.13.

If B_a denotes the field intensity at top of atmosphere, B_o the field magnitude at the equator and α_a the equatorial pitch angle of a particle which mirrors at B_a, then the conservation of the first adiabatic invariant implies that the loss cone is defined for all equatorial pitch angle α_o which satisfies :

$$0 < \alpha_o < \alpha_a = \arcsin \sqrt{\frac{B_o}{B_a}} \tag{1.35}$$

Any particle having its equatorial pitch angle in this range will not survive more than few bounces and will be lost into the atmosphere. From a mathematical point of view the loss cone represents a perfectly absorbing boundary at which the flux is forced to vanish. Thus, even if the adiabatic invariants are conserved, these trajectories will not contain particles. However, when the eccentricity of the Earth's magnetic field is taken into account, it is necessary to make a distinction. We can define the *bounce loss cone* which contains particles that will precipitate within few bounce periods, and the *drift loss cone* for particles absorbed into the atmosphere within the drift period. They are expected to be identical at their maximum in the SAA [28].

The deterministic approach for the single particle analysis may not be appropriate in several circumstances. The drift shells are filled by the action of several process as acting together, like injection and loss of charged particles in the shell and possible acceleration and diffusion mechanisms. The chain is possibly operating at a rate in which on long term the system would be in equilibrium. The time dependent fields are not known precisely and therefore is not possible to predict the motion of the single particle. In this case, only statistical treatment is possible leading to the diffusion and transport theory with the Fokker-Plank equation, in the adiabatic invariant phase space. Since the drift period is the largest, the third adiabatic invariant is more likely violated by fluctuations of the electric or magnetic fields leading to radial diffusion [28]. Depending on the radial gradient particles may diffuse inward or outward in L space in such a way that, if the first invariant remains conserved, particles gain energy as they move to regions with stronger field for the inward diffusion and are decelerated in the outward diffusion.

Violation of the first two invariants produce scattering in the pitch angle, leading to losses of particles when the pitch angle becomes too small and bringing the mirror points into the atmosphere. Typically, this may be due to particle-particle and wave-particle interactions. Moreover, the three adiabatic oscillations are non linear because their frequencies depend on the magnetic moment of the particle. There are conditions where the adiabatic conservation does not hold, and the magnetic moment is not conserved over the entire particle orbit. This occur when non-adiabatic motion becomes important.

The lack of conservation of the invariants may be caused by non linear resonances between motion components. The larger are the differences in the components frequencies, the weaker is the effect of resonances, and the more stable is the motion. The most dangerous resonances are those between the gyromotion and the higher harmonics of the longitudinal oscillations. One crucial place where adiabatic theory breaks down is in the vicinity of a sharp bend in a magnetic field line. Particles that lie within this range frequently have non-adiabatic orbit behaviour. In other words, the guiding center assumption that the orbit is separable is not longer valid. One way of characterizing the degree of non-adiabaticity in an orbit is the *smallness parameter* ϵ ([29],[30]):

$$\epsilon = \frac{\rho}{R_m} = \frac{pc}{qB_o R_m} \tag{1.36}$$

which is defined to be the ratio of the gyration radius ρ of a particle with the curvature of a magnetic field line R_m at the equator. It depends on both the energy and mass of a particle, as well as the magnetic field magnitude. Adiabatic orbits have typical values of $\epsilon \leq 0.3$. For higher values, chaotic orbits begin to show up. Chaotic orbits generally do not conserve the magnetic moment. The cumulative effects of many small scattering in μ can significantly affect the trapped populations and lead to stochastic instability as described in [8]. They often magnetically mirror close to the current sheet, bouncing in and out several times with small parallel velocities until they either stay trapped or exit the current sheet with a large parallel velocity.

1.4.3 Origin and Properties of the Radiation Belts

The radiation belts are the highest energy component of the inner magnetosphere, where the kinetic energy range is well above $3 KeV$. The shape of the belts encircling the planet is toroidal-like around the magnetic axis. Approximatively, the motion of each particle is at constant energy,

subject only to the Lorentz force.

The phenomena in the Earth's magnetic field have been studied intensively, since Van Allen's discovery in 1958. In addition a serie of artificial belts were produced both by USA and USSR between $1958 \div 62$ as a product of radioactive fission nuclei injected into the belts by nuclear explosions at high altitude (sigh!). Other temporary radiation belts may be formed naturally in the deep magnetosphere during injection due to solar events. The terrestrial radiation belts consists of two components, an *inner belt* in which the main energetic components is protons and the *outer belt* made of energetic electrons. A schematic picture of the Earth's radiation belts is given in fig. 1.4. The charge neutrality is not an issue since the radiation belt particles are very few compared to the ambient thermal plasma and charge balance is made through particles at lower energies. The average extension of the inner belt ranges between an equatorial distance from the lower boundary, the atmosphere, up to $1.8R_e$, the outer belt from this limit outward to $9.4R_e$ with some overlap. The inner belts consists mainly of protons in the energy range $0.1 - 500\ MeV$ from an altitude $L \sim 1$ out to $L = 3.5$ with a maximum between $L = 1.5$ and $L = 2$; the dominant species in the outer belts are the $KeV - MeV$ electrons with highest fluxes between $L = 3$ and $L = 6$. The energetic trapped protons are confined below $L \sim 3$, while lower energy protons are spread over a wider region. Anyway it is clear that the actual population is very dynamic over different time scales. Slow variations arise from the 11 year solar cycle, inducing a periodicity of the low altitude trapped population, and from the secular changes in the geomagnetic field which drifts the dipole center away from the center of the Earth at a rate of $2.5\ Km/year$. The population distribution of electrons is characterized by two zones of high intensities, separated by a slot region. There is a significative relativistic electron population also in the inner belt, but between $L = 2$ and $L = 3$ there is a clear slot region void of electrons above $1\ MeV$. The location of the inner, outer and slot region depends on the electron energy, with lower energy electron populating the outer belt. However during strong storm events, the slot region may be filled up with charged particles accelerated by induced electric fields. The outer radiation belt is highly variable and during strong storms the electron belts expands beyond geostationary orbit. High fluxes of relativistic electrons (above few MeV) have been associated to several spacecraft failures at geostationary orbit. The physical mechanisms of magnetospheric phenomena are of electromagnetic nature. In a generalized sense there are as many different radiation belts as there are different species of particles and energy ranges that one wishes to distinguish.

There is a major asymmetry in the near field of the Earth, known as *South Atlantic Anomaly (SAA)*. This is a region where the field is much weaker than at other longitudes. Thus an orbiting particle must plunge deeper into the atmosphere to reach a particular B_m determined by the equatorial pitch angle. The net result is an increase in the magnitude of the loss cone as the particle drifts across the longitudes corresponding to the SAA. This is the ultimate sink for inner zone radiation belt particles. The SAA is a region where the offset and the tilt of the geomagnetic axis with respect to the Earth's rotation axis brings in the inner edge of the inner radiation belts to low altitudes over the SAA. For altitude below $800Km$ and inclination below 40^o, the SAA dominates the spacecraft radiation environment, although at high latitude the outer belts are encountered. In this region fluxes are extremely variable with altitude, because of the interactions in the upper atmosphere layers which absorb particles. The resulting large

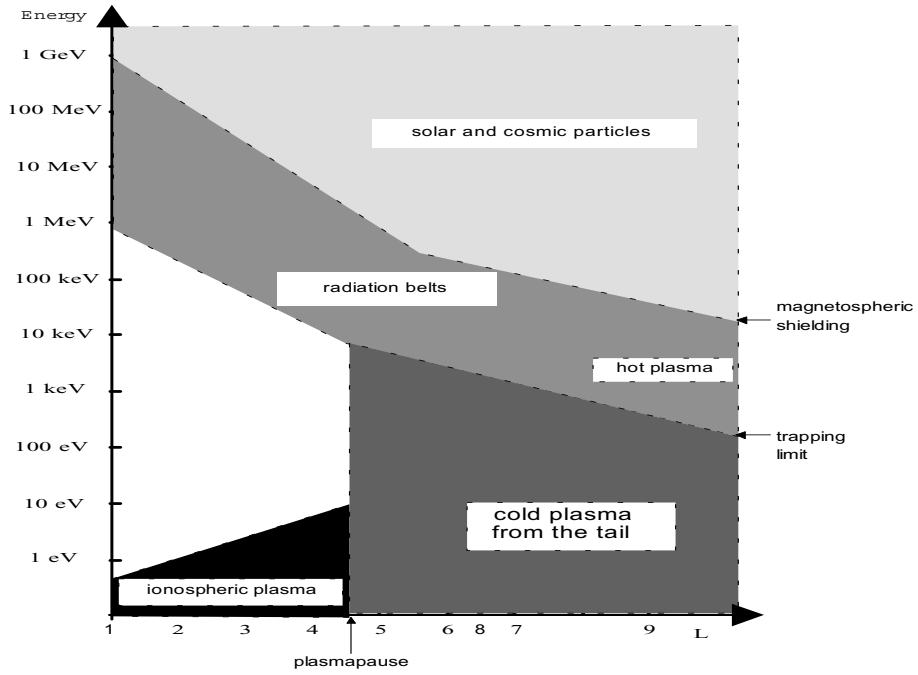

Figure 1.14: *Particle energy related to L in the inner magnetosphere [45].*

spatial gradients are difficult to model accurately, because small errors in B or L coordinates can result in large flux change.

Moreover they cause anisotropy of the trapped particle fluxes. At a given point the guiding centers moving from west to east are located below that point. Therefore particles coming from west experience denser regions of the atmosphere and are more easily absorbed. The effect is most important a high energies, where gyroradii are large and therefore the difference in altitude of the guiding center is larger. At $400\,Km$ of altitude we can have and east-west ratio of a factor 4 at $200\,MeV$. This anisotropy is linked to the atmospheric density and solar cycle dependence.

1.4.4 Radiation Belts Models and Data

To identify the magnetic particle direction, following [16] a natural definition for an intrinsic coordinate system is given by (see fig. 1.15) :

$$\mathbf{z} = \frac{\mathbf{B}}{B} \qquad \mathbf{x} = \frac{\nabla_\perp B}{|\nabla_\perp B|} \qquad \mathbf{y} = \mathbf{z} \times \mathbf{x} \tag{1.37}$$

In this way the polar and azimuthal angle (α, β) for a particle coming from the direction $\mathbf{d}$, are defined by

$$\cos\alpha = \mathbf{d} \cdot \mathbf{z} \qquad \tan\beta = \frac{\mathbf{d} \cdot \mathbf{y}}{\mathbf{d} \cdot \mathbf{x}} \tag{1.38}$$

The particle direction on the drift shell at the equator will have looking direction (α_o, β_o). Due to the particular choice of the intrinsic reference system it can be shown will result $\beta_o = \beta$

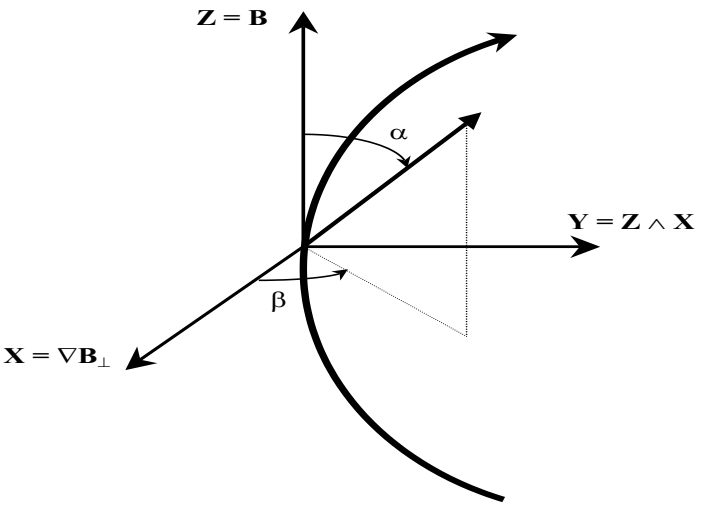

Figure 1.15: *The intrinsic coordinate system for the definition of the particle direction* (α, β)

[23]. According to the Liouville theorem, the directional flux expressed as $J(\mathbf{r}, E_k, \mathbf{d})$ of trapped particles of kinetic energy E_k, observed at $\mathbf{r}$ in the direction $\mathbf{d} = \mathbf{d}(\alpha, \beta)$ can be converted as a function of E_k and the adiabatic invariants only. We can use (E_k, B_m, L) coordinates (or any combinations of adiabatic invariants like α_o for example) the following relation holds:

$$J(\mathbf{r}, E_k, \alpha, \beta) = j_\perp(E_k, B_m, L) \tag{1.39}$$

where $j_\perp(E_k, B_m, L)$ is the perpendicular flux observed at the mirror points [15] where $B_m = B_m(\mathbf{r}, \alpha, \beta)$, $L = L(\mathbf{r}, \alpha, \beta)$. Generally for radiation belts model the small gyroradii approximation is applied and the guiding center trajectory coincides with the magnetic field line. One has to remember that this approximation is no longer valid in region where the flux scale lenght become of the same order, or lower, than the gyroradii. The distribution of the omnidirectional flux of protons and electrons has been measured since 1958 using many different types of particle detectors, flown in all regions of the magnetosphere.

The latest versions of the NASA electron model are called AE-8 MIN and AE-8 Max [17]. These models refer to conditions of minimum and maximum solar activity, respectively. The corresponding proton models are AP-8 MIN and AP-8 MAX [18]. The (E, L, B) dependence of the omnidirectional proton and electron fluxes is stored as a three dimensional array, and are of public domain [http://nssdc.gsfc.nasa.gov].

Both AE-8 and AP-8 models are static representations of trapped radiation environment, with local time dependence averaged out. The Institute of Nuclear Physics (INP) of the Moscow State University also developed various models of space radiation, since 1970's. The most recent models are described in [20] and called INP models. The INP models are static representation of trapped radiation particles flux, with local time dependencies averaged out like AE-8/AP-8 models, and arranged for solar minimum and maximum activity. The INP model uses the (B, L) coordinates system to identify a drift shell, while in the NASA model B/B_0 is used instead of B. In constructing the models, energetic particle observations obtained with various instruments (Geiger-Muller tubes, scintillator/photomultiplier tubes, ionization chambers, solid

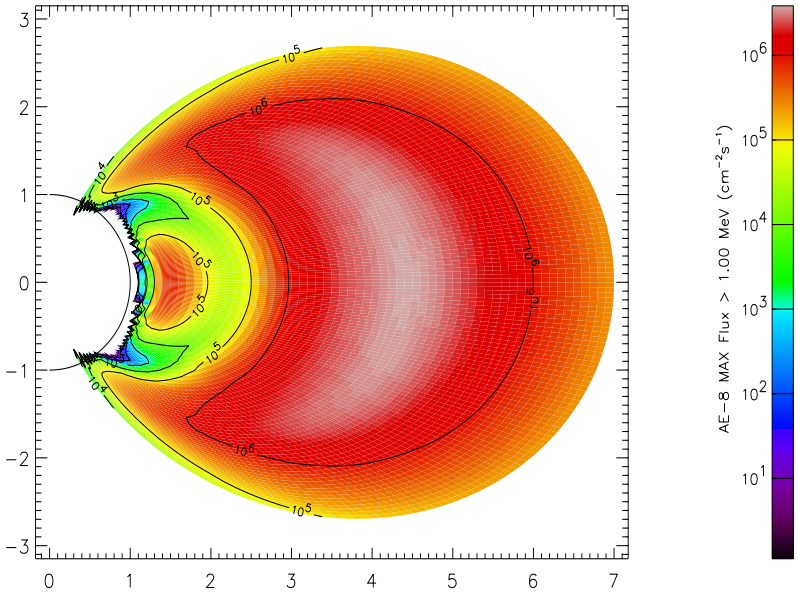

Figure 1.16: *AE8-MAX integral electron flux above* 1 MeV *[24].*

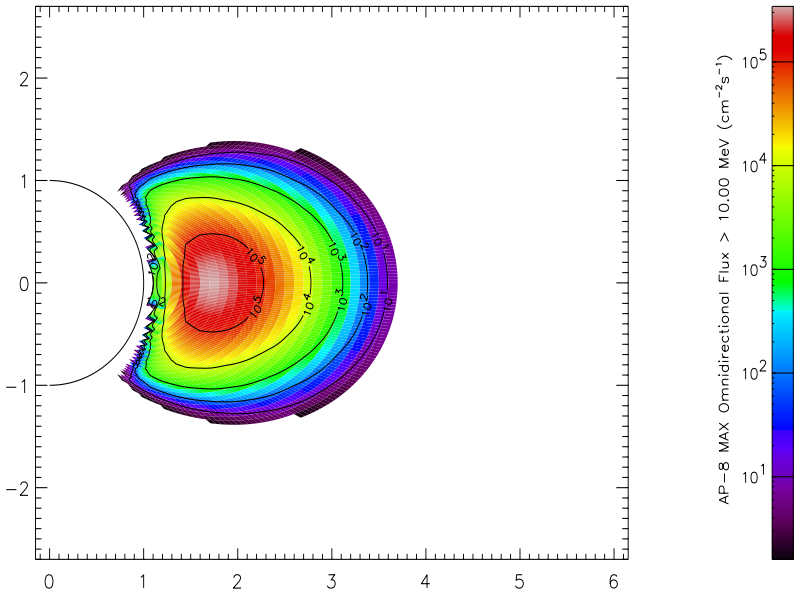

Figure 1.17: *AP8-MAX integral proton flux above* 10 MeV *[24].*

Characteristic	AP-8	AE-8	INP p	INP e
Energy Range (MeV)	0.1-400	0.04-7	0.1-400	0.04-7
L Range	1.15-6.6	1.2-11	1.2-6.6	1.2-7
Epoch	1964-70	1964-70	1959-73	1959-73
Publication	1976	1983	1991	1991
Num Satellites	24	24	5	5
Flux Range ($cm^{-2}sr^{-1}s^{-1}$)	10.	10.	1.	1.

Table 1.2: *Comparison between NASA and INP model parameter*

state detectors, beta ray spectrometers, solid state telescopes and others) were used. Though solar protons, galactic cosmic rays and high charge state particles data were excluded from the trapped radiation data base, the residual energetic electrons coming from the Starfish experiment in 1962 were included.

A comparison between NASA and INP models can be found in ([19],[21]) together with a comparison with more recent observations. The static NASA radiation belt models have been extensively used in the past for spacecraft design and post-event analysis. After intensive studies in 1960's and 1970's the interest in radiation belt studies faded and their main physical features including source and loss processes, were assumed to be resolved, at least in principle. Recent measurements have, however, shown that the radiation belts are extremely dynamic, and vary significantly over relatively short periods of time. Radiation belt particles cause radiation damage to electronic components, solar cells, and materials. Spacecraft shielding enclosures are typically a few millimeters thick and composed of aluminium. To penetrate 2 mm of Al, an electron must have an energy of above $1 MeV$ and a proton above $20\,MeV$. The International Space Station (ISS) and the Space Shuttle operate essentially in the inner edge of the radiation belts. Recent interest in the radiation-belts was due to the recognition that many future missions will carry onboard radiation-sensitive advanced technologies or non-hardened technologies, and on missions such as CRRES, SAMPEX, and small satellites (e.g. UoSAT's, APEX, STRV). CRRES was comprehensively instrumented to provide a data set of energetic particle fluxes for the development of new radiation belt models. The satellite also contained important radiation effects experiments. In figs. 1.16 and 1.17 the AE8-MAX above $1 MeV$ and AP8-MAX above $10\,MeV$ are shown, respectively in invariant coordinate space from [24]. In 1991 CRRES discovered the unexpected formation of a new intense radiation belt of ultrarelativistic ($E > 15\,MeV$) electrons in the slot region at $L \sim 2$ which decayed very slowly. The acceleration of electrons and ions was associated with the large magnetospheric storm of March 24, 1991 [48] when the interaction of a strong solar wind shock with the magnetosphere caused the creation of a new radiation belt in the inner trapping zone. Particles gained tens of MeV by inward motion and formed long lasting new radiation belts around $L = 2.5$.

Moreover, short term variations may be induced, especially in the outer zone, over periods of few hours due to changes in the magnetospheric activity. In addition, there are important interactions between the inner belts and the atmosphere, leading to slow changes. At altitudes below $0.3 R_e$, anisotropies in the proton flux are observed, indeed the gyroradii of trapped protons with energy much above $1\,MeV$ is comparable with the atmospheric scale height, meaning that they cross different atmospheric densities during the gyration motion. This important aspect of inner magnetosphere physics was still quite incomplete. This initiated a renewed interest

for the study of the processes involved in trapped radiation belts physics. For example, the polar-orbiting SAMPEX satellite of NASA provided much additional information on relativistic particles injections into the radiation belts. Thus, further work is required before the onset of these particle flux enhancements can be modelled and predicted especially for the lack of reliable high energy data. Several efforts for more dynamic radiation belt models and standards are presently underway.

In Europe, this effort is lead by the Belgian Institute of Space Aeronomy (BIRA/IASB) in Brussels. BIRA/IASB has lead a series of ESA Contracts on Trapped Radiation Environment Model Development (TREND) [25]. These studies used the AE8 and AP8 models. An important part of the TREND studies was the incorporation of the Russian radiation belt, the INP, with the AE8/AP8 NASA models.

The applications of these developments are included in the Space Environment Information System (SPENVIS, also developed under an ESA Contract) [26]. SPENVIS is a web-server based service which can be used to generate spacecraft trajectories or a co-ordinate grid. It calculates the geomagnetic coordinates B and L, trapped proton and electron fluxes, solar proton fluences, radiation doses, damage equivalent fluxes for Si and GaAs solar panels, Linear Energy Transfer (LET) spectra and Single Event Upsets (SEU), trapped proton flux anisotropy, atmospheric and ionospheric densities and temperatures, atomic oxygen erosion depths and spacecraft charging. Magnetic field line tracing is implemented, as well as the generation of flux world maps and altitude dependence plots of the magnetic field and the current models of the neutral atmosphere and the ionosphere. The server is continuously updated.

In this work, the SPENVIS resources have been extensively used.

Models trying to reproduce the dynamical structure of radiation belts with a diffusion approach exist. Among them, we quote the Salammbo model, developed at CERT-ONERA in France [33]. The model solves diffusion and convection equations in the inner magnetosphere assuming a dipole magnetic field and simple convection and corotational electric fields. The model computes the particle fluxes from convection-diffusion equations.

Using statistical theory, a particle population is completely described by a six-dimensional phase space distribution function, $f(J_1, J_2, J_3, \varphi_1, \varphi_1, \varphi_1, t)$ where φ_i is a space coordinate and J_i the corresponding conjugate moment. The formalism allows to find the distribution function f resulting from the solution of a parabolic partial equation called convection-diffusion equation derived from the Fokker-Plank equation:

$$\frac{\partial f}{\partial t} + \sum_{i=1}^{3} \frac{dJ_i}{dt}\frac{\partial f}{\partial J_i} + \sum_{i=1}^{3} \frac{d\varphi_i}{dt}\frac{\partial f}{\partial \varphi_i} = -\sum_{i=1}^{3} \frac{\partial}{\partial J_i}(D_{J_i} f) + \sum_{i=1}^{3}\sum_{j=1}^{3} \frac{\partial^2}{\partial J_i \partial J_j}(D_{J_i J_j} f) + Sources - Losses \tag{1.40}$$

On the left side of eq. 1.40, we have the undisturbed trajectory of a particle population in the electric and magnetic fields, on the right the mean effect of the weak interactions where D_{J_i} are the dynamic coefficients, or friction terms, and $D_{J_i J_j}$ the dispersion coefficients. The transport coefficients in the Fokker-Plank equation correspond to the violation of the adiabatic invariants which can result either by collisions (with atmosphere) or interactions (magnetospheric wave or magnetic disturbance). Without collisions the Fokker-Plank equation reduces to a diffusion

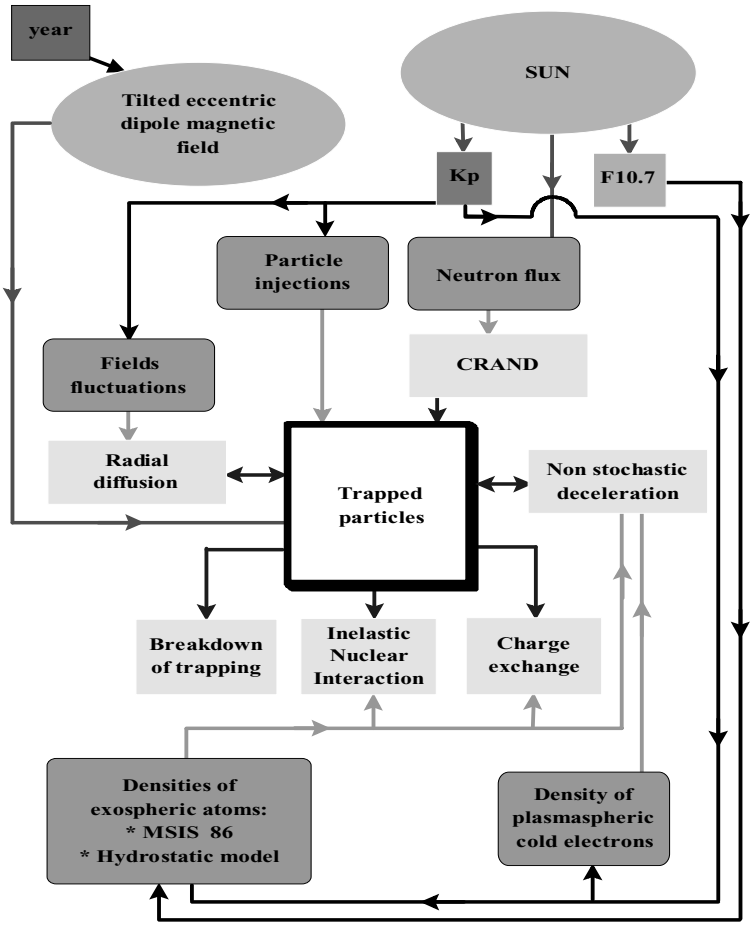

Figure 1.18: *General description of radiation belt Salambo model [45]*

equation. The most recent model allows for an eccentric dipole and thus has three spatial dimensions, and energy as the fourth dimension. The Salammbo model has some attractive feature: it calculates the particles from realistic diffusion equations, including the most important diffusion mechanisms: wave particle and neutral atmosphere interactions. More problematic from the operational point of view is that, to produce realistic results, the model requires inputs from several other models in addition to the background electric and magnetic fields, and the correct description of the upper ionosphere and atmosphere is essential. Furthermore, the outer boundary conditions as well as more complex background fields require further investigation. The complexity required for the model is shown in fig. 1.18, where all the input and relations can be seen.

1.4.5 Source and Loss Processes in Radiation Belts

Magnetic field structure fixes the geometrical characteristics of the drift shell on which particles can move. The steady structure of the belts is determined by a dynamical equilibrium depending

on many different processes as depicted in eq. 1.40. The engine fuelling the belts are solar particles and the cosmic ray impinging the atmosphere described in the next chapter.

Protons A flux of CR reaches the Earth regularly. When entering the atmosphere, cosmic rays collide with atmospheric nuclei producing secondary particles, from leptons to heavy nuclei, which may become trapped into the belts. Among the secondaries, neutrons may diffuse out into space. Due to their radioactive decay, these albedo neutrons contribute to inject protons into the radiation belt. This Cosmic Ray Albedo Neutron Decay (CRAND) is the dominant source of low energy protons at low altitudes [34]. Note that cosmic ray also produce albedo that may be trapped directly in the belts. CRAND can account for processes which can be relevant for the study of the inner edge of the proton radiation belt ($L < 2$) at low energy. Albedo neutrons are also produced by solar protons when they collide with atmospheric components in the auroral regions. The Solar Proton Albedo Neutron Decay (SPAND) corresponds to a source about ten times less intense than the CRAND source.

The theoretical computations and experimental measurements of the cosmic ray albedo neutrons has been extensively reviewed by [42]. The energy range where neutrons are the principal proton source extends to about $30\,MeV$ while the CRRES data show that protons well above $50\,MeV$ are accelerated and injected by shock waves, and this process can be source of protons in the O(100 MeV) region.

The neutron leakage flux at the top of the atmosphere (i.e. about 100 km) depends on the neutron energy, the geomagnetic latitude at which a neutron leaves the Earth and the zenith angle made of the neutron velocity vector. It is commonly accepted that these dependencies can be treated separately. Less neutrons are produced in the equatorial region since the geomagnetic cut-off is higher than in the auroral region [42]; the neutron energy spectrum does not follow a simple spectral law, as found in early studies [43]. The dependence on the zenith angle is not well known.

Since neutron production depends on the cosmic ray flux, it varies during a solar cycle. It increases from solar maximum to solar minimum by $\sim 25\%$. The solar proton albedo neutrons depends on the occurrence of solar flares. Compared to the cosmic ray albedo neutron, their energy spectrum is much steeper and their production is concentrated at high latitudes.

The proton injection rate due to albedo neutron is usually evaluated for a drift shell under the assumption that the gravitational forces are negligible. The mean neutron lifetime is long compared to residence time in the radiation belts. Neutrons move along a straight line, decay anywhere along the trajectory with equal probability, with proton conserving the direction of flight and energy of neutron during the radioactive decay. At a given point along the drift shell, the proton injection is obtained only taking into account the neutrons with a correct local pitch angle.

The residence times of single particles in the radiation belts of the Earth, controlled by ionization losses in the atmosphere below $400Km$, increases rapidly to the order of years at distance of $1.25R_e$ and then decline in a complex way to the order of weeks, days in the outer belt. Different models have been used to describe the dynamics of the proton radiation belts. Each model takes into account some physical processes and neglects some others. The processes can be classified by their location in the diffusion equation 1.40: source, loss, friction and

diffusive terms. A inner zone proton will encounter in general residual atmospheric density along the orbit. Very likely it will collide with atomic electrons in the upper ionosphere. Since it is massive compared to electrons, it will undergo small or negligible scattering in pitch angle, but will be decelerated. In general, the lifetime of a typical proton against deceleration by Coulomb collisions is of the order of $1000\,years$. This is comparable to the time scale for secular variation of the magnetic field ($\sim 0.016\,G/century$), so that contraction of drift shells can make up the energy loss. This follows from the fact that if the magnetic field increases and the magnetic moment is conserved, then the energy must increase as well.

For protons at the lower end of the radiation belt energy scale, there is another sink which is more effective than Coulomb deceleration. This sink is charge exchange. The charge exchange reaction transforms a trapped proton into neutral hydrogen by the transfer of an electron from an atmospheric ion, atom or molecule. Such a reaction only occurs at low altitudes and for low energy protons. It is generally admitted that charge exchange represents an important mechanism for the removal at energies lower than 1 MeV, while nuclear interaction losses at $O(100\ MeV)$ energies. For both mechanisms, the absorption rate is given by $\Lambda = \nu \sum_i \rho\sigma_i$ where the sum is over the different atmospheric components, ρ_i is the density of component i, σ_i is the cross section for inelastic nuclear collisions and charge exchange, and ν is the proton velocity. The energetic proton becomes a fast neutral hydrogen atom which is no longer confined by the magnetic field, while the newly created ion will have a much lower energy and will not be a radiation belt particle.

For proton of magnetic moment $1MeV/G$, the lifetime against charge exchange with ambient hydrogen atoms is a fraction of a day at $2R_e$. Energetic protons may undergo to inelastic nuclear collisions with atmospheric constituents. During these inelastic nuclear collisions, the proton can be absorbed or slow-down and deviated, secondary protons may be produced as well as other particles such as neutrons, light nuclei, and leptons. It is generally assumed that the incident proton does not remain geomagnetically trapped after the inelastic nuclear collisions and that no secondary protons are produced.

Protons can be diffused or transported into an unstable trapping region, i.e. a region where J_i are not more defined or invariant. Different situations may cause a breakdown of the adiabatic conditions. Open field lines at high latitudes above the auroral region, where the magnetic field lines extend indefinitely to the geomagnetic tail; they are linked to the interplanetary magnetic field or they are close to the neutral sheet In this region, charged particles bounce eventually once and then escape from the vicinity of the Earth. Note that the first adiabatic invariant can still be defined. In some parts of the outer magnetosphere, the guiding center of charged particles can be located on a closed magnetic field line, such that both first two adiabatic invariant are well defined, but the particles are unable to complete the whole drift around the Earth. The particles are said Quasi-Trapped. In particular, particles mirroring at low latitudes on the night side at $L \simeq 8$ abandon the Earth's magnetosphere before reaching the noon meridian and particles mirroring at high latitudes on the day side run into the tail before reaching the midnight meridian.

At high energies, when the Larmor radius of the particle is too large with respect of the magnetic field curvature, the invariance of J_2 or J_3 can breakdown. The particle orbits become unstable and the particles may be lost from the trapped region. The breakdown of the adiabatic

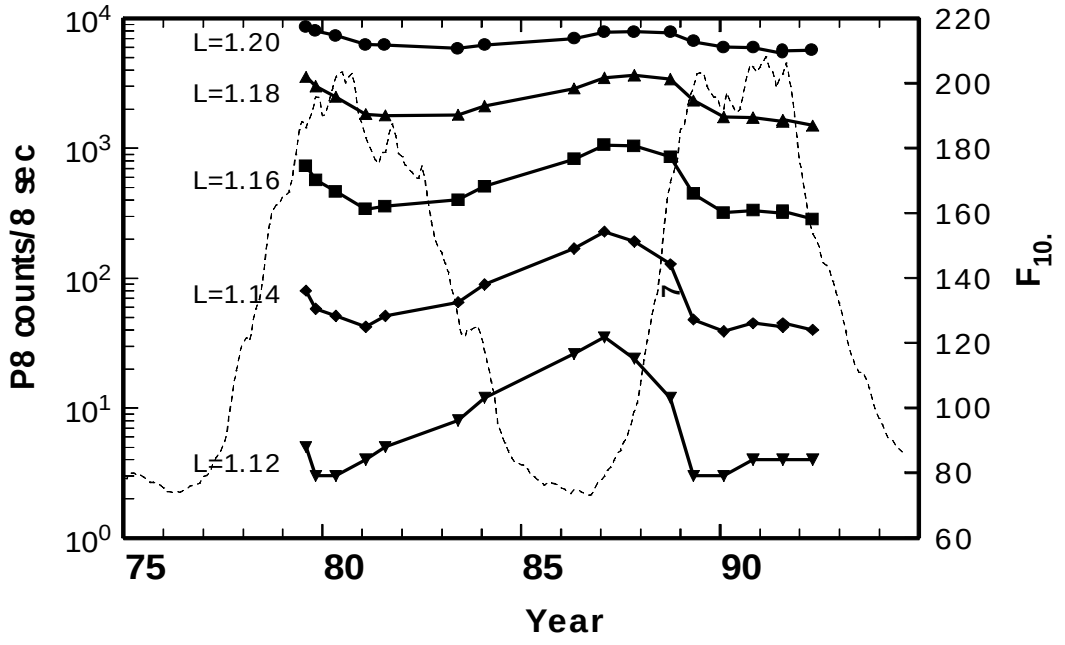

Figure 1.19: *Proton flux in the $E = 80 \div 215\ MeV$ channel at equator as a function of time showing the solar cycle variations (the dotted line shows the 13-month smoothed $F_{10.7}$) more pronounced at small L [35]*

conditions based on the Alfven discriminant gives a cutoff energy. The dependence of the cutoff energy in L has also been studied by numerical simulations [71].

In the atmosphere, the protons loose energy by ionization and excitation of the nitrogen and oxygen atoms at low altitudes, of helium and hydrogen at higher altitudes.

The multiple scattering dominates at low energies. In the intermediate energy range, i.e. $1\ MeV \div 1\ GeV$, the stopping power decreases with increasing proton energy. The inner shell correction plays a role mainly at large atomic numbers and low proton energies. Multiple Coulomb scattering causes diffusion in particle pitch angle and for protons has been proposed as a possible important loss mechanism [40], [150], [148] but his role has been rejected by other researchers [149], [156]. At very low altitudes, a slight change in pitch angle can produce a rather large change in the location of the mirror points and in the average atmospheric density experienced by the protons. Drift resonant fluctuation in the magnetospheric magnetic field and in the convection electric field induce a violation of the third invariant and radial diffusion of the trapped particles [28]. Time scales of losses and radial diffusion for high energy protons are of the order of years and we can expect the inner proton belt to be very stable.

Long term variations can be also related to the solar cycle. The CR flux is lower during solar maximum due to the enhancement of the solar modulation effect of the solar activity. The atmosphere changes density in the upper part due to enhanced solar heating and this enhancement leeds to enhanced absorption of protons in the upper atmosphere. The combination of both effects leads to high fluxes during solar minimum and low flux during solar maximum. In fig. 1.19 proton fluxes in the inner belts measured with the instruments onboard the TIROS/NOAA satellites are shown as a function of time over a period of two solar cycles. The principal sources

of particles for the outer belt is the solar wind, while for the inner belt sources are electrons and protons from the neutron decay produced by CR and Solar Energetic Particle (SEP) in the tenuous gas of the upper atmosphere. Usually the high energy proton flux in the outer belt region is very small. Protons, emitted from the sun during solar proton events, can penetrate the inner magnetosphere and form short lived radiation belts [36]. SEP events can be divided in two classes which are usually described as impulsive and gradual referring to the time scale of the accompanying soft X-ray flare. In general SEP events associated with impulsive flares have low ion intensities, high electron to proton flux ratios and abundance of heavy elements. The typical time scale of such events is several hours, and the frequency of events varies with the solar cycle from ≈ 1000 per year at solar maximum to only few at the solar minimum. The gradual or long duration X-ray events are associated with Coronal Mass Ejection (CME) which can drive coronal and interplanetary shock waves. These shock waves may accelerate particles in the solar corona and interplanetary space. The energetic particle population is dominated by protons. In the lower panel of fig. 1.20 the flux of $50\,MeV$ protons measured onboard GOES in a GEosynchronous Orbit (GEO), is shown as function of time where there is a clear evidence of the increasing of a factor 100 in the October 19, 1994. The upper panel in fig. 1.20 shows $35\,MeV$ proton flux for the same period as a function of L onboard STRV-1b in equatorial Geosynchronous Transfer Orbit (GTO). Before the increase at GEO the GTO proton count rates are at background level in the outer zone and the increase below $L = 3$ is due to the inner belt. During the proton enhancement at GEO the GTO rates are enhanced down to $L = 4$. Afterwards they decay together with GEO fluxes. The SEP penetration at these energies is not expected due to the geomagnetic cutoff, however such events are associated with magnetic disturbances that can modify the cutoff threshold and even accelerate particle to carry them to low L [38].

Electrons Trapped electrons are present both in inner and outer belts, the two structure zone being the consequence of the balance between radial diffusion and steady losses [39]. The subject of the electron source is still unclear. As far as we know the CRAND produces also energetic electrons but the process is too weak to provide a significant amount of energetic electron belts. The energy of electrons in the ionosphere is below $1\,eV$, while for solar wind electrons is about $10\,eV$.

The Earth's radiation belts energy instead is believed to range between 400 KeV and 15 MeV. An acceleration mechanism is required to explain the feature, related to the violation of the adiabatic invariants for the electrons. The energy of the particle may be increased if it moves into stronger magnetic field regions, violating the third invariant while conserving the other two. The energy which can be gained by radial transport, through fast injection or slow radial transport, by violation of the third invariant, is limited by the ratio of the magnetic field intensities of the final and initial positions in the region of radial transport.

Currently, it is believed that only a fraction of trapped electrons can be of solar wind origin. The phase space density in the solar wind being too low, part of the electron source population must be created into the magnetosphere [47]. The main loss mechanism for inner belt electron, is precipitation into the atmosphere and Coulomb scattering, while in the outer zone are dominated by scattering in the pitch angle. Trapped electrons are scattered randomly in

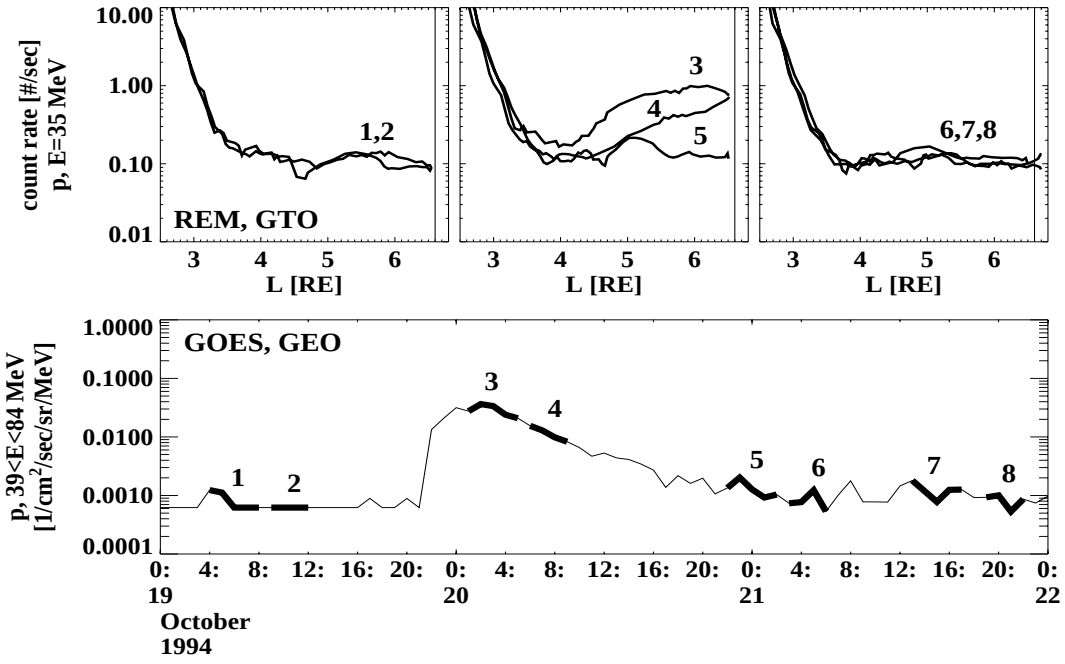

Figure 1.20: *Protons observed at GEO and GTO during SEP. The upper panel show radial proton profiles measured at GTO at different times. The lower panel shows the* $50\,MeV$ *proton flux measured at GEO versus time [36].*

pitch angle by plasma waves or by particle-particle interactions and ultimately reach the loss cone by diffusion. The process is self-driven, the energy for the waves comes from the particles themselves because as they scatter towards smaller pitch angles, they lose energy gained by the wave. Alternatively, electrons may be scattered by externally generated waves. Whatever the source of waves, the effect is the same: particles diffuse in pitch angle to the loss cone and, as a result, their distribution develops a maximum at 90^o and decreases monotonically towards the field aligned direction. The process has been analyzed mathematically by a number of authors ([28], [31]) by deriving a diffusion equation from the Fokker-Plank equation. Thus an electron not on a trajectory reaching the atmosphere, may eventually, be scattered into a trajectory that will reach the atmosphere. In general, the scattering takes place in the upper atmosphere and in a symmetric dipole, an electron mirroring above the atmosphere would continue to do so indefinitely. When the energetic electron flux beyond $1.25R_e$ is increased (by a magnetic storm or a high altitude nuclear explosion), it is found to decay more rapidly than expected as a result of atmospheric interactions only. The situation is most extreme at larger distance, beyond $4R_e$ where storm associated enhancements of the flux at $E = 0.5\,MeV$ will decrease by $1/e$ on a time scale of ~ 5 days. At these distances would require thousands of year to be produced by similar rapid decay trough collisions with the local residual atmosphere and it is, therefore, natural to invoke other types of interactions involving *wave-particle interactions.*

The main point of these interactions is that changes can be produced violating some of or all the adiabatic invariants. For example, a wave with a frequency comparable to the gyrofrequency

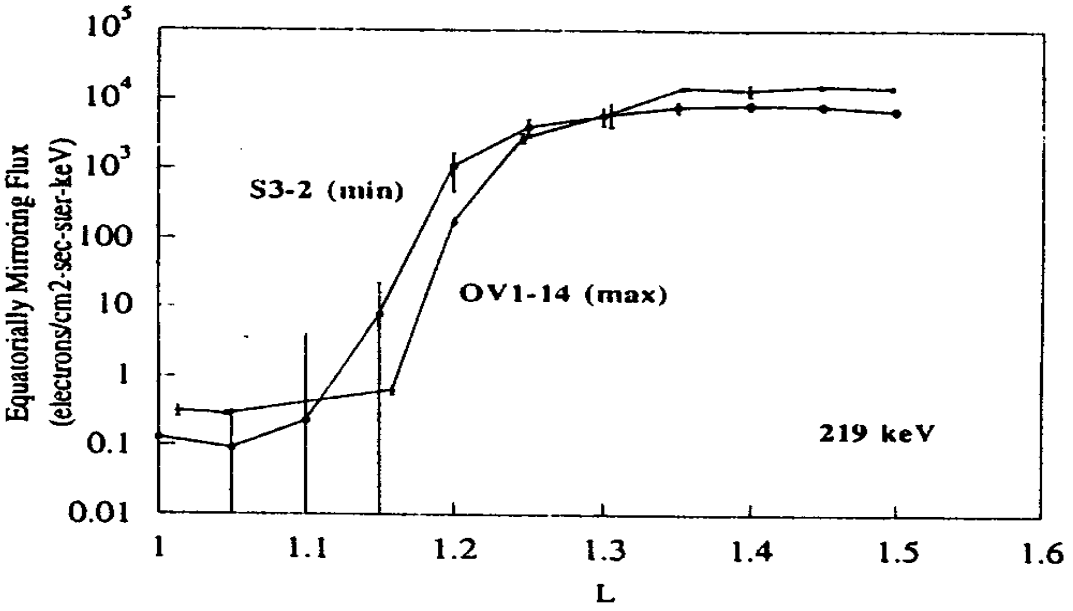

Figure 1.21: *Radial profiles of inner and outer electron during solar min and max [41]*

or with wavelength comparable with the gyroradius of a particle may invalidate the condition that the magnetic field does not vary significantly over a gyroperiod or over a gyroradius. If a particle encounters such a wave, its magnetic moment may be changed; if the interaction is elastic, the only thing which can be changed is the pitch angle; if an electron encounters a wave with a period close to the bounce orbit, the second invariant may be violated.

Inner belt electrons exhibit asynchronously variations with the solar cycle [41]. The atmospheric losses as well electron sources are expected to be enhanced during solar maximum. This may be seen in fig. 1.21 where two regions of the inner electron belts are shown as a function of L. In the outer region, the source dominates and the electron population is enhanced during solar maximum, while in the inner part the losses dominate and electron fluxes are suppressed during the solar maximum compared to the solar minimum. The outer electron belts are highly dynamic on a short time scales. The variation are closely related with the solar activity, and driven by the fast solar wind. In fig. 1.22 a typical sequence of this type of event is shown. The solar wind speed as a function of time onboard of WIND [44] is shown in uppermost panel while the second panel shows the D_{st} index. It is clear that the arrival of the fast solar wind stream on January 28, 1995 caused in the following days the build up of a magnetic storm ($D_{st} = -50\,nT$) slowly recovered in the following days. The three panels in the third row show a series of radial electron count rate profiles with $E > 1MeV$ measured in the same period from the GTO. During the storm main phase, the electrons decreased in the outer zone markedly at higher L. (profiles 1-3). After one day the electron rates started to increase rapidly by a factor $10 \div 100$ within one day at $4 < L < 6$. First, the increases are observed at lower energies and afterwards at higher (profiles 4-7). Slower variations are observed after few days where the electron flux continues to increases slightly (profiles 8-12). The three phases are typical of outer belts variations depending on the type of event. The question of how to get energetic electrons to low L values is still very

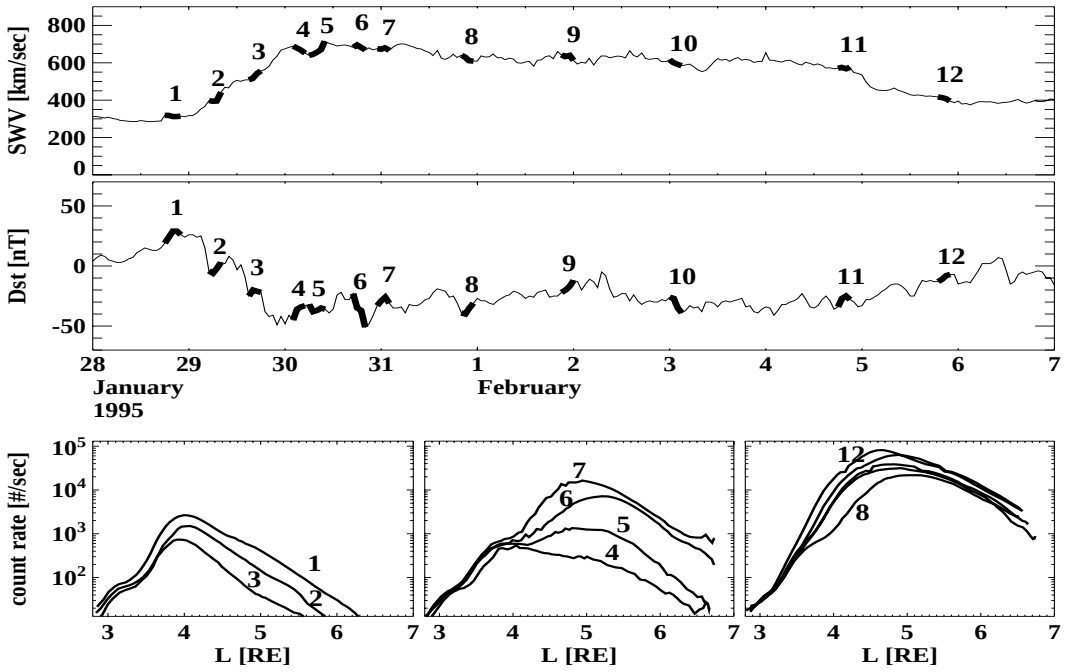

Figure 1.22: *Outer electron radiation belt variation during fast solar wind [44]*

open.

In [32] studies of the energetic electrons during magnetic storm of May 15, 1997 was presented. It was concluded that to get electrons of $0.2-0.8 MeV$ down to $L = 4.5$ can be explained in terms of radial transport with conservation of the first adiabatic invariant. However, the observed enhancements of $0.8-3.2 MeV$ electrons peaking at $L < 4.5$ appear to require energization that does not conserve the magnetic moment. When [32] compared the observations between different storms, also the relationships between D_{st} index and electron enhancement turned out to be rather unclear. The details of energization of the very high-energy radiation belt particles in conjunction with large magnetospheric disturbances are yet poorly understood. Statistically, it is known that the energetic particles appear as a response to high-speed solar wind streams and CMEs.

Anomalous Cosmic Rays The Anomalous component of Cosmic Rays (ACR) became evident in 1973 when the differential flux was observed for some elements such as He, N and O in the energy range below 60 MeV/n [52]. The peak appeared during a minimum of the solar activity around 10 MeV/n in the range of energies between solar energetic particles and CR.

The energy spectra of this component have shown, for instance, a He/p ratio > 1 at $30 MeV/n$ and a C/O ratio < 0.1 at $10 MeV/n$, not compatible with solar or galactic cosmic ray abundance. The apparent overabundance of elements with large first ionization potential (He, N, O, Ne) led to the hypothesis that the ACR component originates from interstellar particles penetrating the inner heliosphere. After the discovery of ACR [51] proposed a model suitable to explain their origin (fig. 1.23). According this model, neutral atoms enter the solar system; some of them can

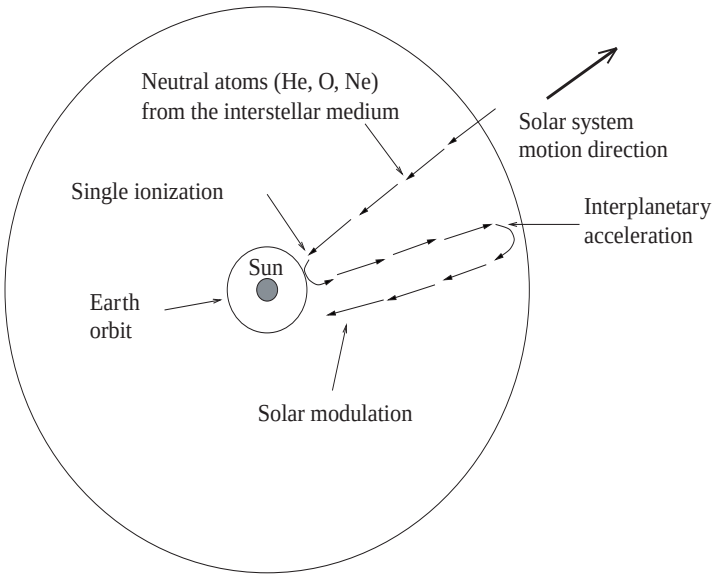

Figure 1.23: *The Fisk model for the formation of the ACR [51]*

be singly ionized from the UV radiation or from processes of charge exchange with low energy protons or ions of the solar wind. After the ionization, the particles may be pushed by the solar wind which carries them away to the heliosphere limit, where they may be accelerated, by still unclear mechanism, gaining energy up to tens of MeV/n at the termination shock. As a result, a fraction of the accelerated nuclei can return to the inner part of the solar system, modulated like the CR. It has been shown in [62] that the process can be multiple with a charge state of $+1$ or $> +2$. The main difference between ACR and CR is the single ionization of anomalous atoms. In fact ACR having charge lower than CR are able to penetrate more deeply in the Earth's magnetosphere. The intensity of ACR is anticorrelated with the solar activity, similar to the CR intensity with a maximum of $\sim 0.1\, m^{-2}\, sr\, s\, MeV/n$ for O at $\sim 5\, MeV/n$ at $1\, UA$. However the modulation effect is much larger than for CR resulting in a variation of the intensity from solar minimum to maximum of a factor ~ 100. The possibility of trapping singly charged ACR was suggested by [49]. This is related to the possibility that a singly charged ACR may penetrate to lower geomagnetic latitudes than CR or SEP with the same energy/nucl, because they have greater rigidity. These ions may loose some of the remaining electrons in the upper atmosphere by charge exchange. Rigidity would decrease by a large factor and depending on pitch angle, they might become trapped. [50] gives an estimation of ACR lifetimes from weeks up to months before loosing energy with the upper atmosphere.

The existence of a weak but persistent belt of charged N, O, Ne near $L = 2$ was established by SAMPEX [46]. The SAMPEX spacecraft provided the first detailed description of ACR trapped within the SAA. The trapped ACR form a specific radiation belt which includes abundances of N and Ne, O and other elements up to energies of $100\, MeV/n$. In fig. 1.24 the L distribution of the observed O, N and He peaked at $L \approx 2$ is shown. Although trapped He has been observed by SAMPEX, it is not thought to be of ACR origin [105]. The composition of such belts is

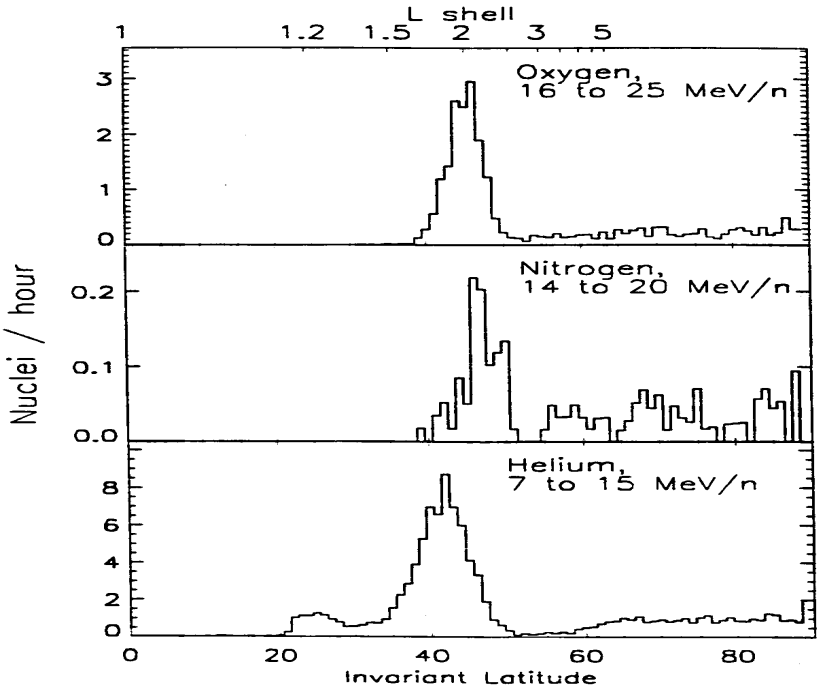

Figure 1.24: *Trapped nucleon belt at $L \approx 2$ from ACR component [46].*

considered consistent with that observed for ACR in the interplanetary space, but not with other possible sources of magnetospheric particles.

1.4.6 Radiation Effects on Spacecraft and Aircraft

With energetic particles, the main problem arises from penetrating particles. From fig. 1.25 it can be seen that for a typical spacecraft box thickness of few mm of Al with electrons $E = 0.5 \div 5 MeV$ are needed in order to penetrate, while protons need $E = 10 \div 100\ MeV$. With the exception of neutrons, the various type of radiation making up natural environment, X-rays, $\gamma - rays$, electrons, protons, $\alpha - particles$ and heavier ions, all deposit significant amounts of ionizing energy in semiconductor devices. In semiconductors and insulators, the absorbed ionizing energy manifests itself as electron-hole pairs that separate, migrate through the material and become trapped at certain locations, often resulting in an alteration of the properties of the device. Effects occurring when electronic devices are exposed to space radiation can be: Total Ionizing Dose (TID), Single Event Effects (SEE), Displacements Damage, Background noise in sensors, electrostatic charging.

TID happens when high energy protons or electrons pass through the device, produce electron-hole pairs within the gate and field oxides of MOS structures. The electrons produced have high mobility in the oxide and are quickly swept out by internal fields, while due to the lower mobility of holes, they will be transported to the Si/SiO_2 interface where they become trapped. In this way the voltage threshold and the mobility of the MOS gate will change modifying the device characteristics.

Part of the energy-loss coming from the energetic radiation goes into lattice displacement

damage. This effect scales with a quantity defined as the non-ionizing energy loss per unit mass (NIEL). Examples of damage effects are reduction in bipolar transistor gain, charge transfer inefficiency in CCD and degradation of the resolution in solid state detector. SEE happens when high energy particles produce fast ionization in the device, causing internal latches or register to switch state and introducing random errors in digital devices, called Single Event Upset (SEU).

Other possible effects include latchup, snapback and burnout in power MOSFET, in general much more difficult to recover than SEU and may cause permanent damages. A commonly used measurements of the effectiveness of an ion in causing SEE is the Linear Energy Transfer (LET) which is the energy loss per unit of length divided by the density of the semiconductor and has unity of $MeV\,cm^2\,mg^{-1}$. The mean LET value in silicon for a particle depositing an energy E_d with an incidence angle ϑ in a silicon layer of thickness d can be expressed as $LET_{Si} = E_d \cos\vartheta/d$, while for a particle stopping in the material instead of d we have to use the range R.

LET values range from $1 \div 10\ MeV\,cm^2\,mg^{-1}$ for protons of various energies to values approaching $100\ MeV\,cm^2\,mg^{-1}$ for heavy ions such as X_e with energies of hundreds of MeV. The absorbed dose and dose equivalent for water can be evaluated using the relation $LET_{water} = 1.193 \cdot LET_{Si}$, assuming that particle are relativistic. Devices are characterized in terms of cross-section (effective area presented to the beam for a SEE to occur) which is a function of LET. For each device there is a LET threshold below which SEE does not occur. In LEO, important upsets can be produced by proton nuclear reactions in the SAA region and at higher latitudes due to solar and galactic cosmic rays.

For radiation effects on biological systems it is found that there is a strong dependence on LET dose equivalents are used. An additional problem due to penetrating energetic radiation is the internal charging coming from the stopping of electrons in internal spacecraft dielectric materials or ungrounded metallic parts. An electrostatic charge build up may result in discharge, disrupting the spacecraft. The LET distribution at altitudes of $300 - 400\ Km$ both from CR and trapped protons are shown in figs.1.26 from [53]. For the CR component, there is the indication of the various contributions from the CR elements abundance. Moreover, there is a clear peak around $0.2\ KeV/\mu m - water$, due to relativistic protons. For the trapped protons a broad peak around $0.5\,KeV/\mu m - water$ is observed and they dominate in SAA. The differential flux of the SAA region is higher than CR contribution for a factor of $10 - 100$ in the LET range $1 - 90\ KeV/\mu m - water$ which is caused mostly by trapped protons. The analysis of the integrated dose fraction as function of LET reported in [53] shows how the 60% of the total radiation dose is due to the CR in the LET range $0.5 - 90\ KeV/\mu m - water$.

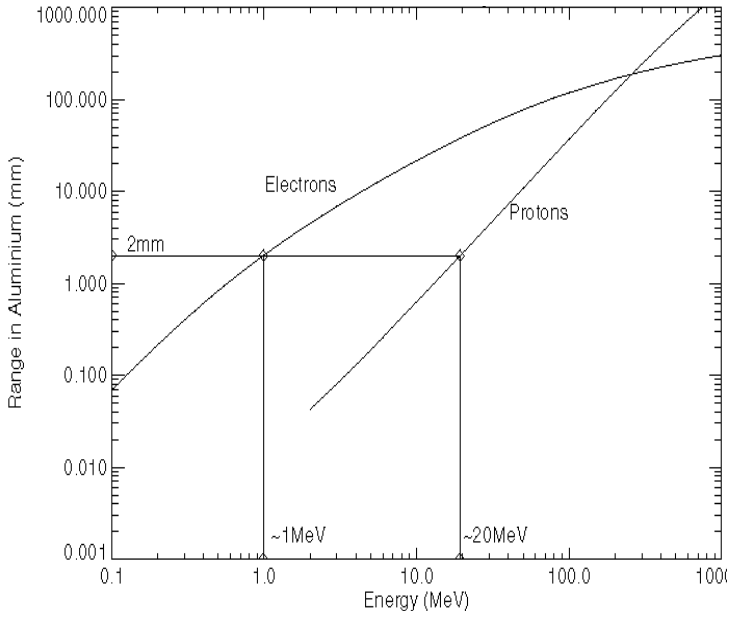

Figure 1.25: *Electron and proton mean range in Al*

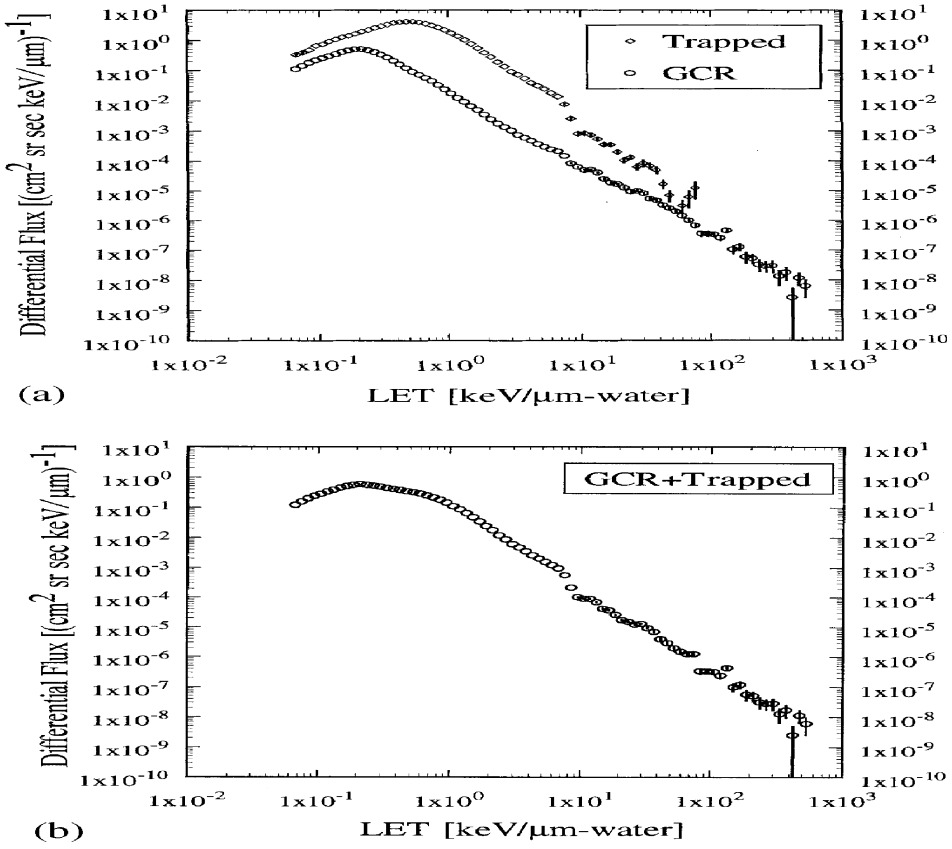

Figure 1.26: *LET distribution for CR particles and trapped protons [53]*

Chapter 2

Cosmic Rays near Earth

2.1 Introduction

The atmosphere surrounding the Earth's surface is continuously bombarded by particles coming from the outer space. The description of the basics phenomena involving the radiation reaching the Earth are described in this chapter. We start with a short introduction on the cosmic ray composition and main features. Then the role of the Earth's magnetic field in the screening of such particles and their geomagnetic modulation is given and the spectra of principal components of cosmic rays are presented. Finally, we conclude the chapter defining the model of interaction of cosmic rays with atmosphere and the basic equations governing the phenomena, illustrating also the different kind of secondary particles produced and the role of the Earth's magnetic field.

2.2 Cosmic Rays Sources and Composition

The discovery of high energy cosmic radiation reaching the Earth from space was a consequence of experiments based on ionization chambers undertaken at the beginning of the last century ([56],[57]). From the increase of the radiation levels observed with altitude above 1 Km, the extraterrestrial origin was inferred [59]. The corpuscular nature of the radiation dates to 1928 [60]. The dominant particle sources in the near Earth environment are primary Cosmic Rays (CR), particles of solar origin like Solar Energetic Particles (SEP), particles of interstellar origin, accelerated in the outer heliosphere or at the termination shock like the Anomalous Cosmic Rays (ACR), and particles trapped in the Earth's magnetosphere.

CR paths in the galaxy are determined by the irregular interstellar magnetic fields so that all the information about the direction of the sources is lost during their travel and CR reach the Earth isotropically. CR consist of two components, a primary component, representing the composition of the source and a secondary component produced by fragmentation of heavier nuclei (Li, Be, B, sub-iron elements) produced in the interaction with the interstellar medium [61]. CR are composed of 98% nuclei, with the main contribution coming from H (87%) and He (12%) and a small fraction (1%) of heavier nuclei, 2% of which comes from leptons, but all the elements of the periodic table are present in CR, as shown in fig. 2.1. The general trend of the abundances shows a decrease with the nuclear charge, nuclei with even charges being more abundant and there is a remarkably overabundant presence of He, Ca, O and Fe compared to

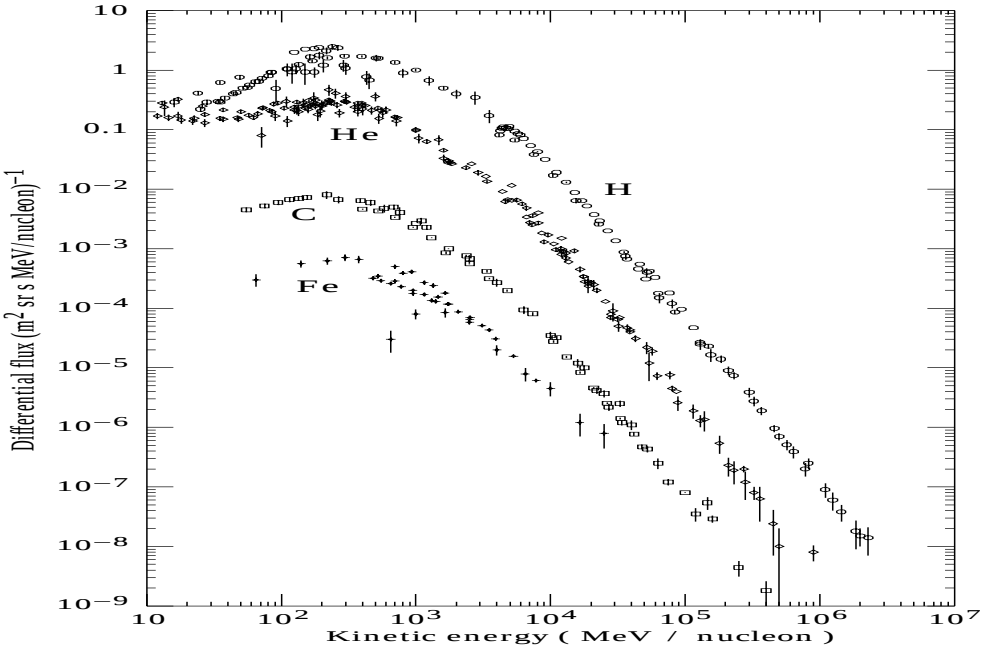

Figure 2.1: *CR differential energy spectrum for different nuclei [63]*

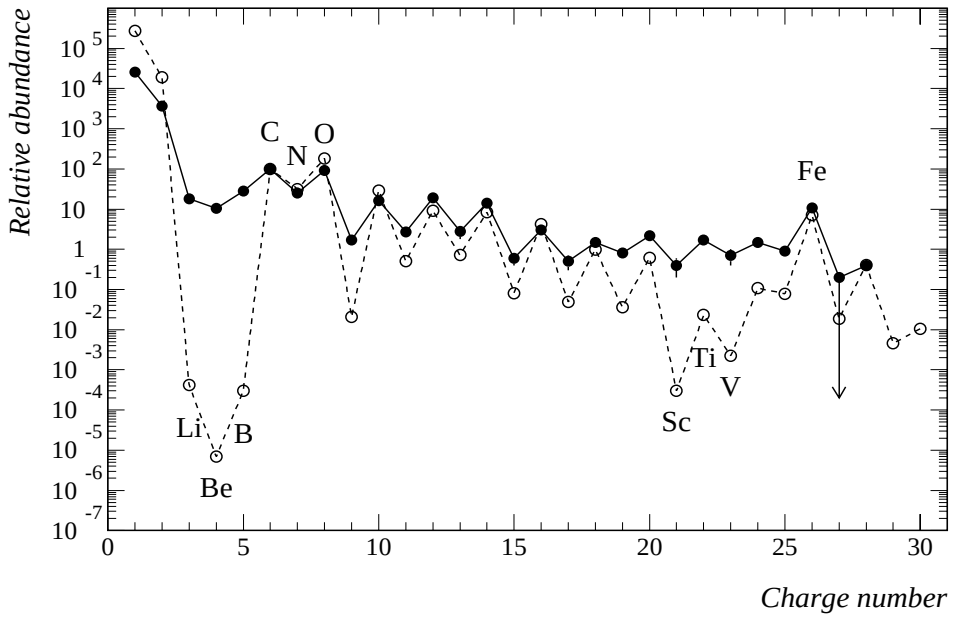

Figure 2.2: *Comparison between CR (filled circle) and Solar system element (open circles) composition [63].*

the adjacent elements in the periodic table. [63]. Different composition is observed between CR and ordinary matter in the galaxy, especially for the most abundant H and He, relatively less abundant in CR and peaks at the C, N, O and Fe. (fig. 2.2). The most evident difference between the two composition is the overabundance in CR of Li, Be, B and sub-Fe elements. Such elements are usually thought to be formed in nuclear interactions of CR with nuclei of interstellar medium, during the propagation from the sources to Earth. As energy losses for a high energy particle are related to the γ_M Lorentz factor, for a CR with N_n nucleons of average mass m_n, the mass can be written as $M \approx N_n m_n$. Assuming $m_n \approx m_p$ with m_p and m_n the proton and neutron mass respectively, the kinetic energy of the particle can be written as $E_k = (\gamma_M - 1)Mc^2$; the *kinetic energy per nucleon* is defined as $E_{kn} = (\gamma_M - 1)Mc^2/N_n \approx (\gamma_M - 1)m_n c^2$ with the advantage that all nuclei with the same E_{kn} have the same velocity.

Below TeV/n energy, CR are thought to be of galactic origin, produced and accelerated during supernova explosion [54]. The energy spectra as a function of the kinetic energy per nucleon of the primary ion components are very similar. CR energy spectrum extends over more than 11 decades in energy. At energies above $\approx 10\, GeV/n$ the spectra approach a power law $N(E_{kn}) = N_o E_{kn}^{-\gamma}$ with a negative slope around $\gamma = 2.7 \div 3.1$. The maximum is located around few hundred of MeV/n while at lower energies, below $20 \div 30\, MeV/n$, an increasing of the flux due to the solar activity and the presence of the anomalous component is observed. Between $10^9 \div 10^{12} GeV/n$ the spectrum steepens and the change in the slope is believed to reflect a change in the propagation of CR in the interstellar medium or in the source and acceleration mechanisms.

Over $10^{12} GeV/n$ CR are believed to be of extra galactic origin since the composition changes from predominantly heavy to lighter nuclei composition, while those below that energy limit originate from our galaxy and diffuse with a typical time scale of the order of $10^7 years$. However, it must be noticed that above $1 TeV/n$ the CR flux is very low and is known within an accuracy of at most 15%.

Below $1\, GeV/n$ the spectra are strongly affected by the solar modulation, meaning by the effect of the outward streaming of the solar wind and interplanetary magnetic field. The spectra of all species flatten, with a maximum in the range $200 \div 300\, MeV/n$. CR loose energy during the interaction with the solar wind, so differences in the differential energy spectra inside and outside the heliosphere are expected at low energy. The solar modulation reduces significantly the intensity for $E_{kn} < 100\, MeV/n$ in LEO. The modulation effect causes the CR flux to vary with the solar cycle with maximum intensities at the solar minimum conditions as in fig. 2.3. It clearly shows that the CR intensity is anti-correlated with solar activity, and that at energies above $1\, GeV/n$ the intensity variation is relatively small [61]. It can also be noticed that the intensity profile changes with the solar cycle, with indications that the transport of CR in the heliosphere follows a $22 - year$ period rather than a $11 - year$ period and suggests a modulation sensitive to the polarity of the solar magnetic field (which follows a $22 - year$ cycle).

A way to parameterize the CR solar modulation is to use a diffusion model where particle interaction with the solar wind is described in terms of convection, diffusion and change of energy of the CR at magnetic scattering centers as a result of the expansion of the solar wind and of the radial distance. If we consider the solar wind velocity $\mathbf{v}(\mathbf{r})$, a typical diffusion coefficient $D(\mathbf{r}, E_{kn})$, with a spherical symmetry, the particle density $f(\mathbf{r}, E_{kn})$ can be obtained solving the

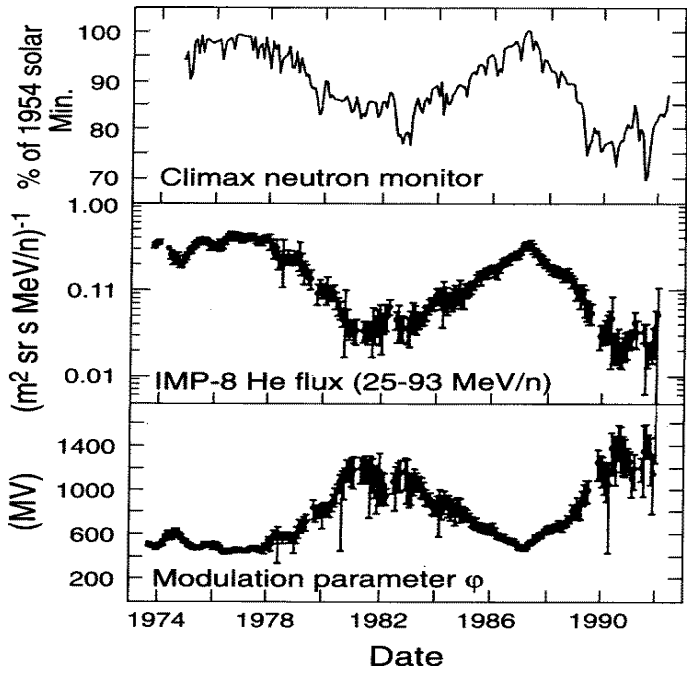

Figure 2.3: *Sun activity and CR flux from 1973 to 1995 [65]*

Fokker-Plank equation [64]:

$$\frac{\partial f}{\partial t} = \nabla D \cdot \nabla f - \nabla \cdot (\mathbf{v} f) + \frac{1}{3} \nabla \cdot \mathbf{v} \frac{\partial}{\partial E_{kn}} (\alpha E_{kn} f) \tag{2.1}$$

The diffusion terms on the right side, due to the magnetic irregularities, can be addressed by putting the diffusion coefficient $D = \lambda v/3$ where v is the particle speed and λ the scattering mean free path which also depends on the particle energy E_{kn}. The convection term depends on the solar wind speed $\mathbf{v}$ and the third term in eqn. 2.1 describes the adiabatic deceleration of the expanding solar wind which depends on the particle kinetic energy by the parameter $\alpha = (E_{kn} + 2E_o)/(E_{kn} + E_o)$ with E_o the particle rest energy.

Solving the eqn. 2.1 under the assumption of constant D, $\mathbf{v}$ and α and an isotropic distribution of CR brings to a parameterization of the CR differential flux intensity in terms of the unmodulated flux $J(\infty, E_{kn})$ and parameter $\Phi = Ze\varphi$ depending on the solar activity:

$$J(r, E_{kn}, t) = \frac{v v_n}{4\pi} = \frac{E_{kn}^2 - E_o^2}{[E_{kn}^2 + \Phi(t)]^2 - E_o^2} J(\infty, E_{kn} + \Phi(t)) \tag{2.2}$$

here φ has the dimension of a potential (in MV) and ranges between $\approx 350\, MV$ on the solar minimum and $\approx\ 1500\, MV$ on the solar maximum as it can be seen in fig. 2.3 which is based on Climax [65] continuously monitoring the neutron flux produced by the CR interactions with the Earth's atmosphere.

2.3 Acceleration and Propagation of CR

Acceleration mechanisms are requested to justify the power law energy dependence for the observed spectrum in primary CR [68]. Acceleration for a plasma can be summarized by the simple equation

$$\Delta E_k = q \int_0^{\Delta t} \mathbf{v}(t) \cdot \mathbf{E}(\mathbf{r}(t), t) dt \tag{2.3}$$

where $\mathbf{E}$ is the electric field determined by currents and charges in the plasma, ΔE_k is the change in particle kinetic energy, $\mathbf{v}$ is the particle speed and q the charge. In a static magnetic field no work is done on particles but if the field is time varying the work is done by the induced electric fields.

In astrophysics, the best known stochastic acceleration mechanism is Fermi acceleration. Fermi suggested that cosmic rays may collide with moving magnetized clouds, the collision being effective via the magnetic mirroring effect; in this way the particle can suffer energy gain or loss proportional to the velocity of the cloud and energy of the particle. The Fermi model is based on the assumption of repeated acceleration events on crossing the shock and by a finite probability of escape. For relativistic particles, the average gain is $\Delta E_k = \pm \beta E_k$, the sign being determined by the relative motion between particle and cloud. Statistically head-on collision predominate with particle gaining energy on average. In the steady state, the number of particles for a given energy can be written as $N = N_o E_k^{-\gamma}$ which fit the data extremely well with $\gamma = 2.7 \div 3.1$. When created and afterward accelerated, a CR does not reach us along a simple path, but slowly diffuses through the electromagnetic fields in the galaxy, approximately from region distant up to few hundreds of parsec. Therefore we can explore only a small fraction ($\sim 1\%$) of the galaxy volume.

The propagation of cosmic ray in the galaxy is determined by a diffusive process, where the charged particles interact with the irregularities of the galactic magnetic field. With a galactic magnetic field of $3 \div 4\,\mu G$ the Larmor radius of a $1\ GeV$ proton is of the order of $10^{12}\ cm$, $\sim 10^{-6}\ parsec$. Remembering the galactic disk thickness of the order of 500 $parsec$, for an observer out of the galaxy the trajectory is connected to the galactic magnetic field. The transport equation describes the propagation of CR in the galaxy balancing generation and loss processes. A sufficient general expression can be found in [55] where the particle density of a given kind is related to the diffusion of CR in the galaxy. The process is determined by the diffusion coefficient $D_i = \lambda_i v_i$ where λ_i is the mean free path in the galaxy and v_i is the particle speed. Moreover, the possible energy loss processes experienced by particles while travelling in the ISM play also an important role. The losses by collision and decay happens with a probability

$$P_i = \rho \beta c \sigma_i + \frac{1}{\gamma \tau_i} \tag{2.4}$$

where β is the particle speed, $\gamma\tau_i$ the nucleus lifetime, $\rho(r)$ the density of the interstellar gas and σ_i the inelastic cross section with the medium.

The production of a given kind of nuclei from the interaction of another particle depends on the inclusive cross sections. A complete solution of the problem requires the knowledge of

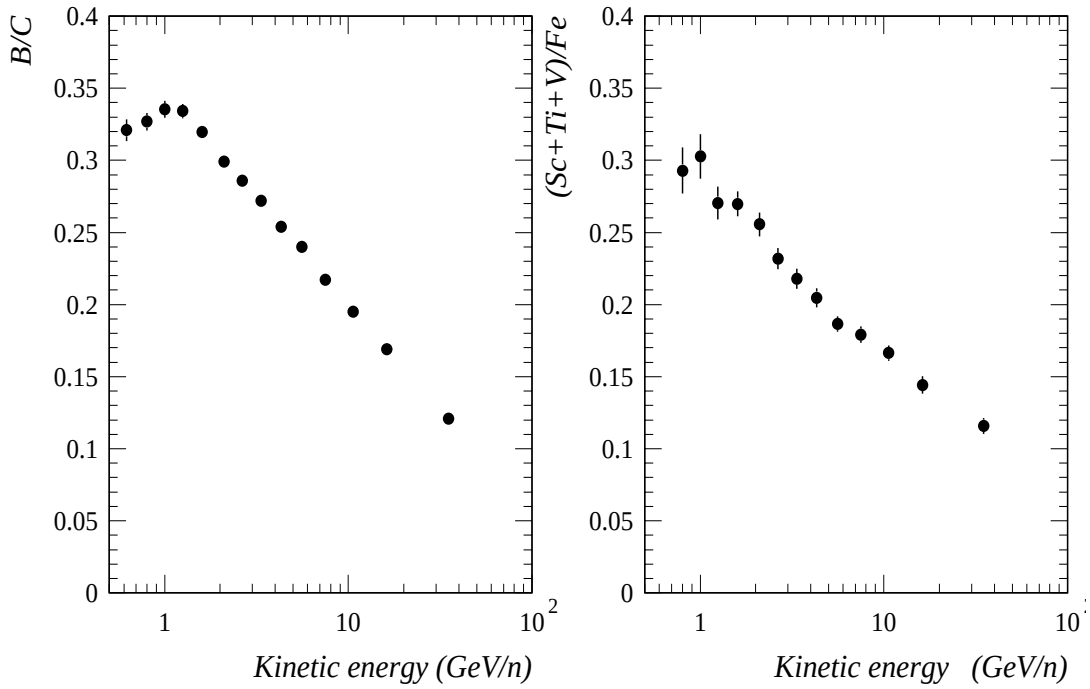

Figure 2.4: *Energy dependence of the B/C ratio (left) and sub-Fe/Fe (right) [70]*

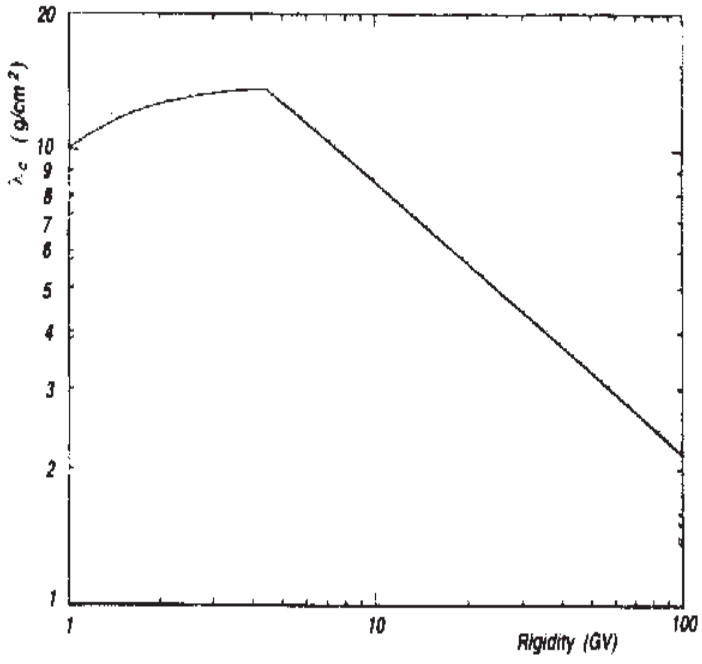

Figure 2.5: *Rigidity dependence for the λ_{esc} in the LBM [70]*

the shape and size of the propagation regions of cosmic rays in the galaxy together with the distribution of sources and interstellar gas density. Moreover, it is usually assumed that lifetimes for nuclear decay and fragmentation cross section are known.

The general approach used is to get the parameters of the theory from the observed secondary abundances and then infer the source composition from the observed primary abundances. Several models have been proposed for the galactic confinement hypothesis; the simplest is the *Leaky Box Model* (LBM) [69] where a constant and uniform distribution for sources and cosmic ray in the galaxy is assumed. Therefore, the escape probability per unit time $1/\tau_{esc}$ from the galaxy become a constant and the only free parameter in the model is $\lambda_{esc} = \rho\beta c\tau_{esc}$ which represents the mean amount of matter, in $[gcm^{-2}]$, crossed by a cosmic ray before escaping from the confinement volume.

In the framework of LBM several results can be derived. If the observed spectrum has a power law, $N(E_k) \propto E_k^{-(\gamma+1)}$, the source spectrum must be something like $Q(E_k) \propto E_k^{-(\gamma+1+\delta)}$. The observed abundances at few GeV/n of the stable secondary light nuclei (Li, Be, B) produced by spallation of C, B, O and Fe are well described assuming $\lambda_{esc} = 5 \div 8\, gcm^{-2}$. A rigidity dependence at high energy is expected for λ_{esc} which can be measured from the energy dependence of the ratio of secondary to primary (fig. 2.4) From the observed dependence of secondary to primary ratio on energy, one can infer that the mean amount of matter crossed by CR before the escape from the galaxy decreases with the energy. An important consequence of this model results for the heavy nuclei like ^{10}Be decaying time scales comparable with τ_{esc} and may be used as radioactive clocks for the measurement of τ_{esc}. Moreover, from the ratio between the density of radioactive and stable isotopes, the confinement time of stable elements may be evaluated.

2.4 Geomagnetic Cutoff

The transparency of magnetosphere for primary CR has been studied for long time. The typical approach is to study the transport of observed particles above the site of measurement by means of numerical tracing of the primary particle trajectory with a model of the geomagnetic field. In [71] a review on the approach can be found.

If we consider a position around the Earth, cosmic ray particles can only be observed in sets of directions, which are called *allowed* or *forbidden* directions. The cones have a complex structure and they can be determined making numerical calculations on a large number of trajectories (see fig. 2.6). If particles with a given rigidity and pitch angle are injected in a magnetic field, they will have the same dynamics.

Using the Stoermer theory for the Earth's magnetic field, it has been shown that at each point $\mathbf{r}$ and direction $\mathbf{d}$, for a charged particle, exists a threshold rigidity, called *geomagnetic cutoff rigidity*, below which the particle cannot reach the position and the magnetic field acts like a filter. Since the system is conservative, if we ignore the presence of the solid Earth, it follows that the Liouville theorem is applicable. If we assume the flux distribution of the CR at infinity homogeneous and isotropic, the intensity at any point of the allowed directions is, by the Liouville theorem, the same. If, however, the radiation at large distance from the Earth is not isotropic, it is necessary to compute individual trajectories to find the initial direction of the particle. In this way the question of calculating the intensity at any point around the

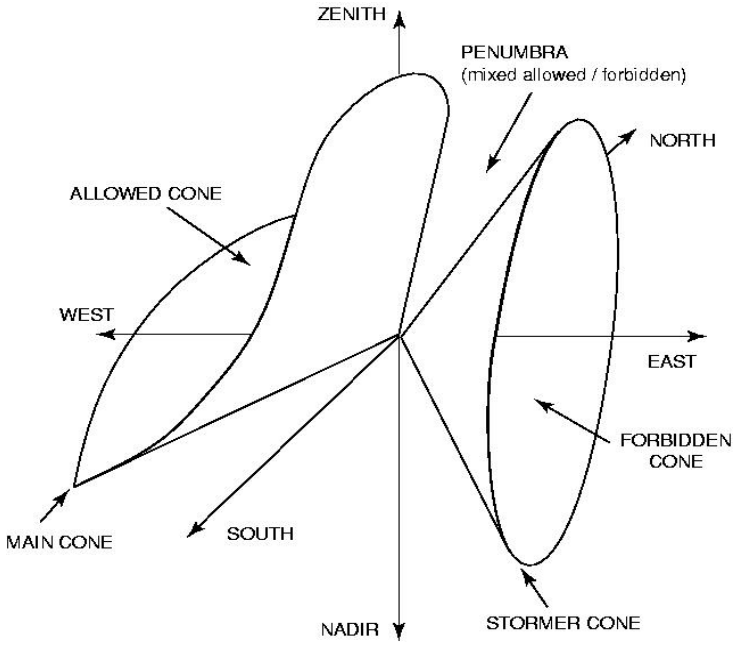

Figure 2.6: *Schematic of the allowed, forbidden cone for positively charged particle of a generic rigidity in a dipole field [75].*

Earth reduces to that of finding which direction reaches infinity from that point. We have three possibilities, either all directions are forbidden, they are all allowed or some of them are allowed and the rest is forbidden.

At any point we can define a cone which encloses all trajectories coming from infinity and reaching the point. If we include the presence of the Earth as a possible sink of particle, in general, attention must be paid in the application of the Liouville theorem. The presence of the Earth modifies the number of allowed trajectories in the near Earth but does not affect the isotropy of the incoming flux.

If we apply the Stoermer theory to the Earth we can find that at each point at distance r, the charged particle can experience three types of trajectories: the particle comes from the outer space very far from the Earth, or it remains confined in the magnetospheric volume, or it originates from the Earth's surface. The second and third class of trajectories are called forbidden.

From [6], in a dipole field it can be shown that the rigidity cutoff at magnetic latitude λ_m and longitude ϕ_m for a particle coming from the zenith with angle θ and from the local east ϕ can be expressed analytically as:

$$R_c = (\frac{M_o}{2r^2})\frac{cos^4\lambda_m}{[1+\sqrt{1-\hat{q}\cos^3\lambda_m \sin\phi_m \sin\theta\cos\phi}]^2} \tag{2.5}$$

with $\hat{q}$ the sign of the charge (± 1) and M_o is the Earth's magnetic dipole moment $\approx 8\cdot 10^{25}\, Gcm^3$ There are certain directions within the Stoermer cone which are such that they have already intersected the Earth's surface one or several times. As those trajectories are stopped when they meet the Earth for the first time, these directions will lie within the shadow of the Earth. In

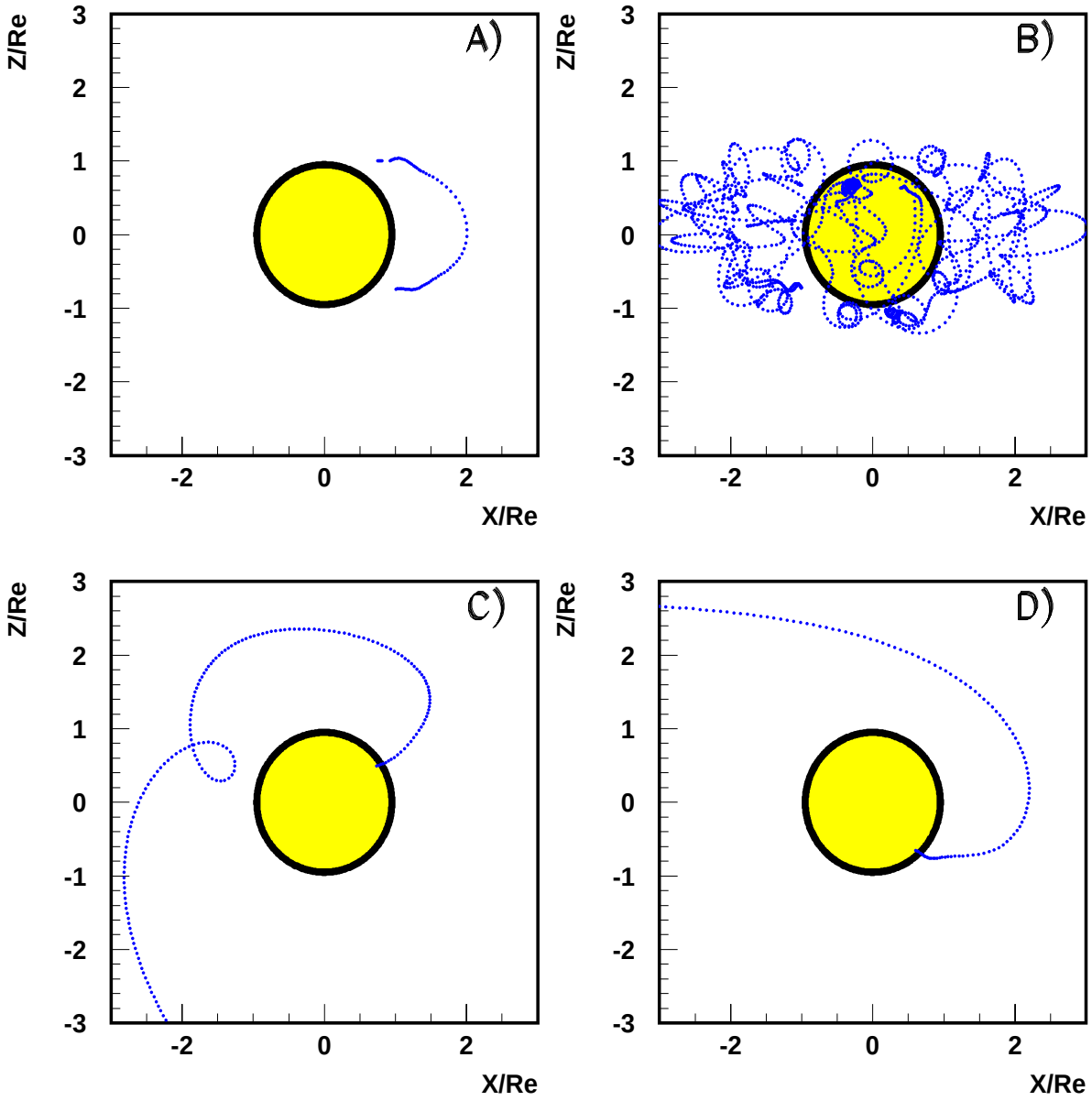

Figure 2.7: *Representation of possible trajectories near cutoff A) much below cutoff(trapped), B) below cutoff (chaotic), C) above cutoff (complex), D) much above cutoff (primary)*

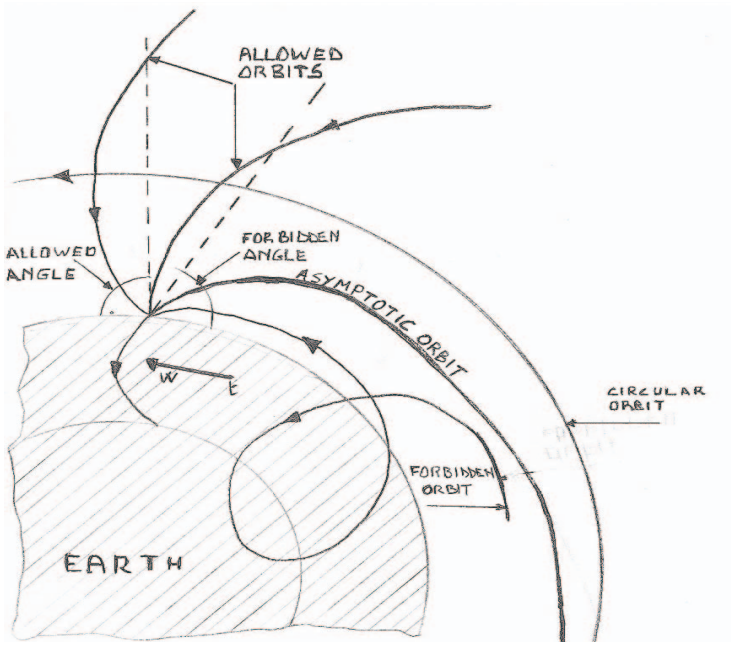

Figure 2.8: *Motion in the equatorial plane for positive charge with the shadow effect of the Earth [76].*

practice the presence of the Earth excludes from observation most of the particles with arrival direction immediately to the west of the Stoermer cone. An example of the Earth's shadow is shown in fig. 2.8, where some trajectories are plotted in the equatorial plane experiencing the shadow effect of the Earth.

Between the region of complete darkness and of complete light, exists a region where many alternating bands of light and darkness are possible, called *penumbral region* and is it extended at intermediate latitudes. Such a region is difficult to evaluate because the trajectories are very complex near the cutoff threshold, with chaotic motion. Examples of trajectories in the magnetic field are shown in fig. 2.7. The penumbra can be described as a system of allowed and forbidden trajectories of particles whose rigidity is between lower and upper cutoff rigidities. At any observation point a Transmissivity Function TF can be defined as the probability of a particle within a defined rigidity range ΔR to access that point. Although Stoermer's theory was done for a dipole field, the theory applies to any other axially symmetric field. Other approaches have been proposed using different approximations for the magnetic field such as eccentric dipole field [73] or non-dipole terms in the field [74] but it has been shown their results are not really accurate [77].

The method for making a rigorous determination of the rigidity cutoff by calculating the trajectories of particles in the Earth's magnetic field requires a tremendous amount of calculation and the complexity of the problem does not make it practicable for a high statistics cases. The trajectory tracing approach results in a complex structure of allowed and forbidden orbits, called *penumbral band*, around the cutoff as shown in fig. 2.9. For this effect, transition between allowed and forbidden is not sharp but it goes smoothly from 0(allowed) up to 1(forbidden) as depicted

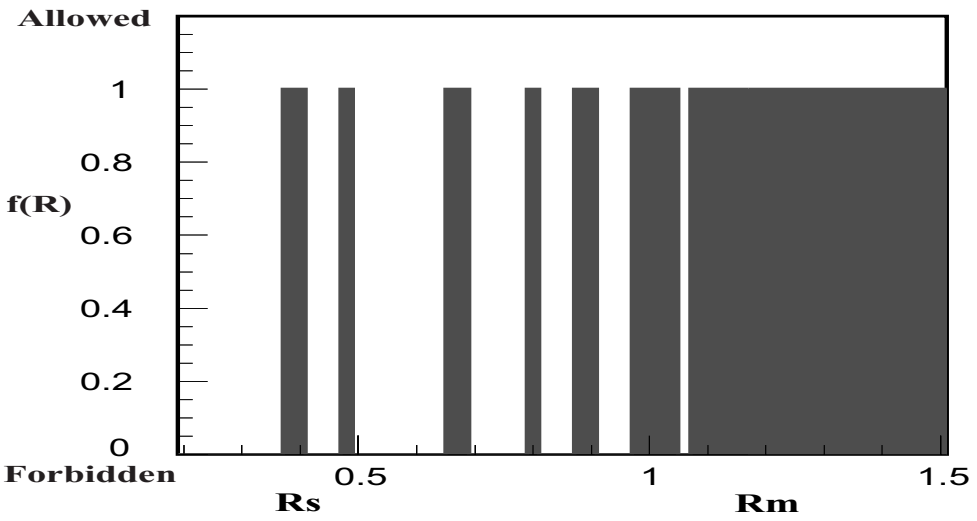

Figure 2.9: *Schematic structure of allowed and forbidden rigidities near the cutoff. Below the Stoermer cutoff R_s all rigidities are forbidden, above the main cutoff R_m all rigidities are allowed.*

in fig. 2.10. It is common to define three distinct cutoff rigidities [72] as the main cone cutoff R_m above which all rigidities are allowed, the Stoermer cone cutoff R_s below which all rigidities are forbidden and an effective cutoff rigidity R_{eff} where we take into account the opacity of the Earth which can be defined as:

$$R_{eff} = R_m + \int_{R_s}^{R_m} f(R) dR_{allowed} \tag{2.6}$$

A useful approximation can be obtained inserting in the Stoermer expression instead of the Earth's magnetic moment M_o an effective moment $M_o^{'}$ evaluated using the real magnetic field B. In a dipole field the following relation holds

$$B = \frac{\mu_o M_o^{'}}{4\pi} \frac{\sqrt{1 + 3\sin\lambda_m^2}}{r^3} \tag{2.7}$$

Inserting $M_o^{'}$ an analytical expression for this effective Stoermer cutoff can be derived as:

$$R_{seff} = \frac{\mu_o B\, r \cos\lambda_m^4}{4\pi\sqrt{1 + 3\sin\lambda_m^2}\,(1 + \sqrt{1 - \hat{q}\cos\lambda_m^3 \cos\phi_m \sin\theta\cos\phi}\,)^2} \tag{2.8}$$

The accuracy of this model depends on the geomagnetic location and it has been shown at $400\,Km$ is below 20% [79]. It is also possible to express the rigidity cutoff in terms of $L - shell$ parameter; for example, for particles arriving from the vertical direction the recommended relation is [71], [15]

$$R_s = \frac{58}{L^2[1 + \sqrt{1 + (r/L)^{3/2}}]^2} \tag{2.9}$$

in GV, where r is the distance from the dipole center in R_e. It has been shown [71] that for two different locations A and B at different distances on the same radius vector from the center of

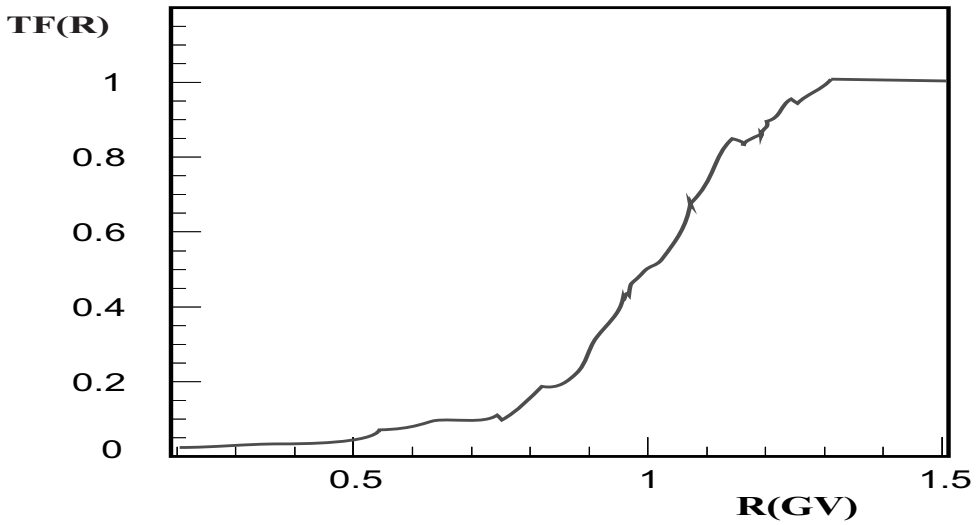

Figure 2.10: *Transmissivity function for a given location around the rigidity cutoff averaged over all the arrival directions*

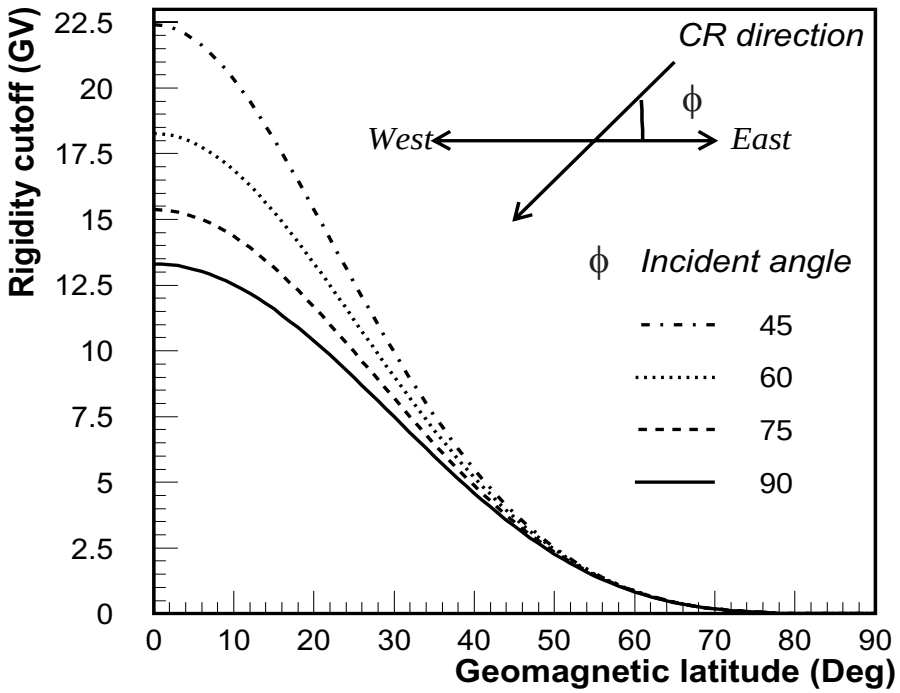

Figure 2.11: *Stoermer rigidity cutoff for different incident angle φ at an altitude of* 380 Km

the dipole the vertical cutoffs are related by

$$\frac{R_s(A)}{L^2(B)} = \frac{R_s(B)}{L^2(A)} \tag{2.10}$$

and the evaluation of a grid of vertical cutoff values can be determined at any position along a satellite orbit by interpolation.

2.5 Cosmic Ray Measurements

Cosmic rays can be studied either outside the atmosphere using satellites by direct detection, by balloon borne instruments in atmosphere and on the Earth's surface by analyzing the characteristics of the air showers produced in the atmosphere. In the following, the current situation of proton and helium fluxes, the most abundant component reaching the Earth, is presented The lepton fluxes are presented which, despite of their relative abundance, play an important role in the study of the propagation models of CR in the galaxy.

Proton Measurements Protons represent the main component of the cosmic rays reaching the Earth and accurate measurement of their absolute fluxes are of fundamental importance to the understanding of the CR physics. Moreover, they are needed for the evaluation of secondary products coming from the interaction of CR with the interstellar medium and for atmospheric neutrino studies. Atmospheric neutrinos produced by interactions of CR with atmosphere via the meson decay allows for the evaluation of the flavor ratio $R_\nu = N(\nu_e + \bar{\nu_e})/N(\nu_\mu + \bar{\nu_\mu}) \sim 0.5$. Atmospheric neutrinos have the potential to probe the oscillation effects in the baseline range of $1 < L/E < 3 \times 10^4\ Km/GeV$ [67] and an oscillation effect has been evidenced from the measurement of R_ν [78]. The range of neutrino energies involved are $1 < E_\nu < 10^4\ GeV$ while the corresponding primary CR should have energy per nucleon ten times higher. Proton contribution to the total flux is about 81% at $10 GeV$, dominating the overall uncertainty. Recent measurements in the energy range $0.1 \div 200\, GeV$ have been made by balloon-borne experiments using different implementation of the NASA/NMSU Balloon Borne Magnet Facility (BBMF) such as [83], [85], [86], [88] and the [89] collaborations. The systematics in the spectra below 5% made [89] the most accurate among them. The fig. 2.12 shows measurements of the proton flux spectra (multiplied by a factor $E^{2.5}$) with a comparison of data from balloon-borne experiments. It is clear that data are not consistent, having differences being of the order of $20 \div 30\%$ reaching 40% above $\sim 60\, GeV$. [89] measurements do not agree with the other experiments, being the differences due to solar modulation and to systematic effects. At energies above $10\, GeV$, the differences cannot be easily related to the estimation of errors and a physical origin of those differences cannot be excluded. A possibility exists that those differences might be ascribed to long time scale fluctuations of the proton flux due to energetic phenomena at the sources sites and clearly other investigations are required.

Helium Measurements Helium is the second most important element in cosmic rays and represent the 12% of the total flux reaching the Earth. Therefore, the contribution for the evaluation of secondary fluxes produced in the atmosphere may be quite compelling. Such a contribution has to be taken into account when evaluating the atmospheric neutrino fluxes, as

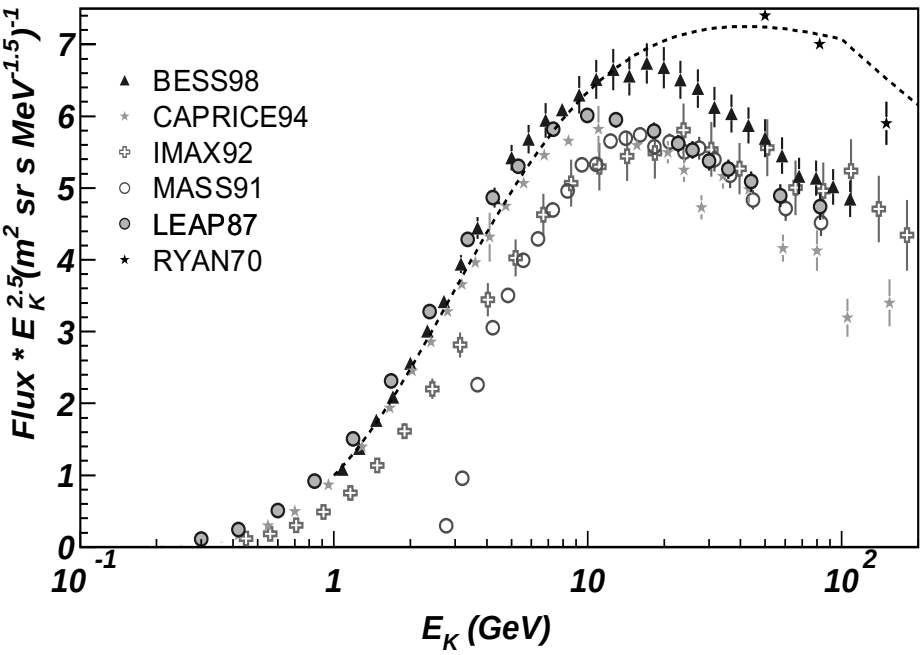

Figure 2.12: *Collection of measurements for the differential primary proton spectrum from balloon borne experiment [81]. The superimposed dashed line comes from [82] being used for the neutrino flux calculation.*

well as those of antiprotons and leptons as well as diffuse gamma ray radiation. Finding no significative difference in the energy spectra of protons and helium suggested the same sources and propagation histories for both species.

The isotopic helium composition shows a dominance of ^4He while only a small fraction, less than 10% of ^3He is present.

The primary cosmic ray spectrum can be parameterized by a power law in rigidity as for primary protons. However, some experiments ([88],[84]) show differences in the spectral index in the rigidity range of $10 \div 100\,GV$. The most accurate measurements to date come from balloon and suffer for the systematics due to the correction for the residual atmospheric overburden. The experimental situation for Helium measurements shows certain ambiguity, because of the large uncertainties affecting data from different experiments, with discrepancies up to a factor of 2 at $50\,GeV$, as shown in fig. 2.13 [89]. Precise measurements from Bess98 quote errors on Helium nuclei at level of $O(10\%)$ and seem to favor lower fluxes than previously assumed for the atmospheric neutrino calculation especially above tens of GeV.

Lepton Measurements Leptons (electrons and positrons) represent only a small fraction of the CR flux reaching the Earth and are dominated by the negative charge component. The lepton dynamics during the propagation is dominated by the interaction with the interstellar medium, leading to ionization, bremsstrahlung and synchrotron radiation losses. This can be clearly seen from the steepening of the spectrum compared to ions at energy above $10\,GeV$. Several experiments have been carried out for the measurements of the electrons using stratospheric

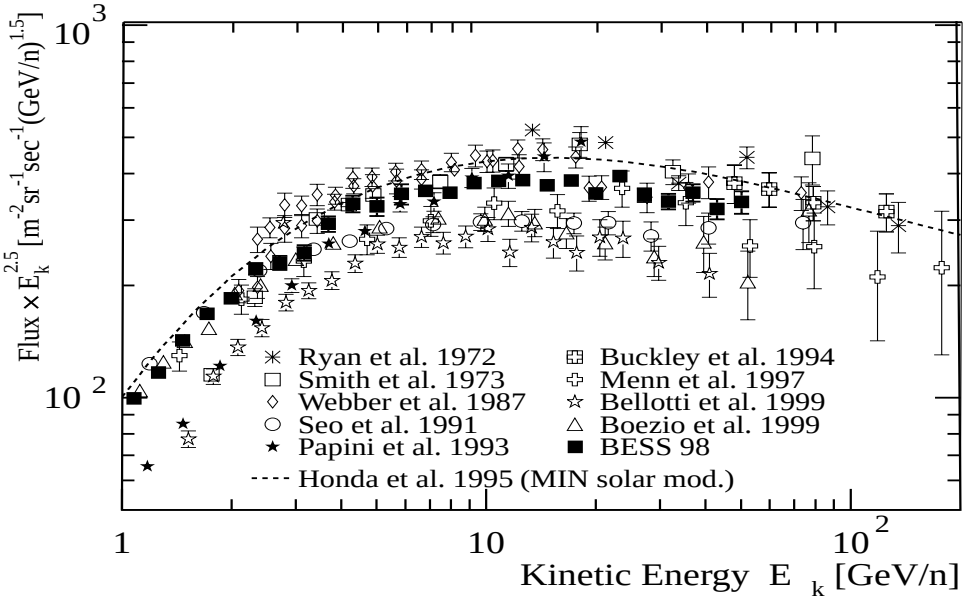

Figure 2.13: *Collection of measurements for the differential primary helium spectrum from balloon borne experiment [89]. The superimposed dashed line comes from [82] used for the neutrino flux calculation.*

balloons. Measurements of electrons in the CR must take into account the low intensity of the signal, the vast production of secondary leptons in the interaction of CR with the atmosphere and the presence of high background from the CR nuclear component ($e^-/p \sim 10^{-2}$, $e^+/p \sim 10^{-4}$ @ $10\,GeV$). Quite different experimental approaches have been used in order to separate positive and negative lepton components or to extend the energy range.

It is believed that most of the CR electrons are of primary origin, produced and accelerated in the same sources as the ions, so that they are expected to have basically the same spectrum at the origin. The secondary contribution comes from the pion decay produced in the interaction of CR with the interstellar medium. Such a secondary contribution can be estimated from the separate measurement of electrons and positrons and also measuring the charge composition in particular the fraction $R_+ = e^+/(e^+ + e^-)$ where systematic errors partially cancels out.

Secondary leptons are important for modelling cosmic ray propagation and to study the solar modulation effect. At energies below $10\,GeV$, the solar modulation and the geomagnetic effects strongly modifies the electron spectrum. In fig. 2.14, the measurements of the $e^+ + e^-$ spectrum are shown, amplified by a factor E^3 to better appreciate different experimental results. Discrepancies are clearly seen in these measurements even by a factor 2. Detector systematic uncertainties (acceptance, resolution, background) together with different procedures to evaluate atmospheric correction are responsible for the differences. With this experimental situation, it is not possible to come to a stringent conclusion for propagation models. In fig. 2.15 the result on positron fluxes are shown with the same scale as for electrons. Large error bars are present in the high energy part of the spectrum due to the low intensity of the signal and the difficulty to separate positrons from protons and electrons ($e^-/e^+ \sim 10$ @$10\,GeV$) and to correct for the atmospheric secondaries. However, some of the corrections cancel in the evaluation of the ratio

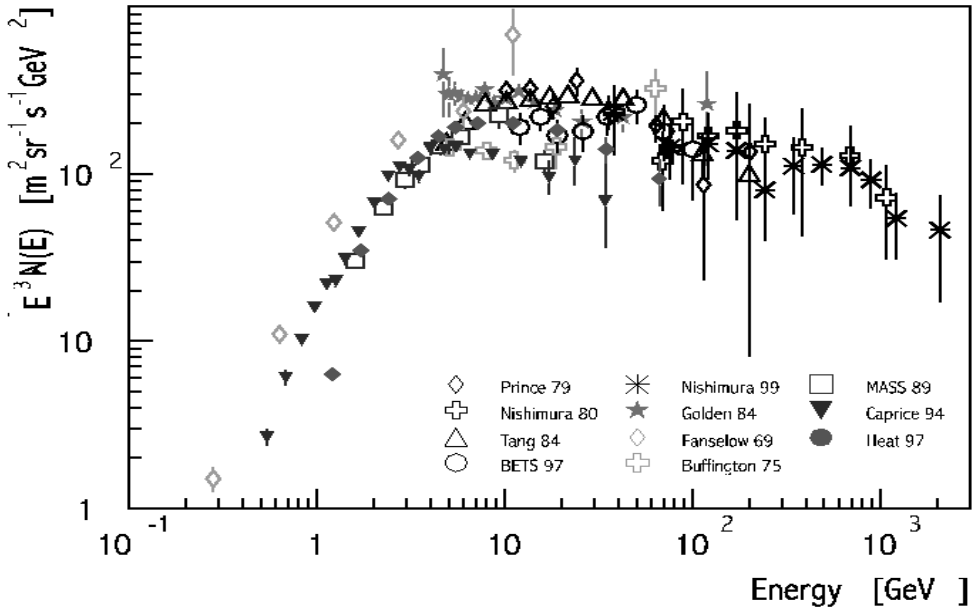

Figure 2.14: $e^+ + e^-$ *differential flux measurement collection (multiplied for* E^3*) [94]*

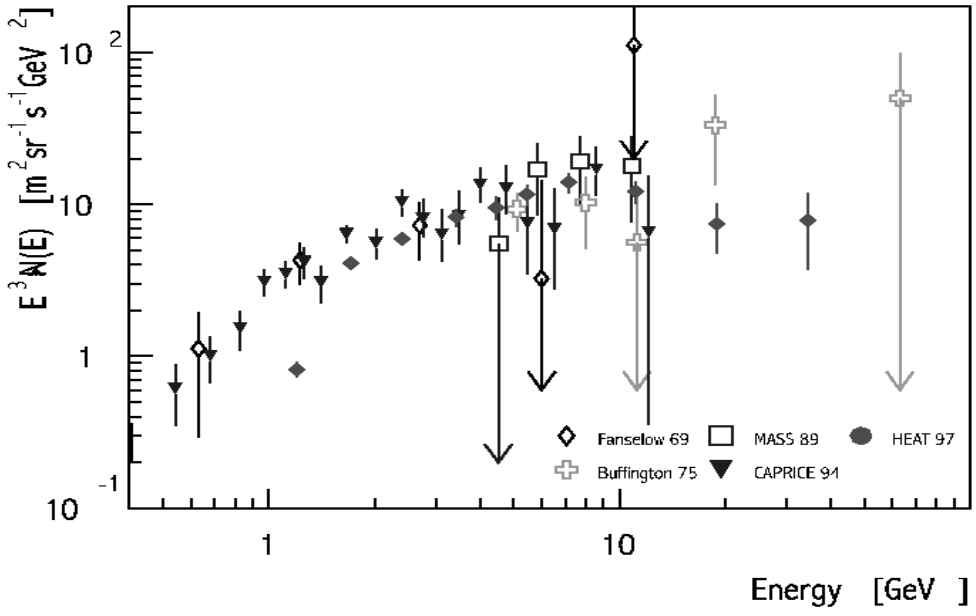

Figure 2.15: e^+ *differential flux measurement collection (multiplied for* E^3*) [94]*

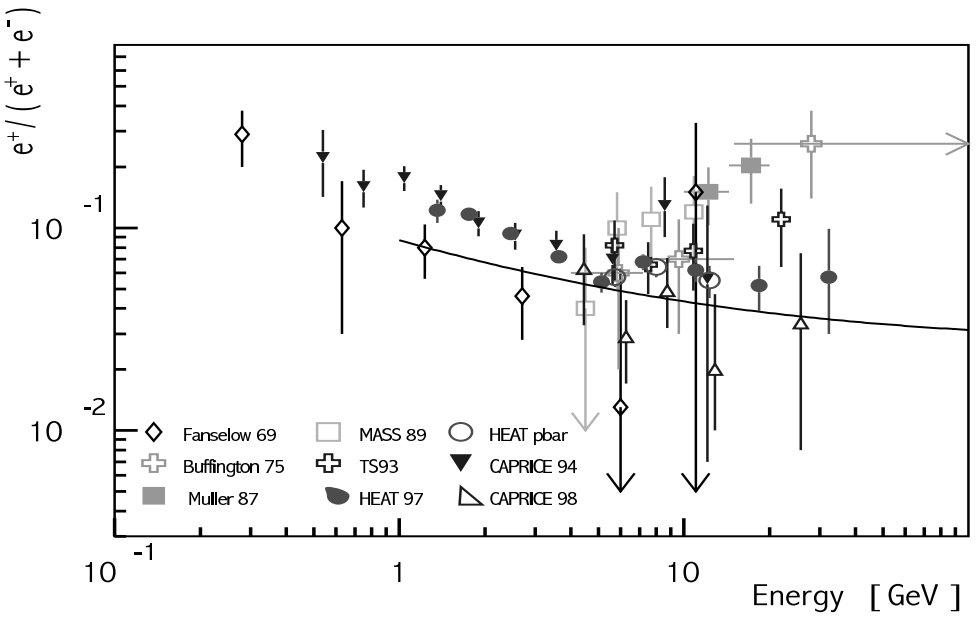

Figure 2.16: $e^+/(e^+ + e^-)$ *differential flux measurement [94]. The superimposed line shows the expectation from the LBM [115]*

R_+ presented in fig. 2.16 with superimposed the precision of the LBM. The measure for R_+ in the energy range $1 \div 10$ GeV shows a value around 10% which accounts for a positron component of secondary origin approximately comparable with the secondary electron component. At energies above 10 GeV, the positron excess does not agree in the framework of LBM boosting a theoretical effort in order to explain such discrepancy [114].

2.6 Cosmic Ray Interaction with the Atmosphere

As already mentioned, CR are the principal engine for high energy radiation belts. Every time a CR enters the Earth atmosphere the interactions produce an *air-shower*: a spray of new particles. Each constituent of this secondary flux can interact with air nuclei or eventually decay, depending on the lifetime. The development of the air shower is determined by the properties of the atmosphere and cross sections of the processes.

The simplest model used for the atmosphere is the isothermal gas approximation extending up to ~ 25 Km in height; in this model the Earth's curvature has to be taken in account only for zenith ϑ angle $> 60^o$. Calling $\rho(l, \vartheta)$ the atmosphere density at distance l along the particle trajectory starting from the Earth's surface, as shown in fig. 2.17 the definition of the slant depth and vertical slant depth are:

$$X(l, \vartheta) = \int_l^\infty \rho(l^{'}, \vartheta) dl^{'} \qquad X_v(h) = \int_h^\infty \rho(h^{'}) dh^{'} \tag{2.11}$$

expressed in $[gcm^{-2}]$, with the vertical altitude h given by $h \simeq l \cos\vartheta + l^2 sin^2\vartheta / 2R_e$, the second term being important only for $\vartheta > 60^o$. The vertical slant depth X_v, at height h is simply $X_v = p$. The atmosphere scale height is defined as $h_o = X_v/(-dX_v/dh)$, and the following

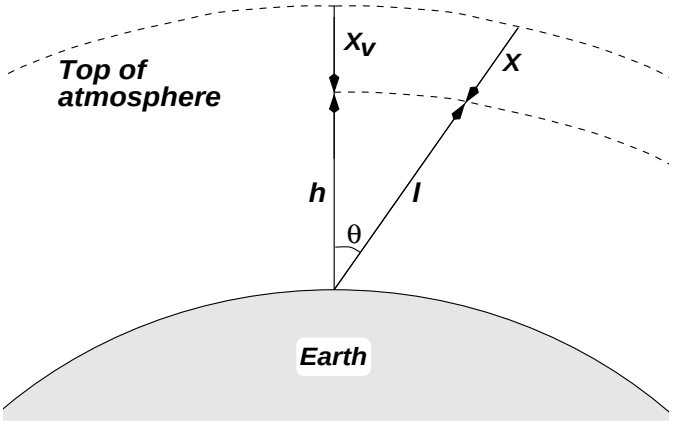

Figure 2.17: *Definition of the slant depth* X_v

relation holds $h_o = p/\rho = RT/M$, R being the gas constant and M the molecular weight of the atmospheric constituents. The profile of the vertical depth X_v is given by $X_v = X_o\, e^{-h/h_o}$ where $X_o \simeq 1030\, gcm^{-2}$ defined the TOA.

As a result, the density can be expressed as $\rho = -dX_v/dh = X_v/h_o \simeq X \cos\vartheta/h_o$ for $\vartheta < 60^o$ and shown in fig. 2.18.

The real atmosphere is far from isothermal and the temperature decreases with the altitude up to the tropopause. The variation of temperature in the region between the tropopause and the mesopause is due to the absorbtion of UV light by ozone, while the increase above $100\, Km$ is due to the extreme UV light and X-rays absorbtion by N and O.

Above $1500\, Km$, the ionized component of the atmosphere becomes predominant and the magnetosphere begins. For $X_v > 200\, gcm^{-2}$ results $h_o \simeq 8.4\, Km$ while for $X_v < 200\, gcm^{-2}$, $h_o \simeq 6.4\, Km$. Major atmospheric constituents below $100\, Km$ are O_2, N_2, O, and H_e.

Models of atmosphere are based on empirical and theoretical work: the COSPAR International Reference Atmosphere model is known as Mass Spectrometer Incoherent Scatter (MSIS) thermospheric model [66] covering an altitude range from $25\, Km$ up to $2500\, Km$ and including detailed modelling of atmosphere variations. The MSIS is based on extensive data compilation and analysis, using as input time, coordinates, solar flux, magnetic activity, and determining densities of He, O, N_2, O_2, Ar, and N, total mass density and temperatures. The latest version of the code called MSISe-90 is also available as a stand-alone code or via web interactive from the NSSDC homepage (http://nssdc.gsfc.nasa.gov/pub/models/msise90).

The development of the shower depends on mean energy available to each particle in the shower. If the energy available falls below the threshold for the production of a given particle, the energy will gradually be lost by ionization and radiative processes. As a consequence there is a maximum number of particles that can be obtained as a function of the atmospheric depth and starting energy. The shower extends laterally as a function of the depth mainly due to multiple Coulomb scattering of the electromagnetic component of the shower, and to the increasing opening angles of the particle interactions in the Earth's reference frame. Two types of air shower are possible according to whether the primary particle is hadronic or not. An hadronic

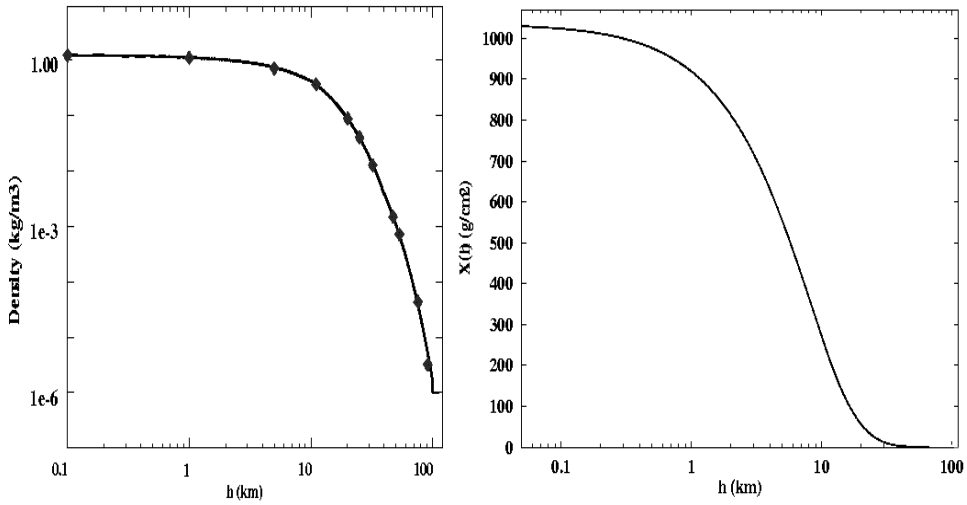

Figure 2.18: *In the left panel model data for the atmospheric density, in the right panel the vertical atmospheric depth both as a function of vertical altitude over sea level.*

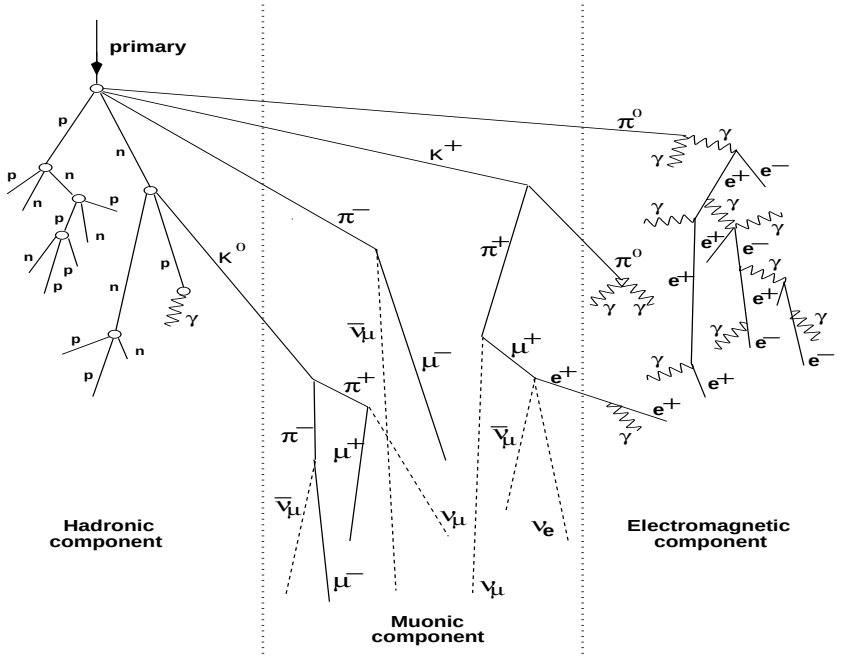

Figure 2.19: *Schematic development of an air shower of hadronic origin*

Particle type	ϵ_i [GeV]
$K^{\pm}$	850
K_S	1.2×10^5
K_L	205
$\pi^{\pm}$	115
π^o	3.5×10^{10}
$\mu^{\pm}$	1.0

	λ_i $[gcm^{-2}]$		
Lab Energy [TeV]	p-air	π-air	K-air
0.1	86	116	138
1.0	83	107	-
1000	60	70	-
10^6	43	50	-

Table 2.1: *Mean decay constant ϵ_i and interaction length λ_i for particles in atmosphere [68].*

shower involves strong interactions in the collision of primaries with atmosphere, with hadrons, mesons and leptons as decay products. If the primary is not an hadron, the composition of the shower is dominated by bremsstrahlung and pair production processes.

The hadronic production of meson or heavy leptons via photoproduction ($\gamma + nucleus \rightarrow hadrons$) is low due to the suppressed cross sections. Muon production typically proceeds through photoproduction with consecutive hadron decay.

The ratio between the two processes: $\sigma_{\gamma \rightarrow hadrons}/\sigma_{\gamma \rightarrow e^+e^-} \approx 3 \times 10^{-3}$. Pair production of muons is suppressed by a factor $(m_e/m_\mu)^2 \approx 2 \times 10^{-5}$ relative to pair production of e^- and e^+. As a result the muonic content of a photon shower will be much less (a factor ≈ 30) than for the hadronic case, making experimentally possible the distinction of the two kind of showers. Barions and mesons are produced by interactions of particles with air nuclei. The secondaries can re-interact and/or decay. It is also possible to have disintegration of air nucleus or creation of low energy gamma rays by nuclear excitation.

In case of decay of secondaries, the creation of mesons feeding the electromagnetic and muonic component of the air shower is expected. Heavier leptons decay into lighter particles or interact. The mean particle energy decreases rather quickly, while the radiation length for electrons is $(X_o)_{elm} \sim 37\, gcm^{-2}$.

The muonic component is the most penetrating part of the air showers. Muons are created mainly by decay of pions and kaons from the hadronic component and propagate in atmosphere loosing energy only by ionization. Muons are also produced in the decay of charmed particles but this production is very low compared to the other types of processes and the contribution is negligible for energy well below $100\, TeV$.

The strength of the decay and interaction processes experienced by the particles of species i in the air shower can be expressed in terms of respectively *mean decay length* d_i and *nuclear interaction length* λ_i. For a particle of kinetic energy/ nucleon E_i, proper lifetime τ_i and rest mass m_i the definition of d_i is the slant depth X_v which the particle traverses before decaying $d_i = \rho\gamma_i c\tau_i = \rho c\tau_i E_i/m_i c^2 = X \cos\vartheta E_i/\epsilon_i$ where $\epsilon_i = m_i c^2 h_o/c\tau_i$.

The nuclear interaction length in a medium with nucleons density ρ_N depends on the total inelastic cross section σ_i on air for a particle type i and with the assumption of a mean number of nucleons $A \simeq 14.5$ in an air nucleus, $\lambda_i = \rho/\rho_N \sigma_i = A m_p/\sigma_i$ where m_p is the proton mass. In tab.2.1 a qualitative evaluation indication of the numerical value of ϵ_i and λ_i are shown for some particles.

The nucleonic flux $N(E, X)$ is altered by interaction in atmosphere which decreases the

initial flux and increases the secondary flux by newly created nucleons. The nucleon transport equation can be written as

$$\frac{dN(E,X)}{dX} = -\frac{N(E,X)}{\lambda_N} + \frac{1}{\lambda_N}\int_E^\infty N(E^{'},X)F_{NN}(E,E^{'})\frac{dE^{'}}{E} \tag{2.12}$$

where the subscript N denotes a nucleonic particle. In this equation the first term on the right-side is the depletion of nucleons by interactions with atmospheric particles, the second term represents the enhancement of nucleons by the internucleon interaction. In eq. 2.12 $F_{ij}(E_i,E_j) = E_j\, dn_{ij}(E_j,E_i)/dE_j$ represents the dimensionless inclusive cross section for an incident particle i producing particle j. However, eq. 2.12 does not take into account the magnetic field so the leakage of the particles from the atmosphere is neglected. To solve the eq. 2.12 one may use a MonteCarlo method or try to find out analytical solutions making some approximation [68]. Usually at the zero-th order one assumes that:

i) an incident nucleus of mass number A and energy E_n can be treated as A independent nucleons of energy E_n/A, ii) the inclusive cross section F_{ij} for bremsstrahlung and pair production follows a scaling behavior with the particles center of mass energy [68], meaning that for any interaction the distribution of the longitudinal momentum of the secondary reflects the momentum distribution of the constituents of the incident particle, iii) the ionization losses are neglected iv) the nuclear interaction length λ_N does not depend on the particle energy. Under all the conditions, the solution of the eq. 2.12 can be factorized as $N(E,X) = Q(E)g(X)$. Primary CR flux follows a power law, therefore assuming $Q(E) = E^{-(\gamma+1)}$ the solution become [68]:

$$N(E,X) = N_0 E^{-(\gamma+1)} e^{-X/\Lambda_N} = N_0(E) e^{-X/\Lambda_N} \tag{2.13}$$

where Λ_N is called *atmospheric attenuation length* and contains the interaction dependence from F_{ij} and λ_N, with typical values for 100 GeV particles for nucleons, pions and kaons of 120, 160, 180 gcm^{-2} respectively. Here N_0 represents the primary CR flux at ToA. This is the basic mechanism of proton production in atmosphere while the lepton production in atmosphere involves decay of short lived particles created during collisions of CR with atmospheric nuclei, cascade of primary electrons and delta rays whose contribution is negligible below 50 MeV. As a result the main mechanisms for the production of electrons and positrons in atmosphere can be summarized from the following processes:

a) decay of short lived energetic particles such as $\pi^\pm \to \mu^\pm + \nu_\mu(\bar{\nu_\mu})$ ($\sim 100\%$), $K^\pm \to \mu^\pm + \nu_\mu(\bar{\nu_\mu})$ ($\sim 63.51\%$) with the kaon channel strongly suppressed with respect to the pion channel due to the K suppressed production cross section. The process depends on the atmospheric density.

b) neutral pion decay in leptons through gamma ray $\pi^o \to 2\gamma \to 2(e^+ + e^-)$ which is indeed proportional to the square of the atmospheric density.

Following the methodology in [116] for the evaluation of the lepton fluxes, we have to consider the transport of the charged and neutral pion decay contribution.

I- For the evaluation of the meson flux another transport equation has to be solved

$$\frac{dF_\pi(E,X)}{dX} = -(\frac{1}{\lambda_\pi} + \frac{1}{d_\pi})F_\pi(E,X) + \frac{1}{\lambda_\pi}\int_0^1 F_\pi(E/x_L)F_{\pi\pi}\frac{dx_L}{x_L^2} + \tag{2.14}$$
$$+\frac{1}{\lambda_N}\int_0^1 N(E/x_L)F_{N\pi}\frac{dx_L}{x_L^2} \quad (x_L = E/E')$$

with a similar equation for the K meson spectrum. The first term on the right side in eq. 2.14 represents the depletion of pion by interaction and decay, the second term the regeneration by $\pi - N$ interaction and the last term is the pion production spectrum $P_\pi(E,X)$ by nucleons on air. Neglecting the pion regeneration, factorization of the energy and depth dependence of primary spectrum by $N(E,X) = Q(E/x_L)g(X) \approx (E/x_L)^{-(\gamma+1)}g(X)$ brings to the expression of the pion production spectrum

$$P_\pi(E,X) = Q(E)\frac{e^{-X/\Lambda_\pi}}{\lambda_N} = Z_{N\pi}N_0(E)\frac{e^{-X/\Lambda_N}}{\lambda_N} \tag{2.15}$$

where $Z_{N\pi} = \int_0^1 (x_L)^{\gamma-1}F_{N\pi}(x_L)dx_L$ and $x_L = E_\pi/E_N$ is the spectrum weighted momentum. Using again the same factorization for the pion flux $F_\pi(E,X) \sim E^{-(\gamma+1)}q(X)$ the solution for the eq. 2.14 can be written as:

$$F_\pi(E,X) = Q(E)\frac{e^{-X/\Lambda_N}}{\lambda_N}X^{\epsilon_\pi/E\cos\vartheta}\int_0^X dX' e^{-X'(1/\Lambda_N - 1/\Lambda_\pi)}X'^{\epsilon_\pi/E\cos\vartheta} \tag{2.16}$$

which for $E\cos\vartheta << \epsilon_\pi$ (meson decay favored above interaction) resulting $\Lambda_\pi \sim \Lambda_N$, the flux expression can be simplified

$$F_\pi(E,X) \approx Q(E)\frac{e^{-X/\Lambda_\pi}}{\lambda_N}\frac{XE\cos\vartheta}{E+\epsilon_\pi} \tag{2.17}$$

Due to the short lifetime mesons produced will decay without interacting giving new mesons and leptons. The pion spectrum, for not too much high energies, can be written as

$$D_\pi = \frac{dF_\pi(E,X)}{dX} = \frac{F_\pi(E,X)}{d_\pi} = \frac{F_\pi\epsilon_\pi}{XE\cos\vartheta} \tag{2.18}$$

with a similar equation for K-mesons. The production spectrum of μ-mesons from π and K decays is evaluated from parents secondaries via

$$P_\mu(E,X) = \frac{dN_\mu(E,X)}{dEdX} = \sum_j \int_{E_{min}}^{E_{max}} dE_j' D_j(E_j',X)\frac{dn_{\mu j}(E_\mu,E_j')}{dE_\mu} \tag{2.19}$$

being $j = \mu, K$ and $dn_{\mu j}(E_\mu,E_j')/dE_\mu$ is the inclusive spectrum of produced muons from the decay of type j meson with energy E_j and mass M_j.

For a two body decay particles, as π and K mesons are, this term is $dn_{\mu j}(E_\mu,E_j')/dE_\mu = B_{\mu j}/(P_L(1-r_M))$ where $B_{\mu j}$ is the branching ratio for the decay channel $j \to \mu + X$, P_L is the parent particle momentum in the lab frame, and $r_M = (m_\mu/M_j)^2$ with m_μ the muon mass. For both these channels the decay distribution is flat in energy as well as in solid angle in the meson rest frame, and in average the muon and neutrino energies are: $< E_\mu >= q_{\pi\mu}E = 0.79E$, $< E_\nu >= q_{\pi\nu}0.21E$, $< E_\mu >= q_{K\mu}E = 0.52E$, $< E_\nu >= q_{K\nu}E = 0.48E$.

In these approximations, the μ production spectrum is given by:

$$P_\mu(E_\mu,X) = \frac{B_{\mu\pi}}{1-r_\pi}\int_{E_\mu}^{E_\mu/r_\pi}\frac{F_\pi(E_\pi',X)}{d_\pi}\frac{dE_\pi'}{E_\pi'} + \frac{B_{\mu K}}{1-r_K}\int_{E_\mu}^{E_\mu/r_K}\frac{F_K(E_K',X)}{d_K}\frac{dE_K'}{E_K'} \tag{2.20}$$

Some muons decay in the atmosphere and the flux at any depth is governed by the diffusion equation with interaction term neglected:

$$\frac{dF_\mu(E,X)}{dX} = P_\mu(E,X) - \frac{F_\mu(E,X)}{d_\mu} \tag{2.21}$$

The solution can be written as:

$$F_\mu(E,X) = X^{\epsilon_\mu/E\cos\vartheta}\int_0^X X^{'\epsilon_\mu/E\cos\vartheta} P_\mu(E^{'},X^{'})dX^{'} \tag{2.22}$$

From the three body decay of the muon channel, the electron energy distribution is:

$$\psi_e(E_\mu,E) = \frac{dn_{\mu e}(E_\mu,E)}{dE} = \frac{5/3 - 3(E/E_\mu)^2 + 4/3(E/E_\mu)^3}{E_\mu} \tag{2.23}$$

and the production spectrum of the electrons is

$$P_e(E,X) = \int_\epsilon^\infty \frac{F_\mu(E^{'},X)}{d_\mu}\psi_e(E^{'},E)dE^{'} \tag{2.24}$$

with $\epsilon = E$ for $E > m_\mu$ and $\epsilon = m_\mu$ with $E < m_\mu$. Neglecting the electromagnetic multiplication but taking into account radiation loss, the energy spectrum of electrons at any depth is given by [116]:

$$F_e(E,X) = \int_0^X P_e(E^{'},X^{'})\frac{\partial E^{'}}{\partial E}dX^{'} \tag{2.25}$$

where $E^{'}$ is the energy at $X^{'}$ and $\partial E^{'}/\partial E$ is the Jacobian for the transformation from $E^{'}$ to E.

II- Another contribution to the lepton spectra comes from the decay of neutral π^0 via the channel $\pi^0 \rightarrow 2\gamma \rightarrow 2(e^+ + e^-)$. Since the lifetime of π^0 is about $\sim 1.8\cdot 10^{-16}$ s, they decay rapidly in photons. The production spectrum can be written as:

$$P_\gamma(E,X) = \int_{E'=\epsilon}^\infty 2P_{\pi^0}(E',X)\frac{dE'}{\Psi_\gamma(E')} \tag{2.26}$$

where $\epsilon = E + \frac{m_{\pi^0}^2}{4E}$ and $\Psi_\gamma(E') = \sqrt{E'^2 - m_{\pi^0}^2}$.

For a power law spectrum for P_{π^0}, $P_\gamma \approx E^{-\beta}$ for $E > 70\,MeV$ and $P_\gamma \approx E^{\beta}$ for $E < 70\,MeV$ where β is the spectral index for the pion production spectrum [116].

The γ rays flux at any depth can be described by the diffusion equation:

$$\frac{dF_\gamma(E,X)}{dX} = P_\gamma(E,X) - \frac{F_\gamma(E,X)}{L_c} \tag{2.27}$$

where the second term in the right side represents the rate of conversion of γ rays in the atmosphere and $L_c = 48.5\,g/cm^2$ the conversion length in air. The solution for the eq. 2.27 is

$$F_\gamma(E,X) = e^{-X/L_c}\int_0^X P_\gamma(E,X')e^{X'/L_c}dX' \tag{2.28}$$

When high energy photons interact in the atmosphere, e^+e^- pair are generated, with a flat energy spectrum $N_e(E)dE = 2dE/E_\gamma$ which becomes zero at $E = 0$ and $E = E_\gamma$. Then the production spectrum can be written as

$$P_e(E, X) = \int_{E'=E}^{\infty} F_\gamma(E', X') \frac{2dE'}{L_c E'} \tag{2.29}$$

Neglecting electromagnetic multiplication but taking into account radiation losses, the energy spectrum for the electrons at any depth is given by

$$F_e(E, X) = \int_0^X P_e(E', X') \frac{\partial E'}{\partial E} dX' \tag{2.30}$$

The production spectrum of electrons from charged pion results to be independent of the depth of the residual atmosphere, while the contribution coming from the neutral pion decay is proportional to the depth of the residual atmosphere [100],[116]. The result can be generalized in case of curvilinear trajectory [100]

$$F_e(\mathbf{p}, \mathbf{r}) = \int_0^\infty P_e(\mathbf{p}, \mathbf{r}'(X')) \frac{\partial p'}{\partial p} dX' \tag{2.31}$$

where $\mathbf{r}(X)$ represent the electron trajectory eventually in the Earth's magnetic field and X the amount of material along the electron trajectory.

It has been shown in [100] and [91] that an equation similar to eq. 2.31 holds for the proton spectrum once we substitute the proton production spectrum $P_p(\mathbf{p}, \mathbf{r}'(X'))$ instead of the lepton production spectrum $P_e(\mathbf{p}, \mathbf{r}'(X'))$.

To evaluate the integral in eq. 2.31 one has to model the energy losses which for electrons and positrons in the Earth's magnetic field are due to ionization, bremsstrahlung and synchrotron losses. If B is the magnetic field, ρ the atmospheric density and c the speed of light, energy losses can be parameterized for leptons by [113] as $dE/dx = 0.002 + 0.028E + 3.86 \times 10^{-6} E^2 B^2/(\rho c)$ in $[GeV\ g^{-1}\ cm^2]$ where only the ionization term is present for protons. It is clear that some approximation must be done to get an analytical solution or a MonteCarlo simulation approach has to be used in order to describe the full production process.

2.7 Albedo Particles

The term *albedo* cosmic ray is used for particles produced by interactions of CR in the Earth's atmosphere. Albedo fluxes were measured since pioneering rocket experiments ([104],[106]) and confirmed later during balloon flights ([107],[108]). Balloons reach an altitude of about $38 \div 40\ Km$, where the residual atmospheric pressure is $\sim 1\%$ of that at sea level with a typical flight duration of O(days).

During the flight on balloon, the residual atmosphere (overburden) ranges in the interval $3 \div 8\ gcm^{-2}$ corresponding to a flight altitude of $30 \div\ 40\ Km$.

The name *splash albedo* is used for particles emerging from the atmosphere and moving upward, while the term *reentrant albedo* denotes downward moving particles below the geomagnetic cutoff. The reentrant albedo particles with rigidity below the local geomagnetic cutoff are able to spiral along the magnetic field lines and to reenter the atmosphere in the opposite hemisphere

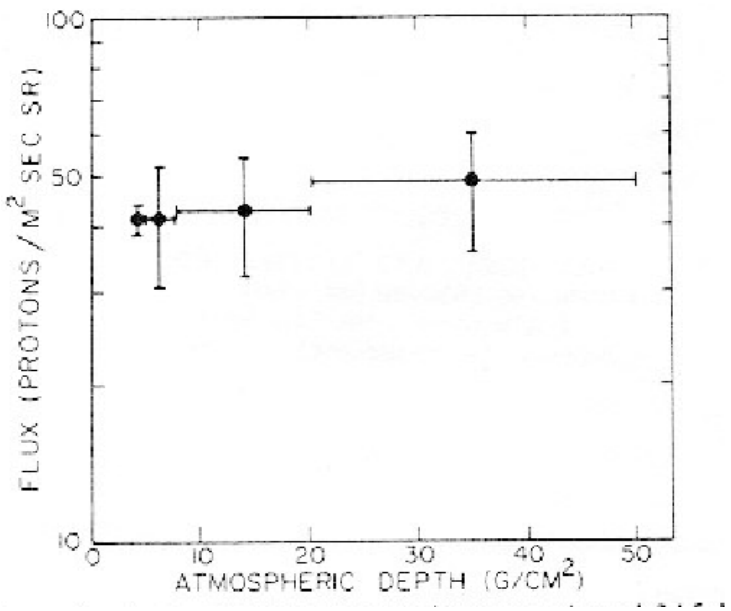

Figure 2.20: *Integral flux of splash albedo protons in the energy range* $4 \div 315\ MeV$ *as function of atmospheric depth [103]*

at about the same magnetic latitude. Therefore the intensity of splash and reentrant albedo are expected to be of the same order.

Several satellites experiments were carried out in LEO to measure the component of the albedo fluxes (see [101] and [141] for a collection of data). The flux densities measured in these experiments were of the same order of those measured with balloons in stratosphere. It was then concluded that fluxes observed in both cases have the same origin.

Missions in LEO cover all the positions around the Earth, outside and inside the SAA. Inside the SAA the radiation trapped in the Earth's magnetic belts is observable, with drift shells having mirror heights above $\sim 100\ Km$, the atmosphere limit. Outside the SAA, mirror points go very deep in the atmosphere with mirror altitudes well below the Earth's surface. In general we expect complex paths of the particle in this region. Extensive theoretical models do not exist, but the basic ideas can be found in ([90],[91],[97],[95],[100],[99]).

To distinguish splash and reentrant albedo in the secondary population, the flux intensity below the geomagnetic cutoff must be examined as a function of the depth in the atmosphere. The intensity of splash albedo is expected more intense at large zenith angles provided they are produced by the air showers of primary CR with atmosphere more effective at large zenith angles [96], and depending on the amount of material crossed by the particle after the production; the splash albedo show no significant variations with altitude [103]. Ionization energy losses and eventually bremsstrahlung losses during propagation in the atmosphere are responsible for this dependence.

Moreover, the intensity is also dependent on the secondary production mechanism assumed and on the path followed by particle after the trapping in the Earth's magnetic field. However, after the particles leave the Earth, the complex bending in the magnetic field is able to wash out

this angular dependence. As a result the reentrant albedo are expected to be nearly isotropic. The determination of the reentrant albedo flux in balloon experiments is a difficult task because one has to determine the particle momentum and direction accurately enough to distinguish between primary and under-cutoff particle and then to separate the contribution coming from the atmospheric secondary from the reentrant albedo. The separation between reentrant albedo from the atmospheric secondaries below geomagnetic cutoff is based on the different dependence on atmospheric depth, even though this functional dependence is not known with great accuracy. The reentrant albedo must be corrected to the top of atmosphere taking into account the energy loss in the residual atmosphere of the order of few $[gcm^{-2}]$ above the balloon altitudes with relative uncertainties at level of $10 \div 20\%$. Moreover, for leptons energy rescaling is necessary to compensate for bremsstrahlung or synchrotron losses giving systematics of the order of $\sim 5\%$. For the splash albedo such correction is less important because the amount of residual atmosphere is small compared to the relative amount of matter between the balloon and the production altitude. The correction to the top of atmosphere can be calculated using an effective approach based on the evaluation of the probability $w(E_o, E)$ for a particle of initial energy E_o to loose energy down to the limit E in the interaction with the residual atmosphere [80].

The intensity of secondary protons created in nuclear interactions of primary cosmic rays was originally evaluated under simple hypothesis by [91],[92] including the effects of nuclear interactions and the presence of the magnetic field. In [93] several balloon based measurements of splash and reentrant albedo proton fluxes are compared with the Ray model [93] as reported in fig. 2.21. [101] measured the albedo fluxes at altitudes of $\sim 500\, Km$ on the Interkosmos-17 satellite finding latitude dependent fluxes on the horizon line of sight with proton integral fluxes of $\sim 60\ m^{-2}s^{-1}sr^{-1}$ with $E > 0.5\, GeV$. In fig. 2.22, the intensity of atmospheric under-cutoff total flux of e^- and e^+ from [102] as a function of the atmospheric overburden is shown. In the same plot, a MonteCarlo simulation result for the evaluation of the atmospheric secondaries contribution is also shown. The splash albedo are removed from the sample in order to accept downward particles and then the difference between data and MC are attributed to reentrant particles. The net flux is presented in fig. 2.23 together with a comparison with other balloon borne experiments. Note the large uncertainties affecting the data.

The MEPHI group reported in a number of papers (see [141] for a review) the result of electron and positron albedo fluxes inside and outside the SAA with energies of $\leq 100\, MeV$. [97] suggested that in interactions of CR with atmosphere, high energy leptons are produced via the $\pi\mu e$ chain. In [97] model, the role of the magnetic field is taken into account together with the transport equations for the air shower. It plays an important role in increasing the leakage of albedo leptons from the atmosphere to the Earth orbital space. Depending on the pitch angle, they may leave the atmosphere bound to a field line. The flux intensity of such electrons is expected to be of the same order of primary flux, weakly depending on the altitude. Due to the magnetic field, trapped particles may experience many drifts around the Earth or can be Quasi-Trapped, bouncing many times but experiencing only one or even a fraction of drift.

In [97], the intensity of albedo electrons depends on the incoming CR flux and on the interaction probability with the residual atmosphere, while the lifetimes depend on the energy losses.

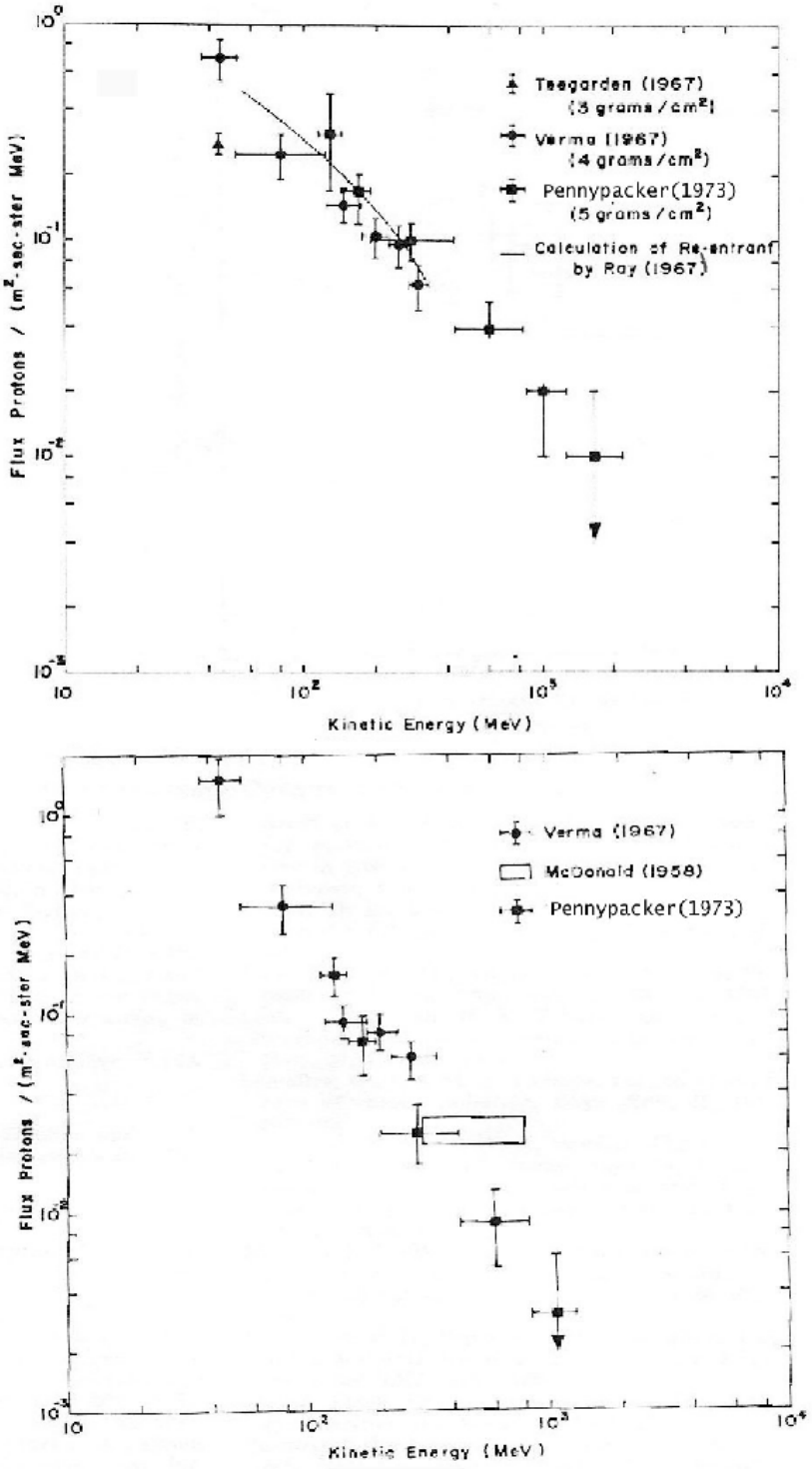

Figure 2.21: *Differential proton fluxes measured in balloon experiments - reentrant plus atmospheric secondaries and Ray calculation on upper panel, splash albedo on the bottom panel [93]*

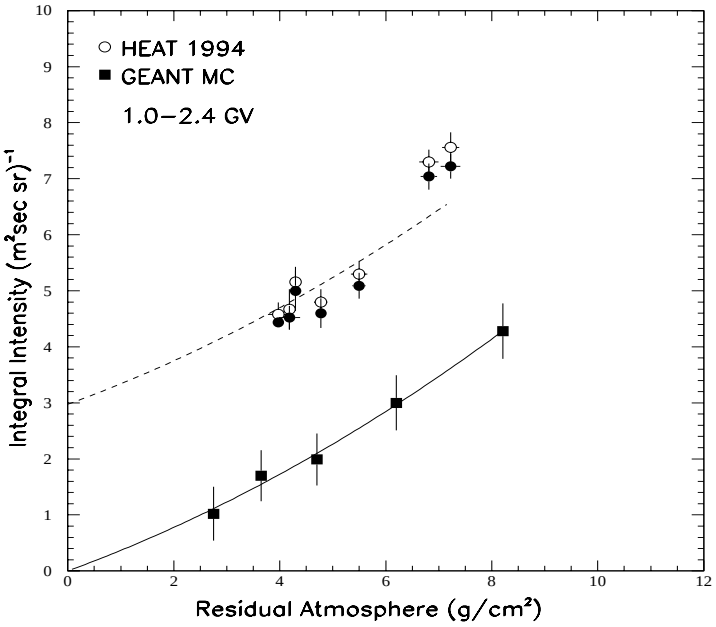

Figure 2.22: *Intensity of secondary leptons in the energy range* $1 \div 2.4\ GeV$ *as function of residual atmosphere and secondary MC evaluation. The solid circle include a correction for bremsstrahlung in atmosphere for the primary electrons [102]*

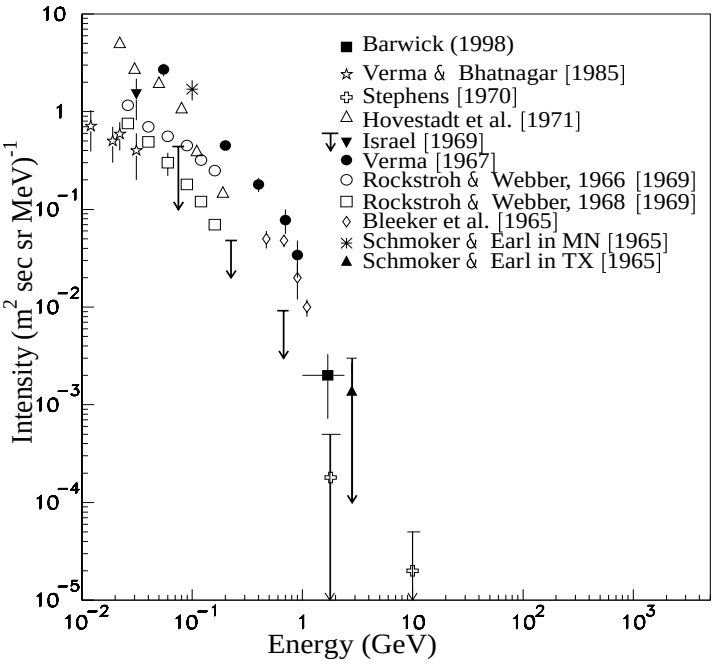

Figure 2.23: *Collection of reentrant albedo electron measurements from [102]*

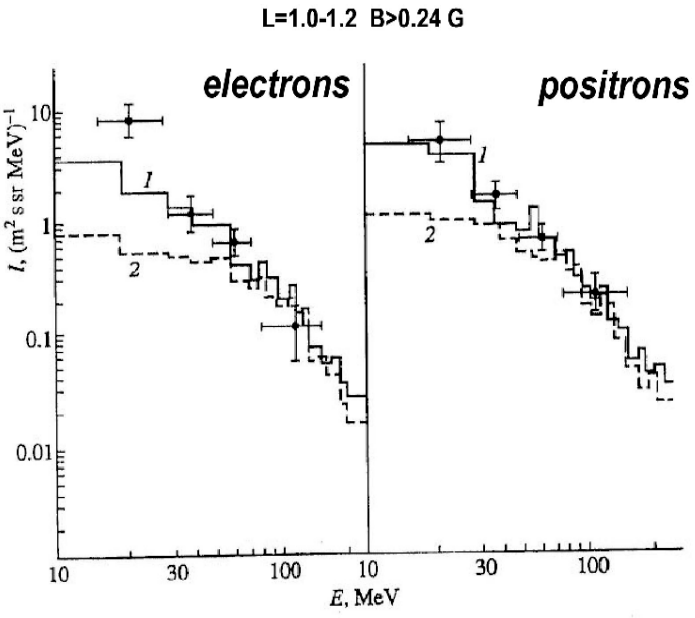

Figure 2.24: *Differential energy spectra of albedo electron and positron (with pitch angle* $< 50^o$ *from the MARYA-2 experiment onboard MIR compared with MonteCarlo simulation 1) and without the* π^o *decay 2) from [112]*

The difference in the terminology used for balloon born and satellite born experiments may be somehow confusing. However, it is clear from the models depicted formerly that splash and reentrant albedos are just the name of particles Quasi-Trapped in the Earth's magnetic field depending on pitch angle and detection position.

One of the main criteria to test the hypothesis on the origin of trapped relativistic leptons is the study of the charge composition. In [110], the MEPHI group found that the lepton flux outside the SAA at the geomagnetic equator (with pitch angle $< 50^o$) shows a ratio of $N_{e^+}/N_{e^-} = 1.8$ which supports a generation mechanism based on proton interactions with the Earth's atmosphere. In the SAA the total intensity of electrons increases in comparison with outside SAA at the geomagnetic equator, with a charge ratio $N_{e^-}/N_{e^+} = 3.4$. The electron component shows an increase of 13 times more while the increase for positrons is about ≈ 2.

A new generation mechanism, based on electron acceleration in the magnetosphere, was invoked by [112], with preference to plasma fluctuations. In [111] a three dimensional MonteCarlo simulation with isotropic CR flux was used, assuming exponential atmosphere and dipole field. The simulation takes into account contribution of the $\pi\mu$e decay channel for the production of the leptons energy spectrum. Fig. 2.24 shows the simulated differential energy spectra of electrons and positrons (with pitch angle $< 50^o$) at $L = 1.1$ together with data outside the SAA, from MARYA-2 experiment [109]. The histogram 2 shows the contributions to lepton flux from the decay of charged pions, while the histogram 1 gives the contribution from the neutral pion. It is clear that the neutral pion contribution plays an important role only below $50\,MeV$. The gamma rays moving in the horizontal direction have a great probability to produce lepton pairs with efficient leakage from atmosphere due to the low amount of matter crossed by the particles.

Within this model, a lepton charge composition with an excess of positrons up to energies of the order of GeV is expected. Above $10\,GeV$, the high multiplicity of the pion produced brings to a generation of an equal number of positrons and leptons. Taking into account the magnetic field we see that the leakage is more efficient for high magnetic latitudes, due to the lower geomagnetic cutoff. As a consequence the positron excess is expected to decrease increasing the latitude. Similar results were also presented in [100] and [87].

Chapter 3

The AMS01 Experiment

3.1 Introduction

The Alpha Magnetic Spectrometer (AMS) is a high energy physics experiment scheduled to be installed on the International Space Station (ISS) in the year 2005 for an operational time of three years. Principal scientific objectives are the search for antimatter, dark matter and cosmic rays spectra and composition. During 1998 a precursor flight was performed onboard the Space Shuttle Discovery at an altitude of $\sim 400\,Km$ for an observational period of ten days, collecting more than 100 million events. The technical details of the prototype detector, called AMS01, are described in this chapter, as well as its performance during the flight. Moreover, the analysis of CR proton and lepton fluxes is presented together with a comparison with previous measurements. The principal features of the under-cutoff particles observed are also described, while a more detailed analysis is discussed in the fourth chapter.

3.2 AMS Physics Goals

The Alpha Magnetic Spectrometer (AMS) ([118], [131]) is able to measures the charged CR with very high sensitivity thanks to the large acceptance ($0.5\ m^2 sr$). It will be installed on the International Space Station (ISS) for three years. AMS has the potential to address fundamental questions like the existence of antimatter and dark matter. For the detection of antimatter, or eventually a result of its non observation, AMS has to be able to distinguish a potential antihelium nucleus from an estimated $10^9 \div 10^{10}$ He that will be recorded during the three years on the ISS.

The current cosmological theories of the universe, assume that matter and antimatter were equally abundant at the beginning. The observational evidence of cosmological antimatter can be excluded both from the measurements of gamma ray flux with energies of the order of MeV and the lack of distortions in the microwave background spectrum up to the scale of tens of megaparsec. Baryogenesis predicts a universe non baryon symmetric and domain structures of matter and antimatter larger than cluster of galaxies. The eventual presence of antimatter of cosmological origin would have important implications for particle physics. The evaluation of the ratio of secondary ${}^3\bar{H}e$ or $\bar{C}$ to secondary $\bar{p}$ is of the order $O(10^{-11})$ and $O(10^{-56})$ respectively bringing to the conclusion that the observation of an antinucleus by AMS should originate from

nucleosynthesis of antimatter domains. Since no antimatter has been observed in CR at galaxy supercluster scale, only limits on antimatter are up to now quoted. The possible determination by AMS of antimatter beyond our local supercluster of galaxies, even if the universe does not contain antimatter domains, is very important in the understanding of fundamental physics processes in the early universe.

The evidence for the existence of large amount of non radiating matter in the universe has been known since long time. Using the gravitational motion information of stars and galaxies combined with emission of hot gas in the galaxy halos, the presence of dark matter can be inferred. There are several dark matter candidates, the most promising of which, in a super symmetric scenario, is the neutralino [121]. Since the neutralino is coincident with its antiparticle, it can annihilate in ordinary particles, and would result in an enhancement of positron flux in CR compared to those produced by interaction of primary CR with interstellar medium. The measurements of positron and antiproton spectra could lead to the confirmation of the existence of dark matter candidates, decay of which would result in a significant signal over expected background. Additional sources of antiprotons have been suggested, from the neutralino annihilation expected with softer energy spectrum.

The measurement of the nuclear and isotopical composition of CR can be also used to validate particle propagation models in the interstellar medium. The light elements (Li, Be and B) are much more abundant in CR than in the solar system resulting from spallation of heavier nuclei in interaction with inter stellar medium. Positrons and antiprotons result from secondary production with relative abundance providing information about CR propagation. The accurate determination of the B/C ratio over a wide range of energies will be of paramount importance to determine the thickness of the galactic halo [119]. Moreover the study of the ratio of the radioactive isotope ^{10}Be to the stable ^{9}Be can bring to the determination of the time of confinement of the CR in the galaxy [68].

3.3 AMS01 Detector

In AMS the physical measured quantities are the particle charge, mass, rigidity and direction. In June 1998, an AMS prototype called AMS01, flew on a precursor flight on board the space Shuttle Discovery during the STS-91 mission [135]. The orbit was circular and inclined of about 52^o at an altitude between $370 \div 390\, Km$.

In fig. 3.1, the AMS01 version of the detector is depicted [122]. The cylindrical permanent magnet, with a field strength along the +X axis of about $0.15\, T$ at the center, encloses a multilayered microstrip silicon tracker (T1-T6) which measures the momentum of the charged particles traversing the volume. For the STS-91 mission the tracker was equipped with 38% of the total amount of the silicon sensors resulting in a limited acceptance of $\sim 0.3\, m^2 sr$ for events within 4 tracker planes. Scintillator planes (S1-S4) and an Aerogel Threshold Cerenkov (ATC) counter complete the detector by measuring the particle velocity and dE/dx. A layer of anticoincidence scintillator counter (ACC) covers the inner surface of the magnet to veto triggers due to stray trajectories and background particles which may be produced by interactions in the detector material.

To minimize the dead time, a low energy particle shield (LEPS) was mounted on the top

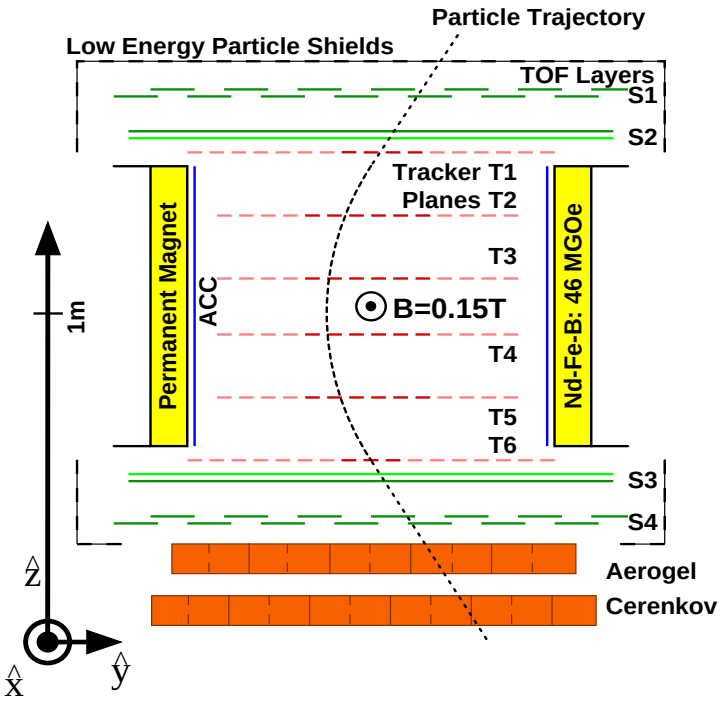

Figure 3.1: *Schematic view of the AMS01 detector during the STS-91 flight [135]*

to absorbs low energy particles ($< 5\ MeV$) above the scintillator planes. The particle mass is determined from the measured velocity and momentum, while the energy loss measurements from the scintillators and the silicon tracker together with the velocity from the time of flight measurement, provide for the charge of the particle. The sign of the charge is determined from the curvature of the reconstructed track.

3.3.1 The AMS01 Magnet

In the AMS01 detector, the analyzing power is provided by a permanent magnet, designed optimized to achieve the best performance, keeping minimum weight and flux leakage. Moreover, it provides the largest possible geometrical acceptance and large bending power BL^2. With these requirements, the geometry was chosen to be cylindrical with a height of $80\,cm$ and inner/outer radii of $55.7/65\,cm$ resulting in a geometrical acceptance of $0.82\,m^2sr$. The magnetic flux inside the bore is of $B = 0.15\,T$ with an analyzing power of $BL^2 = 0.14\,Tm^2$. The fig. 3.2 shows the average field of B_x at different z cross sections which quickly drops to near zero outside the magnet. The final weight was of about $1.92\ tons$ and the fringe field at the order of $3\ G$ at a distance of $2.6\ m$ from the center while the final geometrical acceptance is $0.82\,m^2sr$.

3.3.2 The AMS01 Time of Flight

The Time of Flight (ToF) system provides a fast trigger signal, a measurement of the speed of the particle by measuring the time needed to traverse the detector; it measures the particle charge using the energy deposited in the plastic scintillators.

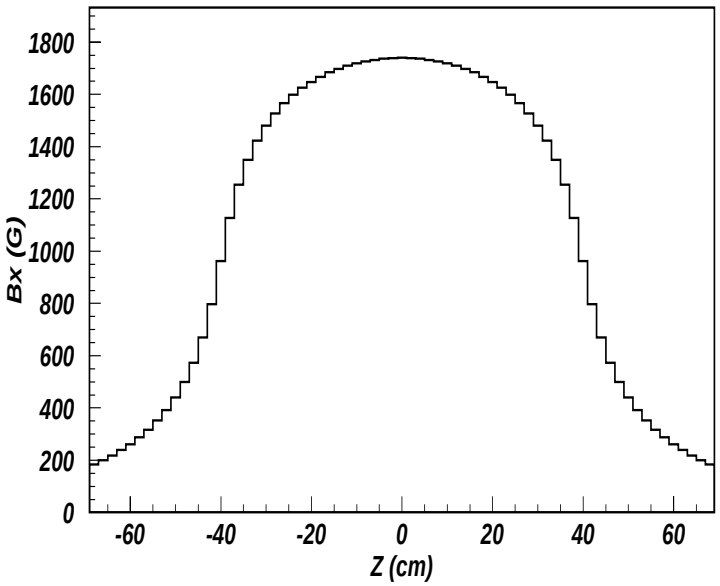

Figure 3.2: *Average B_x at different z cross sections [135]*

Each plane of the ToF consists of 14 plastic scintillator (Bicron Bc408) paddles 1 cm thick, 11 cm width and with lengths between 71 cm and 136 cm to match the circular cross section of AMS01 magnet. Two planes are located on the top and two on the bottom of the magnet. The paddles of one plane have 0.5 cm overlap to avoid geometrical inefficiencies [123]. They are oriented orthogonally to the paddles of the second plane to allow for the identification of the particle impact point (X,Y). Each scintillator paddle is read by six photomultipliers, three per side. The PMT are shielded from the residual magnetic field ($\sim 200\,G$) by a 0.5 mm thick mumetal case. To extend the dynamic range of the ToF system, the analog signals from both the first and the second to last dynodes are transferred to the readout electronics. The anodes signal were discriminated to reproduce a logical signal sent to the AMS01 trigger electronics to define the fast trigger signal (see sec. 3.4). The analog signals from both anodes and dynodes were addressed to the readout electronics based on a Time to Digital Converter (TDC) devices, which provides the time information.

The absolute transit time in the ToF for a particle can be obtained from the average value of the measurements on the two sides, t_1 and t_2, of a counter, $t = (t_1 + t_2)/2$. The position along the paddle can be derived from the difference between the times $x = v_{eff}(t_1 - t_2)/2$ where v_{eff} is the effective velocity of light in the scintillator paddle, ($v_{eff} \sim 15.5\,cm/ns$), obtaining a spatial resolution of $\sigma_x < 2\,cm$. The direction of a particle traversing the detector can be determined with great reliability.

The time measurement is used for the determination of the particle velocity β and the minimum time of flight of a relativistic particle depends on the distance L between two pair of ToF planes. Considering $L = 150\,cm$ for a relativistic particle we have $\beta = v/c = L/tc \sim 5\,ns/t$. The velocity resolution due to a time resolution of about $\sigma_t = 125\ ps$ results in $\Delta\beta/\beta = \Delta t/t \sim 0.025$. The time of flight distribution between two planes for a relativistic particle of unitary

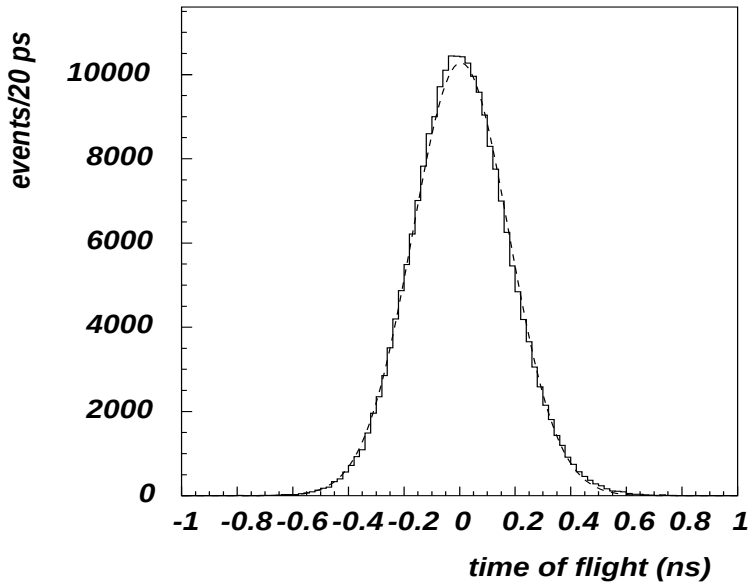

Figure 3.3: *Time of flight between the scintillators plane 1 and 2 corrected for the track length for STS-91 AMS events. The dashed line shows the gaussian fit with a* 178.1 *ps std dev [135]*

charge is shown in fig. 3.3. It exhibits a normal distribution with a standard deviation $\sigma_t = 178.1ps$. In average the typical accuracy of the ToF system for a $Z = 1$ charge particle is obtained combining the measurements coming from the four planes through $\sigma_{ToF} = \sqrt{\sigma_{12}^2 + \sigma_{34}^2}/2 \sim 125\, ps$.

The ACC counters are made of 10 mm thick plastic scintillator material, arranged in barrel staves just inside the magnet bore and just outside the inner tracker support shell. A signal in the anticounters indicates that a particle entered (or exited) through the detector not through the ToF counter, crossing the magnet or disturbing the measurement of a going through track. Multitrack events produced for example in δ electrons hitting the magnet can be therefore identified and they can be rejected. At the Level-1 trigger stage more than 90% of the multitrack events are then rejected in this way.

3.3.3 The AMS01 Tracker

The core of the detector is the silicon tracker which measures the points of intersection of a charged particle trajectory with six planes. The track reconstruction allows for the determination of the particle rigidity. The rigidity resolution is limited by the multiple scattering at low energies (below few GeV) while for higher energies is limited by the intrinsic spatial resolution and bending power.

The tracker provides also a measurement of the absolute particle charge $|Z|$ by the energy loss in the silicon planes. To achieve the desired sensitivity for particle rejection, the AMS01 tracker was designed to provide a momentum resolution of 7% at energies of $\sim 10\, GeV/n$ thanks to a resolution of 10 μm (30 μm) in the bending (non bending) plane [125].

The silicon tracker is built with double sided microstrip sensors ($40.14 \times 72.04 \times 0.300$ mm^3).

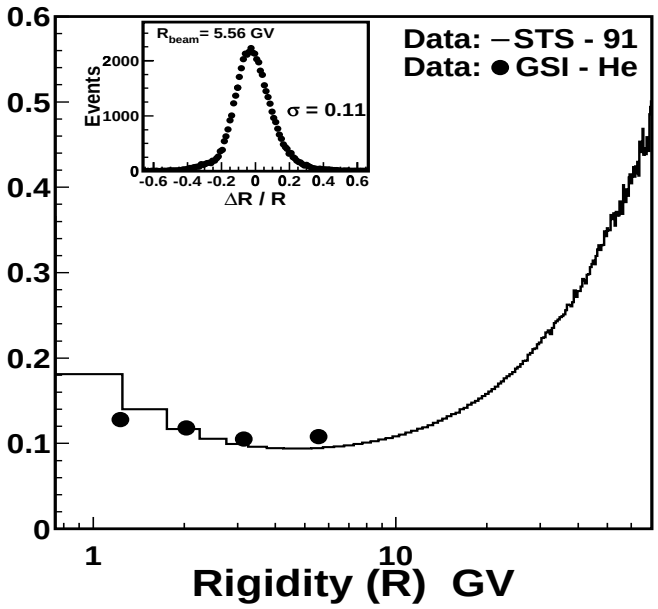

Figure 3.4: *The rigidity resolution for a Z=2 particle compared with the GSI He test beam [135].*

The sensor design makes use of capacitive charge coupling with implantation (readout) strip pitches of 27.5(110) μm for the y-coordinate (p-side) and 26(208) μm for the x-coordinate (n-side). Glued directly to the silicon sensors is a kapton foil, used as fan-out for the n-side signals to the n-side front-end hybrid. The average material thickness of a tracker plane represents $\sim 0.65\%$ of a radiation length at normal incidence.

The silicon sensors are grouped together for readout and power supply in ladders of variable length (7 to 15 sensors) to match the cylindrical geometry of the magnet, with a maximum length of 60 cm. The relatively large input capacitance (70 pF) as well as the need for a high dynamic range ($< 100\, MIP$) led to the design of a front-end chip called VA_hdr. Each VA_hdr consists of 64 channels with a charge sensitive amplifier, a CR-RC semi-Gaussian shaper and a sample and hold stage. After signal shaping and sampling, the chip is sequentially read out at a rate of 5 MHz by an analog multiplexer.

Further amplification and digitization of the signals occurs in the Tracker Data Reduction (TDR) boards, which performs also the data reduction and calibration. The determination of the position of each hit, due to the passage of an ionizing particle, is performed by a clustering algorithm. The calibration for the tracker consists in the determination of the pedestal values and widths for each channel and of the VA_hdr common noise for each chip. During the STS91 flight measured noise level $\sigma_{PED} < 4\, ADC$ on the n-side and $< 3\, ADC$ on the p-side, with a strong correlation with the measured temperature.

Tracker calibrations were made automatically every 30 minutes during data taking. The energy losses from fired strips yield the center of gravity of the cluster charge and consequently the coordinate. The online clustering uses a threshold of $3\sigma_{PED}$ to define a seed strip, while the neighbor strips are included, provided their signals exceed a $1\sigma_{PED}$

The final alignment was done with tracks at the ladder level. In fact, the assembly technique,

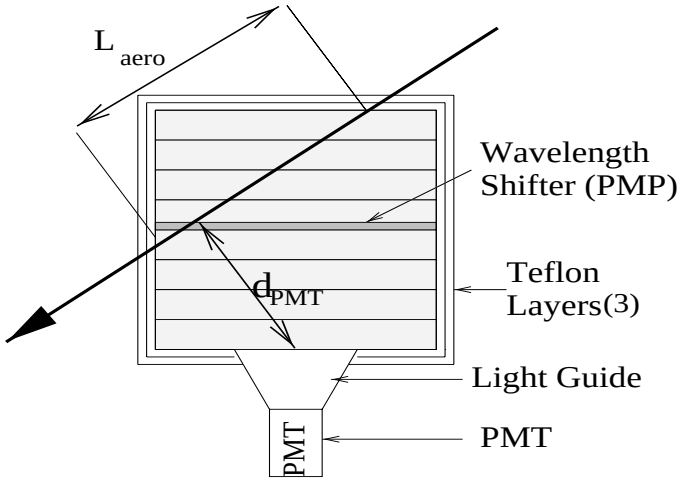

Figure 3.5: *The ATC cell made of 8 blocks of aerogel wrapped within 3 teflon layers, and a PMP wavelength shifter is located in the middle of the cell [135].*

yielded a precision better than 5 μm, in the relative alignment of the wafers in each individual ladder. Precise metrology before the flight, monitoring with laser beams during the flight and testbeam with high momentum particles after the flight have shown that there has been little mechanical variations in the tracker. The tracker momentum resolution is of 9% in the rigidity range $1 - 10\,GV$ as shown in fig. 3.4.

3.3.4 The AMS01 Aerogel Threshold Cerenkov Counter

The ATC provides an additional measurement of the particle speed and allows for e^+/p discrimination up to $3.5\,GeV$. The counters are located at the bottom of the detector below the last scintillator plane. The elementary component is the aerogel cell ($11 \times 11 \times 8.8\,cm^3$), filled with eight $1.1\,cm$ thick aerogel block with refractive index $n = 1.035$ wrapped in teflon and viewed by a Hammamatsu R5900 photomultiplier [124]. In fig. 3.5 a schematic view of a cell is shown. The 168 cells are arranged in 2 layers, shifted one respect to the other in order to minimize the loss of tracks passing in between cells. The emitted photons are reflected by three 250 μm teflon layers surrounding the aerogel blocks, until they reach the photomultiplier window. A wavelength shifter allows the shifting from 300 nm to 420 nm to get the maximum efficiency of the PMT.

The threshold values for velocity and momentum are respectively $\beta_{thd} = 1/n$ and $p_{thd} = \frac{mc}{\sqrt{n^2-1}}$ where m is the mass of the particle. The number of Cerenkov photons created by a charged particle in a material of index of refraction n is given by $N_{pe} \propto L_{aero} \times Z^2 \times \sin^2\vartheta = L_{aero} \times Z^2 \times (1 - 1/(n^2\beta^2))$ where L_{aero} is the path-length in the material, ϑ is the Cerenkov angle and Z the charge of the incoming particle. The closest distance of the track to the center of the PMT d_{PMT} shown in fig. 3.5 is defined as the impact parameter and is strongly correlated with the cell signal. The number of photoelectrons is expected to increase with the impact parameter.

The choice of aerogel depends on the value of the refractive index n which gives the best

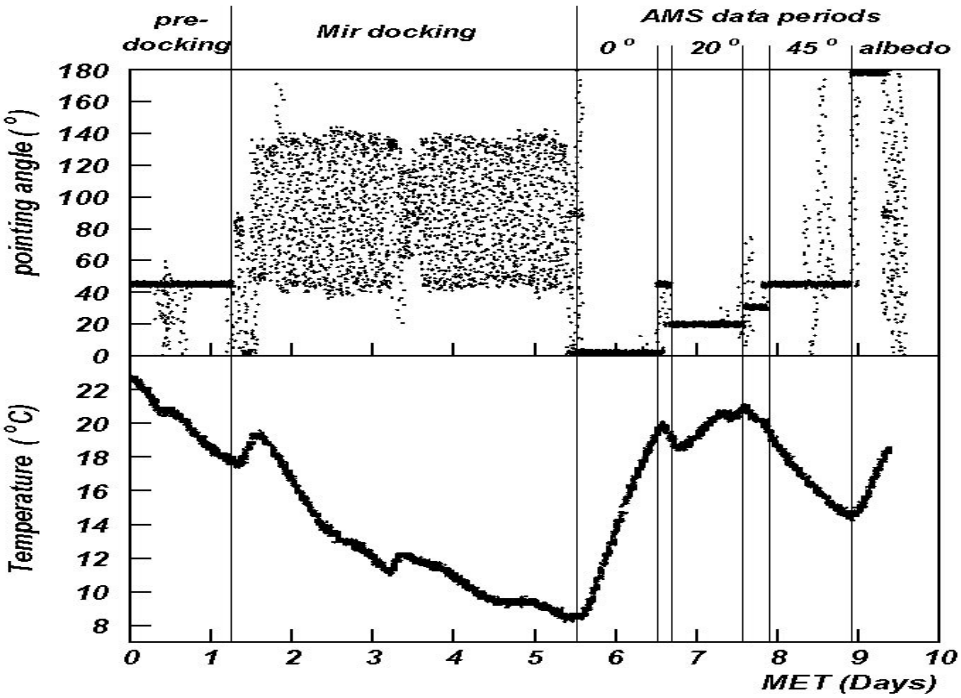

Figure 3.6: *On the top the AMS01 z-axis pointing angle measured with respect the zenith is showed as a function of the Mission Elapsed Time (MET). The bottom panel shows correspondingly the variation of the temperature during the same periods [131].*

compromise between threshold, β_{thd}, close to one and a sufficient number of photoelectrons. The ATC uses the Cerenkov effect to separate p from $e^{\pm}$ up to 3.5 GeV due to the fact that in the energy range $0.5 \div 3.5\, GeV$ leptons are above the threshold whereas, in principle, $p(\bar{p})$ gives signal only above $3.5\, GeV$. The ToF readout electronics was used for the ATC conversion of the charge by a TDC in a time signal where its length depends on the logarithm of the charge. The calibration of the ATC is done with relativistic particles, by equalizing the cell response and by determining the threshold and the level of the non-relativistic background signal in each cell. An average number of photoelectrons $n_{pe} \sim 3.1/cell$ is produced by relativistic protons. This value depend on the d_{PMT} the closest distance to the track center of the PMT window due to the losses for absorption and multiple reflections.

3.4 The AMS01 STS-91 Mission

During the STS-91 mission the AMS01 flew for $\sim 10\, days$, starting on June 2^{nd}, 1998. The Shuttle attitude, shown in the upper panel of fig. 3.6 was fixed during most of the flight. After an initial period with the AMS pointing 45^o from the local zenith, the Shuttle docked to the MIR Space Station with attitude continuously varying. After the MIR undocking the attitude of the Shuttle was kept stable with angles of 0^o, 20^o, 30^o, 45^o, 180^o from the local zenith. AMS data were collected during the total flight time, but the mission was devoted to AMS investigations only during the undocking period for a total of 111 hours while each complete orbit lasted about

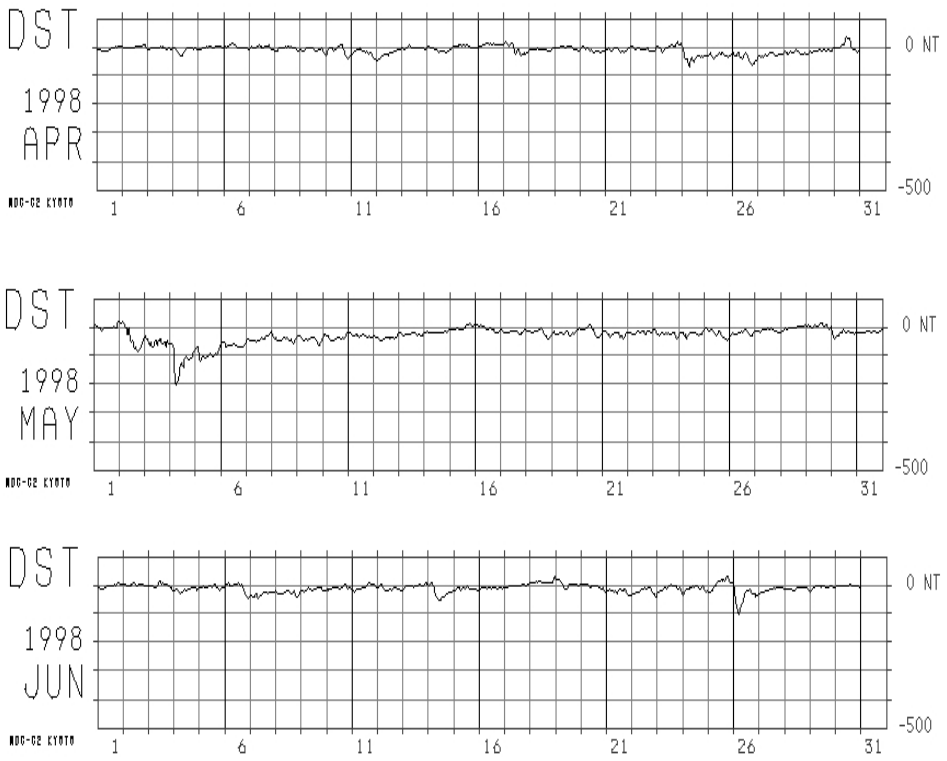

Figure 3.7: *The Dst index as function of time in the period April-June 1998 [136].*

90 minutes. AMS was located in the Shuttle cargo bay with the doors kept open during the flight. The detector performances depend on the temperature which was continuously monitored during flight by several sensors distributed over the detector as shown in the lower panel of fig. 3.6. The tracker temperature was in the range $9 \div 27\ ^oC$. The orbital parameters during the flight were provided by NASA and are described in [126]. During the flight, the magnetic conditions were quiet, as can be seen in fig. 3.7. However, severe geomagnetic and solar condition, with $D_{st} \sim -218\, nT$ and solar wind speed of $\sim 850\, Km\, s^{-1}$, where reached on May 3^{rd}. Injection of high energy electron ($E > 3\ MeV$) for this event were reported on SAMPEX Heavy Ion Large Telescope (HILT) where intense relativistic electron flux appeared at $L \sim 3$ with a formation of a new radiation belt formed at $L \sim 2.2$ [137].

3.5 Trigger and Livetime

The purpose of the trigger is to provide a fast and efficient decision whether an event is to be readout. The AMS01 trigger logic was subdivided in three stages, named fast, level-1 and level-3 triggers.

A given stage is processed only if all the conditions of the previous stages are met. For the fast trigger a four-fold coincidence from the four planes of the ToF system is required. The fast trigger implement an AND logic of four signals which are the output of an OR logic of the two ends of each paddle in a plane. The fast trigger logic signal is the seed of the trigger logic chain

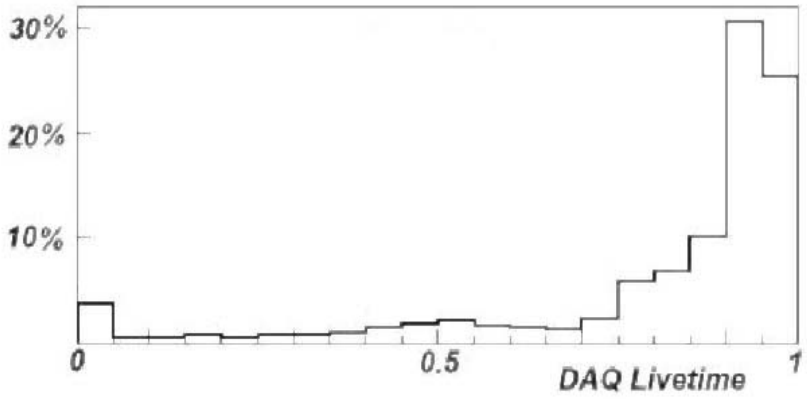

Figure 3.8: *DAQ livetime distribution with the average time value for particles outside the SAA*

of the AMS01 electronics. If within the next 200 ns, one of the other conditions is not satisfied the event is discarded.

The level-1 trigger has the purpose to select events in which at least one charged particle cleanly traversed the magnet volume. During the flight the tracker was only partially equipped, with a reduced geometrical acceptance. In order to avoid triggered events without track measured in the tracker, a correlation matrix between paddles of the two outer ToF planes was set up and only specific combinations of the paddles are accepted. To eliminate possible fake triggers due to interactions in the magnet, no signal from the ACC veto counters was required. The trigger ranged during the flight from $\sim 100\,Hz$ up to $\sim 700\,Hz$ depending on the detection location.

The level-3 ToF trigger refines the requirement for a good track asking for only one cluster in the first and fourth plane of the ToF. Afterward, a coincidence with at least one cluster in the second and/or third ToF plane is searched for. A straight fiducial road of 6 cm width connecting the hits in planes one and four of the ToF is considered in the bending projection. In case of coincidence with planes 2 and 3, the same road is taken in consideration in the non-bending projection. Finally the level-3 tracker trigger implements a pattern recognition inside the straight path defined by the level-3 ToF logic. This consists of scanning all the clusters found along the road defined by ToF and selecting only those such that in the bending projection had at least one strip with a signal to noise > 4. It requires that at least 3 clusters on 3 different tracker planes meet this condition.

During the 10 days of the STS-91 mission roughly 100 million triggers were recorded on a local disk, while an online down-link had been foreseen during the whole flight on the space station. For the purpose of trigger efficiency studies, a set of events was recorded requiring only the fast trigger conditions to be me met. Those *unbiased* events are about 0.1% of the total amount. In the published AMS papers, the analysis of the trigger efficieny was done using the unbiased events outside the SAA region; a check on the trigger efficieny was also done in the SAA for the present analysis, using the unbiased events in that region. The trigger efficiency

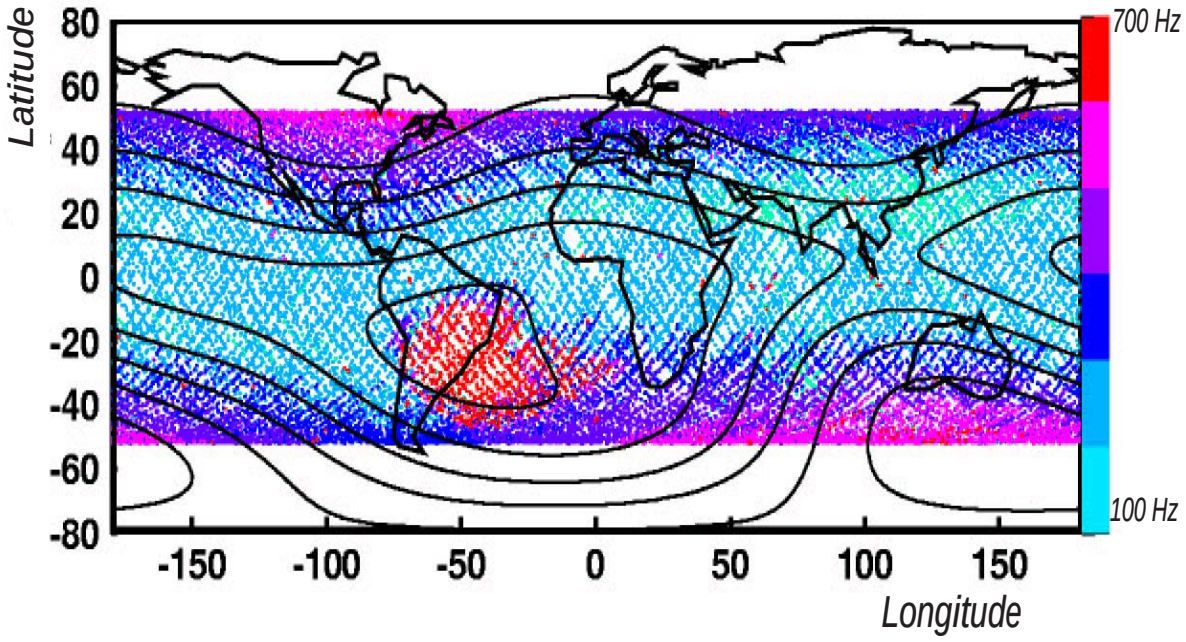

Figure 3.9: *Cosmic rays rates during STS-91 Shuttle orbits. The highest rates are at high latitudes and in the SAA.*

turns out to be ≥ 0.9 as for the region outside the SAA for DAQ livetime above 40%.

The Data Acquisition (DAQ) system consisted of several layers, including the collection of the digitized signals from each subdetector, event building, data buffering, disk storage and down link. The sensitivity of the tracker is optimized at $t = 0$, when the particle crosses the silicon sensors. The time required by each charge amplifier to integrate and amplify the signal is about $4\,\mu s$. The ToF provides a time gate of $\sim 12\,\mu s$ centered at $t = 0$ recording the history of the ToF detectors before the trigger and until the level-1 trigger is consulted. To read, digitize and buffer the readout $80\,\mu s$ are required. The information after the event is accepted by the level-1 trigger, leaving in the following few μs the DAQ system ready for a new event. During the flight there were considerable variations of the DAQ livetime as the AMS01 passed through different region of the Earth's magnetic field. The average livetime of the DAQ changed according to the particle rates ranging between $0 \div 95\%$. The lower livetime corresponds to the higher particle flux observed at high latitude and especially in the SAA.

3.6 Event Reconstruction

The physical quantities measured with the detector are the arrival direction, its signed rigidity, mass and charge. Particles are identified through the measurements coming from all the subdetectors. The signed rigidity comes from the fit of the particle trajectory in the magnetic field of the tracker, the particle velocity and direction come from ToF and ATC, the charge from the measurements of energy losses in the ToF and silicon planes. Sign of the charge and particle

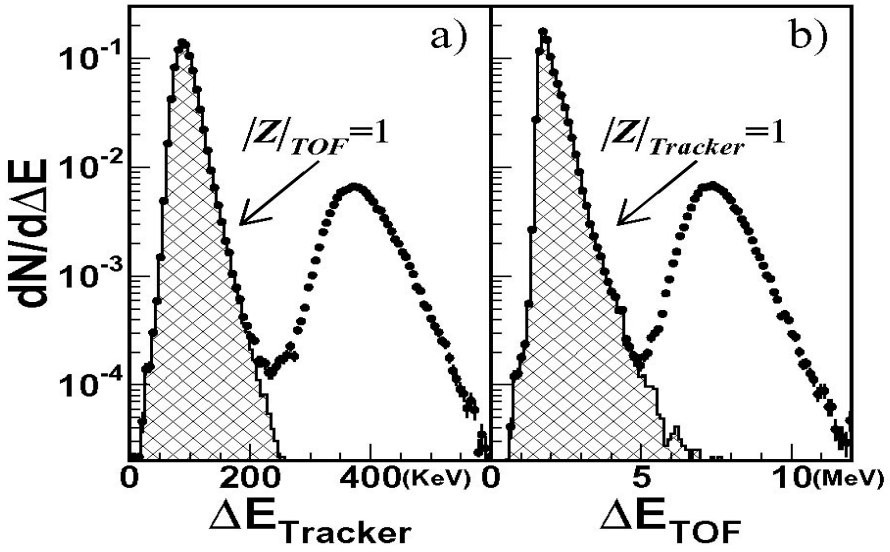

Figure 3.10: *Energy loss measurements made independently in tracker and ToF for* $|Z| \leq 2$ *events. The hatched histograms shows events with assigned* $|Z| = 1$ *by the other subdetectors [135].*

mass are derived from the above mentioned quantities and complete the information to identify the particle.

The trajectory of a particle traversing the detector is reconstructed from the hits recorded in the tracker planes. The motion of a particle in the magnetic field can be parameterized by the curvature η, the particle direction and location for a total of five parameters. The parameters of the trajectory are found by means of an iterative procedure. The track fitting procedure is able to determine the parameters.

Two different fitting algorithms have been applied and compared to get the parameters. First of all, the GEANE [127] tracking program for inhomogeneous magnetic field, integrated in the GEANT3 [128] package, has been used to evaluate the particle trajectory, the transport matrix and the error covariance matrix. The path of the particle is then evaluated using a Kalman filtering technique for the dynamic integration through the geometry and the detector elements.

The second procedure is based on the method of the track propagation through the inhomogeneous magnetic field by numerical integration. With this procedure the fitting parameters are obtained by minimizing the χ^2 of the fits, using the measured coordinates the particle trajectory, weighted with the errors. To allow for a better estimation of the errors on the parameters for the low energy particles, the procedures are repeated without the effect of the multiple scattering responsible for large deviations in the track. After the estimation of the particle track curvature and incident direction, the measured points are divided in two groups (first and second three layers hits) requiring consistency between the two groups. The events affected by large scattering angles, and also the spill-over at high energy which mixes the sign of the charge can be efficiently removed in this way.

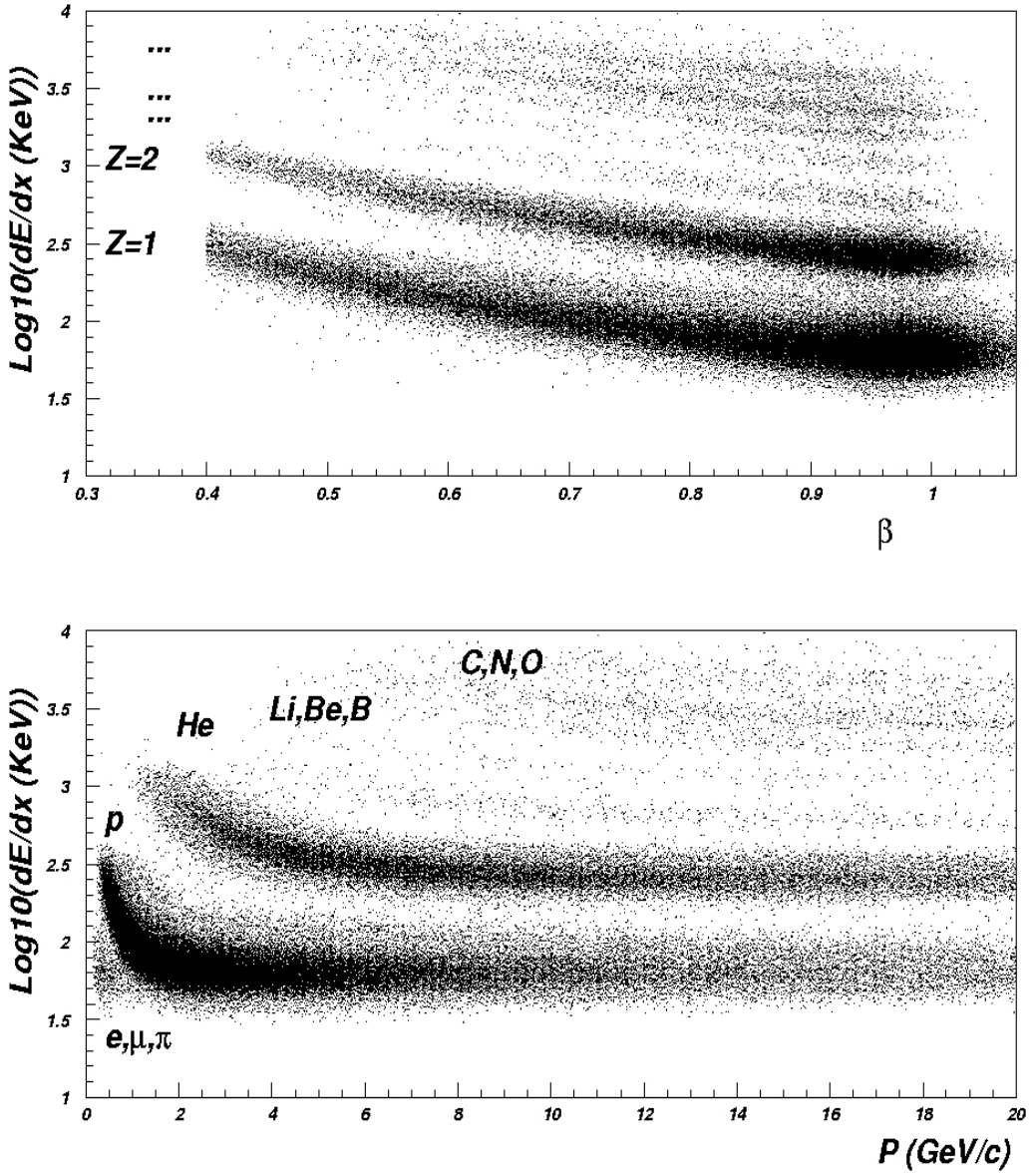

Figure 3.11: *Distribution of the measured energy loss in the tracker as function of the particle velocity β (top) and momentum p (bottom) [131].*

Comparison of different rigidities obtained with different fits allows for the identification of tracks undergoing to important change in direction inside the tracker. Finally a pattern recognition among the hits of the ToF planes was applied to find tracks fitting those reconstructed in the tracker. To estimate the goodness of the choice, a linear extrapolation of the track from the tracker up to the first and the last plane of the ToF was performed, by comparing the residuals between the hits coordinates and the extrapolated ones.

The charge of the particle is determined through the energy deposited in the ToF and separately in the tracker planes. In fig. 3.10, the energy losses measured in the tracker and ToF for events selected with $|Z| \leq 2$ are shown. Energy losses in the tracker are obtained from the mean values of the measurements of the collected charge from the hits of the track after the removal of the plane with the largest collected energy loss. The energy scale was normalized to fit to the expected energy loss value coming from a MIP in 300 μm of silicon. The absolute charge, $|Z|$, can be obtained by fitting the data coming from the calibrations made at CERN PS and heavy ions GSI test beams facilities. A probability is defined using the measured energy losses in the ToF and the p-side of the tracker corrected for the path-length and β. The charge is then assigned based on the maximum probability for each event using the product of the probability from the tracker and the ToF.

3.7 Flux Evaluation

For the evaluation of the directional flux $j(E, \vartheta, \varphi)[s^{-1}m^{-2}sr^{-1}GeV^{-1}]$ of the particles measured with the AMS01 detector, one has to deal with a standard procedure, starting from the measured count-rate $\Delta N/T$ as a function of the measured energy and direction. The count-rate can be related to the flux through the differential geometrical acceptance $A(E, \vartheta, \varphi)$, the energy resolution function $R(E_m, E)$ of the detector and the detection efficiency $\epsilon(E, \vartheta, \varphi)$ through the general expression:

$$\frac{\Delta N}{T} = \int_S \mathbf{r} \cdot \mathbf{d}\sigma \int_\Omega d\omega \int_E dE\, R(E_m, E)\, \epsilon(E, \omega)\, A(E, \omega)\, j(E, \omega) \tag{3.1}$$

where ω is the solid angle around the direction $\mathbf{r}$ and oriented area $\boldsymbol{\sigma}$, E_m and E are the measured and the true energy [138]. To invert the eqn. 3.1, we need to determine the differential acceptance $A(E, \omega)$ and to unfold the measured energy E_m with the true one E.

The procedure for the evaluation of the flux starts with the particle identification and selection criteria which define the detection efficiency ϵ. A full MonteCarlo simulation using the GEANT package was applied to evaluate the detection efficiency, the differential acceptance and the resolution function. The MonteCarlo was instructed using the information from the calibrations at the CERN PS and GSI test beams. The effect of energy loss, multiple scattering, interactions, decays and the measured detector efficiency were included in the simulation, and the folded flux spectrum is given by

$$j(E_m, \omega) = \frac{\Delta N(E_m, \omega)}{T \Delta E_m \epsilon(E_m) A(E_m, \omega) \Delta\Omega} \tag{3.2}$$

With the aid of the simulation, the acceptance was evaluated using the full trigger chain from level-1 to level-3 and asking for reconstruction conditions like: at least one hit in at least four

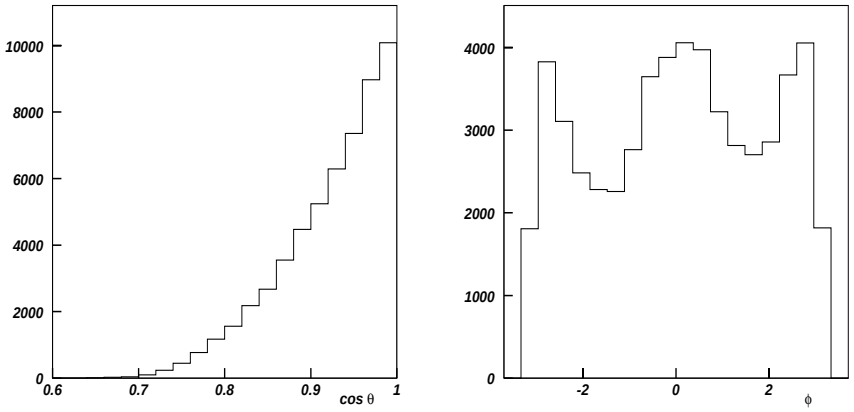

Figure 3.12: *Differential acceptance for protons as function of the particle incident direction angles (ϑ, φ). The peaks in φ reflects the incompletely installed silicon detectors [131].*

tracker planes on the bending coordinate, out of a maximum of six, clean ToF track with a given velocity and charge, requiring the particle trajectory to match the ToF coordinate hits.

The differential geometrical acceptance as function of the incoming particle direction (ϑ, φ) is shown in fig. 3.12. As the tracker planes were armed of ladders only in their central part, the dependence in the azimuthal angle shows peaks for $\varphi = n\pi$. The acceptance estimated with the MonteCarlo takes into account the geometry of the subdetectors, implements the logic of the AMS trigger and the reconstruction requirements for each detected events.

However, the MonteCarlo predictions must be corrected for possible subdetector inefficiencies. The corrections may be, in general, evaluated applying the trigger logic to the unbiased data collected during the flight, and then comparing the results to a proper set of simulated data. Corrections depend on the fast trigger inefficiencies due to the ToF paddle performances. The evaluation of the fast trigger inefficiency takes into account the ratio between the unbiased events using the readout information of the two paddles for each plane. In fig. 3.13 the study of such inefficiencies is showed for the four planes.

The average data/MC correction for the fast trigger inefficiency is estimated in $-3 \pm 1.5\%$. The contribution form the level-1 trigger inefficiencies due to the ACC resulted negligible comparing unbiased data and MC events and the data/MC correction has been estimated in $0 \pm 1\%$. The ToF inefficiencies in the level-3 trigger depend on the energy deposited in the paddles and the data/MC correction as function of the deposited energy is shown in fig. 3.14 and the overall correction for $Z = 1$ particle resulted in $-4 \pm 2\%$. Another correction arises from the energy dependence of the tracker level-3 probability which depends on the particle β. As a result the data/MC correction is $-2 \pm 1.5\%$. Other corrections related to the reconstruction efficiency are due to the paddle inefficiency in the track fit which turned to be $-3 \pm 1.5\%$ and to the track reconstruction algorithm estimated in $-2 \pm 1\%$. The overall correction to the MC acceptance for $Z = 1$ particle was then evaluated to be $-14 \pm 3.5\%$.

Such a correction can be applied both for protons and leptons, both in the region outside

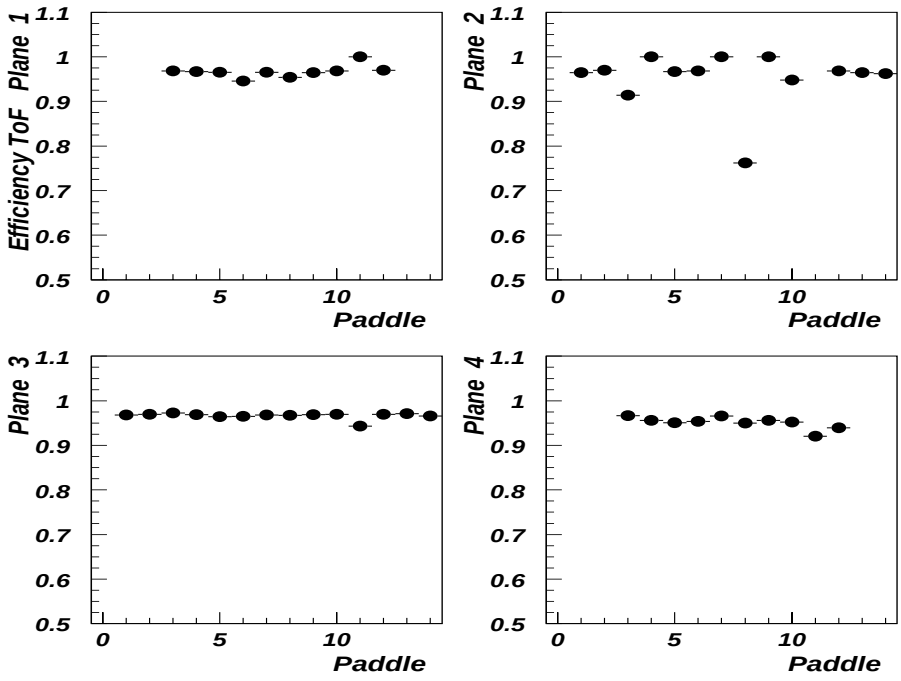

Figure 3.13: *Fast trigger ToF paddles efficiency [131].*

the SAA and inside for DAQ livetime above 40%. The original spectrum $j^{'}(E)$ can then be obtained from the measured $j(E_m)$ solving the Fredholm equation of the first kind

$$j(E_m) = \int_{E_{min}}^{E_{max}} R(E_m, E) j^{'}(E) dE \tag{3.3}$$

The unfolding problem reduces to a matrix equation since the data are binned $j_i = \sum_k M_{ik} j_k^{'}$ where j_i and $j_k^{'}$ are the vectors corresponding to the observed and measured spectra and M is the resolution matrix obtained binning the resolution function $R(E_m, E)$. It should be noticed that the solution of the problem is not trivial and the inversion is often an ill-posed problem.

Two different methods to find the unfolded spectrum were applied to the AMS01 data. In the method based on the Bayes theorem [130], it is assumed that the measured spectrum is influenced by some unknown effects. For an incident particle with a given energy (cause), several values of the experimental effects are possible as outcome of the measured energy. The level of knowledge of the detector resolution function is then translated in terms of bin to bin migration from the true to the smeared energy distribution. Then the unfolding problem consists in finding the expected number of events due to each cause, using an iterative procedure through the Bayes theorem for the estimation of the unfolding matrix, i.e. the degree of confidence in the hypothesis that a given effect was due to a given cause. However for energies above $50\,GeV$ the method was checked with the classical unfolding by regularization [129] trough the minimization of the functional

$$(\frac{\int f(x')k(x,x')dx' - g(x)}{\epsilon(x)})^2 + \alpha(\frac{d^2 f}{dx^2})^2 \tag{3.4}$$

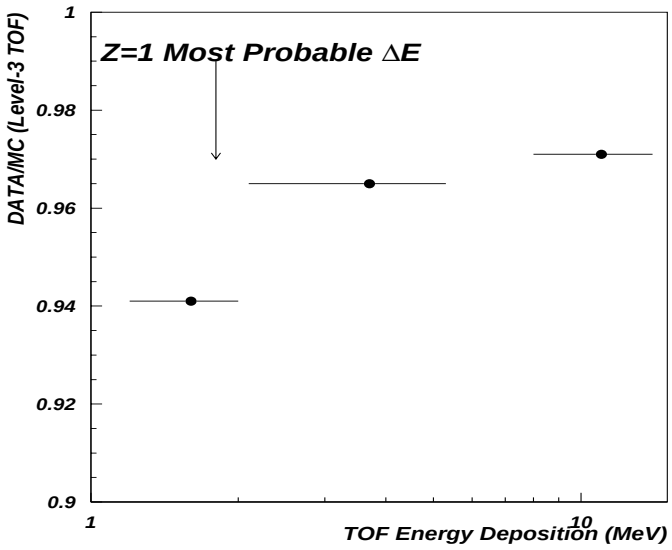

Figure 3.14: *Level-3 ToF efficiency from data/mc comparison as function of the energy loss in the scintillator counters [131]*

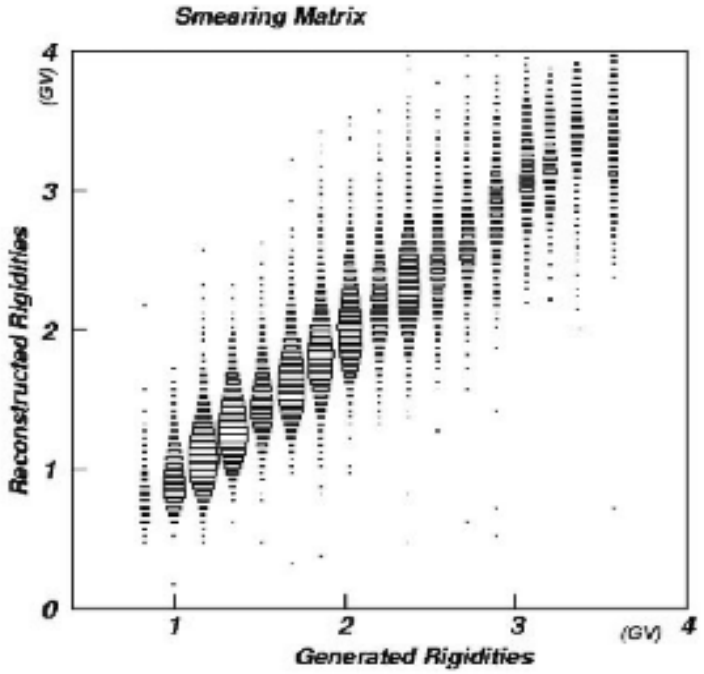

Figure 3.15: *Smearing matrix determined by the MonteCarlo simulation for reconstructed protons in the rigidity range* $0.3 - 4\,GV$

where $g(x)$ is the measurement, $\epsilon(x)$ its error, $k(x,x')$ the smearing matrix, $f(x)$ the solution and α is a regularization parameter. The method gives smoother solution with respect the Bayesian approach, as the function f is assumed to be smoother. The smearing matrix for an AMS proton sample is shown in fig. 3.15.

3.8 Proton and Lepton Spectra

The AMS collaboration has published results on proton and lepton fluxes collected with the STS91 flight in ([132], [133], [134]). Full details about selected periods can be found in the references.

Events collected in four different periods of the flight were used to determine proton spectra namely while the Shuttle attitude was kept pointing at 0^o, 20^o, 45^o and 180^o of the zenith direction. Data coming from the SAA were excluded in the published papers. A sample of simulated events triggered by the fast trigger logic and generated above the geomagnetic cutoff according to both the exponential expected spectrum and a uniform rigidity dependence spectrum were used for efficiency and acceptance studies. Samples of fixed rigidity events, triggered by the fast trigger logic were used for unfolding and acceptance calculations.

3.8.1 Protons

Selection Criteria The quality of the velocity determination for potential candidates was defined using the two different criteria.

The β measurements obtained using less than three scintillator planes of ToF hits were rejected since they gave poor values of the χ^2_β for the selected events. Moreover, the residuals between the ToF hits coordinates and the expected impacts points from the extrapolation of the trajectory reconstructed from the tracker were cut to an absolute value of 5.5 cm. The average selection efficiency resulting from the above set of ToF cuts was 95.5% for data and it was 98.8% for protons MonteCarlo. The discrepancy between data and simulated events when applying the ToF cuts was due mainly to the inefficiency of the fourth scintillator plane during the flight, which was not included in the MonteCarlo.

A second set of selection criteria concerned the quality of the charge $Z = 1$ determination. Charge measurements from both the ToF and tracker were required to be consistent. Events were accepted if both likelihood probabilities were > 0.03. The Landau tails of the energy loss distribution of voted charge $Z = 1$ events were cut.

In this way, the contamination from residual $Z = 2$ particles with wrongly measured charge was reduced to a negligible level ($< 10^{-4}$) (fig. 3.10). The average selection efficiency resulting from the above set of ΔE cuts was 99.3% for data and 99% for MonteCarlo.

A specific cut was applied on the quality of track reconstruction, namely the value of $\beta^2\chi^2_{no-ms}$ was accepted within an upper value of 400. The average selection efficiency resulting from this cut was 88.5% for data and 93.8% for MonteCarlo. The final average selection efficiency was 84% for data and 92% for MonteCarlo with a combined discrepancy of $8 \pm 2\%$. The above cuts provides a selection of about $5.6\ 10^6$ events.

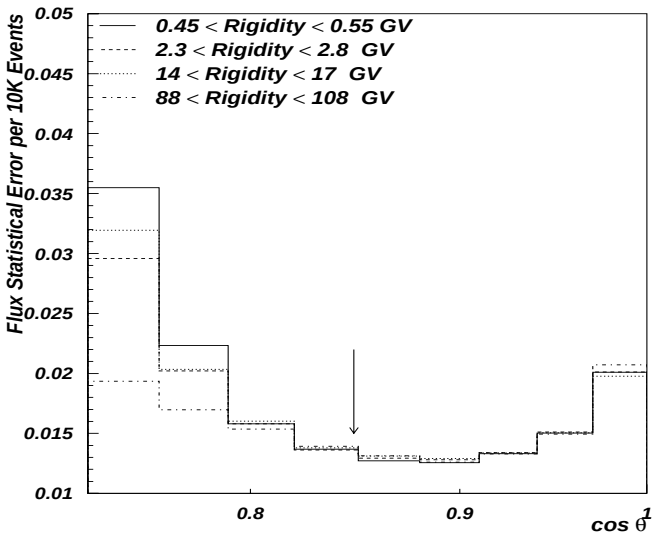

Figure 3.16: *Proton flux statistical errors as function of the incoming direction for different rigidity bins [131].*

Background Determination Selecting events with $Z = +1$, the proton sample has minor background because protons and helium nuclei constitutes the main part in CR. As a result the proton sample can be contaminated by charged pions and deuterons.

The fraction of pions produced by the interaction of CR with the upper part of the AMS detector has been estimated in the MonteCarlo simulation. This fraction turned out to be 1% below 0.5 GeV and decreases rapidly with increasing energy. The deuterium fraction in CR is ~ 2 %.

To remove low energy charged pions and deuterons, a cut has been applied on the measured mass requiring to be within 3 standard deviations of the proton mass. The particle mass is not directly measured with AMS but indirectly determined from the momentum and velocity of the particle through $M = p\sqrt{(1-\beta^2)/\beta^2}$. The measured velocity β distribution is gaussian while the momentum distribution is not since the momentum is proportional to the inverse of the trajectory curvature which is the effectively measured parameter. As a result, the distribution of $1/p$ is approximately gaussian. The background is reduced to a negligible level over all the energies by rejecting about 3 % of the events.

Acceptance The dependence on AMS acceptance of the particle incident direction is not a negligible effect. Fig. 3.16 shows the statistical errors for the protons flux as a function of the incident direction of the particle, determined from a sample of candidates as function of $\cos\vartheta$, while in fig. 3.17 the rigidity dependence of the proton acceptance is shown.

The interval of the local zenith angle was limited to $\vartheta_{max} = 32^o$ ($\cos\vartheta \simeq 0.85$) and events detected at larger inclination were not taken into account in the flux determination, keeping minimum the statistical errors, as may be seen from fig. 3.16.

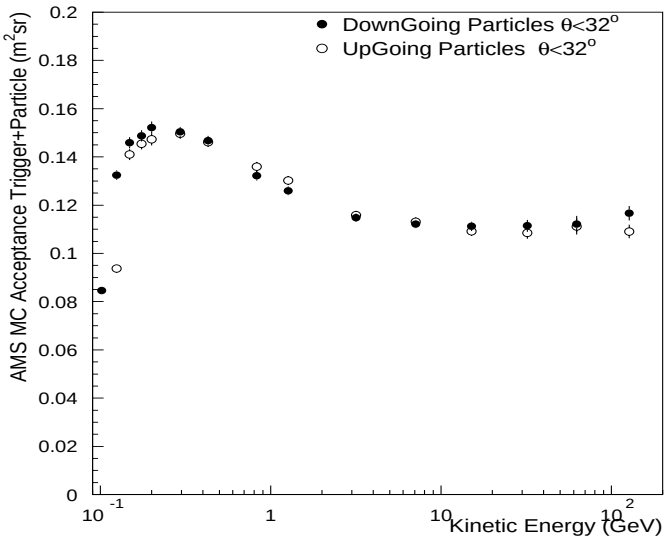

Figure 3.17: *Proton acceptance as function of the rigidity for events within incoming direction $\vartheta < 32^o$. The maximum at low rigidity depends on the high tracker reconstruction efficiency for low β particle [131].*

The correction due to trigger efficiency variations applied to the acceptance to remove systematics from the MonteCarlo was in average $\epsilon_{s1} = 3.5\%$. Some other sources of systematic uncertainties must be considered. Particles interacting with the detector produce new charged particles in the fiducial volume that were assumed to be rejected by the veto counters. Secondly, a discrepancy between data and MonteCarlo at low rigidity shows an underestimation of the multiple scattering. The two contributions bring to a systematic error of the order $\epsilon_{s2} \sim 3\%$. Systematics from the unfolding procedure due to the bin to bin migration of information with correlations with the observed data ranges between $\epsilon_{s3} = 1 \div 5\%$, increasing with energy. Details about the estimation of the several contributions can be found in [134].

Results The differential spectra as function of kinetic energy for downward and upward going protons integrated over incoming direction within 32^o of the z-axis are presented in fig. 3.18. The results are separated in geomagnetic latitude regions ϑ_m at which they were observed [132]. A clear effect of the geomagnetic cutoff can be seen. This reflects a separation between primary protons and under-cutoff protons (called *second spectrum* in [132]). The two spectra differ mainly at equatorial regions becoming less evident at higher latitude due to the decreasing of the rigidity cutoff.

For upward going events, all the protons are below the geomagnetic cutoff. To separate primary and under-cutoff component of the fluxes one has to know the rigidity cutoff for each particle which depends on location and incoming direction. In [132], the Stoermer cutoff R_s was used, evaluated using the geomagnetic latitude ϑ_m and incrementing this value by the rigidity uncertainty $\sigma(R_s)$ by the formula $R > R_s[1.2 + 2\sigma(R_s)]$. In this way, the features of the primary

component can be studied. However, to better check the features of the under-cutoff spectra and clearly separate it from the primary component, one has to trace particles in the geomagnetic field. The features of the tracing results for protons are discussed in the fourth chapter. Fig. 3.19 shows the flux variation $\delta = (flux/aveflux - 1)$ as a function of the kinetic energy for data collected at different orientations of the Shuttle to estimate systematic error effects [134]. The comparison shows that fluctuations are consistent with the systematic expectations.

Fitting the measured spectrum in the rigidity range $10 < R < 200\,GV$ (to exclude the solar modulation) with a power law j(R)=$j_o R^{-\gamma}$ yields:

$$\gamma = 2.780 \pm 0.009(fit) \pm 0.019(sys) \tag{3.5}$$
$$j_o = 17.1 \pm 0.15(fit) \pm 1.3(sys) \pm 1.5(\gamma)\ \frac{GV^{2.78}}{m^2\,s\,sr\,MV}$$

In fig. 3.20, the AMS results for primary protons are compared with previous measurements.

The AMS spectrum is well consistent with the Bess98 [89] spectrum in the energy range $1 \div 100\,GeV$. This is important because AMS and Bess98 collected data in the same year and the consistency within 5% of uncertainties give a precise measurement of primary cosmic proton spectrum. As a result new primary proton flux parameterizations have been considered for neutrino calculations [145]. The AMS flight occurred close to the solar minimum and the best fit yield to a modulation parameter of $\Phi = 600 \pm 30\,MV$, which is identical to the one quoted by Caprice94 [83]. This result is also consistent with what is expected from neutron monitor and sunspot observations.

The proton flux below geomagnetic cutoff shown in fig. 3.18, where the second spectrum consisting of particles trapped in the Earth's magnetic field is also evident. Upward and downward going fluxes are most intense at equatorial latitudes and quite constant elsewhere with peculiar properties described in details in chapter 4. At geomagnetic equatorial latitudes $\vartheta_m < 0.2\,rad$, the second spectrum extends from $0.1\,GeV$ up to $\sim 6\,GeV$ with a flux $\sim 70\,m^{-2}s^{-1}sr^{-1}$. Moving to $\vartheta_m = 0.3\ rad$ causes the proton to drop by a factor $2 \div 3$, depending on the energy while over a much wider internal $0.3 < \vartheta_m < 0.8\ rad$ the flux is almost constant. In the range $0. \leq \vartheta_m \leq 0.8\ \ rad$ detailed comparison in different latitude bands indicates that upward and downward fluxes are nearly identical, agreeing within 1%. Moreover, as we move up to polar latitudes $\vartheta_m > 1.0\,rad$ the downward second spectra is gradually obscured by the primary spectrum and the penumbra effects become more important. The GLAST collaboration tried to parameterize the AMS proton albedo in order to evaluate the expected background. In [139] the fit of the albedo flux $j(E, \vartheta_m)$ in $[m^{-2}\,s\,sr\,MeV]$ has been parameterized by the expression

$$j(E, \vartheta_m) = 1736\ e^{-min(\vartheta_m, 0.38)/0.245}(0.015\ e^{-E/1.03} + 0.12\ e^{-2E/1.03}) \tag{3.6}$$

such approximation shows an accurate normalization in the lowest latitude bin while significant discrepancies appear at higher latitude.

3.8.2 Leptons

Selection Criteria Electrons and positrons are relatively rare components of the cosmic radiation. The intensity of electron fluxes is $\sim$ 1% of protons, the positron fraction relative to electron of O(10%) at $1\,GeV$ for primaries. Therefore, their selection is a quite challenging task.

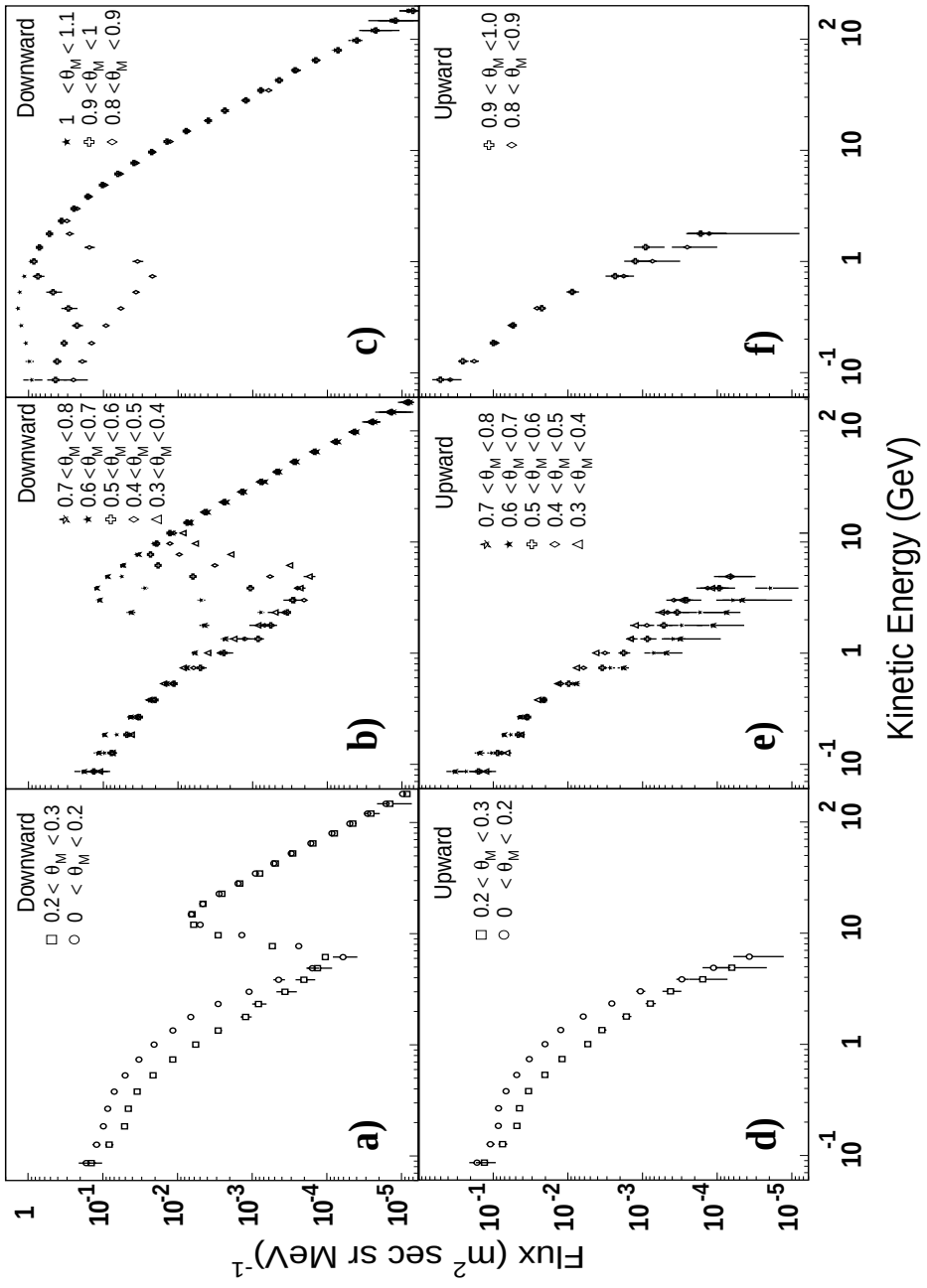

Figure 3.18: *Proton spectra for a), b), c) downward and d) ,e) ,f) upward going protons in different intervals of geomagnetic latitude ϑ_m [132]*

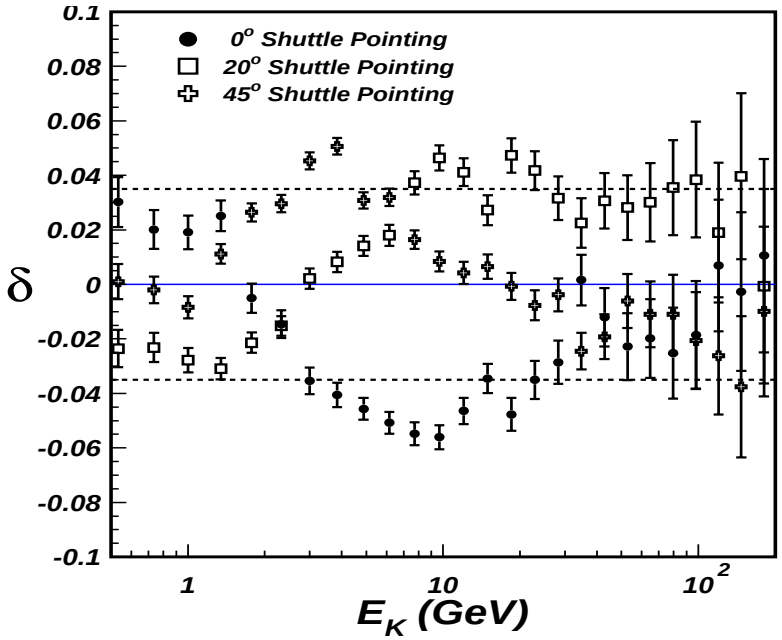

Figure 3.19: *Flux variation δ as function of the proton energy for different Shuttle orientation. The dashed line show the range of systematic errors [134].*

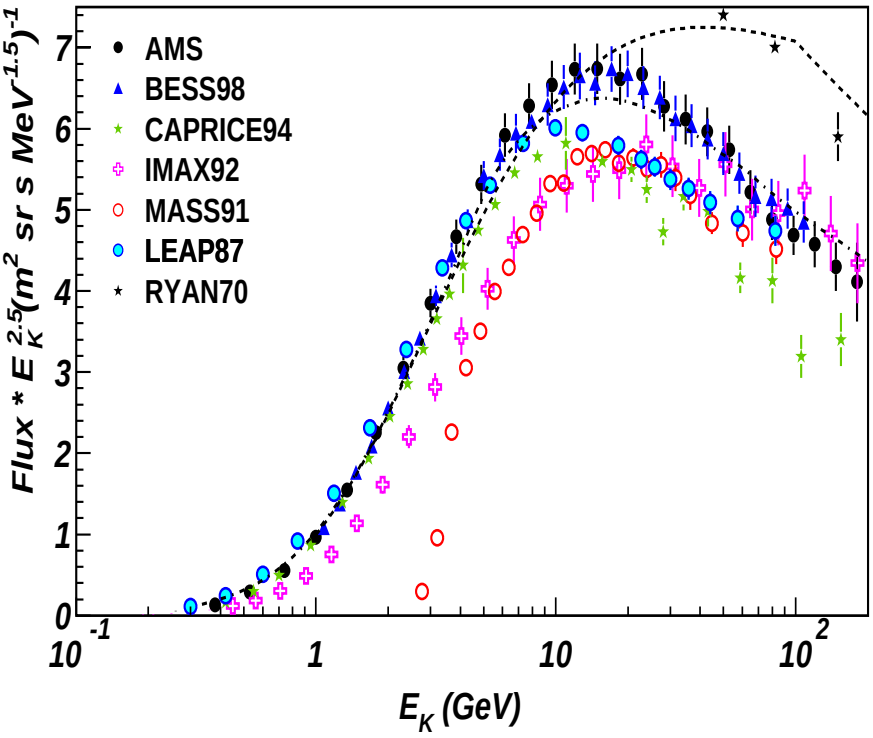

Figure 3.20: *AMS01 cosmic proton spectrum compared with previous measurements [81].*

Electron candidates were selected requiring the measured particle to be $Z = -1$ and the particle velocity β compatible with the speed of light. The β measurements were asked to have more than three scintillator planes of ToF hit to have good values of the χ^2_β of the selected events. A cut of 5.5 cm on the residuals between the ToF hits coordinates and the expected impacts points from the extrapolation of the trajectory reconstructed from the tracker was put as for protons. The resulting selection efficiency was 87% for data and 99% for MonteCarlo.

Cuts were applied also on the quality of reconstructed tracks, based on the χ^2 to remove events with large multiple scattering, bringing to an the average selection of 75% for data and 78% for MonteCarlo. For the compatibility with the speed of light the cut on β was asked to be within the range $-3\sigma(\beta^{-1}) < \frac{1-\beta}{\beta} < \sigma(\beta^{-1})$. The efficiency from this cut was 80% for data and 81% for MonteCarlo.

The positron candidates were selected by requiring the charge to be $Z = +1$, the velocity β compatible with the speed of light as for the electrons. The rejection against protons with poorly measured β measurements can be improved requiring stringent conditions on the signal from the ATC. Separation relies on the fact that up to the threshold of $\sim 3.5\, GeV/c$, positrons provide a much stronger signal than protons. A clean selection can be made up to $\sim 3\, GV$ of rigidity, achieved with a reduction of efficiency of about 72% with respect to electrons.

The ATC bad cells were excluded (89% data and MC efficiency) and the impact parameter was asked to be $d_{PMT} > 1.5\, cm$ (89% data and MC efficiency). Moreover, a combination of signals from the two ATC layers was used differently depending on the particle type and momentum. In the upper panel of fig. 3.21, the positron ATC efficiency is shown for events selected from the tracker and ToF with $p > 0.7\, GeV/c$, asking for ATC signal in each layer more than 1.5 photoelectrons. The average selection efficiency was 58% for data and 67% for MonteCarlo. The lower panel of fig. 3.21 shows the ATC efficiency for electron selected by the tracker and the ToF and for positron with $p < 0.7\, GeV/c$ asking for the sum of the two ATC layers to be > 3.5 photoelectrons. The average selection efficiency was 81% for data and 94% for MonteCarlo. The total particle selection efficiency for electrons was about 39% while for positron 28%.

Background Estimation For the electrons, the background is due to protons with wrongly measured momentum and from secondary pions produced in the detector materials above the tracker.

To remove tracks with large single or multiple scattering, a cut has been applied on the χ^2 obtained in the fit of the particle trajectory. A second cut related to the number of hits close to the reconstructed trajectory both in the tracker and the ToF scintillators was applied, requiring no hits within $5\, mm$.

The cuts resolve in an overall probability of a proton event to be accepted as an electron from the MonteCarlo and confirmed at the CERN test beam to be at level of $O(10^{-4})$ with the electron selection efficiency of 75 %. To furtherly reduce the pion background only particles passing through the ATC active area were selected providing an independent velocity measurement.

For positron candidates, the main background came from proton events with poorly measured velocity. The rejection power against this background decreases rapidly with the increasing proton momentum. Below $1 GeV/c$, protons were rejected by requiring energy loss measurements

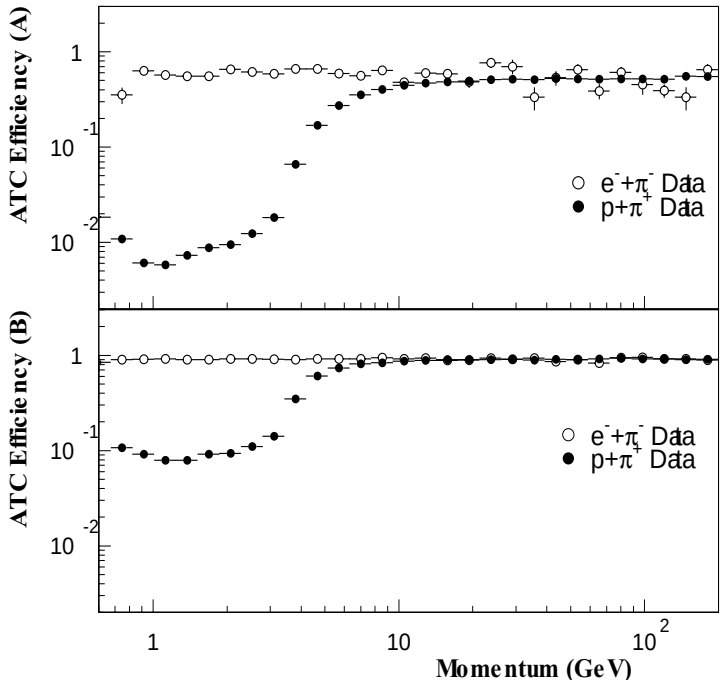

Figure 3.21: *ATC efficiency as function of the momentum for proton and lepton selected according to the variant A and B (see text)*

in four layers of ToF counters and six double layers of silicon tracker to be compatible with a positron.

For $1 < R < 3\ GV$, protons were rejected by requiring the two independent ATC measurements layers to be compatible with protons. The overall probability of a proton event to be accepted as a positron was estimated from the MonteCarlo was $O(10^{-3})$. A convolution of the background rejection function with the measured proton spectra provided an energy dependent background estimation as shown in fig. 3.22 for the geomagnetic polar regions where the contamination condition were most severe.

Acceptance To study electrons and positrons, the track must pass through the ATC and therefore the acceptance was limited up to 28^o from the z axis. As for the proton analysis, the MonteCarlo events have been used for the estimation of the acceptance and the resolution matrix for the energy unfolding procedure. An average acceptance of 0.01 m^2sr was found at 0.15 GV, and level off 0.1 m^2sr at 0.7 GV with a systematic uncertainty of 5%. The differential spectrum was obtained from the measured one using the unfolding technique based on the Bayes theorem with a resolution function obtained from the simulation. The resolution function was also confirmed with calibration measurement in the CERN test beam. The data/MC corrections to the lepton acceptance were assumed to be the same as for high energy protons.

Results In fig. 3.24 the lepton spectra integrated over incident angle within 28^o of the z-axis is shown. The measurements have been binned according to the absolute value of the geomagnetic

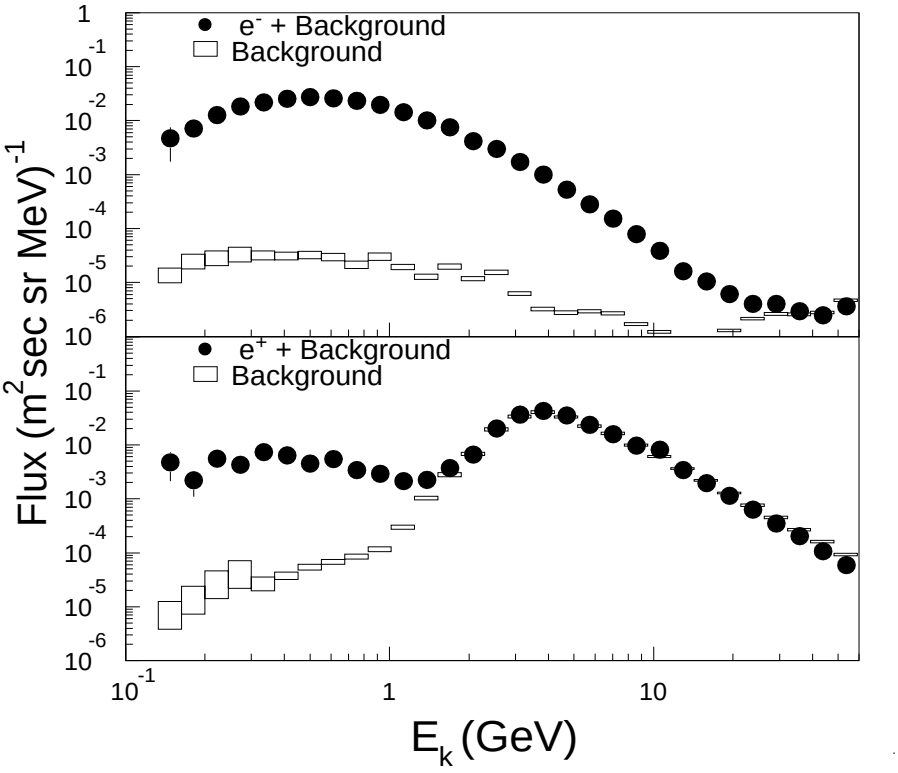

Figure 3.22: *Primary lepton fluxes and background evaluation in the geomagnetic polar region ($\vartheta_m > 0.9$) [133].*

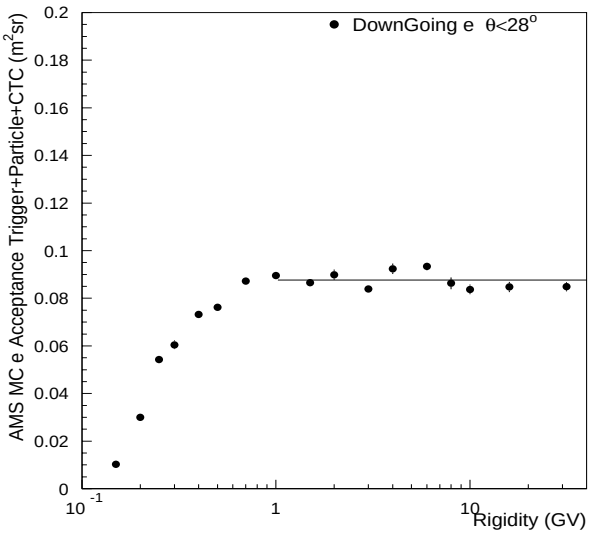

Figure 3.23: *Geometrical acceptance as function of the rigidity for events within incoming direction $\vartheta < 28^o$ [131].*

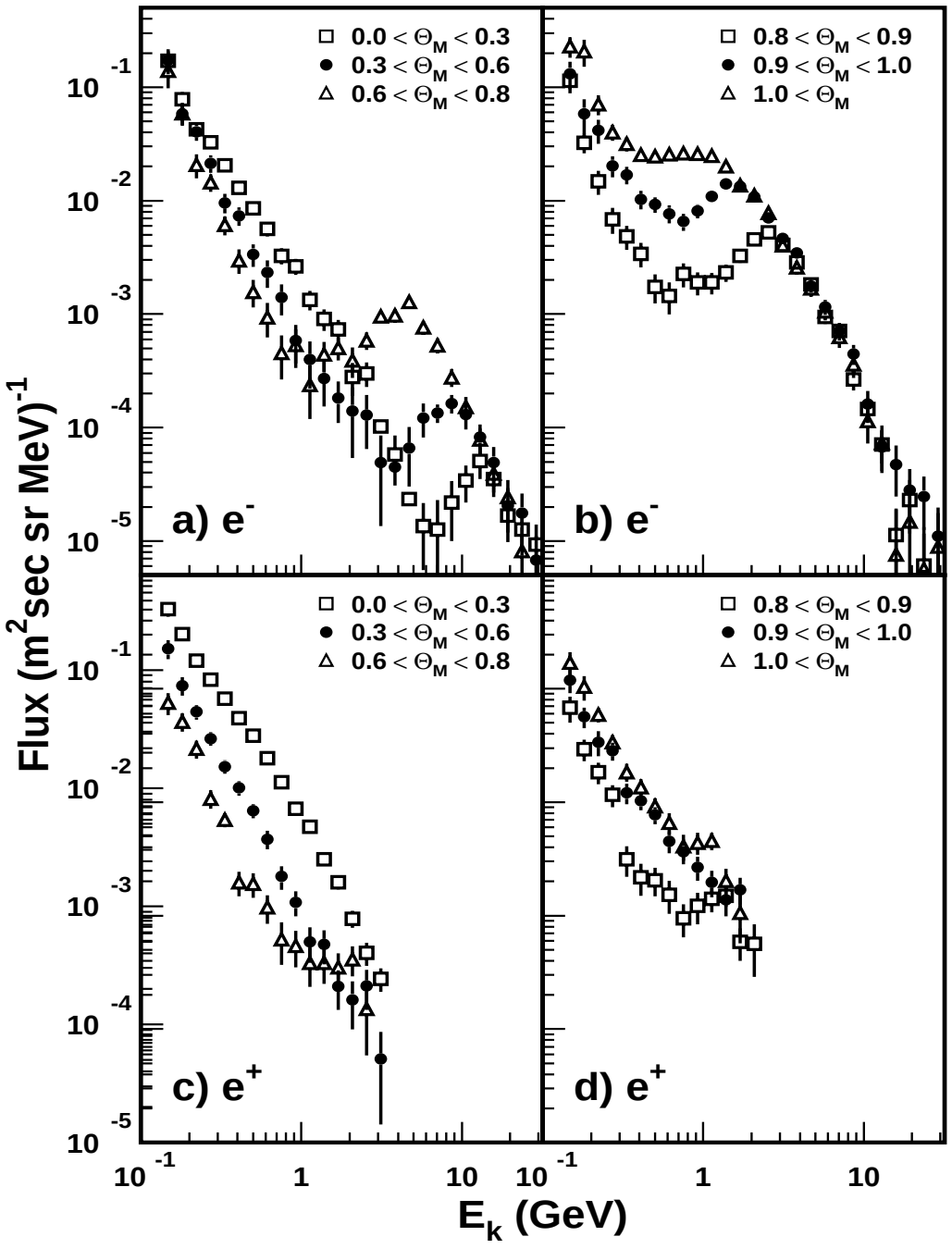

Figure 3.24: *Flux spectra for downward going electrons a), b) and positrons c), d) in different intervals of geomagnetic latitude ϑ_m [133].*

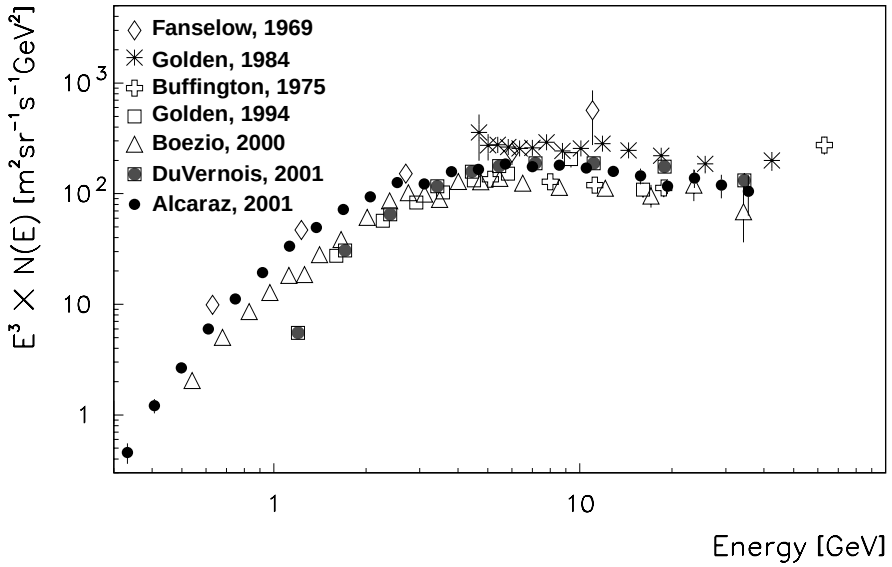

Figure 3.25: *AMS01 primary electron spectrum compared with previous measurements [94]*

latitude ϑ_m at which they were detected. The presence of a second spectrum under the geomagnetic cutoff is evident also for leptons as already discussed for protons. Clearly the cutoff effect decreases with increasing ϑ_m. For the downward going particles the primary component of the spectra are absent. To separate the primary and under-cutoff spectra, the lepton trajectories were traced backward and forward from their measured incident angle, location and momentum through the geomagnetic field. The features of the tracing results for the leptons under-cutoff are discussed in the fourth chapter. The properties of the primary component agree with the expectations in the electron flux intensity and in the predominance of electron over positron. Comparisons of primary electron and positron fluxes with a compilation of previous experiments are presented in fig. 3.25 and 3.26 respectively. Fig. 3.27 shows also the observed cosmic positron fraction the results of which is also consistent with previous measurements.

The lepton second spectra in fig. 3.24 exhibit similar qualitative behaviour as for the protons. The lepton flux is maximum at equatorial region dropping off faster for positron than for electron with increasing latitude. At polar latitudes, the downward second spectrum of leptons is gradually obscured by the primary spectrum due to the decrease of the geomagnetic cutoff. The second spectrum of upgoing leptons was clearly observed, and for both electrons and positrons the upward and downward fluxes are nearly identical as seen for protons. To be noticed that undercutoff lepton fluxes below $1\,GeV$ are roughly one order of magnitude larger than the protons in the same energy range.

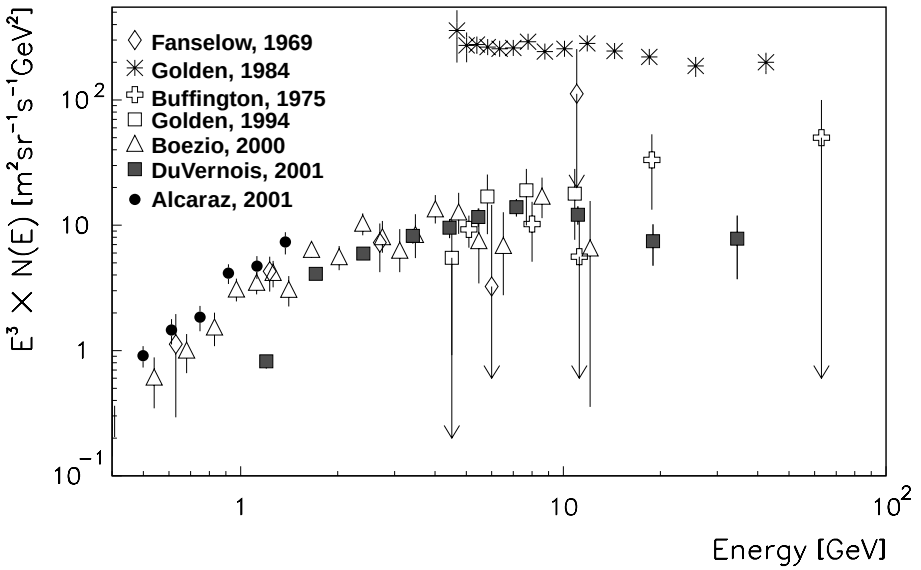

Figure 3.26: *AMS01 primary positron spectrum compared with previous measurements from [94]*

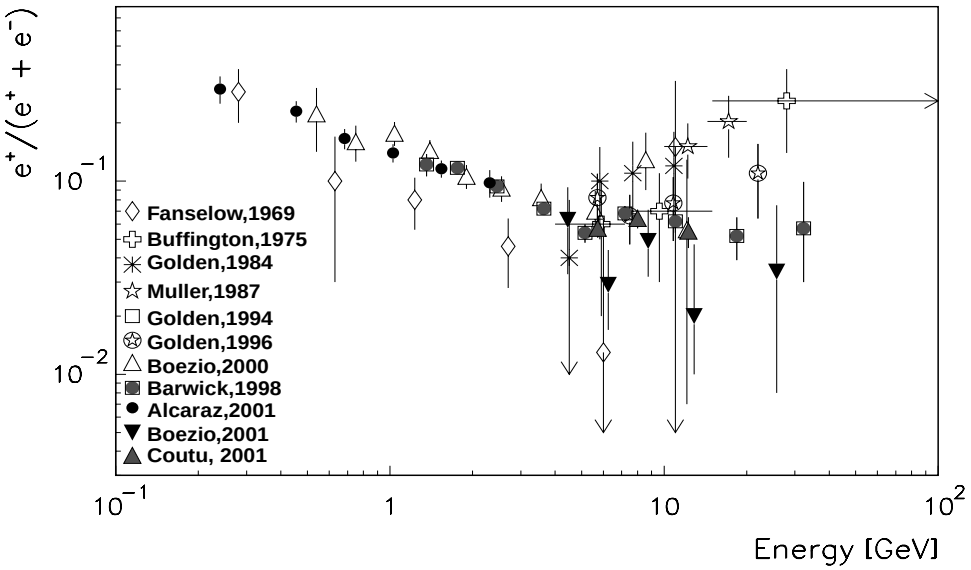

Figure 3.27: *Positron fraction for primary leptons as function of the kinetic energy compared with previous measurements [94]*

Chapter 4

Analysis of under-cutoff protons and leptons

4.1 Introduction

The remarkable property of the AMS measurements is the possibility to study fluxes at $\sim$ 400 Km, measured with unprecedented accuracy at high energies. In the first two chapters, the radiation at LEO and the CR environment near Earth are described, which are involved in the proton and lepton fluxes measured by AMS01. This chapter is focused on the analysis of protons and leptons under the geomagnetic cutoff. The description of the tracing technique used to separate primary and under-cutoff particles observed by AMS is given, discussing the method, the errors and the interpretation of the result. The result of the tracing is then used to evaluate the flux maps in terms of the adiabatic invariants coordinates (α_o, L) and the kinetic energy E_k. A separation between particles observed inside and outside the SAA is then proposed; differences and similarities are pointed out. Longitudinal dependencies as well as invariant latitude maps are presented. Finally, proton and lepton under-cutoff fluxes are compared and interpreted with the aid of the MonteCarlo simulation presented in [146].

4.2 Tracing in the Geomagnetic Field

The aim of this section is to introduce the particle tracing in the geomagnetic field, showing the details of the algorithm. The definition of the effective cutoff using the result of the tracing are shown, and the evaluation of the errors discussed. An interpretation of the results is finally given in terms of the drift shell model.

4.2.1 Tracing algorithm

Numerical tracing of CR trajectories in the magnetospheric field is widely used to study the access of CR in the Earth's magnetosphere, as described in chapter 2. The tracing technique uses a realistic model for the geomagnetic field to reconstruct the particle trajectory. We are mainly concerned with the study of the peculiar features of the under-cutoff particle populations. The initial position, momentum and direction of the particle are used to integrate numerically the equations of motion and to find the trajectory of the particle $\mathbf{r}(t)$.

The equations of motion for a charged particle in a magnetic field $\mathbf{B}(t, \mathbf{r})$ can be written as:

$$\dot{\mathbf{r}} = \frac{\mathbf{p}}{m\gamma} \qquad \dot{\mathbf{p}} = \frac{q}{m\gamma}\mathbf{p} \wedge \mathbf{B} \tag{4.1}$$

where $\mathbf{r}$ and $\mathbf{p}$ are the particle position and momentum, m the rest mass, q the charge and γ the Lorentz factor. The time dependence can be converted in a spatial dependence, taking into account that the elementary path-length in the time step dt is $dl = \beta c dt$, so that the trajectory $l(\mathbf{r})$ can be evaluated.

If $\mathbf{x}$ is defined as the 6-dimensional vector in the phase space $(\mathbf{x}_1, \mathbf{x}_2) = (\mathbf{r}, \dot{\mathbf{r}}/|\dot{\mathbf{r}}|)$, the equation of motion can be written as a first order 6-dimensional ordinary differential equation $d\mathbf{x}/dl = f(l, \mathbf{x})$ which in our case assumes the expression:

$$\frac{d\mathbf{x}_1}{dl} = \mathbf{x}_2 \qquad \frac{d\mathbf{x}_2}{dl} = 0.3\frac{q}{p}\mathbf{x}_2 \wedge \mathbf{B} \tag{4.2}$$

(q in $Coulomb$, B in $Tesla$, p in GeV/c, r in R_e). To integrate the equations of motion for protons and leptons, a standard Runge-Kutta method with adaptive step-size control was used. For the magnetic field, IGRF95 and Tsyganenko96 are used for internal and external components, respectively. To solve a first order differential equation, the initial condition $\mathbf{x}_o = \mathbf{x}(l = l_o)$ should be provided. The algorithm is based on the $4 - th$ order expansion of the function $f(l, \mathbf{x})$, with an accuracy of the order $O(\delta l^4)$.

The step size δl during the integration has to be tuned to get the best accuracy in the integration and the best performances in terms of CPU time. After several tests, we settled with a dynamical stepsize using the *turning angles* method. In this scheme, the step size δl, is evaluated using the turning angle $\delta\vartheta$ in the local magnetic field. CPU time is saved and accuracy optimized, using large steps in regions of weak magnetic field and small steps in regions of strong field and gradients. A value of $\delta\vartheta = 3\ m\,rad$ was chosen, corresponding to a step size $\delta l = p\delta\vartheta/1.9qB = p\,3\ 10^{-3}/1.9\ qB$.

The accuracy for each adaptive step evaluation was defined as $\epsilon = 10^{-4}$. Particles measured with the AMS detector were traced backward to find their origin, and forward up to their destinations as if they were not interacting the detector. The total path-length used was $L_{tot} = 1500R_e$ both for backward and forward integration resulting in a total path-length of $L_{tot} = 3000R_e$.

All leptons collected by AMS and protons with rigidity below 18 GV were traced, for a total number of 67656 electrons, 118034 positrons and 1164181 protons.

Particles are classified as cosmic if they reach a distance of $30R_e$, trapped if they do not. If classified trapped, a particle may reach the Earth's dense atmosphere limit at some point of its trajectory, is fixed at 40 Km of altitude, where the probability of interaction is $\sim 50\%$. Alternatively, it can stay very likely in flight around the Earth, remaining at a radial distance between 1.006 R_e and 30 R_e, for more than the maximum path-length, corresponding to a fixed time, taken as 30 s in our case because if in flight for more than that, it will stay in flight indefinitely. The two components are denoted *Quasi-Trapped* (QT) and *Stably-Trapped* (ST), respectively.

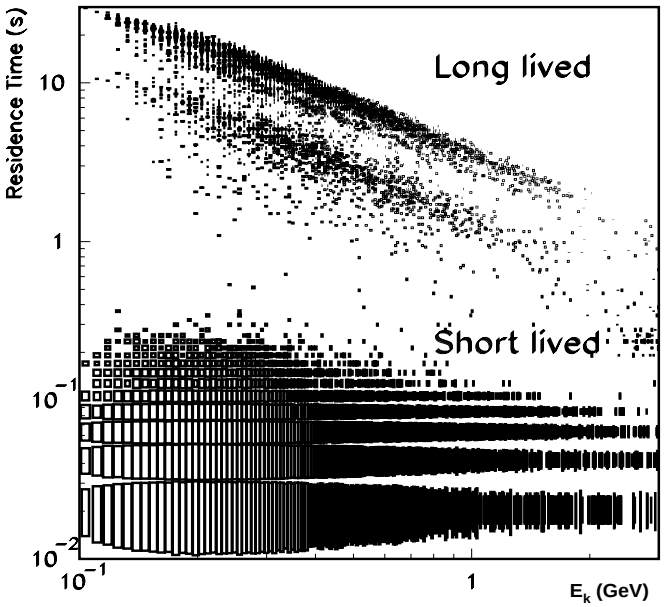

Figure 4.1: *Residence time vs kinetic energy for e^+. The same structure is observed for e^-.*

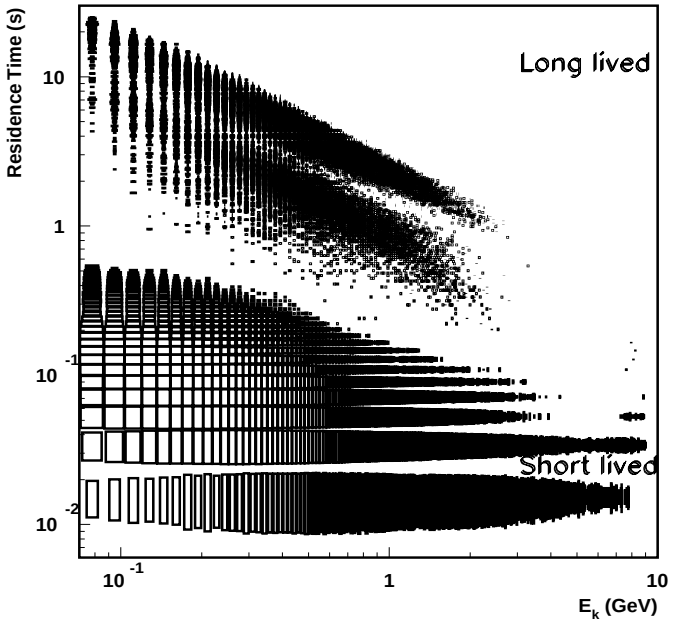

Figure 4.2: *Residence time vs kinetic energy for protons. The separation among short and long lived particle is slightly dependent on the kinetic energy.*

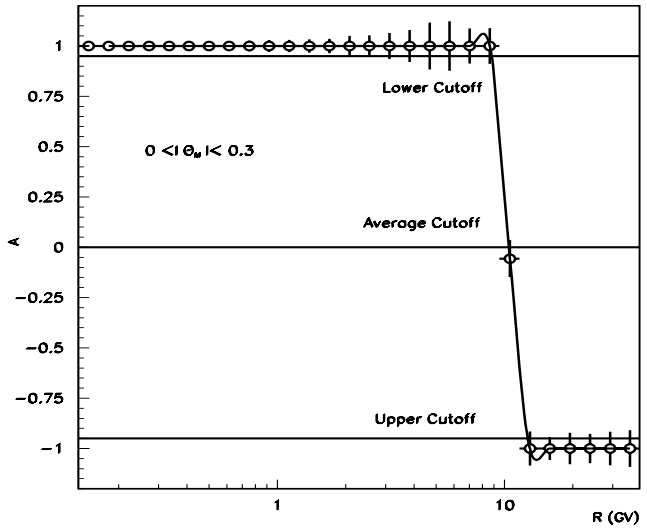

Figure 4.3: *The asymmetry function A used to define the lower, average and upper rigidity cutoff at the magnetic latitude interval* $0 \leq \vartheta_m \leq 0.3$. *The horizontal lines define the -0.95,0,0.95 limit respectively for the Lower, Average and Upper cutoff.*

4.2.2 Tracing Results

The main goals of the tracing are to disentangle primary CR from locally produced particles (to minimize the trapped contamination) and to study the properties of trapped. For the QT component, it is also possible to compute the residence time, T_f, i.e. the total time spent by each particle in the motion above the atmosphere, before and after detection and the locations where the trajectories intercept the atmosphere, called the particle's *production* and *impact* points.

The residence time distribution of QT leptons as a function of the kinetic energy is shown in fig. 4.1. All observed QT leptons fluxes have residence times below $\sim$ 30 s, with 52% of the e^- and 38% of the e^+ having a $T_f < 0.3$ s almost independent of their energy. A scaling law, $T_f \approx E_k^{-1}$, is observed for the remaining leptons: they are disposed in two diagonal bands separated by a difference in T_f of $\Delta t \approx 2.2/E_k$ s. In the published AMS analysis [133], the terminology of *Short-Lived* and *Long-Lived* was used to classify the particles with T_f below or above 0.2 s, observed at equatorial regions outside the SAA. For the QT protons, the residence time distribution as a function of the kinetic energy is shown in fig. 4.2. The proton residence times do not exceed $\sim$ 30 s, with $\sim$ 50% of protons having a $T_f < 0.3$ s almost independent of their energy, referred to as the *Short-Lived* populations in [132], where the proton sample was limited to the equatorial regions outside the SAA. A similar scaling law, is observed for the *Long-Lived* protons which are present mostly under $E_k \sim 6\ GeV$. A closer look to the proton residence times shows a dependence of T_f on the velocity β, as it is expected for bouncing and drifting motion of not-fully relativistic protons. Due to this, the separation is dependent on E_k and can be parameterized as $T_f \lesssim 0.25/E_k^{0.5}$. For leptons, the β dependence is hidden because they are ultra-relativistic at the energies measured by AMS and therefore $\beta \sim 1$.

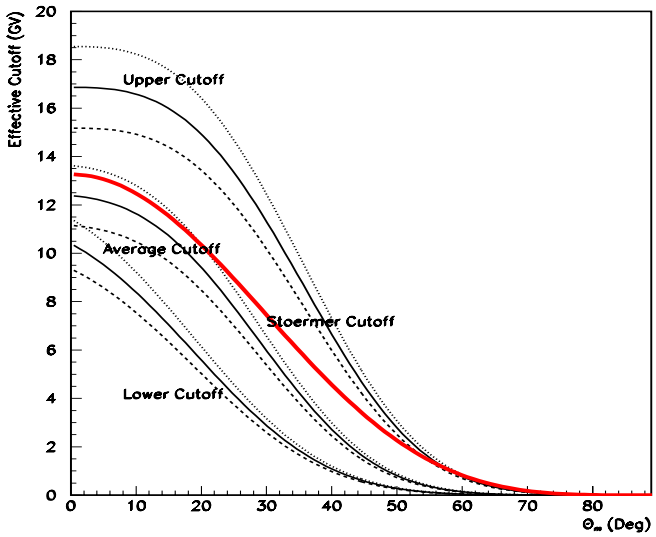

Figure 4.4: *Effective cutoff as function of the magnetic latitude defined as the lowest rigidity below which no primaries are found (Lower cutoff) with the error band (dotted lines). The highest rigidities above which all the leptons are primaries (Upper cutoff) and* 50% *are trapped (Average cutoff) are also shown.*

The impact/production points spread in general over two symmetric bands on both sides of the magnetic equator, as indicated by the yellow bands in fig. 4.7 and 4.8 for leptons and protons, respectively; the same points for Long-Lived are instead localized in the red/blue spots in the same figures. The analyzed proton sample covers a rigidity range larger than for positrons (where it is limited to $E_k \leq 3\,GeV$). The impact/production point distributions have the same structure independently of the particle type and are due to the peculiar structure of the geomagnetic field, as will be explained in the next paragraph. Due to the opposite drifting of positively and negatively charged particles, sources for positive charged particles will be the sinks for negative and viceversa.

The tracing allows for a good separation between primary and trapped particles. Although satisfactory in most cases, this approach is less stable when the particle rigidity falls in the penumbra region, close to the cutoff value. In this case, the trajectories become chaotic and small uncertainties in the reconstructed rigidity and in the knowledge of the local magnetic field can lead to misclassification. To avoid such effects, an effective cutoff, R_{eff}, was defined as the maximum rigidity value at a given magnetic latitude θ_m for which no traced particles were found to be of cosmic origin (Lower cutoff). Using the traced particles to evaluate differential fluxes, it is possible to define an asymmetry function $A(R, \vartheta_m)$ as:

$$A(R, \vartheta_m) = \frac{j_{trap}(R, \vartheta_m) - j_{prim}(R, \vartheta_m)}{j_{trap}(R, \vartheta_m) + j_{prim}(R, \vartheta_m)} \tag{4.3}$$

shown in fig. 4.3, which by definition ranges between ± 1. Using the level of confidence shown in fig. 4.3 the Lower, Average and Upper cutoffs have been defined.

	$\Delta B/B$	$\Delta R/R$
Primary	2%	0.7%
Quasi-Trapped ($T_f < 30\,s$)	4.2%	1.5%
Trapped ($T_f > 30\,s$)	2.7%	3.3%

Table 4.1: *Errors on the tracing classification induced by detector resolution and IGRF errors*

The R_{eff} values as a function of the magnetic latitude ϑ_m are shown in fig. 4.4. The highest rigidities above which all the particles are primaries (Upper cutoff) and 50% are trapped (Average cutoff) are also shown. For any given ϑ_m, the region between the Upper and Lower cutoff defines the rigidity width of the Earth's penumbra region, where the motion may not conserve the adiabatic invariants. All particles in the sample with $R > R_{eff}$ were rejected, even when classified as trapped. It is also interesting to remark a nice correlation between the tracing classification with the effective cutoff and the criteria based on the smallness parameter ϵ defined in pararagraph 1.4.2; all the under-cutoff particles are compatible with a value of $\epsilon \leq 0.3$ as shown in fig. 4.5.

4.2.3 Tracing Errors

Several elements contribute to the tracing errors: the knowledge of the initial conditions, the intrinsic accuracy of the numerical integration and the error on the magnetic field value. On the initial conditions, the rigidity resolution plays the most important effect. Particles were traced with a known error on rigidity and magnetic field to evaluate the tracing performance.

We used the gaussian distribution of the detector resolution function ($\sigma_R \leq 10\%$ for $R < 10\ GV$) and the error induced by the IGRF and Tsyganenko models for the magnetic field ($\Delta B/B = 0.1\%$ in average). In the left panel of fig. 4.6 σ_{T_f}, the error on the residence time T_f, is shown as a function of the rigidity resolution, with a linear correlation between σ_R and σ_{T_f}, for residence times above $300\,ms$. The error is quite insensitive to σ_R below that threshold, as expected by the drifting and bouncing components of the motion. On the right panel of fig. 4.6, the error on the residence time T_f as a function of the relative error on the magnetic field intensity B is shown. It is practically constant below 5%.

The existence of a critical value has been found for the magnetic field error, $\Delta B/B \sim 0.5\,\%$, above which the tracing errors may become very large. The critical error on the magnetic field is related to the model accuracy which may be considered below $10\,nT$ on the Earth's surface and in any case well below 0.5% at $400\,Km$ [140]. The error induced by the rigidity and magnetic field uncertainties, gives also an error on the particle classification as primary or trapped. The error contributions on the classification in the whole sample, due to rigidity and magnetic field errors are reported in tab. 4.1, and can be considered negligible. The overall error on the residence times can be considered under control and below 10%. The evaluation of the error on the particle direction was done using a gaussian distribution which at low rigidity exhibits the worst resolution ($\sigma_\vartheta \sim 3.5^o$). This smearing is of the same order of the numerical integration error and the relative contribution is negligible.

The analytical result of Stoermer provides the possibility to test the accuracy of the numerical

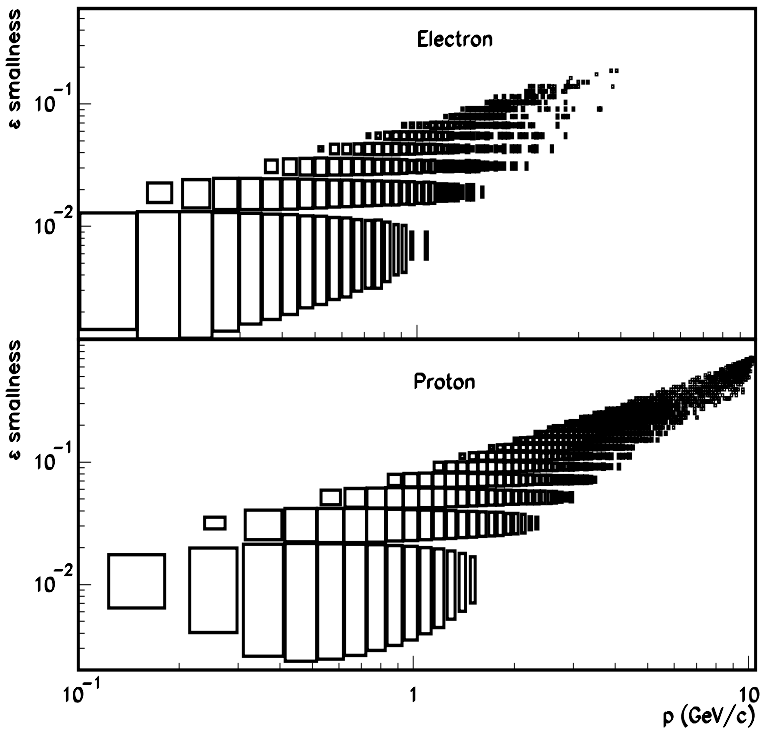

Figure 4.5: *The smallness parameter ϵ as function of the momentum p for AMS electrons (upper panel) and protons (lower panel).*

integration method, and the quality of the criteria chosen. Using an ideal dipole geomagnetic field and not taking into account the constraint $r > R_e$ (i.e without solid Earth), the numerical procedure reproduce the Stoermer cutoff analytical result within 1%.

The tracing is a time consuming task and average CPU time needed to trace one event strongly depend on the particle's trajectory. For instance, using a Digital Alpha (453 MHz) processor, the CPU time to trace a primary is on average 0.1 s while 1 (10) s are requested to follow the motion of a trapped particle outside (inside) the penumbra region.

4.2.4 Tracing Interpretation

In [132],[133],[134] no interpretation was proposed to describe the observed residence times and impact/production points distributions. [145] discussed the AMS results qualitatively using the shifted dipole approximation for the Earth's magnetic field, which is a quite simple approximation.

An exhaustive explanation must take into account the geometry of the drift shells relevant to the AMS measurements and the fact that most of these shells partially extended into the atmosphere. Only for measurements in the SAA region closed shells are encountered and stable trapping is observable at the AMS altitude.

In this framework, the residence times are determined by the periodicities of the drift (τ_d)

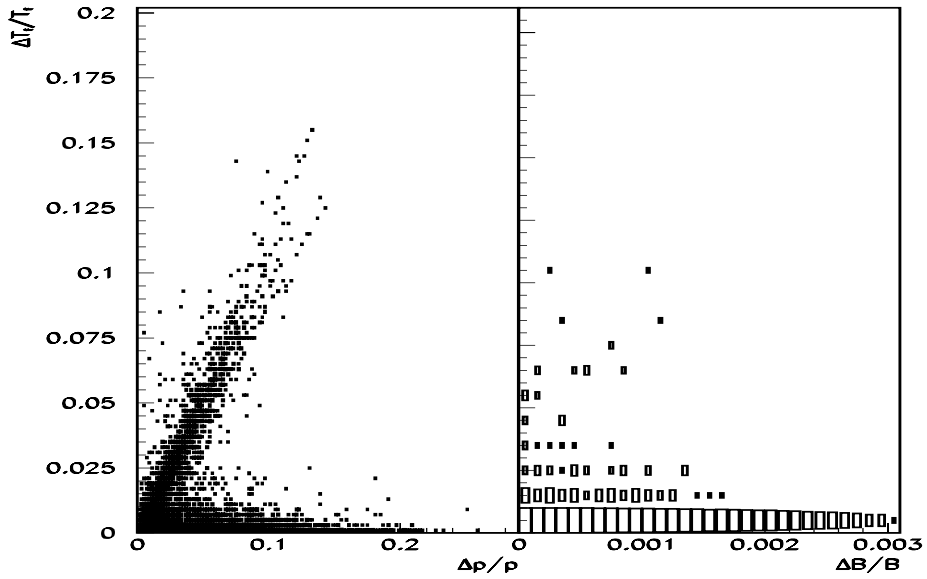

Figure 4.6: *Error in the tracing on the resident time T_f induced by the error on momentum p (left panel) and by the magnetic field B (right panel).*

and bouncing ($\tau_b \ll \tau_d$) motions: the dominant type of motion depends on the relative fraction of the mirror points lying above the atmosphere. The impact/production points (fig. 4.7 and 4.8) correspond to the intersection of the shell surfaces with the atmosphere, as shown in fig. 4.9. At the intersections, particles generated in interactions are injected into the shells. Long-Lived and Short-Lived particles move on shells with different values of B_m or, equivalently α_0, which determine the mirror height on each field line.

A naive interpretation can be given in terms of critical mirror field B_m above which mirror points lie below atmosphere limit. The yellow bands in fig. 4.9, corresponding to the intersections of shells with $\mathrm{B_m} \geq 0.48\,\mathrm{L}^{0.41}\ G$, are well consistent with the impact/production points of the Short-Lived particles. For high B_m or small values of α_0, the mirror height is very low and the shells penetrate into the atmosphere at nearly all longitudes, as shown in fig. 4.10C. Therefore, particles are precipitated rapidly in the atmosphere after injection in the shells.

For the Long-Lived component, the impact/production points are consistent with the blue region in fig. 4.9 corresponding to shell with $\mathrm{B_m} \leq 0.48\,\mathrm{L}^{0.41}\ G$. When B_m is lower, or α_0 closer to 90^o, the shells descend below the atmosphere only in the vicinity of the SAA, as indicated by the blue regions in fig. 4.9, corresponding to shells with $\mathrm{B_m} \leq 0.48\,\mathrm{L}^{0.41}$ G and delimiting the region of the impact/production points of the Long-Lived particles. These particles can drift nearly an entire revolution before absorption in the atmosphere, as shown in fig. 4.10B.

For the Short-Lived component, the bouncing motion is dominant; the residence time is given by $T_f = k\tau_b$, where τ_b is the bouncing motion period, and k is an integer or half-integer between $1/2 \leq k \leq 5$. In a dipolar field model, τ_b is given by $\tau_b = f(\alpha_o)L/\beta$, where f is a slowly varying function of α_o; the upper limit of τ is $\sim 0.3s$ for the AMS data, the dependence

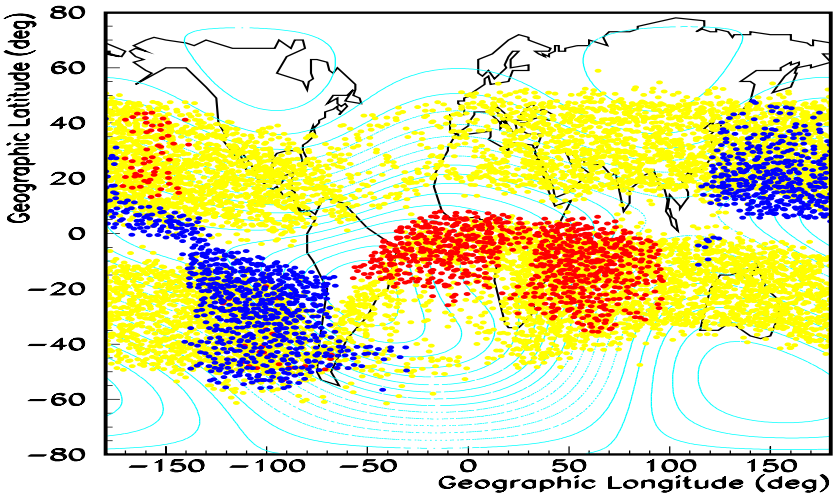

Figure 4.7: *Geographical positions of production and impact points in the atmosphere. Yellow bands show the distribution for Short-Lived e^-, red/blue bands show the production/impact distribution for Long-Lived e^-. A similar but complementary structure is observed for e^+.*

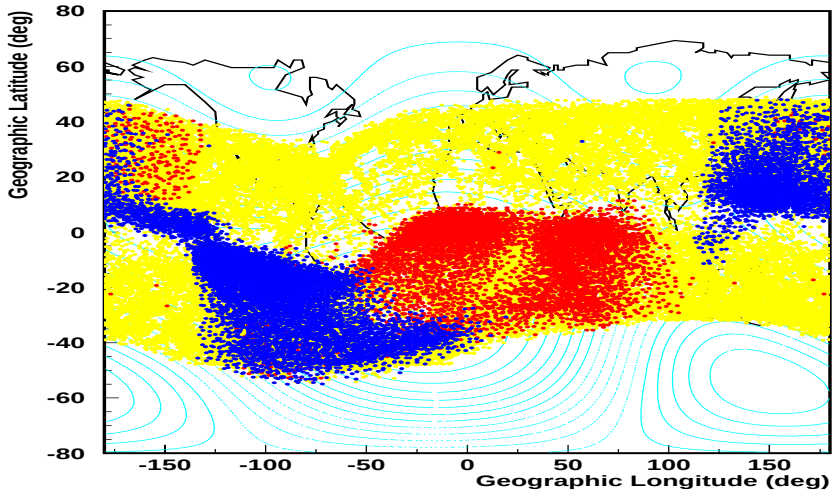

Figure 4.8: *Geographical positions of production and impact points with the atmosphere. Yellow bands show the distribution for Short-Lived protons, red/blue bands show the production/impact distribution for Long-Lived protons.*

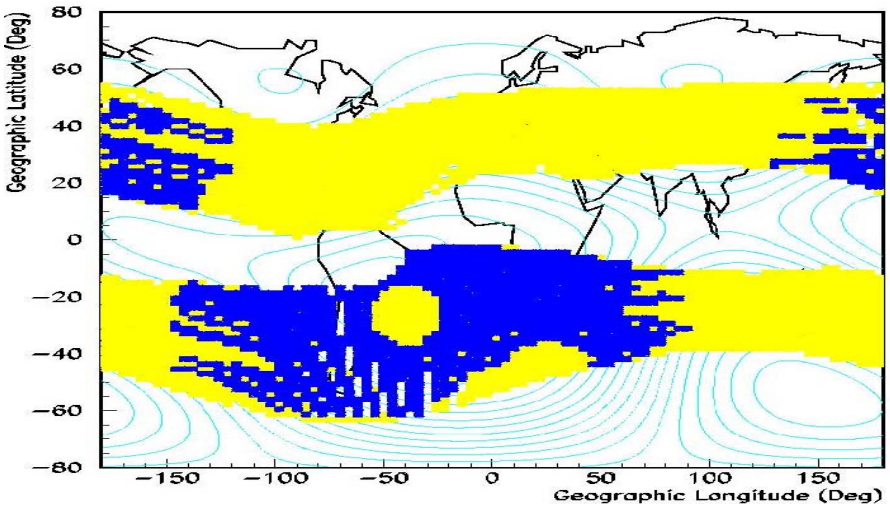

Figure 4.9: *Distribution of intersection points with atmosphere for the drift shells crossed by AMS. Yellow region corresponds to shells with* $\mathrm{B_m} \geq 0.48\,\mathrm{L}^{0.41}\,G$ *, blue one to* $\mathrm{B_m} \leq 0.48\,\mathrm{L}^{0.41}\,G$

on β being observable only for non-relativistic protons. The Short-Lived population seems to be almost independent on the kinetic energy and disposed in horizontal bands. The bouncing period is proportional to $1/\beta$ which is significant only for the protons. The sub-structure seen in the Short-Lived component of fig. 4.1 and 4.2 is due to the discrete values of k and the different L shells crossed during the AMS orbits. For the Long-Lived component, the drift motion is dominant and $T_f = k'\ \tau_d$, where τ_d is the drift motion period, $\tau_d = g(\alpha_o)/L\gamma\beta^2$, where g is a slowly varying function of α_o, and k' is < 1, corresponding to the fraction of a complete drift shell spanned by a particle. The Long-Lived population has residence times inversely proportional to the kinetic energy, due to the dependence on the drift period to $1/\gamma\beta^2$. The two bands seen for the Long-Lived component of fig. 4.1 and 4.2 correspond to fractions of ~ 0.65 and ~ 0.25 of a complete drift and the differences for leptons and protons can be related to the β dependence. The overall picture of the shells crossed by AMS during its orbit is depicted in fig. 4.10. A more appropriate description of the separation is given in terms of bouncing and drifting loss cones and will be given in the following.

4.3 Adiabatic Model Construction

For the description of under-cutoff fluxes, the kinetic energy E_k, the L parameter and the equatorial pitch angle α_0 were used, with α_0 preferred to B_m since naturally limited to $0^o \div 90^o$. The evaluation of (α_0, L) pair for each under-cutoff particle has been done using the UNILIB [27] library with a stand-alone code. During the flight, the AMS z axis assumed all possible orientations with respect to the geomagnetic field lines, independently of the specific attitude. This corresponds to a full scan of the equatorial pitch angle and L range for any orientation of the detector.

The minimum observable value of B_m is determined by the minimum value of the magnetic field reached by AMS along an orbit, because particles mirroring above AMS altitude, cannot

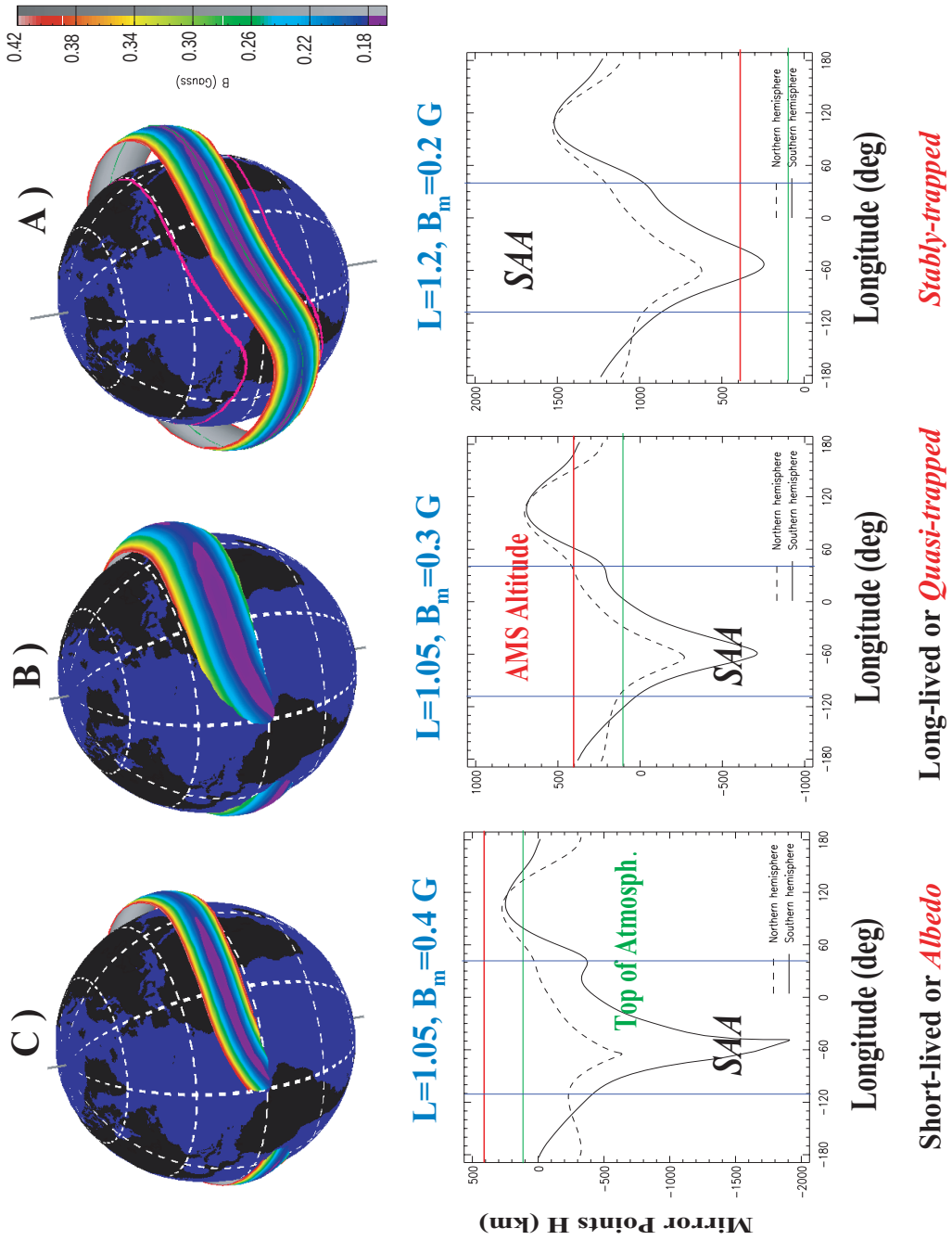

Figure 4.10: *Drift shell crossed by AMS during STS-91. In C) a drift shell typical of short lived particles. On the lower part the altitude of the mirror points are shown as a function of the geographical longitude both for the northern and southern hemispheres. In B) and A) panels are shown the typical drift shell for long lived and stably trapped particle respectively produced with SPENVIS [26].*

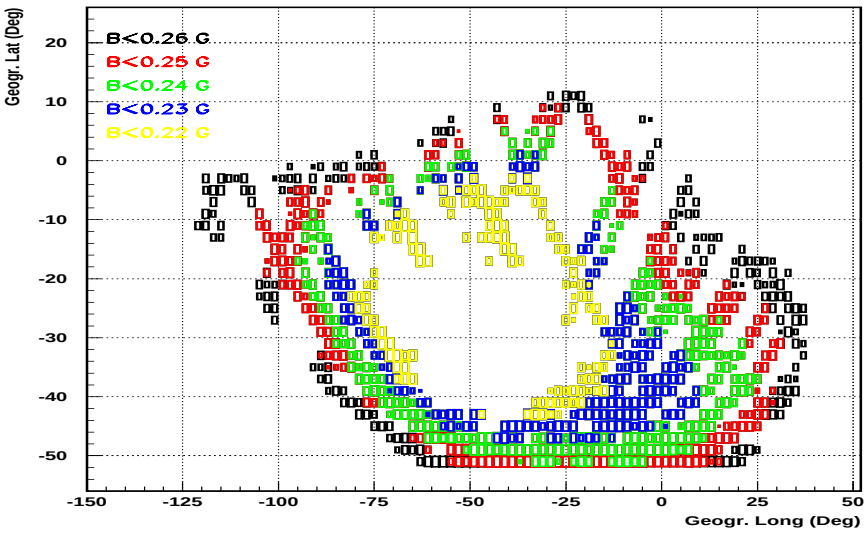

Figure 4.11: *Orbital coverage corresponding to the geographical area where the local magnetic field B is less than 0.26 G. Different colors indicate different values of the max local magnetic field* B_{SAA}.

be observed, while the upper limit of B_m is in principle undefined (formally can be ∞).

For L, the lower limit is fixed to $L \sim 1$ corresponding to the equatorial regions, while the upper limit $L \sim 6$ depends on the maximum latitude reached during the orbit. In practice at high magnetic latitudes, the rigidity cutoff is low and the penumbra effects must be removed by the application of the lower effective cutoff R_{eff}. This results in a limitation of the L range to ~ 3.

Moreover, the validity of the adiabatic approach requires the smallness parameter ϵ to be small. In [30] is shown that the motion becomes chaotic if $\epsilon \geq 0.3$. The AMS leptons and protons are consistent with this limit even though the detected particle energies are relatively high, as already shown in fig. 4.5.

For the definition of the SAA area, the region where $B < 0.26\ G$ was used, as shown in fig. 4.11. The AMS Field of View (FoV) in terms of (α_0, L) along the orbits is shown in fig. 4.12. In the same picture, for comparison, the FoV for AE8/AP8/INP models are shown, together with the typical coverage of balloon flights. Clearly, the comparison is limited in energy for the AE8/AP8/INP models and limited in FoV for balloons. Because of the fixed flight attitudes, the azimuthal β_o coverage in the local magnetic frame, as defined in sec.1.5.2, was not complete, and shown in the insert plot of fig. 4.12. It should be pointed out that although the geographical area corresponding to the region of the SAA is very limited compared to the area outside in fig. 4.11, the L coverage shown in fig. 4.12 is about the same, due to the fact that at the edges of SAA the drift shells drop to very low altitudes resulting in a large L range in a limited geographical region. Therefore, the regions of (α_0, L) covered by observations inside and outside the SAA should describe at least partly the same particle populations.

For the AMS instruments, useful trigger rates varied between 100 and 700 Hz, with maximum

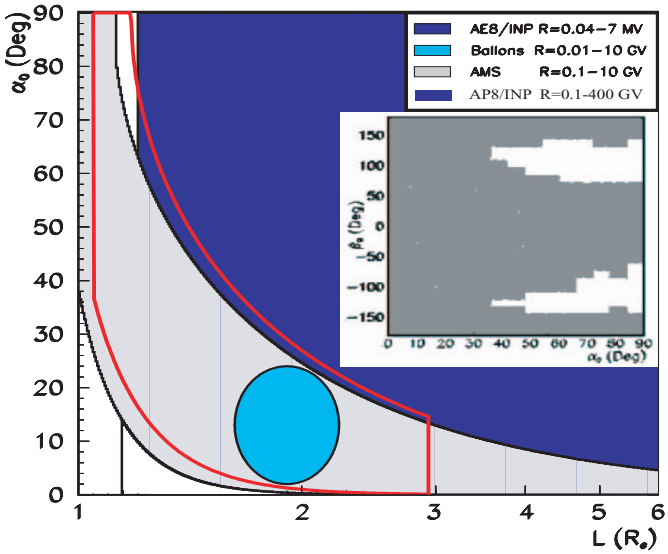

Figure 4.12: *Comparison of the field of view of AMS inside (red contour) and outside (gray region) SAA with balloons and satellite measurements in (L,α_o). In the insert plot the AMS (β_o, α_o) coverage is shown.*

rate in the core of SAA corresponding to $B \leq 0.21\,G$ where detector live-time was very low and AMS did not take data. Data analyzed inside SAA refer therefore to the edges of the SAA where measurements are still reliable, with a detector trigger efficiency ≥ 0.9. The trigger efficiency was checked in the region outside and inside the SAA using the unbiased events, as described in the previous chapter. The region of count rate saturation can be seen in fig. 4.11 as the empty region in the inner region of SAA.

It must be noticed that the fraction of Quasi-Trapped and Stably-Trapped components is a strong function of the maximum field value, B_{SAA}, used to define the SAA region, defined by all the locations such that $B \leq B_{SAA}$, as shown for leptons and protons in the left panel of fig. 4.13. The fraction of Stably-Trapped as a function of B_{SAA} is evaluated as

$$F_{st}(B_{SAA}) = \frac{\int_{B<B_{SAA}} j_{st}(B)dB}{\int_{B<B_{SAA}} j(B)dB} \tag{4.4}$$

where j_{st} is the Stably-Trapped flux and j the total flux in the region delimited by $B < B_{SAA}$. The Quasi-Trapped fraction is then defined as $F_{qt} = 1 - F_{st}$. It can be naively fitted with a power law $F_{st} = 1 - (B_{SAA}/B_l)^{-\alpha} + (B_{SAA}/B_l)^{-\beta}$, with $B_l = 0.21 \pm 0.04\,G$, $\alpha = 10.8 \pm 0.4$, $\beta = 0.61 \pm 0.05$ for leptons and $B_l = 0.21 \pm 0.01\,G$, $\alpha = 8.6 \pm 0.2$, $\beta = 0.86 \pm 0.07$ for protons. B_l is the field value at which the flux becomes entirely Stably-Trapped (F_{st}=1) represents the limit of the full Inner Van Allen Belts (IVAB) at the altitude of AMS orbit. In the right panel of fig. 4.13, the relative fraction of ST protons to leptons is shown as a function of the SAA magnetic field B_{SAA}. It shows that the proton fraction is always above the Stably-Trapped lepton fraction giving an indication of different processes acting on protons and leptons.

The low detector trigger efficiency in the inner part of SAA limits the minimum observable

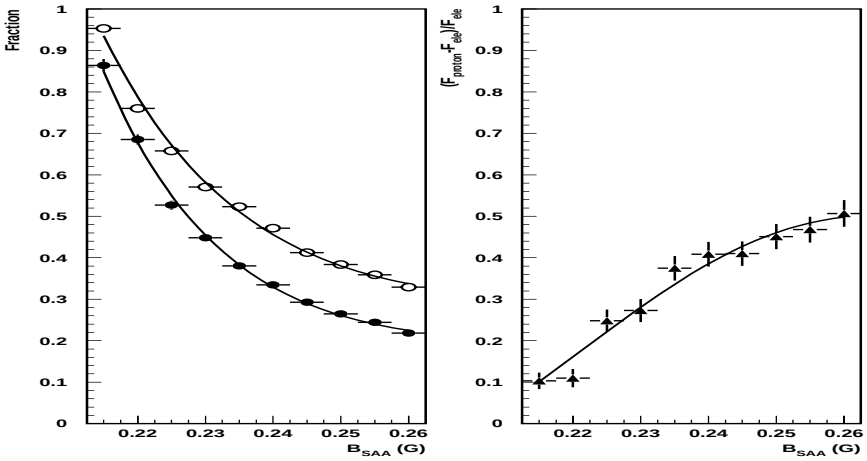

Figure 4.13: *On the left panel the fraction of Stably-Trapped protons (empty circles) and leptons (full cycle) as a function of the maximum local magnetic field B_{SAA}, used to define SAA contours. The power law used of the fit is superimposed to the data points which shows difference among protons and leptons. On the right panel the relative fraction of Stably-Trapped protons to leptons.*

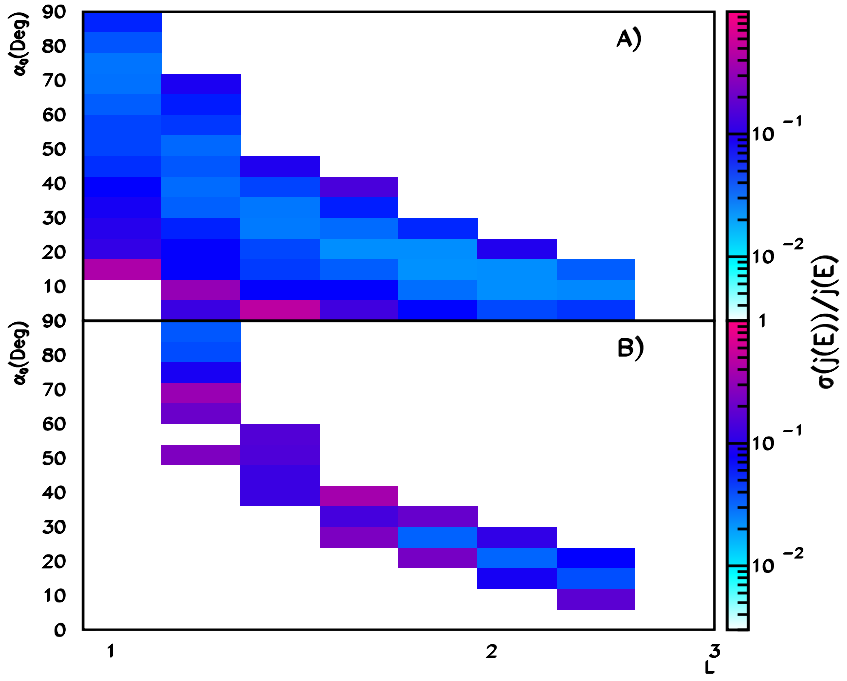

Figure 4.14: *Ratio of the relative error to the average flux as a function of (α_0, L) in the energy interval $0.207 \leq E_k \leq 0.315$ GeV for QT(ST) electrons A(B).*

	N bin	Limit	Bin Width
$R (\simeq E_k)$	9	0.2-10 GV	0.187 (log.)
L	16	0.95-3.	0.031 (log.)
α_0	15	0^o-90^o.	6^o (lin.)

Table 4.2: *Lepton grid limits*

	N bin	Limit	Bin Width
R	9	0.37-10 GV	0.159 (log.)
L	16	0.95-3	0.031 (log.)
α_0	15	$0^o - 90^o$	6^o (lin.)

Table 4.3: *Proton grid limits*

	e^-	e^+	p	Time (s)
ST in SAA	1783	2960	42806	29540
QT in SAA	4990	10683	87295	29540
ST out SAA	417	435	1881	$1.35 \cdot 10^5$
QT out SAA	18487	46517	354902	$1.35 \cdot 10^5$

Table 4.4: *The total number of selected trapped events analyzed for the QT and ST protons and leptons with the time spent inside and outside the SAA.*

field to $B \geq 0.21\,G$. Therefore, we can not observe the full closed Inner Van Allen Belts, but rather the transition region between them and the regions underneath, where drift shells are not closed, a sort of 'gray' spot between two different geomagnetic regions, here called *Mixed Radiation Belts* (MRB). Because of the observed mixing between QT and ST components, this MRB region could be responsible for the filling and depletion of IVAB, especially at high energies, due to possible pitch angle scattering by elastic interactions with residual atmosphere, as explained in the following.

4.4 Under-cutoff Flux Maps

A three-dimensional grid (R, L, α_0) was defined to build flux maps. Linear interval in α_0 and logarithmic variable sizes for L and R were chosen to optimize the statistics in each interval for leptons and protons. The interval limits and widths are listed in tab. 4.2 and 4.3 for leptons and protons, respectively. The flux maps in (L,α_0) at constant R or E_k give the distribution of particle populations at the altitude of AMS. Nine maps at constant R have been made for all the particles. However, the rigidity is converted in kinetic energy E_k for flux studies.

The lower rigidity limits are fixed by the detector acceptance and reconstruction constraints, so that they are different for leptons and protons.

In tab. 4.4 the absolute number of selected events are shown, separated in outside and inside the SAA samples and between Quasi-Trapped and Stably-Trapped components.

Before starting with the analysis of the fluxes, we evaluate the size of the relative error in the AMS average flux maps.

Fig. 4.14 shows the ratio of the standard deviations, $\sigma(\propto \sqrt{N})$, relative to the average flux as a function of (α_0, L). Figs. 4.14A(B) show the error distribution for QT(ST) electrons in the energy interval $0.207 \leq E_k \leq 0.315$ GeV is shown.

The electrons represent the worst case, due to the lower statistics with respect both to positrons and protons; σ increases at the border of the maps, for high L and low α_0 and a

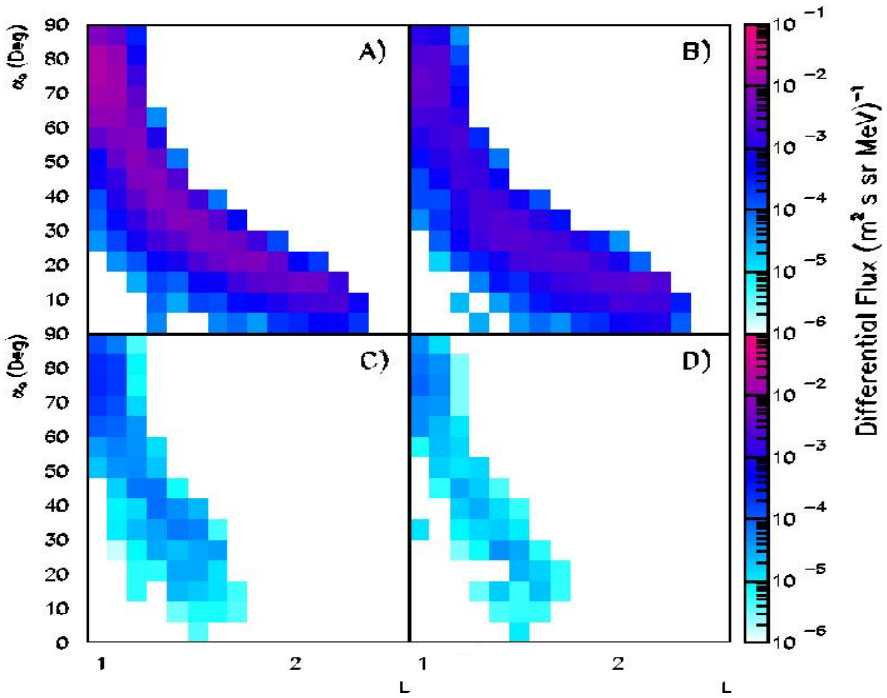

Figure 4.15: *QT differential flux maps outside the SAA for two different energy bins: A), B)* e^+, e^- *between* $0.315 \leq E_k \leq 0.486\ GeV$ *and C), D)* e^+, e^- *between* $1.77 \leq E_k \leq 2.73\ GeV$.

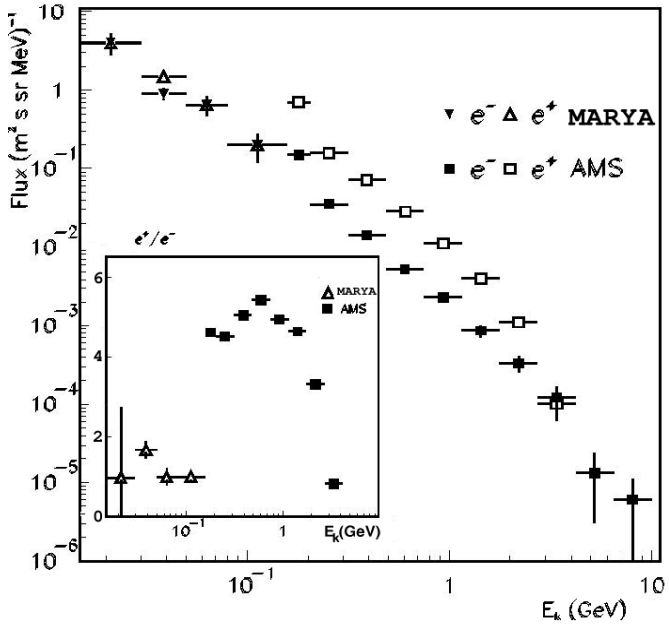

Figure 4.16: *Energy spectrum comparison between AMS and MARYA for* e^+ *and* e^- *for QT particles outside SAA with* $\alpha_0 \geq 70^o$. *In the insert plot, the* e^+/e^- *ratio comparison is shown.*

similar behavior is observed for the other particle species. The relative value of σ is pretty small. It includes the statistical significance, the uncertainties on the magnetic field model and of the (L, α_0) calculations. The contribution to the errors from the detector systematics, described in detail in chapter 3, are not included in the plot, and can be considered of the order O(10%).

The flux has been analyzed following the separation of the drift shells, according to the local magnetic field, in regions inside and outside the SAA. The separation is conventional and in (L, α_o) space the two regions overlap, as seen in fig. 4.12; therefore, common features of the fluxes are expected inside and outside the SAA, as discussed in the following.

4.4.1 Lepton Fluxes

In the following the analysis of the lepton fluxes is presented, starting from the description of the differential and integral QT flux maps outside the SAA, analyzing the charge composition and providing also a comparison with other experiments. Connection of the observed structures with the results of the tracing is suggested. Afterward, the analysis of the QT and ST flux maps inside the SAA are given, remarking differences and similarity with data taken outside the SAA. The section is concluded with a discussion comparing the data with the outcome of the MonteCarlo simulation done in [146] to interpretate the results. Some results from this section have been reported in [157], [158].

Lepton Fluxes Outside the SAA We start analyzing data in the regions outside the SAA for e^+ and e^-; maps of differential fluxes, in the energy intervals $0.315 < E_k < 0.486\ GeV$ and $1.77 < E_k < 2.73\ GeV$, are shown in fig. 4.15.

The flux is limited by the cutoff rigidity R_c: on a given shell only particles with R $\leq R_c$ are allowed to populate the shell, hence lower and lower energy particles populate higher and higher shells and with increasing energy the flux distribution becomes narrower and narrower depleting at the low α_o and high L zones. The differential energy spectra for particles detected at $L \leq 1.2$ with $\alpha_0 \geq 70^o$ are shown in fig. 4.16, superimposed with the lower energy measurements from MARYA experiment [141]. At large pitch angles, the e^+ flux dominates the e^- flux by a factor $\sim$ 4.5, in contrast with MARYA data which indicate the same level of flux for both lepton charges.

e^+, e^- integral flux maps and their ratios in the energy interval 0.2$\div$2.7 GeV are shown in fig. 4.17 and fig. 4.18, respectively. The solid line in the two plots identifies the lower boundary in (L,α_o) below which no leptons can be found with residence times larger than 0.3 s and is defined by the relation $\mathbf{\sin \alpha_c = 0.8 L^{-1.7}}$. Above that curve, for increasing values of α_o, the Long-Lived component of the flux becomes increasingly dominant. This is demonstrated in fig. 4.19 where the same distributions, integrated over α_o (C,D) and L (A,B) respectively, are shown.

The contributions of leptons with $T_f < 0.3$ s and $T_f > 0.3$ s are represented with dashed and solid lines, respectively. Above $\alpha_o > 60^o$ the flux is due substantially to the Long-Lived component; the e^+ flux represents $\approx 80\%$ of the total leptonic flux, while it is at the same level or less than the e^- flux in the low α_o region. The Long-Lived component dominates only at very low L values and high α_o where the positron excess is more pronounced. The same curve

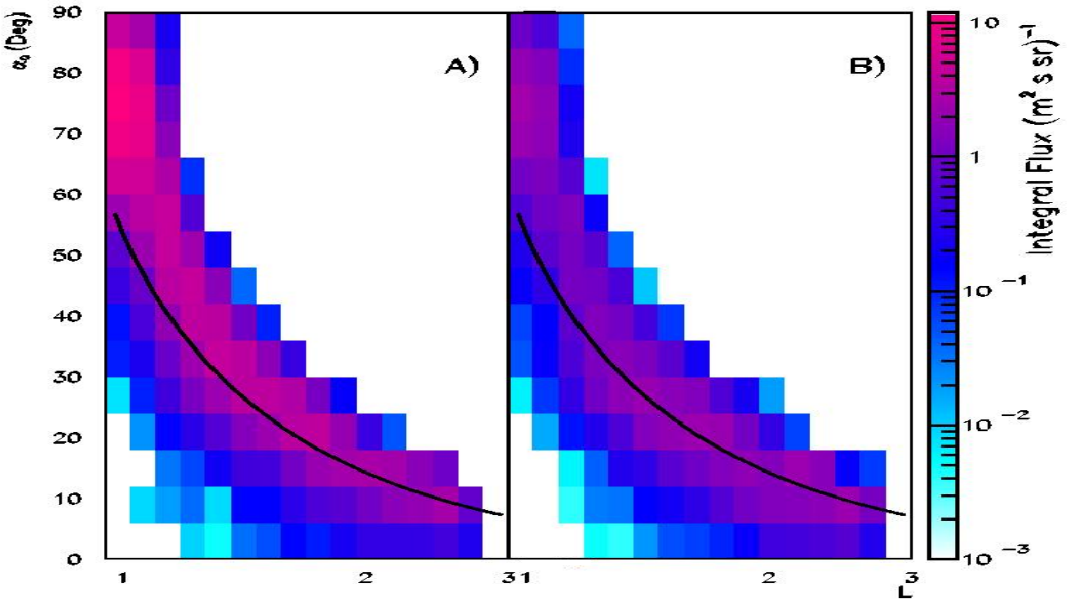

Figure 4.17: *QT integral flux maps outside SAA for e^+ (A) and e^- (B) between* $0.205 \leq E_k \leq 2.73\,GeV$ *outside the SAA. The line shows the curve below which no Quasi-Trapped(Long-Lived) leptons are found.*

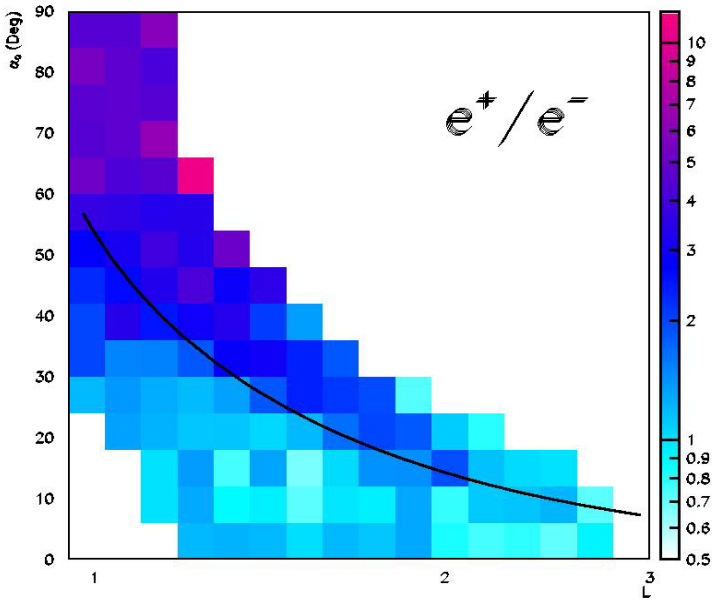

Figure 4.18: *QT integral e^+/e^- ratio outside SAA between* $0.205 \leq E_k \leq 2.73\,GeV$ *outside the SAA. The line shows the curve below which no quasi-trapped leptons are found.*

separates regions in the charge composition map where the e^+/e^- ratio is well above the unity, or around of it, as seen in fig. 4.18.

The critical pitch angle α_c explains the presence of the two well separated components in the residence time: the Albedo or Short-Lived and Quasi-Trapped or Long-Lived ones. Particles inside a cone with a half-opening angle α_c around **B** will enter the atmosphere in few bounces and therefore will disappear rapidly, while those outside will enter the atmosphere after an almost complete drift, only near SAA.

In this context, α_c can be defined as the *equatorial bouncing loss cone angle*, i.e. the largest pitch angle for which particles enter the atmosphere every bounce. Taking into account α_c, the residence time can be written as

$$T_f = k\tau_b\theta(-\alpha_o + \alpha_c) + k'\tau_d\theta(\alpha_o - \alpha_c) \tag{4.5}$$

where θ is the Heavyside step function. The two terms correspond to very different components of motion ($\tau_b \ll \tau_d$), according to the bounce loss cone on that field line. Furthermore, all the QT observed particles are in a drift loss cone angle since all of them enter the atmosphere within one revolution after injection. This explains the absence of a peak at 90^o in the pitch angle distributions of figs. 4.19 A and B where radial and angular distributions are shown. In the following discussion the term of Quasi-Trapped particles will be used to indicate Short and Long Lived populations considered as a whole if not explicitly mentioned.

Lepton Fluxes Inside the SAA The flux inside the SAA has been analyzed in the same way. The corresponding differential flux maps at constant E in (L, α_0) are given in figs. 4.20 and 4.21, for the QT and ST leptonic components inside the SAA and in fig. 4.22 for the QT flux outside the SAA, in the same energy bins for comparison, respectively. Figs. A) and C) give e^+ flux with $0.205 \leq E_k \leq 0.315\,GeV$ and $0.75 \leq E_k \leq 1.15\,GeV$, respectively; figs. B) and D) give the same for e^-.

The QT component fills all the available phase space inside the SAA at all the energies of the differential spectrum. A much narrower distribution is observed for the ST component, which is contained in a limited band corresponding to more central region of the SAA.

A lower limit for the Stably-Trapped component at the altitude of AMS can be described by the relation $\mathbf{\sin\alpha_{st} = 0.95L^{-2}}$. This is the limit for stable trapping in the IVAB, meaning that particles with $\alpha_o \leq \alpha_{st}$ cannot be injected into the IVAB and become indefinitely trapped; α_{st} defines the *equatorial drift loss cone angle*.

The ST component is concentrated at low energies, indicating that the trapping mechanism works only at low energies, as shown in figs. 4.20A and 4.20B; trapping becomes very unlikely for particles with E_k above some hundreds of MeV, where ST flux is almost absent, as evidenced in figs. 4.20C and 4.20D.

This can be seen also in the differential flux at $L \leq 1.2$ and high equatorial pitch angles $\alpha \geq 70^o$ shown in fig. 4.23 and in the energy dependence of the charge ratio of the same data, shown in fig. 4.24. First of all, there is a clear positron dominance in all the components observed by AMS, ST and QT, inside the SAA and also in the QT component outside the SAA. As remarked previously, the observations are in apparent contrast with older measurements at lower energy of the MEPHI group using the MARYA instrument taken in the same phase of

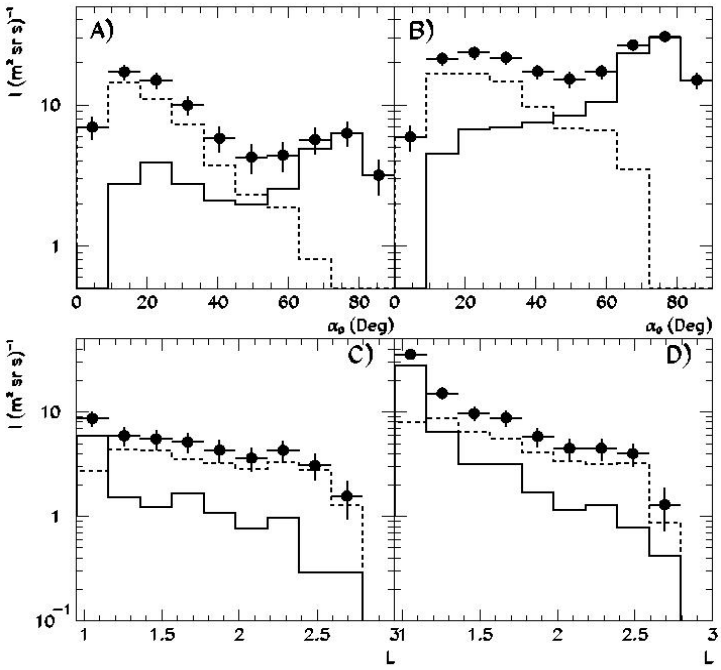

Figure 4.19: *QT integral flux outside SAA as function of* α_0 *and as function of L for* e^- *(A, C) and* e^+ *(B, D) between* $0.205 \leq E_k \leq 2.73\ GeV$. *The full line shows the Long-Lived component, the dashed line shows the Short-Lived component, while the points show the total flux.*

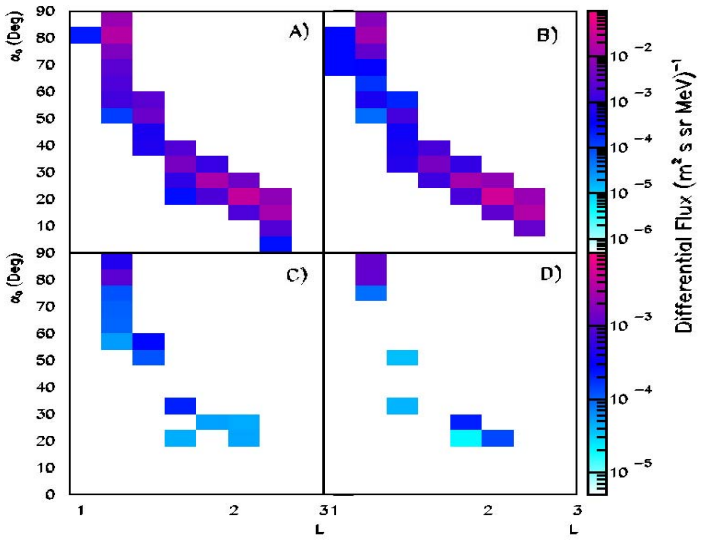

Figure 4.20: e^+ *(A,C) and* e^- *(B,D) differential flux maps for the Stably-Trapped component inside the SAA, for the energy bins* $0.2 \leq E_k \leq 0.315\,GeV$ *(A,B) and* $0.75 \leq E_k \leq 1.15\,GeV$ *(C,D)*

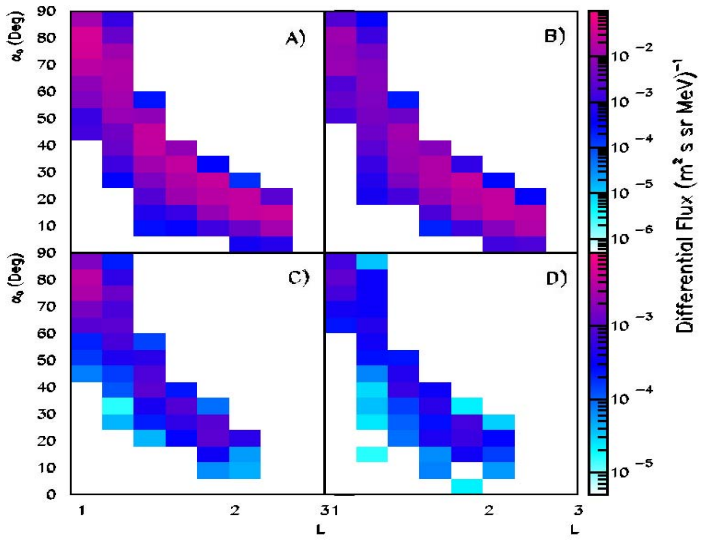

Figure 4.21: e^+ *(A,C) and* e^- *(B,D) differential flux maps for the Quasi-Trapped component inside the SAA, for the energy bins* $0.2 \leq E_k \leq 0.315\,GeV$ *(A,B) and* $0.75 \leq E_k \leq 1.15\,GeV$ *(C,D)*

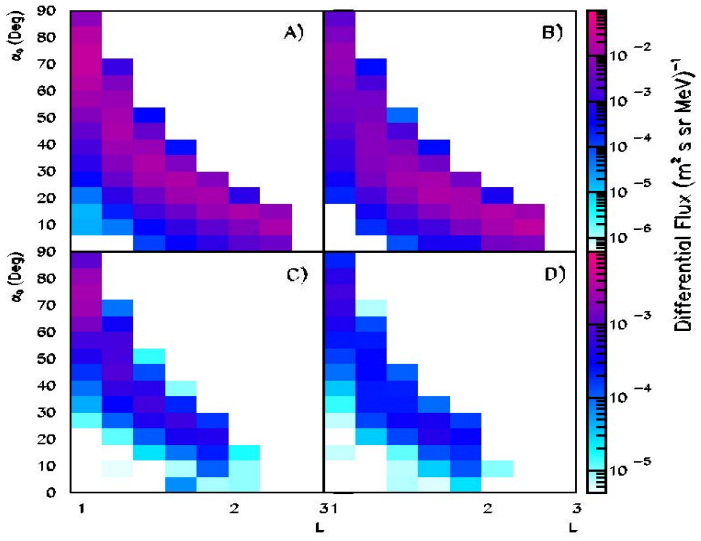

Figure 4.22: e^+ *(A,C) and* e^- *(B,D) differential flux maps for the Quasi-Trapped component outside the SAA, for the energy bins* $0.2 \leq E_k \leq 0.315\,GeV$ *(A,B) and* $0.75 \leq E_k \leq 1.15\,GeV$ *(C,D)*

the solar cycle ([117], [141], [142]): they indicate a strong electron abundance inside the SAA and equivalent fluxes of positrons and electrons outside SAA. It must be noticed that due to the increase of π production cross section in p+N nuclear interactions and due to East-West asymmetry of primary cosmic rays, the charge ratio of e^+ to e^- is expected to increase with energy. This can be observed in the ST component, where high energy data fit the low energy ones.

On the contrary, low energy data outside SAA seem not to fit correctly the high energy component, even if large errors affect low energy data. The energy dependence of the two types of fluxes (ST and QT) is different: the ST component being softer than the QT component on the same shell for both electrons and positrons, a strong indication of an energy limitation for the stable trapping in IVAB.

An important feature is that the differential QT fluxes inside and outside the SAA have the same composition, slopes and comparable intensities, confirming that they are essentially the same population of particles observed on different points of the same shell, as can be seen from figs. 4.21 and 4.22.

In fig. 4.25 the integral flux maps in the interval $0.2 \leq E_k \leq 2.73\,GeV$ for electrons (A, B, C) and positrons (D, E, F) are shown for ST, QT inside SAA and QT outside SAA, respectively. The corresponding positrons to electrons ratio are also plotted (G, H, I).

The integral ST components of lepton flux are confined in a thin band around the SAA, with the lower limit given by $\boldsymbol{\sin\alpha_{st} = 0.95L^{-2}}$, and shown as full lines in figs. 4.25A and 4.25D. The dashed curves correspond to the limit for the IVAB at the altitude of AMS, given by $\boldsymbol{\sin\alpha_{IVAB} = \sqrt{0.311/B_l L^3}}$, with $B_l = 0.21\,G$, the same value found for ST fraction, F_{st}. The region in between the two curves represents the MRB region at the altitude of AMS.

The charge composition map of the ST flux shows a peculiar structure, with a positron dominance in almost all the phase space in SAA and a clear peak at L$\sim$1.2 and $\alpha_o \sim 60^o$ (fig. 4.25G).

The QT component of the flux looks quite different from that of ST, occupying a larger phase space in SAA, as shown in figs. 4.25B and 4.25E. The structure of QT flux inside and outside SAA looks very similar in structure and intensity indicating the common nature for the two fluxes, due to the conventional definition of the SAA. This can be seen also from the charge ratio maps of figs. 4.25H and 4.25I, where a maximum is observed at same L and α_o for the regions inside and outside SAA.

The radial distributions of the flux are shown in fig. 4.26. From figs. 4.26B and 4.26C, results that the radial distributions of the flux, as well as the charge ratio (figs. 4.26E and F), inside and outside the SAA, are very similar due to the common nature of the two fluxes. This is also evident in fig. 4.27B and 4.27D, where the ratio between same sign leptons inside and outside SAA is plotted as a function of L, showing a ratio flat in L and close to ~ 1. The radial distribution of the ST flux shows an evident structure for both electrons and positrons, as shown in fig. 4.26A with two maxima at L $\sim$ 1.2 and $\sim$ 2.1 and a minimum at L $\sim$ 1.4; the ratio of positrons to electrons, in fig. 4.26D, has a maximum in the region of minimum flux. The flux ratios between ST inside and QT flux outside SAA, shown in figs. 4.27A and 4.27C, indicate a lower ST flux at low L with respect to QT.

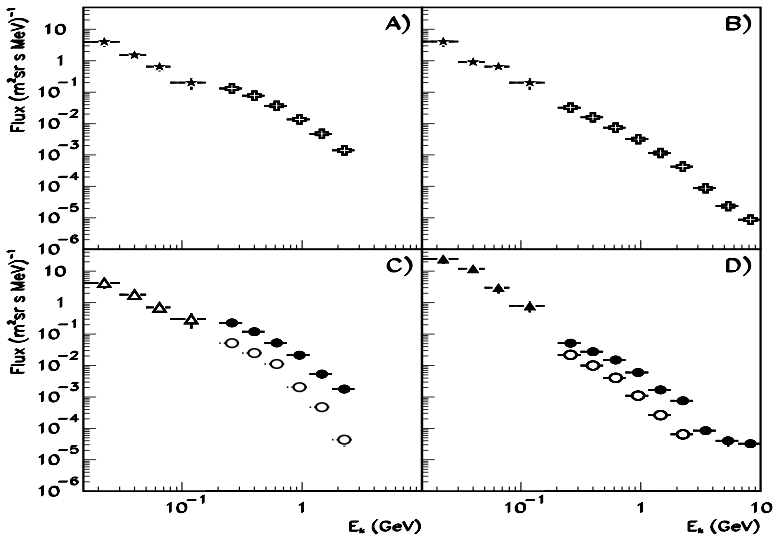

Figure 4.23: *Differential flux of positrons (A,C) and electrons (B,D) in the region L≤1.2 and* $\alpha_o \geq 70^o$. *Triangles and stars show MARYA data inside and outside the SAA, respectively. Full and empty circles show AMS Quasi-Trapped and Stably-Trapped component inside the SAA, respectively. The crosses show the Quasi-Trapped component outside the SAA, measured by AMS.*

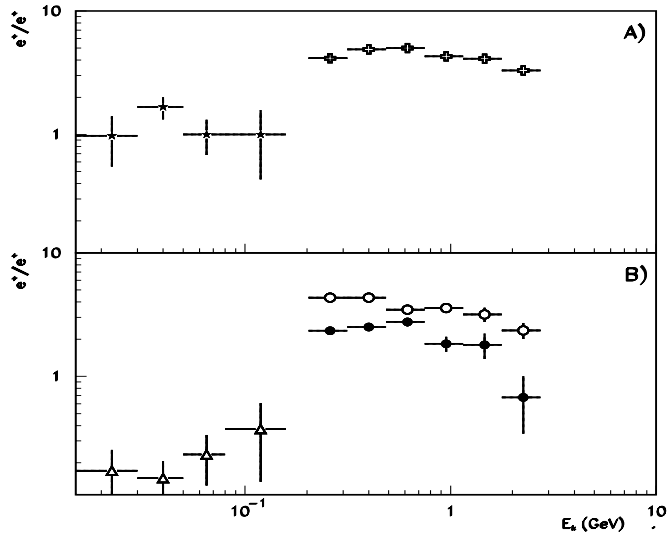

Figure 4.24: *Charge ratio of positrons to electrons in outside A) and inside B) the SAA in the region L≤1.2 and* $\alpha_o \leq 70^o$. *Triangles and stars show the ratio for MARYA data inside and outside the SAA, respectively; the empty and full circles show the measured AMS Quasi-Trapped and Stably-Trapped ratio, respectively; the crosses show the measured AMS ratio outside the SAA.*

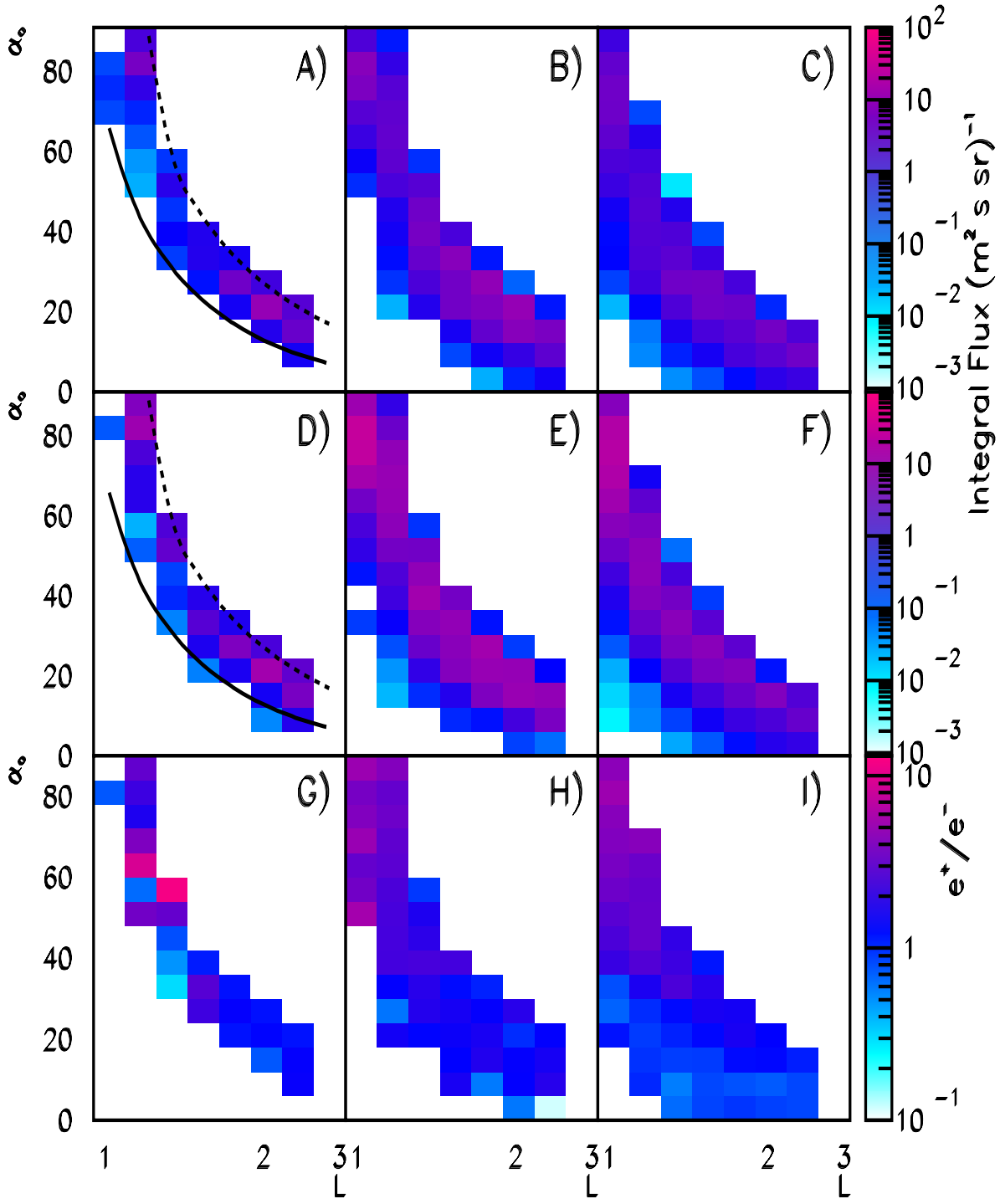

Figure 4.25: *Integral flux in the interval energy 0.205-2.73 GeV for Stably-Trapped A), Quasi-Trapped B) in SAA and Quasi-Trapped outside the SAA C) electrons; for Stably-Trapped D), Quasi-Trapped E) in SAA and Quasi-Trapped outside the SAA F) positrons; the corresponding charge ratios are shown in G), H) and I), respectively. The dotted curve shows the limit for the full IVAB, the full line shows the limit for stable trapping at AMS orbit altitude, as explained in text.*

Anisotropies in Lepton Fluxes At low altitudes, an important parameter to investigate possible flux anisotropies, is the local directional distribution of the particles. The intrinsic azimuthal β_o angle (see sec. 1.5.2) allows for the separation between particles arriving from the local magnetic East/West. According to the definition, leptons coming from West have always $\beta_o < 0$, while those coming from East $\beta_o > 0$. In general, the azimuthal anisotropy brings to fluxes of positrons(electrons) from East(West) higher than from West(East). At low L, the asymmetry is related to the fact that Eastward(Westward) positrons(electrons) have guiding centers below the detection position and may be removed by the interaction with atmospheric nuclei. Due to the limited statistics in the lepton samples, it is possible only to investigate different contributions, in the azimuthal β_o direction, for integral fluxes in the energy range $0.205 \leq E_k \leq 2.73\, GeV$ as a function of L. The East-West flux asymmetry, defined as $\boldsymbol{A = (J_{\beta_o<0} - J_{\beta_o>0})/(J_{\beta_o<0} + J_{\beta_o>0})}$, as a function of L, for QT and ST lepton components, is shown in fig. 4.28A and B, respectively (e^+ full circles, e^- open circles). The East/West asymmetry is due to the different atmospheric drags experienced by particles. The anisotropy effects are averaged out in the QT lepton fluxes, because the residence times are short with respect to time scale needed for asymmetrization. As a consequence, the observed anisotropies in the QT lepton fluxes, appear to be compatible within the statistical errors.

Conversely, the ST fluxes are quite anisotropic at low L values, showing excess of Westward ($\beta_0 > 0$) positrons, while the opposite is observed for electrons, having excess in the Eastward ($\beta_0 < 0$) component. This is clearly related to the high residence time of the ST lepton flux, showing average long-time atmospheric effects. At high L values the asymmetry tends to zero due to geomagnetic cutoff effects.

Discussion of Leptons Results Different kinds of leptonic radiation belts have been observed at $\sim 400\, Km$ of altitude depending on the particles residence times and corresponding wether observation point is inside or outside SAA, with particle energies in the range of O(GeV). Only inside the SAA particles can populate closed shells and stable trapping is possible, while not closed shells reaching the atmosphere in regions outside or close to the SAA can be observed everywhere.

For the QT component, irrespective if inside or outside the SAA, at any given L, a critical value of the equatorial pitch angle, α_c, the *bouncing loss cone*, can be defined to distinguish the Long-Lived, or *Quasi-Trapped*, and the Short-Lived, or *Albedo*, components of the fluxes. The same value is found to separate the regions where the e^+/e^- ratio is above or ~ 1: the charge composition shows a clear dominance of positively charged leptons in a definite region of the (L,α_o) space above $\alpha_c(L)$.

The observed behaviour makes these belts different from the IVAB and limits the possible injection/loss mechanisms to those acting on a time scale much shorter than the typical particle residence times.

The charge ratio distribution provides an important constraint for radiation belt models. The interaction of primary CR (protons and helium nuclei) and inner belt protons with atmospheric nuclei in the regions of shell intersections with the atmosphere is a natural mechanism for the production of secondary leptons through the $\pi - \mu - e$ or $\pi - \gamma - e$ decay chains. This leads to a e^+ excess over e^- and seems suitable to explain the observed charge ratio for the Quasi-Trapped

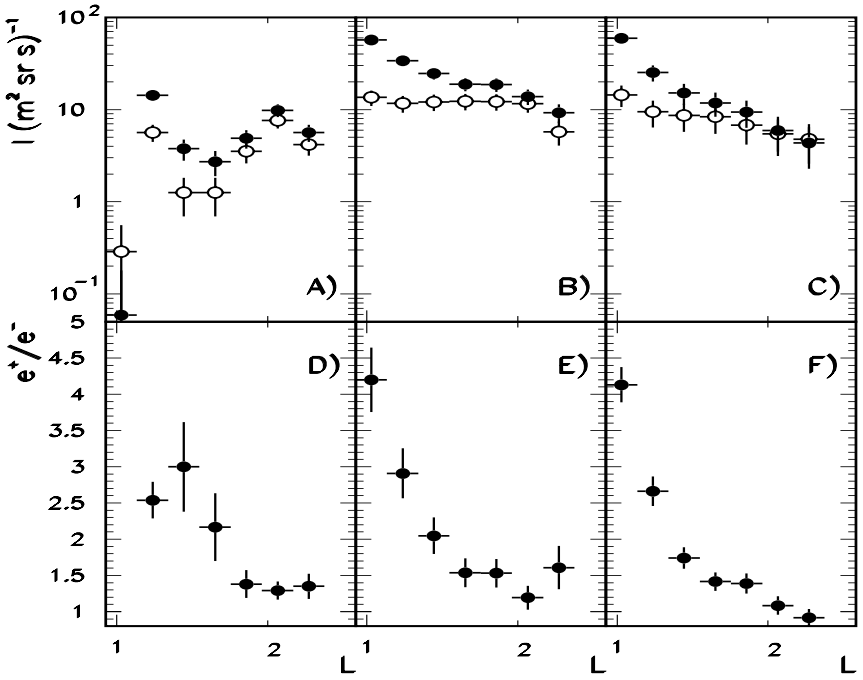

Figure 4.26: *Flux integrated over α_0 in the energy interval 0.205-2.73 GeV as a function of L shell parameter for Stably-Trapped, Quasi-Trapped components in SAA and Quasi-Trapped flux outside SAA is shown in A), B) and C) respectively; empty and full dots show electrons and positrons, respectively; the corresponding charge ratios are shown in D), F) and E) respectively.*

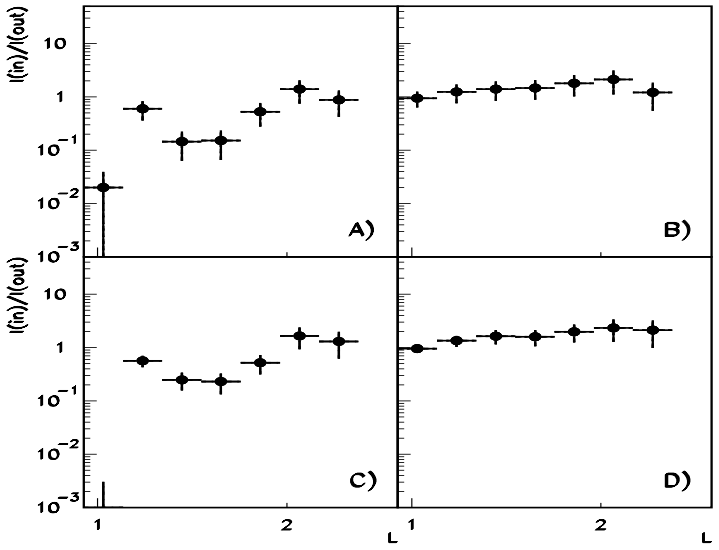

Figure 4.27: *Ratio between same sign leptons inside and outside SAA. A) (C) is the ratio between ST electrons (positrons) inside SAA and QT electrons (positrons) outside SAA. B) (D) is the ratio between QT electrons (positrons) inside SAA and QT electrons (positrons) outside SAA.*

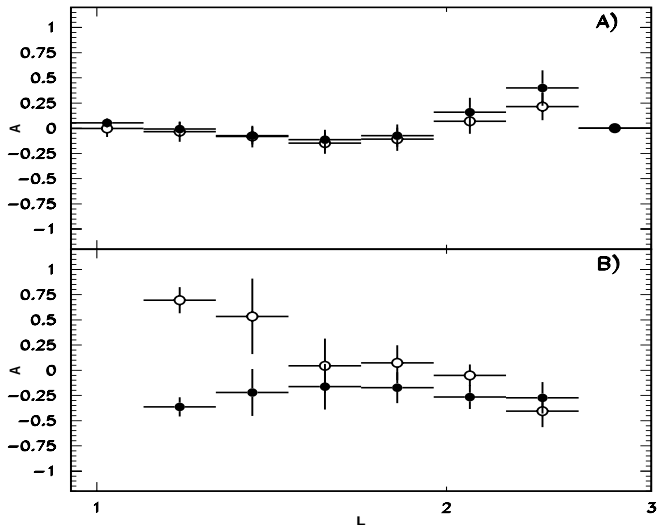

Figure 4.28: *In A) the integral flux asymmetry for QT positrons (full circle) and electrons (open circle). In B), the same distribution is shown, for ST positrons (full circle) and electrons (open circle).*

(Long-Lived) flux ([111],[100]). However, for the Albedo (Short-Lived) flux, the charge ratio is of the order of unity, as seen in fig. 4.18, and other mechanisms might be present.

Recent MonteCarlo studies based on secondary production mechanism have been able to fully reproduce the under-cutoff proton spectrum reported by AMS [143], [146], while a less good agreement for the under-cutoff lepton spectrum [144], [146] was obtained.

In [145] the influence of geomagnetic effects, mainly related to the East-West asymmetry for cosmic protons and helium nuclei, is taken into account to qualitatively explain the observed charge ratio. The same argument were also used by [101] for the Interkosmos-17 data, where it is claimed that, in the equatorial region, leptons are produced by protons and helium nuclei from the West, but only positrons are able to escape to higher altitudes and to drift toward the West. Fewer electrons are produced due to the East-West asymmetry of the cutoff, escaping towards the East.

In [101] the positron excess over electron as function of energy, shows a maximum ~ 4, at energies of $\sim 200\ MeV$. However, more refined studies are needed to definitely exclude contributions from other mechanisms, i.e. acceleration processes acting on the leptons resulting from the decays of β-active secondary nuclei and neutrons of albedo and solar origin [112]. There are clear indications that π decays may account for the Quasi-Trapped component of the flux, while the situation is less clear for the Albedo component where other processes may contribute.

The situation is different inside the SAA. The AMS data in this regions support the existence of a transition region from Stably-Trapped to Quasi- Trapped populations at the altitude of AMS orbit.

The transition region is defined by the curve $\alpha_{st}(L)$ marking the lower limit for stable trapping, given by the equatorial drift loss cone angle and the curve for the upper limit of the

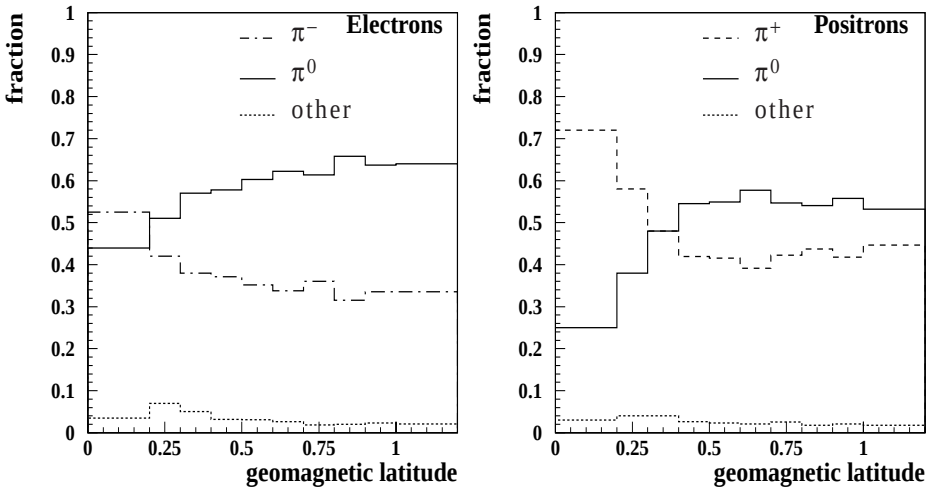

Figure 4.29: *The charged and neutral π decay contributions from atmospheric interactions to electrons and positrons observed at 400 Km as a function of the magnetic latitude [146] for QT leptons outside the SAA region.*

full IVAB. This region, called here Mixed Radiation Belt, could be responsible for the injection and loss of particles into the IVAB. This may be due to the observed mixing of ST flux, typical of IVAB, and QT flux, typical of the regions beneath the belts. The mixing is likely due to Coulomb scattering with residual atmosphere, which partially randomizes particle pitch angles and make them to drift towards closed shells. The amount of mixing depends on the particles energy and on the average amount of matter crossed during the motion. One of the main contribution to the AMS lepton fluxes comes from primary CR incident at large zenith angles. Resulting muons produced in the transverse direction, with respect to the primary, may travel few kilometers before decay. Leptons from this process, are produced at slightly different altitudes than the primary interaction point; one of the consequences is that leptons coming from the charged pions may experience, in average, less atmosphere than leptons and protons produced at lower altitudes.

The features of the two components, ST and QT, are different: ST flux shows a peculiar structure with two maxima and a slot region, limited to relatively low energy ($\sim$ hundreds of MeV); it is found only in a narrow region corresponding to the inner regions of SAA observed by AMS.

The QT component inside SAA seems to be very similar to QT flux outside the SAA, strongly supporting the idea that these two fluxes measure the same particle population observed on different points of the same drift shell.

Another difference between QT and ST fluxes are the East/West anisotropies for the ST component at low L values, while it is almost absent for the QT component. The anisotropy shows that more positrons coming from the East are observed in the ST fluxes at low L, while electrons come mostly from the West. Atmospheric drag effects can be invoked to explain the different behaviour, with direction depending on the sign of the charge.

For all the components of flux, positrons are more abundant than electrons, with a more

pronounced abundance in the QT flux inside and outside SAA, compared to the ST one. This supports a picture where also in the region inside the SAA the dominant processes are the $\pi - \mu - e$ and $\pi - 2\gamma - 2ee$, in particular at energies above $\sim$ tens MeV, and the East-West primary asymmetry effects.

It is interesting to investigate the specific contributions from neutral and charged pion decay channels as a function of the magnetic latitude.

In fig. 4.29 are shown the results of the expected contributions from the pions to leptons QT fluxes at 400 Km, from the MonteCarlo simulation in [146]. The main contribution for the electrons comes from π^- decays which decrease with the magnetic latitude, while the π^o decays, at the same level at the equator, becomes dominant at higher latitudes.

For the positrons the main contribution at the equator comes from π^+ decreasing with latitude together with the increase of the π^o decay, being the two contributions of the same order at high latitude.

The contributions are the results of nuclear cross sections for particle production convoluted with geomagnetic effects which extract and inject more efficiently positive charges. [146] shows that even if the contribution of the helium nuclei to the primary CR flux is small, its contribution in the secondary lepton production is not negligible. This is especially true in the equatorial region where it becomes of the order of 30% for electrons and up to 40% for positrons of the total contribution, due to the combination of rigidity and cutoff effects.

4.4.2 Proton Fluxes

In the following, the analysis of the proton fluxes is presented, starting from the description of the differential and integral QT flux maps outside the SAA, comparing results with existing models. Connection of the observed structures with the results of the tracing is provided. The analysis of the QT and ST flux maps in SAA are given, remarking differences and similarity with data taken outside the SAA. We discuss the results comparing data to the MonteCarlo results from the simulation in [146].

Proton Fluxes Outside the SAA As for leptons, the flux maps in (L, α_0) at constant kinetic energy E_k, equivalent to R, give the distribution of particle populations at the altitude of AMS.

Starting from outside the SAA, the differential flux maps in four energy intervals are shown in fig. 4.30 for Quasi-Trapped(Long-Lived) and fig. 4.31 for Albedo(Short-Lived), with an observed total intensity less than $1\ (m^2 s\, sr MeV)^{-1}$, well below the expected intensity for a typical trapped component. On both QT and Albedo component, the effect of the rigidity cutoff R_c is clearly observed as for leptons: on a given shell only particles with R $\leq R_c$ are allowed to populate the shell, therefore only low energy particles can populate higher shells. A relative difference with leptons is that protons are found up to $\sim 6\ GeV$, while leptons up to $\sim 3\ GeV$. A rapid decay of the intensity is observed as the rigidity increases.

The same kind of separation, as illustrated for leptons, is found for protons in terms of Albedo (Short-Lived) and Quasi-Trapped (Long-Lived) particles. The curve $\mathbf{\sin \alpha_c = 0.8 L^{-1.7}}$, found for leptonic bouncing loss cone angle, can be used to separate the two populations, also in the proton sample. This is naturally related to the structure of the Earth's magnetic field. The

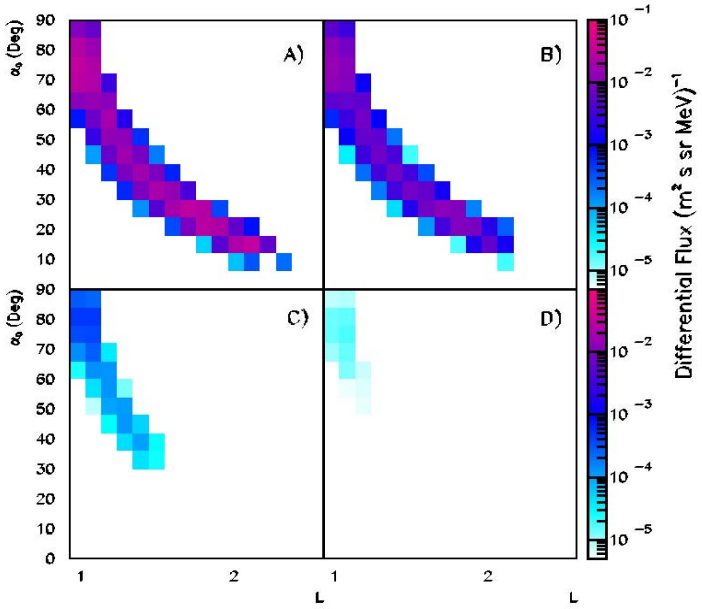

Figure 4.30: *Differential flux maps for QT (Long-Lived) protons outside SAA in the energy intervals A)* $0.07 < E_k < 0.13\ GeV$, *B)* $0.13 < E_k < 0.24\ GeV$, *C)* $1.9 < E_k < 2.9\ GeV$, *D)* $4.3 < E_k < 6.3\ GeV$.

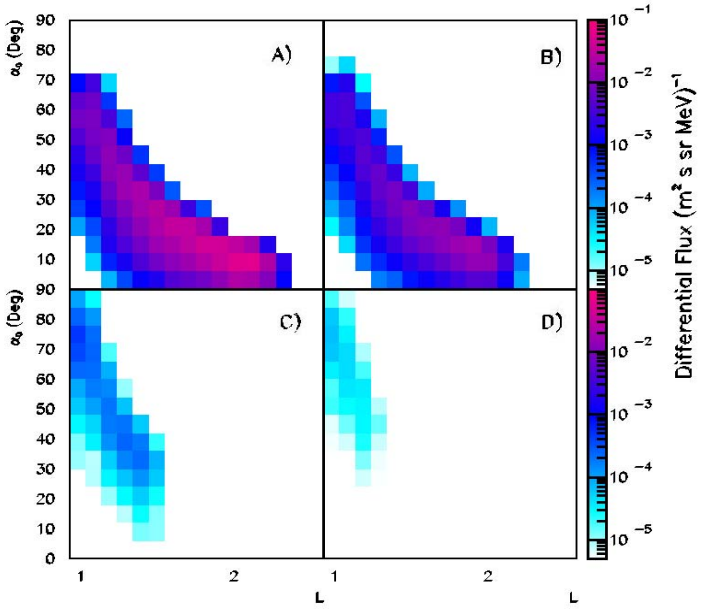

Figure 4.31: *Differential flux maps for Albedo (Short-Lived) protons outside SAA in the energy intervals A)* $0.07 < E_k < 0.13\ GeV$, *B)* $0.13 < E_k < 0.24\ GeV$, *C)* $1.9 < E_k < 2.9\ GeV$, *D)* $4.3 < E_k < 6.3\ GeV$.

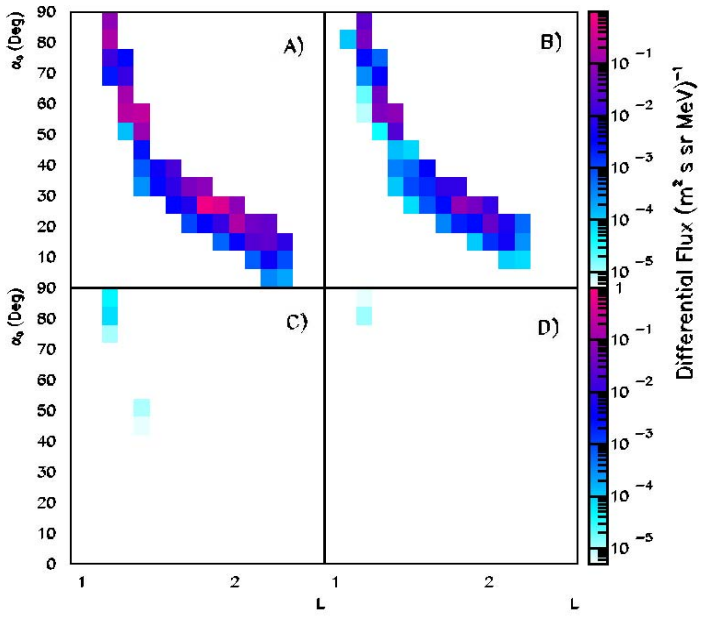

Figure 4.32: *Proton differential flux maps for the Stably-Trapped component inside the SAA, in the energy intervals A)* $0.07 < E_k < 0.13\ GeV$, *B)* $0.13 < E_k < 0.24\ GeV$, *C)* $1.9 < E_k < 2.9\ GeV$, *D)* $4.3 < E_k < 6.3\ GeV$.

curve separating the two populations, not shown in the plots, can be fitted by the same curve $\alpha_c(L)$ found for leptons. The dominance of Albedo (Short-Lived) is evident below this limit, while above the two population are mixed with a QT predominance.

Proton Fluxes Inside the SAA Flux maps were also done inside the SAA. Four differential flux maps in (L, α_0) in the same energy intervals as for outside the SAA, are given in figs. 4.32 and 4.33, for the ST and QT proton components inside the SAA and also for the total QT flux outside the SAA in fig. 4.34 for a direct comparison, respectively. The QT component fills all the available phase space inside the SAA, while a narrower distribution is observed for the ST component, contained in a sharp band corresponding to the inner region of the SAA, as for leptons.

The same lower limit for stable trapping in the IVAB, $\mathbf{\sin \alpha_{st} = 0.95 L^{-2}}$, as illustrated for the leptons, applies to Stably-Trapped protons in the SAA.

The ST component is concentrated at low energies ($0.07 < E_k < 2.9\ GeV$), indicating that the trapping mechanism works only at relatively low energies, as shown in fig. 4.32A and B where the differential flux at constant E_k is given in four energy intervals. Trapping becomes very unlikely for particles with E_k above $3\ GeV$ because pitch angle diffusion due to Coulomb scattering is less important, and flux is virtually absent, as shown in fig. 4.32C and D. Another difference, with respect to lepton fluxes, arises from the fact that the ST proton flux reaches higher energies, while ST leptons are limited to few hundreds of MeV. This is consistent with the different transition profile of the ST fractions F_{st} in the MRB observed for protons and leptons.

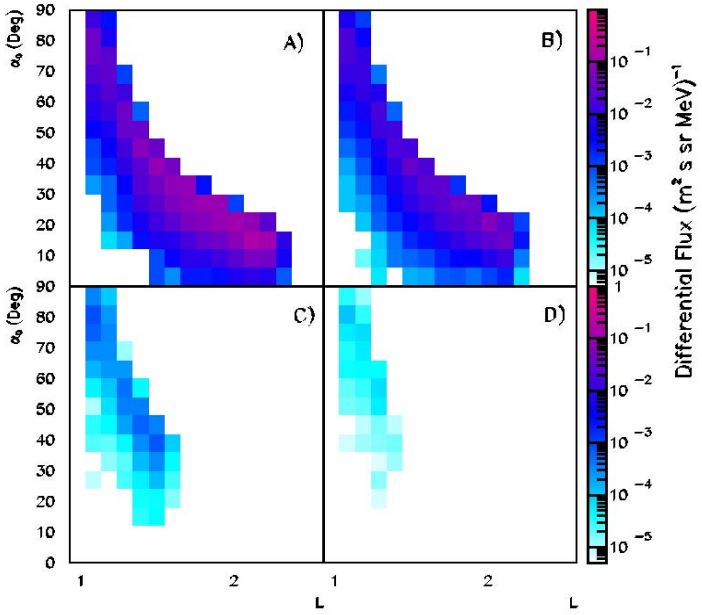

Figure 4.33: *Proton differential flux maps for the Quasi-Trapped component inside the SAA, in the energy intervals A)* $0.07 < E_k < 0.13\ GeV$, *B)* $0.13 < E_k < 0.24\ GeV$, *C)* $1.9 < E_k < 2.9\ GeV$, *D)* $4.3 < E_k < 6.3\ GeV$.

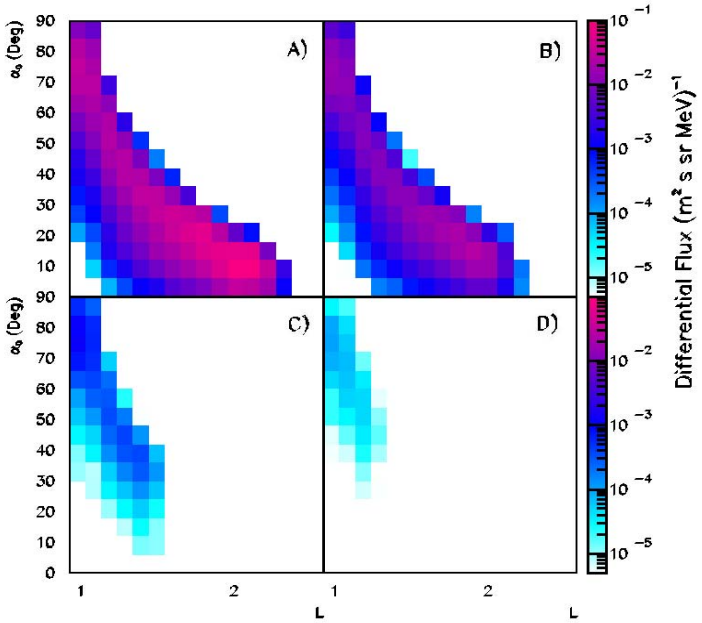

Figure 4.34: *Proton differential flux maps for the Quasi-Trapped component outside the SAA, in the energy intervals A)* $0.07 < E_k < 0.13\ GeV$, *B)* $0.13 < E_k < 0.24\ GeV$, *C)* $1.9 < E_k < 2.9\ GeV$, *D)* $4.3 < E_k < 6.3\ GeV$

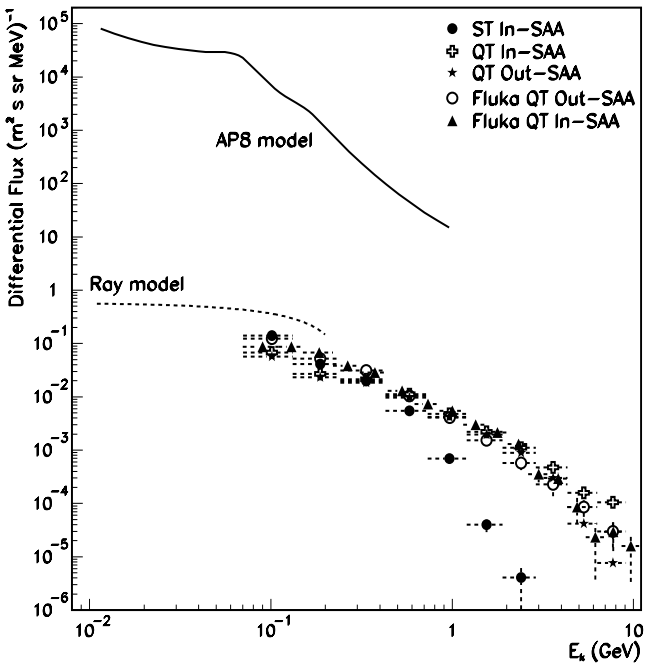

Figure 4.35: *Energy spectrum comparison between AMS, AP8 and MC data for protons with* $\alpha_0 \geq 70^o$ *and* $1.1 < L < 1.2$

Moreover, it is an indication that proton injection is more efficient at high energy. The identity of the loss cone angles for lepton and proton reflects the fact that the structure is entirely due to the magnetic field.

Comparisons of the ST component of the proton flux observed by AMS with the AP8 or INP models have to be done carefully, since AMS did not take data fully inside the SAA.

In fig. 4.35, a comparison between AMS proton fluxes and AP8 for locally mirroring particles for $\alpha_0 \geq 70$ and $L \leq 1.2$ is shown. Significative differences, up to 5 orders of magnitude, are observed in the intensity of the flux. This is due to the fact that the AP8 model holds in regions where $B < 0.21\ G$, corresponding to the full IVAB at the AMS altitude, while the AMS data correspond to the region $0.21 \leq B \leq 0.26\ G$. What may inferred is that the ST flux is very rapidly (orders of magnitude) decreasing as we move from the core of the SAA ($B < 0.21\ G$) to edge regions ($B > 0.21\ G$). A naive computation for the expected secondary component at lower energies, taken from [91], is also shown in the same figure, in qualitative agreement with the QT protons measured by AMS. More refined evaluations come from MonteCarlo simulations developed by different groups, to reproduce the observed AMS under-cutoff proton spectra ([143], [146]). In [146], the Quasi-Trapped component, both inside and outside SAA, are completely explained by secondary production in interactions of primary CR at the intersections of the drift shells with the atmosphere nuclei. The comparison between measured QT and simulated in [146] shows a pretty nice agreement, while the simulation of ST component is not shown because of the limited statistics in the MonteCarlo.

The energy dependence of the two fluxes (ST and QT) is different: as for the leptons, the

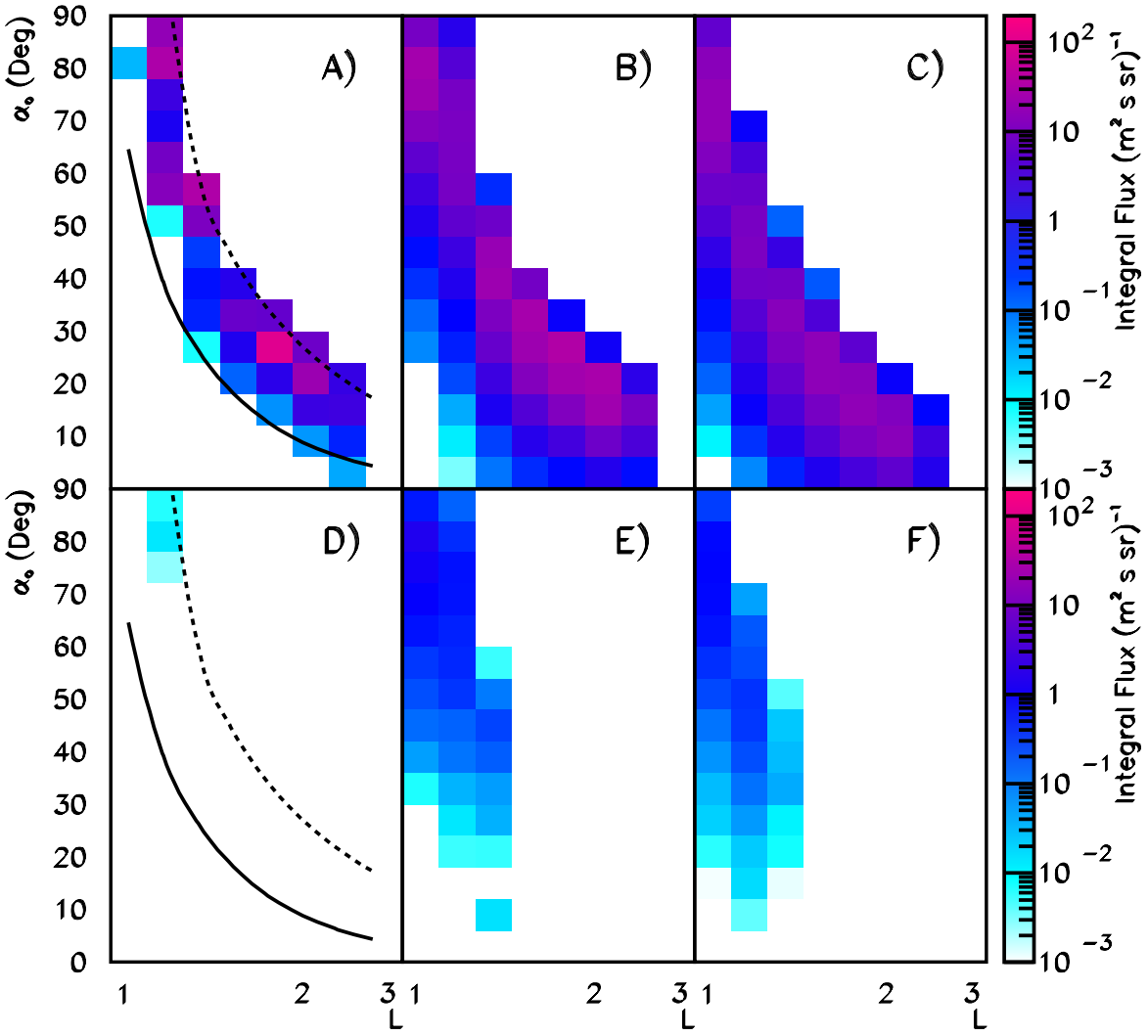

Figure 4.36: *Integral flux in the energy interval* $0.07 - 2.9$ *GeV for ST A), QT B) in SAA and QT outside the SAA C) protons; integral flux in the interval* $2.9 - 9.1$ *GeV for ST D), QT E) in SAA and QT outside the SAA F); The dotted curve shows the limit for the full IVAB, the full line shows the limit for stable trapping at AMS orbit altitude.*

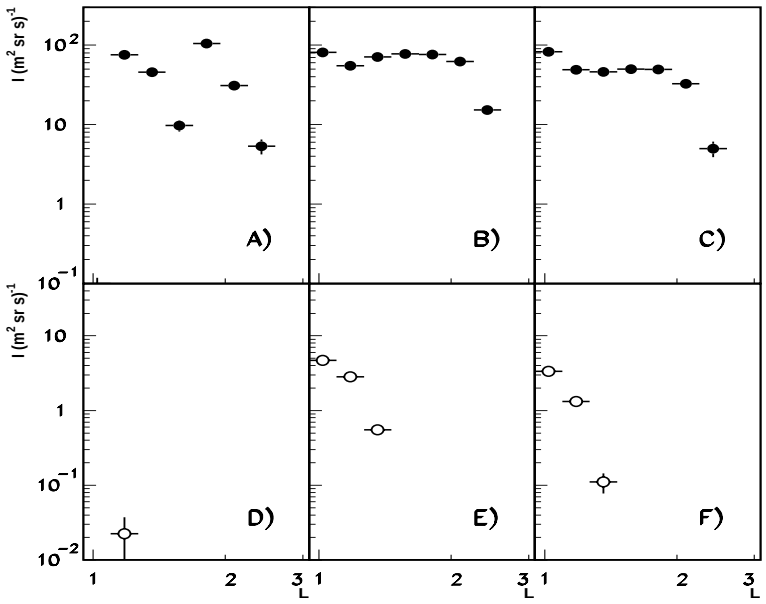

Figure 4.37: *Flux integrated over α_0 in the energy interval $0.07 - 2.9$ GeV as a function of L shell parameter for ST, QT components in SAA and QT flux outside SAA is shown in A), B) and C) respectively; flux integrated over α_0 in the interval $2.9 - 9.1$ GeV as a function of L for ST, QT in SAA and QT outside are shown in D), E), F) respectively.*

ST component is softer than the QT component on the same shell, a strong indication of an energy limitation for the stable trapping in the belts. Another important feature, already seen in leptons, is that the proton differential QT fluxes inside and outside the SAA have the same composition, slopes and comparable intensities, which indicate that they are essentially the same population of particles observed on different points of the same shell, as can be seen from figs. 4.33 and 4.34.

In fig. 4.36 the integral flux maps in the interval $0.07 \leq E_k \leq 2.9$ GeV (A, B, C) and $2.9 \leq E_k \leq 9.1$ GeV (D, E, F) are shown for ST, QT inside SAA and QT outside SAA, respectively. The integral ST proton flux are confined in a thin band around the SAA, with the lower limit given by $\mathbf{\sin \alpha_{st} = 0.95 L^{-2}}$, as for the differential flux and shown as full lines in figs. 4.36A and 4.36D. The dashed curves correspond to the limit for the proton IVAB at the altitude of AMS, given by $\mathbf{\sin \alpha_{IVAB} = \sqrt{0.311/B_l L^3}}$, with B_l=0.21 G, the same value found for ST fraction, F_{st} shown in fig. 4.13. This is the same value observed for the leptons and depends only on the orbit. The area in between the two curves represents the proton MRB region at the altitude of AMS.

The energy composition of ST proton flux shows a peculiar structure, with the high energy component almost absent in all the phase space in SAA. The QT component of the flux looks quite different from that of ST, occupying a larger phase space in SAA, as shown in figs. 4.36B and 4.36E. As for the leptons, the structure of QT flux inside and outside SAA looks very similar in structure and intensity indicating the common nature for the two fluxes.

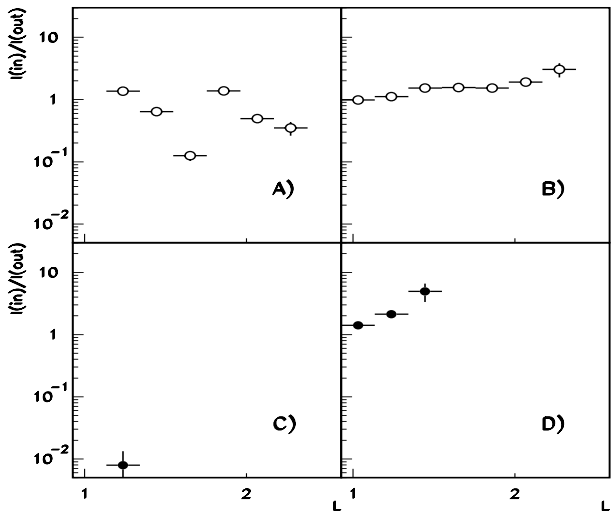

Figure 4.38: *Ratio between integral flux proton inside and outside SAA in the energy intervals* $0.07 - 2.9$ *GeV (low) and* $2.9 - 9.1$ *GeV (high). A) [C)] is the ratio between ST protons inside SAA and QT protons outside SAA in the low [high] energy interval. B) [D)] is the ratio between QT protons inside SAA and QT protons outside SAA in the low [high] energy interval.*

The radial distributions of flux in the belts are shown in fig. 4.37; from fig. 4.37B and 4.37C, the low energy radial distributions of the QT flux come out to be very similar inside and outside the SAA. For the high energy QT flux, shown in figs. 4.37E and 4.37F, appreciable differences are present between inside and outside SAA data.

The same features can be seen in the ratio of QT protons inside to outside SAA, plotted as a function of L in two energy intervals in figs. 4.38B and 4.38D. The ratio at low energy shows the same flux level for the QT component inside and outside the SAA, within a factor ~ 2, while an apparent increase of high energy QT protons inside SAA up to a factor ~ 4 is observed.

The radial distribution of the ST low energy flux shows a clear structure, with two maxima at L ~ 1.2 and ~ 2.1 and a deep minimum at L ~ 1.6, as shown in fig. 4.37A.

The flux ratios between ST inside and QT flux, shown in figs. 4.38A and 4.38C, indicate a ST flux relatively lower at low L with a minimum around $L \sim 1.6$ in the low energy interval. In the radial profile, high energy flux is virtually absent due to the limit in the trapping mechanism.

Anisotropies in Proton Fluxes The large statistics of the proton sample allows for precise study of the anisotropies. Using the same definition presented for leptons, the intrinsic azimuthal β_o angle allows for the separation between particles arriving from the local magnetic East/West. Protons coming from West have always $\beta_o < 0$, while those coming from East $\beta_o > 0$.

Starting from outside the SAA, the integral fluxes in the usual energy intervals, for $\beta_o < 0$ and $\beta_o > 0$ of the QT component, are shown in fig. 4.39. In A) and B) the fluxes integrated in the interval $0.07 \leq E_k \leq 2.9\ GeV$ for $\beta_o > 0$ and $\beta_o < 0$, respectively, are shown, while in C) and D) the same β_o distributions in the interval $2.9 \leq E_k \leq 9.1\ GeV$ are given.

The same distributions integrated over α_o and L are shown in fig. 4.40 A) and B), respectively.

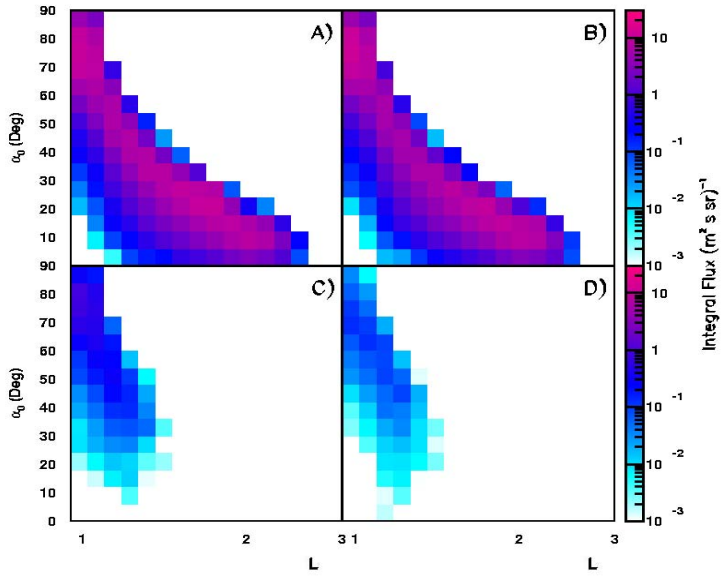

Figure 4.39: *Integral flux map for QT protons outside the SAA in* $0.07 \leq E_k \leq 2.9\,GeV$ *energy range A) with* $\beta_o > 0$ *and B)* $\beta_o < 0$*, and in* $2.9 \leq E_k \leq 9.1\,GeV$ *energy range C) with* $\beta_o > 0$ *and D)* $\beta_o < 0$.

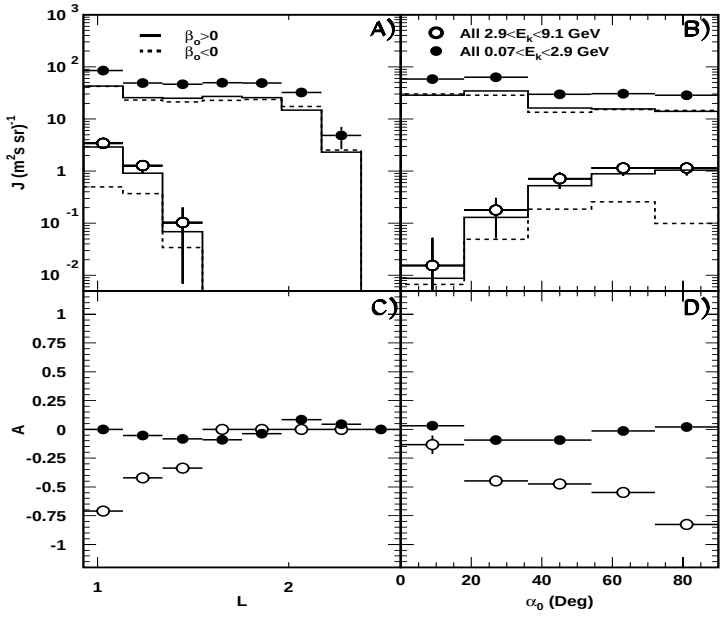

Figure 4.40: *Integral flux and asymmetries for QT protons outside the SAA as function of* α_0 *(B,D) and of L (A,C) separated for the sign of* β_o *and the energy interval.*

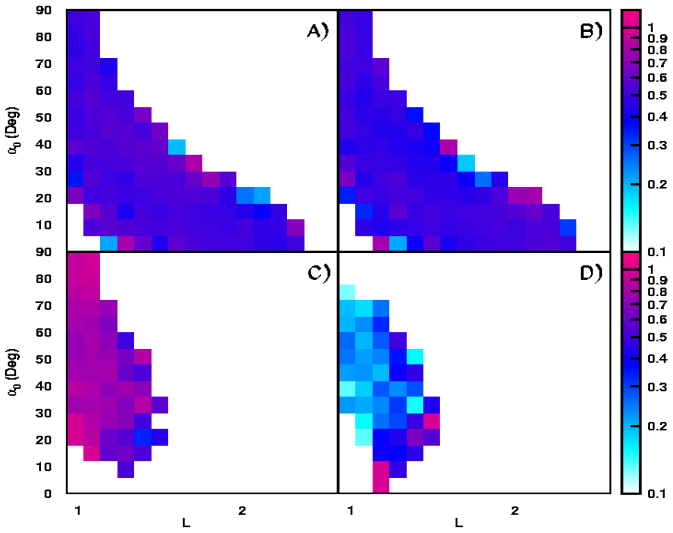

Figure 4.41: *Integral flux East/West fractions for QT protons outside the SAA in the low (high) energy range 0.07≤ E_k ≤2.9 GeV (2.9≤ E_k ≤9.1 GeV), for $\beta_o > 0$ A (C) and $\beta_o < 0$ B (D).*

The East-West flux asymmetry, defined as $\boldsymbol{A = (J_{\beta_o<0} - J_{\beta_o>0})/(J_{\beta_o<0} + J_{\beta_o>0})}$, in the two energy intervals as a function of L and α_o is shown in fig. 4.40 C) and D), respectively. The effects on the trapped proton anisotropy are averaged out thanks to the non fixed orientation of the detector, relative to the magnetic field, during the STS-91 flight. The flux fractions of the East/West components are shown in fig. 4.41.

At low L, the QT proton flux outside the SAA in the energy range $2.9 \leq E_k \leq 9.1\ GeV$ appears to be strongly anisotropic. The flux asymmetry shows a marked dependence on the L shell and α_o in the high energy component, with a smooth and steep transition from Eastward flux at low L to $L \simeq 1.4$, where the two components become at the same level.

In general, the azimuthal anisotropy gives an East-West asymmetry, with the proton fluxes from East more intense than from the West. At low L, the asymmetry arises from the fact that Eastward particles have always the guiding centers below the detection position and are removed by the atmospheric interactions, because the scale length of the high energy proton gyroradius is comparable to the AMS altitude. The atmospheric scale height strongly depends on the energy loss and on the rate of pitch angle scattering of the particles during the drift trajectory; below $400\ Km$ becomes proportional to the atmospheric density.

The asymmetry seems to be almost absent in the low energy component.

Integral fluxes inside the SAA separated in $\beta_o < 0$ and $\beta_o > 0$ components in the same energy range as for QT protons outside the SAA, are shown in fig. 4.42. The same distributions integrated over α_o and L are shown in fig. 4.43 A) and B). The East-West asymmetry A, as function of L and α_o is shown in figs. 4.43 C) and D), respectively. The flux fractions of the East/West components inside the SAA are shown in fig. 4.44. At low altitudes the Stably-Trapped proton flux in the energy range $2.9 \leq E_k \leq 9.1\ GeV$ inside SAA appears to be almost absent, while in the energy range $0.07 \leq E_k \leq 2.9\ GeV$ is strongly anisotropic.

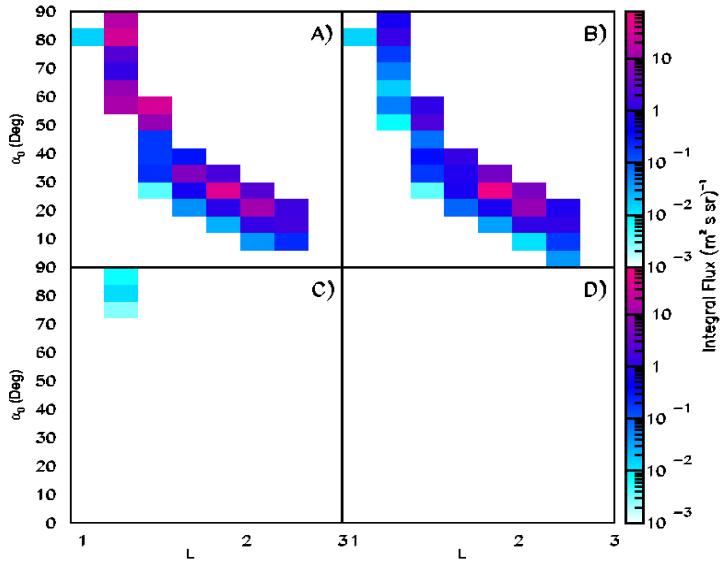

Figure 4.42: *Integral flux map for ST protons inside the SAA in* $0.07 \leq E_k \leq 2.9\,GeV$ *energy range A) with* $\beta_o > 0$ *and B)* $\beta_o < 0$*, and in* $2.9 \leq E_k \leq 9.1\,GeV$ *energy range C) with* $\beta_o > 0$ *and D)* $\beta_o < 0$*.*

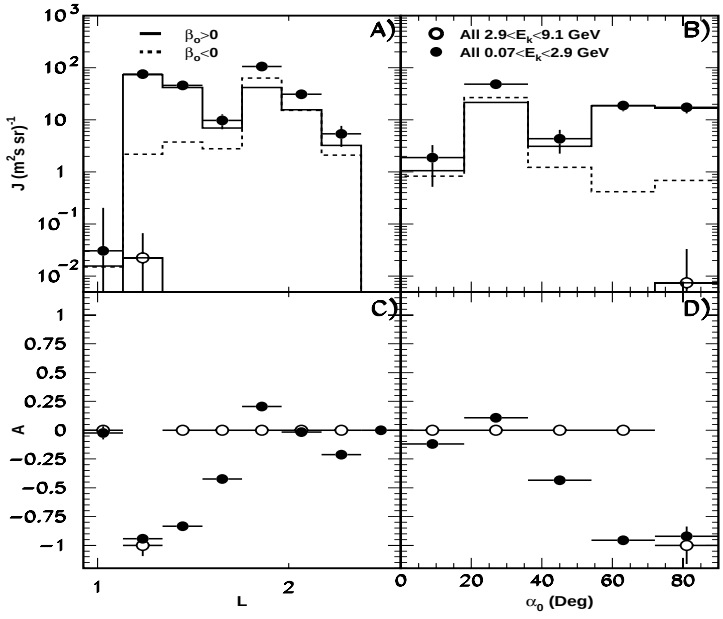

Figure 4.43: *Integral flux and asymmetries for ST protons inside the SAA as function of* α_0 *(B,D) and of L (A,C) separated for the sign of* β_o *and the energy interval.*

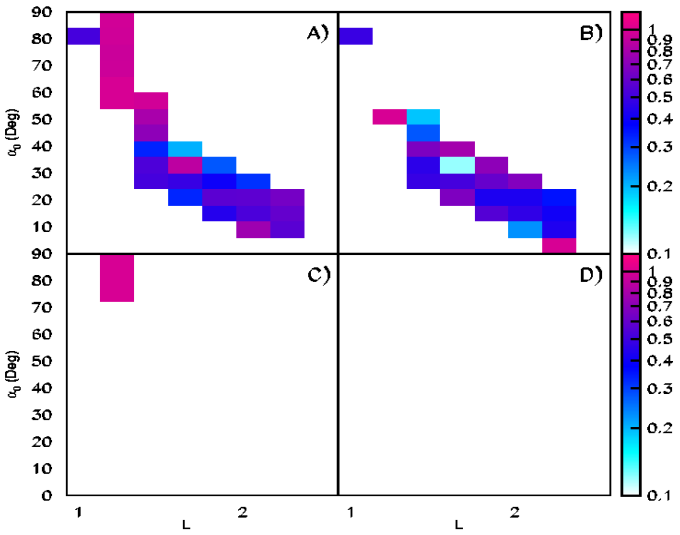

Figure 4.44: *Integral flux East/West fractions for ST protons inside SAA in the low (high) energy range 0.07≤ E_k ≤2.9 GeV (2.9≤ E_k ≤9.1 GeV), for $\beta_o > 0$ A (C) and $\beta_o < 0$ B (D).*

The flux asymmetry shows a marked dependence on the L and α_o in the low energy component, with a smooth and steep transition from Eastward flux at low L to no asymmetry at $L \sim 1.9$, where the Westward component is at the same level. In this case, the asymmetry is still due to the atmospheric drag, but with different intensity than for QT component; ST particles experience higher atmospheric densities with respect to QT, so that asymmetry starts at low energy and completely remove high energy flux.

The ST component has softer differential spectrum with respect all the QT components meaning that the time spent on the shell by ST protons is much higher. As a consequence, the East-West asymmetry is more pronounced and evident at all energies both for the ST component compared to the QT components. This is related to the much higher residence time of ST particles: QT particles with residence time below 30 s precipitate into the atmosphere within one drift and practically experience an instantaneous atmosphere. Conversely, the ST population can experience an average atmosphere less dense and long term averaged atmospheric effects may be present.

Discussion on Proton Results The AMS data indicate clearly the existence of protons radiation belts underneath and at the edges of the IVAB for particle energies up to several GeVs.

Fluxes can be divided in Quasi-Trapped (Long-Lived) and Albedo(Short-Lived) outside the SAA region, while Stably-Trapped population is present in the transition region (MRB) inside the SAA with a transition profile softer than for leptons. The MRB could be responsible for the injection and loss of particles into the IVAB, due the observed mixing of ST flux, typical of IVAB and QT flux, typical of the regions beneath the belts as depicted for leptons. The

mixing could also be due to Coulomb scattering with residual atmosphere, which partially randomizes particle pitch angles and make them to drift in closed shells. Pitch angle scattering of protons has been proposed as a possibly important loss mechanism [40],[150],[148] but his role has been rejected by other researchers [149], [156]. The Coulomb scattering is indeed less important for protons than for leptons due to the higher mass. Moreover, it is proportional to the atmospheric density, increasing with decreasing altitude. The mean squares angular deflection for a singly charged particle, in traversing the atmosphere is given approximatively by $\boldsymbol{d < \vartheta^2 > /dX = (21/pv)^2 (X_o)_{elm}^{-1}}$ with pv in MeV and $(X_o)_{elm} = 37\, gcm^{-2}$ is the electromagnetic radiation length of the air. The diffusion in pitch angle due to multiple scattering is relatively small and becomes stronger at low energy because of the $(pv)^{-2}$ term.

At low altitudes the effect is important even for high energy protons because a small change in pitch angle may produce a quite large variation in the average atmospheric density crossed by a particle. If a particle with a local pitch angle α scatters through an angle $\Delta\alpha$, the mirror field changes by an amount $\Delta B_m/B_m = -2\Delta\alpha\, cot\alpha$ with most of the pitch angle scattering that will occur near the mirror points where the atmospheric density is largest.

In [148] it has been evaluated that approximatively at $L = 1.4$ with $B_m = 0.21\, G$, a 5% change in B_m reflects in a change by a factor 5 in the averaged atmospheric density and even a smaller values of the scattering may produce such effect. Anisotropies are observed at energies above $2.9\, GeV$ inside the SAA for the QT component due to the gyroradius and the relative correction to the guiding center approximation; the same kind of asymmetry is observed for the ST component inside the SAA at lower energies. This depend on the fact that the ST differential spectrum is softer with respect to the QT flux inside and outside the SAA and the longer residence times of ST. The transition region from not closed shells to the IVAB is similar to the lepton transition region, with a different profile, establishing a steady westward motion, while in QT component transient effects of production process dominate.

The interaction of primary CR and inner belt protons with atmospheric nuclei in the regions of shell intersection with atmosphere are a natural mechanism for the production of the observed secondary protons, as for leptons. The MonteCarlo calculations in [144] and [146] support this hypothesis. The two most significant sources of secondary protons in the observed energy range are from the primary CR protons and helium nuclei colliding with atmospheric nuclei, with a negligible contribution of heavier nuclei. The distribution of the proton production altitude has a mean value of $\sim 30\, Km$ almost constant with the geomagnetic latitude; the angular distribution of the secondary protons with respect to the incident direction, shows that the main contribution comes from primary protons and helium nuclei incident at large zenith angles, i.e grazing the atmosphere.

The contribution to the secondary proton flux coming from the primary protons and helium nuclei, evaluated in [146], are reported in fig. 4.45 as a function of the magnetic latitude. The situation described in the picture reflects that helium contributes significatively to the secondary proton flux especially at equatorial regions, where becomes dominant. At higher latitudes, the effect becomes less important due to combination of rigidity and geomagnetic effects.

Depending on the radial location, particles may experience instantaneous interactions with the atmosphere through the Coulomb losses and precipitation at low L, or may experience an average atmosphere at higher L. This depends on the features of the particle sources, expected to

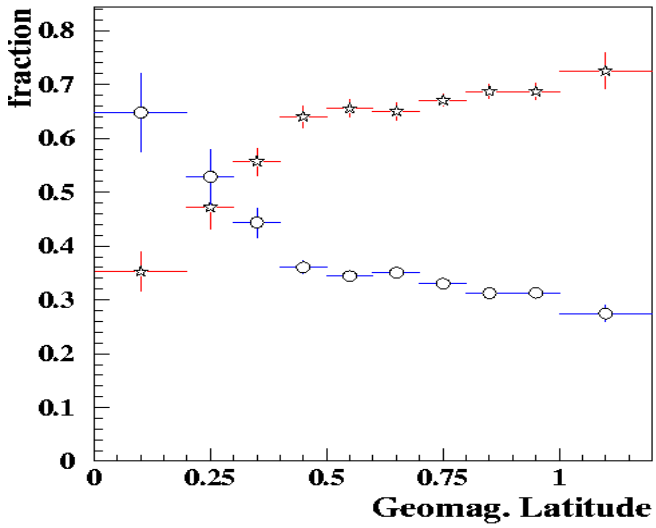

Figure 4.45: *The fraction of primary proton (stars) and primary helium nuclei (circle) to the total production of secondary protons as a function of the magnetic latitude from [146].*

increase with latitude due to the flux leakage at off-equator latitudes, and related to geomagnetic cutoff effects more pronounced at equator. If the source is depending on the primary CR flux, a time dependence would be present because of the solar cycle, affecting the low energy part of the spectra. At $L < 1.15$ lifetime against Coulomb collisions are short compared to the 11 years solar cycle. Therefore, the spectral shape of the source should be governed by the CR spectral index and independent on the loss process with a slight change due to the solar cycle. Conversely the radial profile, as well as the anisotropy of the fluxes should be related to the losses, i.e. to the atmospheric density, likely almost independent on the source and possible diffusion processes.

4.5 Comparison between Proton and Lepton

To conclude the analysis, a comparison between protons and leptons was done, focusing in particular to the differences observed between radial profiles and differential spectra of the QT and ST populations. The integral fluxes are also analyzed as a function of the magnetic longitude, using the invariant coordinate map representation.

Spectra and radial profiles Measurements of radiation belts fluxes occasionally show temporal variations not accompanied by corresponding variations of the local geomagnetic field. The variations indicate a possible violation of the adiabatic invariants. Large depletions of flux result from non-adiabatic processes operating during magnetic storms. The two categories are called temporally varying and temporally static fluxes [28].

The fluxes registered during the AMS STS-91 flight have high statistics, due to the large detector acceptance; however, data were collected during the 10-days flight and the main limit

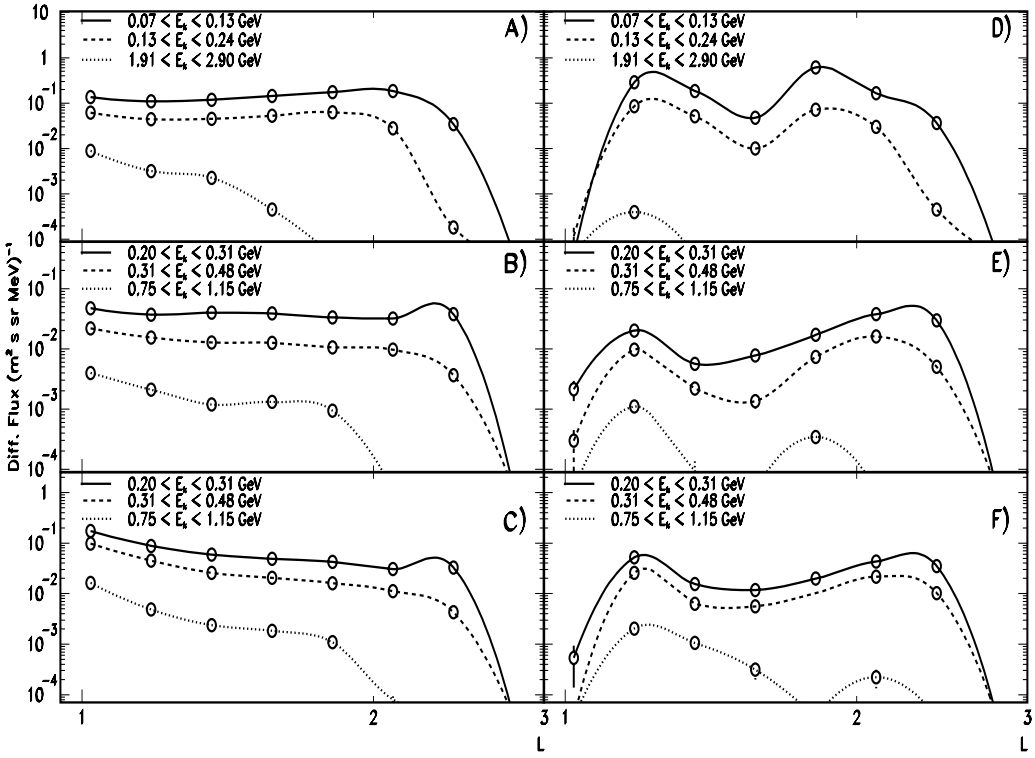

Figure 4.46: *Radial profile of QT differential fluxes for proton A), electron B) and positron C) in three different energy intervals. The ST radial profiles for differential proton D), electron E) and positron F) are shown in the same energy intervals. A smooth curve is superimposed on the data.*

is the short coverage in time; therefore, a self-consistent study of the temporal flux variations is not realistic, and only stationary effects may be accounted for; remarkable is also the limited coverage in (α_o, L) phase space due to the orbit. A consequence is that equatorially mirroring particles ($\alpha_o \sim 90^o$) can be observed only at very low L values and it is difficult to study the fluxes with a classical diffusion equation approach, which requires to have equatorially mirroring fluxes to be measured. The standard procedure for flux computation in the Earth's inner radiation belts is to solve numerically the time dependent radial diffusion equation, introducing source and loss processes. Conversely, when the data consist of stationary flux profiles, it is necessary to assign diffusion coefficients, somewhat arbitrary, in order to reproduce the phase-averaged distribution function $f(\mu, J, L)$ of the particles [151]. Usually, one takes into account diffusion coefficients and atmospheric densities from the best fits of the experimental data.

Studies of the inner zone protons revealed the existence of two regions in L space, namely the lower part ranging up to $L \leq 1.25$ (Zone I) and the upper part above that value (Zone II) [152]. In the zone I the lifetimes against Coulomb collisions are short compared to the 11 years of solar cycle while in the zone II radial diffusion processes start to dominate.

MonteCarlo simulations ([146],[144]) strongly support the hypothesis that the sources for

high energy QT protons and leptons at the AMS altitudes are due to the nuclear interactions of CR protons and helium nuclei with the atmospheric nuclei. MC consistently describes the observed QT fluxes, while it does not describe the ST population due to statistical limits present in the simulation.

One limit for the above mentioned MC approaches is that radial diffusion effects are not included. If CR flux is the engine for the observed QT and ST populations, as for the lower energies CRAND source, solar cycles and rigidity cutoff would play a role in the source modulation. However, due to the relatively high energy, the effects are expected to be less important.

The spectral shape of the observed QT flux is expected to be governed by the source spectrum, both inside and outside the SAA, as has been shown comparing the results with [146] at equatorial regions, and should be independent from the particular loss process; small differences may be related to the solar cycle.

Conversely, the radial profiles and the anisotropies of the fluxes depend mainly on the energy losses, in the crossed atmospheric density and independent from the source. However, if radial diffusion phenomena are present, as the process maintains constant the first two invariants, particles may gain (loose) energy when moving inward (outward) into strong (weaker) magnetic field. It is also possible a diffusion with energy conservation and when both cases are present bimodal diffusion may be invoked [28]. Signatures of such processes might be seen in the combined analysis of differential fluxes and radial profiles.

In fig. 4.46 the differential radial profiles for QT and ST protons, in three different energy intervals, are shown.

QT populations have flat radial profile for all the particle species, while for ST a different shape, with maxima at different L depending on particle species and the energy, is observed. This shows that different processes act on the different kinds of populations, related to the residence times. Processes acting on time scale $>> 30\ s$, the maximum QT drifting time observed, do not play a relevant role for the QT. The structures observed in the ST fluxes may be explained if radial diffusion is present, thanks to the long residence times, while it is not true for the QT particles, due to fast precipitation in the atmosphere, caused by the bounce and drift loss cones. The radial diffusion requires fluctuations in the electric or magnetic fields on the time scale of the drifting to violate the third adiabatic invariant. The same kind of structure is expected for hydrogen and helium isotopes, as discussed in [153]. Using the data of drift-averaged atmospheric densities ρ, the lifetime due to Coulomb losses as a function of the L parameter has been computed for the kinetic energies of $100\ MeV$ and $1000\ MeV$, provided that $\tau_C = E_k/(\rho\beta c\frac{dE_k}{dX})$ [28]. To estimate the effective transport lifetime due to radial diffusion, the expression $\tau_D = 1/D_{LL} = 7 \cdot 10^{-9}L^{10} + 10^{-4}L^{10}/(E_k/B)^2$ has been used. Lifetime due to Coulomb losses increases with increasing L due to atmospheric density decreasing, while the contributions due to the radial transport decrease with increasing L. The two contributions are shown in fig. 4.47. In the case of high energy leptons, in [154] it is shown that large energy losses are expected for inward radial diffusion due to the effects of synchrotron radiation loss at $L < 1.2$. This makes quite unreasonable to expect high energy leptons from radial diffusion at low L values. As a result, the radial diffusion process starts to dominate at higher L.

In fig. 4.47, the diffusive lifetimes come out to be shorter than Coulomb lifetimes for high energy at $L > 1.2 - 1.35$. It is then possible, in principle, to explain the flux enhancement at

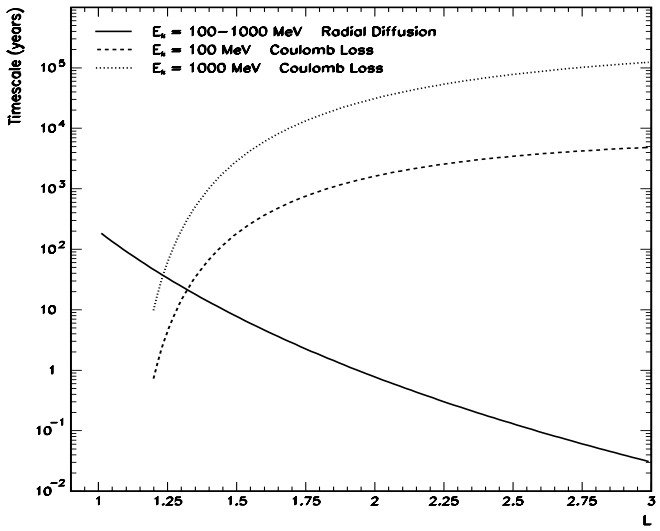

Figure 4.47: *Timescale in years for magnetic and electric radial diffusion and Coulomb collisions using diffusion coefficients of [28] as function of L for protons respectively of* 100 MeV *and* 1000 MeV.

high L values with radial diffusion processes.

As already mentioned, the ST differential spectra turned out to be softer than QT, both for protons and leptons. The differential spectra becomes softer for ST protons and leptons compared with QT, and this softening increases with L. The change in slope of the ST differential flux is observed for protons and leptons at $\sim$ 600 MeV of kinetic energy. Considering the possibility of bimodal diffusion, as described in [155], the differential fluxes may be parameterized in terms of $j(E_k) = j_o e^{E_k/E_o}$. The e-folding parameter E_o is function of L; if diffusion at constant μ is present, spectra become softer at higher L with decreasing E_o. The QT and ST proton differential spectra were fitted with an exponential law in the equatorial regions, where the statistical errors are small. A power law $j(E_k) = j_o E_k^{\gamma}$, similar to the CR spectra was also used for comparison.

In fig. 4.48 the reduced χ^2 of the fits as a function of L are shown. The quality of the fit depends on L and on different statistics. The χ^2 comparisons do not allow for a clear discrimination between the two fits in almost all cases and the results cannot be considered conclusive. More refined analysis, for example using a MonteCarlo approach like in [146], may be performed to better answer this question.

Integral Fluxes The offset and tilt of the magnetic axis are the reasons of the presence of the SAA. At AMS altitudes, drift shells reach the atmosphere around the SAA and particles trapped in such shells precipitate into the atmosphere when drifting through the SAA. Most of the inner-zone electron precipitation occurs in this region, although the pitch angle diffusion is distributed along the magnetic longitudes. Indirect studies of the L dependence of the electron decay rates in inner belts have been made studying the azimuthal variations at low altitudes of precipitating particles [28]. The intensities have significant variations in longitude, attributed to

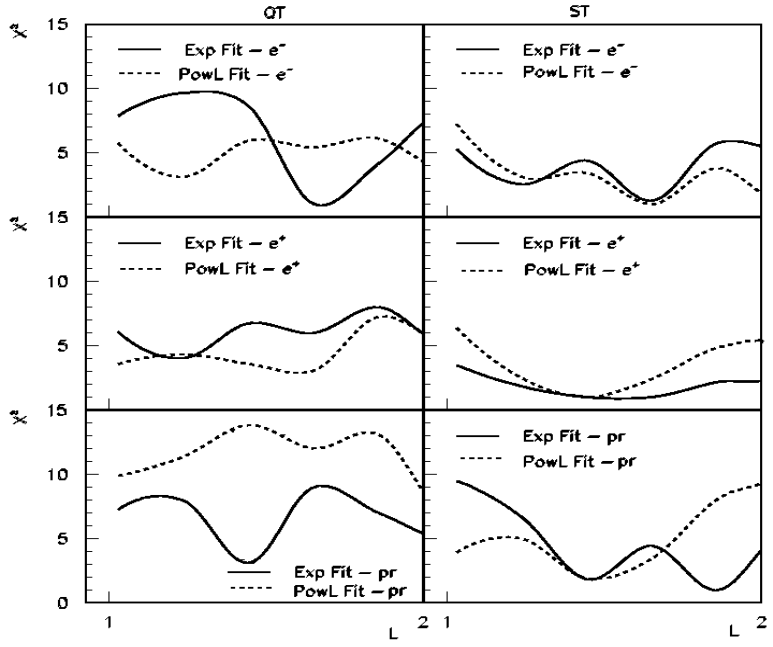

Figure 4.48: *The χ^2 of the fits for the differential spectra of QT and ST protons, electrons and positrons as function of L using exponential and power law fits.*

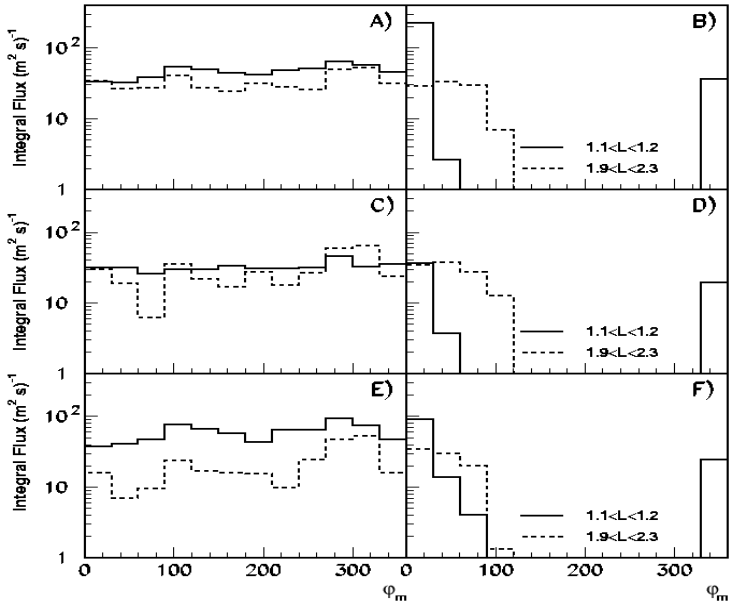

Figure 4.49: *Integral fluxes as function of magnetic longitude φ_m for QT(ST) protons A)(B), electrons C)(D), and positrons E)(D) for two different intervals of L*

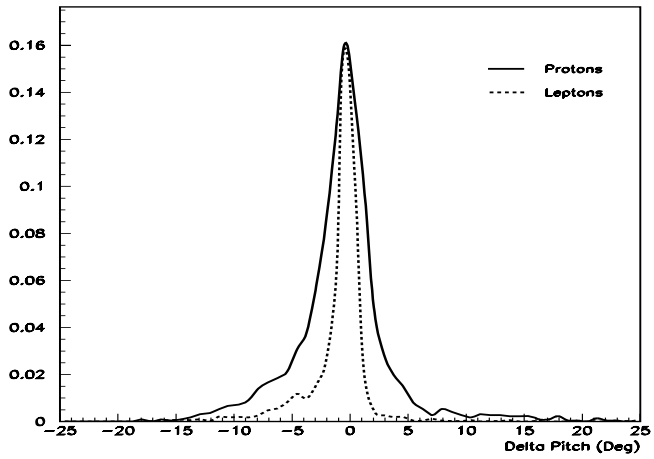

Figure 4.50: *Pitch angle scattering for QT protons and leptons outside the SAA from [146].*

pitch angle diffusion. Fluxes seem higher to the West of the SAA with respect to the East of it. The increase in electron intensity with East suggests a pitch angle diffusion process dependent on L. Measurements of flux at different drift phases of a shell may be used to extract pitch angle diffusion coefficients. The integral fluxes for QT and ST protons, electrons and positrons, as a function of the magnetic longitude φ_m are shown in fig. 4.49, in two different interval of L. From these plots, the effect of SAA longitudinal asymmetry is not clearly evident; for ST population this is due to the limited coverage of the inner region of the SAA and poor statistics, for the QT could be related to the limit on the drifting time.

An estimation of the pitch angle scattering is possible using the MonteCarlo in [146] but due to the limit of the simulation, this could be done only for QT population and the result is shown in fig. 4.50 where pitch angle scattering for QT protons and leptons is plotted. The amount of scattering is expected to decrease with the particle energy and to increase with the amount of matter crossed during the trajectory. The QT protons have a probability to scatter more than leptons because they cross more atmosphere because produced mainly close to the primary interaction point, while leptons coming from the charged pions may be produced at higher altitudes, due to the relatively long distance travelled by muons before decay.

Integral fluxes for the AMS orbit can be investigated using the invariant coordinate representation defined in paragraph 1.4.2. Actually, the coverage in terms of (R_m, Λ_m) is limited due to the low altitude, and a direct comparison between ST and the AE8/AP8 invariant coordinate representation is possible only at low R_m. Each measured pitch angle was converted to the value that would be observed on the same L at a fixed value of $R_m = R_1$. Due to the AMS circular orbit, a value of $R_1 = 1.08$ was adopted, close to the upper limit of R_m values with only a small fraction of particles having the mirror points above it. The flux intensity at R_1 is related to the local intensity by Liouville's theorem by $j(E_k, \alpha_1, L, t) = j(E_k, \alpha, L, t)$ with the new pitch angle

α_1 related to the observed α by [46]:

$$\sin^2 \alpha_1 = \frac{B_o L^3}{B R_1^3} \sqrt{4 - \frac{4R_1}{L}} \sin^2 \alpha \tag{4.6}$$

Knowing the flux map at R_1, it is possible to convert the observed radial distributions integrated over energy to fill a map in (R_m, Λ_m) plane which gives the *spatial* distribution of the particles around the Earth in an adiabatically invariant picture. The assumption for the omnidirectional integral flux is that there are no particles with mirror points above AMS. In this way, the intensity of ST fluxes can bring to an underestimation of the real flux due to possible radial diffusion and loss mechanisms [46]. The results are shown in fig. 4.51 for QT and ST protons (A,B), electrons (C,D) and positrons (E,F). The energy intervals of integration are $E_k = 0.07 \div 9.1\ GeV$ for protons and $E_k = 0.205 \div 2.73\ GeV$ for leptons. In fig. 4.51A,C,E it is visible a smooth radial profile for the QT populations with protons exceeding the electrons and positrons; an excess of positrons at low L is also visible. The ST fluxes in B,D,F show a different picture for the invariant coordinate distributions with a slot region present in all distributions; a ST proton flux higher than the QT one and also higher than QT and ST leptons fluxes is observed. The excess of the QT positrons over QT electrons is also visible in the slot region around $L \sim 1.3$.

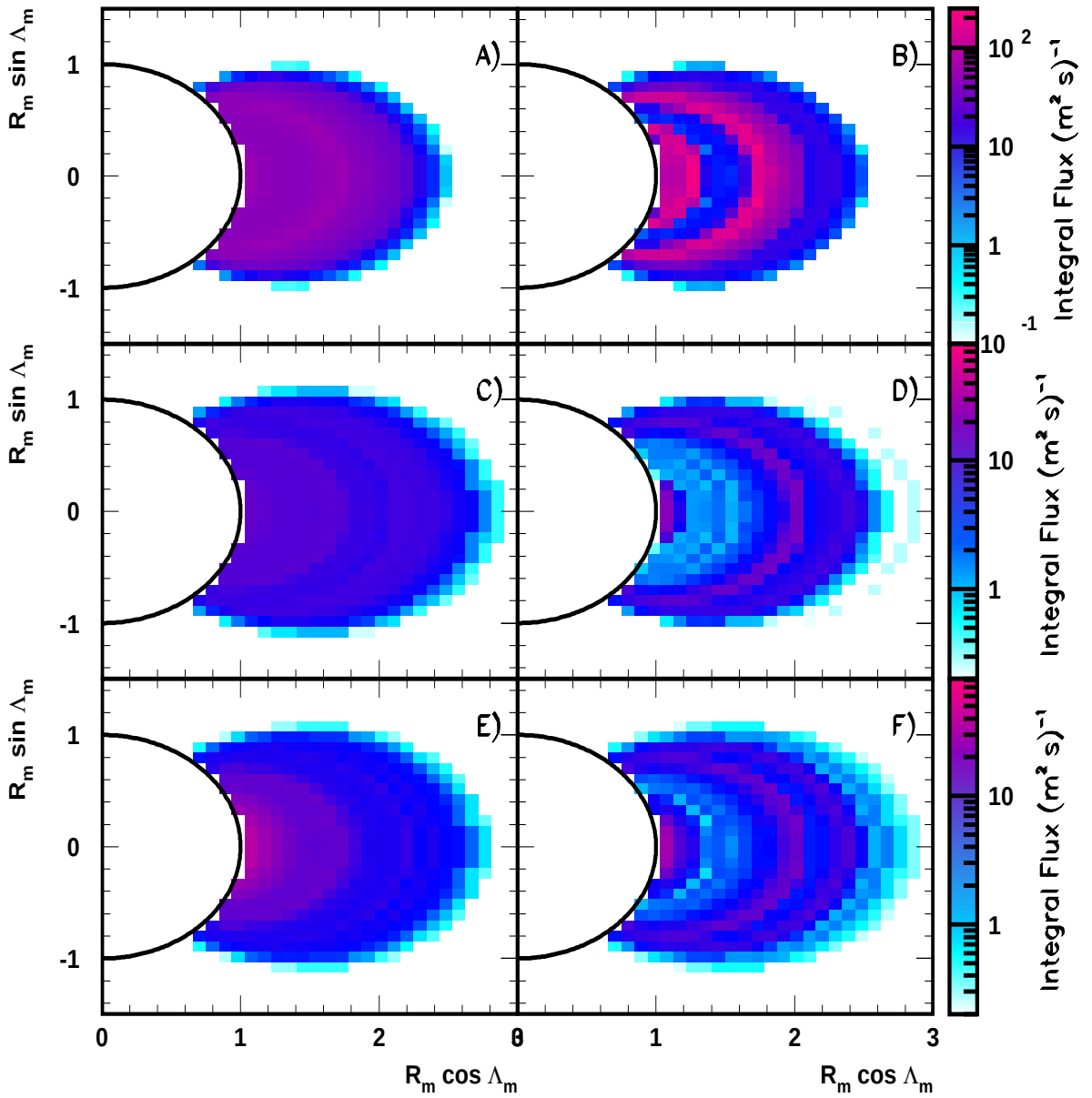

Figure 4.51: *Integral omnidirectional flux maps in* (R_m, Λ_m) *coordinates for QT and ST protons (A,B), electrons (C,D) and positrons (E,F). The energy intervals are* $E_k = 0.07 \div 10\,GeV$ *for protons and* $E_k = 0.205 \div 2.73\,GeV$ *for leptons. The circles represent the approximate* R_m *value of the Earth's atmosphere in the SAA region.*

Conclusions

The complex connection of the Sun-Earth environment brings to the peculiar features observed in LEO environment. The radiation belts consist of energetic particles trapped in the magnetic trap of the dipole-like Earth's magnetic field and represent the most important hazard to spacecraft and radiation sensitive electronic devices.

For the description of the radiation belts, models were built using measurements taken from several different instruments on long-lasting spaceborn campaigns (AE8/AP8/INP) (fig.4.52). The limits of these models are related to the energy coverage and the static description of the proton and electron belts. Moreover, the possibility to accurately discriminate charged particles was limited because limited capabilities of old instruments. In particular, was quite difficult to discriminate the sign of leptons charge. One of the consequence is that radiation belt models do not include positrons but only electrons.

In LEO, the possibility to observe trapped radiation is limited to the region over the SAA. High energy data in LEO were also limited in spatial and energy coverage; data from the MEPHI group describe measurements of leptonic composition of the belts in the SAA region reporting electron excess over positron, but with large uncertainties.

Cosmic rays above cutoff interact with the Earth's atmospheric nuclei producing secondary particles by nuclear interactions. The secondary particles may be injected in trajectories such that they become Quasi-Trapped and Stably-Trapped in the Earth's magnetic field. The resulting fluxes may be measured by instruments on satellites in LEO and on balloon-born detectors travelling at lower altitudes in the atmosphere. Particles of secondary origin, depending on the kind of processes involved, can be the driving source of trapped population (CRAND, albedo mechanism, meson decays).

The study of the trapped component of the spectra was presented in the analysis, for protons and leptons collected with AMS01 instrument. The energy coverage ranges in $0.1 \div 10\,GeV$ for protons and electrons, while it is in the range of $0.1 \div 3.\,GeV$ for positrons because of the ATC efficiency selection. Using the tracing, it is possible to investigate the peculiarities of the trapped particles, in particular the extension and location of the source and sink regions as well as their residence times.

The explanation of such features must take into account the geometry of the drift shells crossed by AMS during the flight. In the SAA region, closed shells are encountered, and Stably-Trapped population is observed, while outside the SAA all the shells crossed by AMS at $400\,Km$, partially evolve into the atmosphere and the stable trapping can occur. In the Stably-Trapped component, depending on the shell, it is possible to separate populations with residence times dominated by the bouncing motion, called Albedo or Short-Lived, from those dominated by the

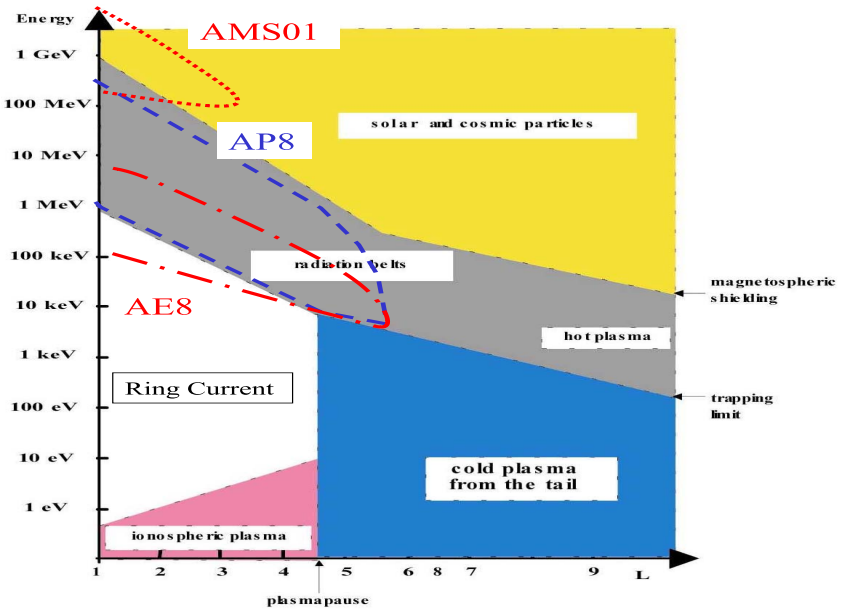

Figure 4.52: *Particle energy versus L plot in the inner magnetosphere.*

drift motion around the Earth, called Quasi-Trapped or Long-Lived. The two populations are generally referred as Quasi-Trapped in this work.

Flux maps were built using the equatorial pitch angle α_o, the L shell parameter and the kinetic energy E_k, with a conventional separation in regions inside and outside the SAA by means of the local magnetic field ($B \gtrless 0.26\,G$). QT fluxes were found to populate both the region inside and outside the SAA, while the ST flux is concentrated in the SAA region. QT and ST fluxes show remarkable differences in the structures, with ST differential spectra softer than QT and complex radial structures. The ST component of the flux is dominated by Coulomb losses at low L, while at higher L the radial diffusion starts to dominate. The low energy ST flux is detected only in the SAA region with spectra softer than QT likely due to the longer residence times of ST, and their more intense average experience with atmosphere.

These observations support the existence of a transition region from Quasi-Trapped to Stably-Trapped populations within a well measured drifting loss cone. In the QT component, a separation can be found between proper QT and Albedo particles; at any given L, the equatorial bouncing loss cone $\boldsymbol{\alpha_c(L)}$ can be defined to distinguish Albedo and Quasi Trapped components of the fluxes. For the leptons, the same value it is found to separate the region where e^+/e^- is above unity with positron dominance above $\boldsymbol{\alpha_c(L)}$.

A transition region (MRB) is defined, between the stable trapping lower limit, given by the equatorial drift loss cone, $\boldsymbol{\alpha_{st}(L)}$, and the upper limit of the full IVAB fixed by the AMS orbit. The MRB can be the region of injection and loss of the high energy particles populating the IVAB, by a mechanism dominated by the Coulomb scattering in the residual atmosphere.

Protons show anisotropies due to the finite gyroradius which is of the same order of the scale height of the atmosphere at $400\,Km$. QT and ST trapped particles show East/West asymmetry, especially at high energy for QT, while for ST asymmetries are observed in the whole energy

range.

MonteCarlo studies of the QT fluxes suggest that positron abundance is related to the pion decays produced in the interactions of primary CR, mainly protons and helium nuclei, with atmospheric nuclei, and East-West asymmetry of cutoff on the source. The simulation supports the idea that QT fluxes of protons are due to nuclear interactions of primary protons and helium nuclei with the atmosphere. Comparisons of QT proton flux with MC results shows a pretty nice agreement, while ST are not reproduced by the simulation due to statistics. However, further studies are needed to explain all the observed features of the AMS trapped fluxes, possibly integrating all the source and loss mechanisms involved. The possibility to measure the leptons charge very accurately confirms previous measurements of Quasi-Trapped positrons and electrons made by the MARYA in the equatorial region. However, AMS and MARYA do not agree in the SAA region on the leptonic composition of the Stably-Trapped population. In the picture emerging from the measured AMS lepton fluxes, positron excess is observed almost everywhere for QT and ST fluxes; as a consequence, it is not necessary to invoke magnetospheric acceleration mechanisms to explain possible electron excess, and the engine of the observed fluxes seems to be the interactions of primary CR with atmospheric nuclei.

In fig.4.52 is shown a classification of magnetospheric particles, using the kinetic energy E_k and the L-shell parameter. The AMS coverage is shown; it improves the knowledge on the magnetospheric particles in composition and energy up to $L < 3$. It also shows the contribution of AMS to the understanding of the processes involved in the trapping of high energy particles in the low L range, which was not covered before. The high accuracy of the data collected by AMS, give to the scientific community the opportunity to study fluxes of high energy particle at LEO, a step towards the investigation of the fundamental physics processes involved in this region of the magnetosphere.

Acknowledgements

During my thesis work I had the opportunity to meet several people whose help made my scientific experience and personal efforts fruitful and quite exciting.

First of all I wish to express my gratitude to Prof. R. Battiston for the opportunity he gave me and for the important suggestions and consideration.

To Dr. B. Bertucci, coordinator of the Perugia analysis group, I would like to express my personal thanks and appreciations for the many helpful suggestions and stimulating discussions.

I want to give a special word of thanks to Dr. E. Fiandrini for the amount of things he taught me and for the way he shared with me his experience. Without his help and friendship this work would not have been possible.

I want to also thank my PhD's colleague Dr. P. Zuccon who shared with me his work and knowledge without any hesitation.

Thanks to Dr. B. Alpat and Dr. W.J. Burger for their kindness and often illuminating suggestions.

My appreciation goes also to the members of the AMS group of Perugia, Terni and Geneva, the technicians and the administrative staff for their help and support.

I would like to thank all the members of AMS collaboration and, in particular, Dr. V. Choutko who shared with us his work and experience.

My appreciation to Dr. D. Heynderick, member of the BIRA-IASB group, sharing with us his knowledge about radiation belts and for the insights about the SPENVIS and UNILIB packages.

My gratitude also goes to Dr. V.V. Mikhailov, member of the MEPHI group, for the useful discussions about the MARYA data.

Perugia, Italy October 30, 2002

Bibliography

[1] Elliot J.A., *Plasma kinetic theory* in *Plasma Physics*, by Dendy R., Cambridge Univ. Press, 1993

[2] Russell C.T., *Solar wind interaction with the Earth's magnetosphere*, in press, 2002

[3] Ichimaru S., *Statistical Plasma Physics*, Addison-Wesley, 1992

[4] Ball B.M., *Non adiabatic features in magnetotail fast flows: orbit tracing and data comparison* , PhD Thesis, Univ. of New Hampshire, UK, 2001

[5] Kivelson M.G., Russel C.T., *Introduction to space physics* , Cambridge Univ. Press, 1995

[6] Stoermer C., *Sur le trajectories des corpuscoles electrisities dans l'espace sous l'action du magnetism terretre*, Arch. Sci. Phys., 24, N.5, 1907

[7] Northrop T.G., Teller E., *Stability of the adiabatic motion of charged particles in Earth's field* , Phys. Rev., 117, 215, 1960

[8] Chirikov B.V., *Stability of the motion of charged particle in a magnetic confinement system*, Soviet. Journ. Plasma Phys., 4, 289-300, 1978

[9] Mc Comas D.J. et al., Journ. Geoph. Res., 103, 1998

[10] Van Allen J.A., *Why Radiation Belts Exists*, EOS, 72, 361, 1991

[11] IAGA Division V Working group 8, *International Geomagnetic Field Reference Field*, J. Geomag. Geoelectr., 47, 1251-1261, 1995

[12] Gustafson et al., *A revised Corrected Geomagnetic Coordinate Systems*, J. Atmos. Terr. Phys., 54, 1609-1631, 1992

[13] Tsyganenko N.A. et al, *Modeling the Global Magnetic field of the Large Scale Birkeland Current systems*, Journ. Geoph. Res., 101, 27187-27198, 1996

[14] McIlwain C.E., *Coordinates for mapping the distribution of magnetically trapped particles*, Journ. Geoph. Res., 66, 11, 3681-3691, 1961

[15] Roederer J.G., *Dynamics of Geomagnetically trapped radiation*, Springer Verlag, 1970

[16] Kruglansky et al., *Analysis of the low altitude proton flux asymmetry methodology*, Rad. Meas., 30, 645-652, 1999

[17] Vette J.I., *The AE-8 Trapped Electron Model Environment*, NSSDC/WDC-A-R&S 91-24, 1991

[18] Sawyer, D.M., Vette J.I., *The AP-8 Proton Environment for Solar Maximum and Solar Minimum*, NSSDC/WDC-A-R&S 76-06, 1976

[19] Fung S.F., *Recent Development in the NASA Trapped Radiation Model*, in Radiation belts: models and standard, AGU Publisher, 1997

[20] Getselev I.V. et al., *Model of spatial energetic distribution of charged particles (protons and electrons) fluxes in the Earth's radiation belts*, INP MSU Preprint MGU-91-37/241, 1991 (in Russian)

[21] Mineev Yu. V. et al., *Low altitude Models of Radiation Belts Based on Data from Russian Satellite*, in Radiation belts: models and standard, AGU Publisher , 1997

[22] Heynderickx D. et al. *Radiation Belts: models and standards*, Geoph. Monogr, 1997, Lemaire, Heynderickx, Baker editors, 1997

[23] Kruglansky et al., *Improvement of the Trapped Proton Anisotropy Description*, TREND3 Tech. Note N.6/2, 7-10, 1998

[24] Heynderickx D., *Review on modelling of the radiation belts*, 2^{nd} MAD Proc., Trento, publ. in Journ. Modern Physics A, Vol.17, N.12-13, 2002

[25] Lemaire et al., *TREND 2 Final Report*, ESTEC/Contract N.9828/92/NL/FM, 1995

[26] *SPENVIS home page, [http://www.spenvis.oma.be/]*, BIRA-IASB, Belgium, 2001

[27] *UNILIB home page, [http://www.magnet.oma.be/home/unilib/home.html]*, BIRA-IASB, Belgium, 2001

[28] Schulz M., Lanzerotti L.J., *Particle diffusion in the radiation belts*, Springer Verlag, 1974

[29] Schulz M., *Canonical coordinates for radiation belt modeling*, in Radiation belts: models and standard, AGU Publisher , 1997

[30] Il'in V.D. et al., *Stochastic instability of charged particles in a magnetic trap*, Cosmic Res., 24, 69-76, 1986

[31] Roberts C.S., *Pitch-Angle diffusion of Electrons in the Magnetosphere*, Rev. Geoph., Vol 7, 305-337, 1969

[32] Li et al., *Rapid enhancements of relativistic electrons deep in the magnetosphere during May 15 1997*, Journ. Geoph. Res., 104, 4467-4476, 1999

[33] Bourdarie S. et al., *Electron and proton radiation belt dynamic simulations during storm period*, J. Geoph. Res., 102, 17541-17552, 1997

[34] Albert et al., *CRRES observations of radiation belts proton*, Journ. Geoph. Res., 103, 9261, 1998

[35] Huston et al., *A new model for the low altitude trapped proton environment*, IEEE Nucl. Sci. Rad. Effect. Conf., 1998

[36] Gussenhoven et al., *Solar particle events as seen on CRRES*, Adv. Space Res., 14, 619, 1994

[37] Benton E.R., Benton E.V., *Space radiation dosimetry in LEO and beyond*, NIM B, 184, 255-294, 2001

[38] Hudson et al., *Radiation belts formation during storm sudden commencement and loss during main phase*, Adv. Space Res., 21, 597, 1998

[39] Lyons et al., *Equilibrium structure of radiation belt electrons*, J. Geoph. Res., 78, 2142, 1973

[40] Lyons et al., *Parasitic pitch angle diffusion of radiation belt particles by ion cyclotron waves*, Journ. Geoph. Res., 77, 5608, 1972

[41] Abel et al., *Solar cyclic behaviour of trapped energetic electrons in Earth's inner radiation belts*, Journ. Geoph., 99, 19427, 1994

[42] White R.S., *High energy proton radiation belt*, Rev. Geoph. Space Phys., 11, 595-632, 1973

[43] Singer S.F., *Radiation belt and trapped cosmic ray albedo*, Phys. Rev. Lett., 1, 181-185, 1958

[44] Buhler P., *Radiation belts* Proc. of ESA Workshop on Space Weather, The Netherlands, 1998

[45] Boscher D. et al. *Dynamic model of high energy proton belt* Proc. of ESA Workshop on Space Weather, The Netherlands, 1998

[46] Selesnick et al., *Geomagnetically trapped anomalous cosmic rays*, Journ. Geoph. Res., 199, 9503, 1995

[47] Li X., et al., *Are energetic electrons in the solar wind the source of the outer radiation belt ?*, Geoph. Res. Lett., 24, 923, 1997

[48] Blake et al., *Injection of electrons and protons with energies of tens of MeV into $L < 3$ on March 24, 1991*, Geoph. Res. Lett., 19, 821, 1992

[49] Blake et al., *A technique to determine the charge state of the ACR*, 15^{th} ICRC Proc., 2, 342-346, 1977

[50] Blake J.B., *Geomagnetically trapped heavy ions from ACR*, 21^{st} ICRC Proc., 7, 30-33, 1990

[51] Fisk L.A. et al., ApJ, 190, L35-L38, 1974

[52] Hovestadt D. et al., Phys. Rev. Lett., 31, L650, 1973

[53] Sakaguchi et al., *LET ditribution measurement with a new real-time radiation monitoring device-III onboard the Space Shuttle STS-84*, NIM A, 437, 75-87, 1999

[54] Longair M.S., *High energy asptrophysics*, Cambridge Univ. Press, 1990

[55] Ginzburg V.L. et al., *Origin of cosmic ray*, Pergamon Press, 1964

[56] Wilson C.T.R., Proc. Royal Society, A68, 151, 1901

[57] Geitel H., Physik. Zeitschrift, 2, 116, 1900

[58] Magnussen N. *Selected result from based cosmic ray and gamma ray experiment*, astro-ph/9805165, 1998

[59] Hess F.H., Physik. Zeitschrift, 13, 1084, 1912

[60] Bothe W. et al., Naturwiss, 16, 1044, 1928

[61] Mewaldt R.A., Advanc. Space Res. , 14, 10, 737, 1994

[62] Mewaldt R.A., ApJ, 466, L43-46, 1996

[63] Simpson J.A., Advanc. Space Res. , 9, 4, 5, 1989

[64] Gleeson L.J. et al., *Solar modulation of GCR*, The ApJ, 168, 1011-1026, 1968

[65] Pyle K.R., *Neutron monitor sensitivity to solar modulation changes*, 23^{nd} ICRC Proc., 3, 609, 1993

[66] Hedin A.E., *Extension of the MSIS thermosphere model into the middle and lower atmosphere*, Journ. of Geoph. Res., 96, A2, 1159-1172, 1991

[67] Ayres D. et al., Phys. Rev., D29, 902, 1984

[68] Gaisser T.K., *Cosmic rays and particle physics*, Cambridge Univ., 1990

[69] Berezinsky V.K. et al., *Astrophysics of Cosmic rays*, North Holland, 1990

[70] Engelmann J.J. et al., Astronom. and Astroph., 233, 96, 1990

[71] Smart D.F. et al., *Magnetospheric model and trajectory computations*, Space Sci. Rev., 93, 305-333, 2000

[72] Smart D.F. et al., *Magnetospheric model and trajectory computations*, Journ. Geoph. Res., 70, 17, 4117-4130, 1965

[73] Vallarta M.S., *On the longitudinal effect of cosmic radiation*, Phys. Rev., 47, 747-651, 1935

[74] Quenby J.J. et al., *Cosmic ray cutoff rigidities and the Earth's magnetic field*, Phil. Mag., 4, 90-113, 1959

[75] Cooke D.J. et al., *On cosmic ray cutoff terminology*, Nuovo Cimento, 14, 3, 213-234, 1991

[76] Hoofer J. E. et al., *The cosmic radiation*, Wiley & Sons, 14, 1958

[77] Freon A. et al., *A note on vertical cutoff rigidities of cosmic rays in the geomagnetic field*, Journ Geoph. Res., 67, 888-890, 1962

[78] Fukuda Y. et al., Phys. Rev. Lett., 81, 1562, 1998

[79] Huang M.A et al., *First result on AMS Tracing I*, Erice Workshop, 2000

[80] Rossi B. *High energy particles*, Prentice Hall, 1952

[81] Bertucci B., *Cosmic ray measurements with the AMS experiment*, Proc. of NOW200, Nucl. Phys. B, Proc. Suppl. 100, 124, 2001

[82] Honda M. et al., Phys. Rev., 52, 4985, 1995

[83] Boezio M. et al., *The cosmic ray proton and helium spectra* $0.2 - 200GV$, ApJ, 518, 457-461, 1999

[84] Buckley M. et al., ApJ, 429, 736-747, 1994

[85] Menn W. et al., *The absolute flux of protons and helium at the top of atmosphere using IMAX*, ApJ, 533, 281-285, 2000

[86] Bellotti E. et al., *Balloon measurement of cosmic ray protons at mid latitude*, Phys. Rev., D60, 052002, 1991

[87] Iyudin A.F. et al., *Composition of the relativistic electron-positron component of the radiation belt of the Earth*, Geomag. Aeronomy, 28, 103-105, 1988

[88] Seo E.S. et al., *Measurement of CR proton and helium from* $200MeV/n$ *to* $100GeV/n$, ApJ, 378, 763-767, 1991

[89] Sanuki T. et al., *Precise measurement of cosmic ray proton and helium spectra with BESS*, ApJ, 545, 1135-1139, 2000

[90] Treiman S.B., *The cosmic ray albedo*, Phys. Rev., 91, 957-959, 1953

[91] Ray E.C., *Reentrant cosmic ray albedo calculation*, Journ. Geoph. Res., 67, 3289, 1962

[92] Ray E.C., *An imporoved reentrant cosmic ray albedo calculation*, Journ. Geoph. Res., 72, 4839, 1967

[93] Pennypacker C.R. et al., *Measuremet of geomagnetic cutoff rigidities near Palestine*, Journ. Geoph. Res., 78, 10, 1515-1527, 1973

[94] Bertucci B., *Review of precision measuremts of high energy electrons*, 2^{nd} MAD Proc., Trento, published in Journ. Modern Phys. A, Vol. 17, N. 12-13, 2002

[95] Konig P.J. et al., *A model for the anysotropic reentry of albedo*, Journ. Geoph. Res., 86, 515-519, 1981

[96] Konig P.J. et al., *The anysotropy of albedo reentrant at midlatitude*, Proc. 14^{th} ICRC,4, 1350-1355, 1975

[97] Grigorov N.L., Akademia Nauk. SSSR, Doklady, 234, 810, 1977

[98] Verma S.D., *Measurement of charged splash and re-entrant albedo of the Cosmic Radiation*, Journ. Geoph. Res., 72, 915-925, 1967.

[99] Verma S.D., *A calculation of the flux and energy spectrum of secondary electrons at the high altitudes in the atmosphere*, Proc. Indian Academy Sciences, Section A, 56, 125-143, 1967

[100] Gusev A.A. et al., *Formation of Albedo electron fluxes in the Geomagnetic field*, Geomag. Aeronomy, 22, 6, 754-758, 1982

[101] Gusev A.A. et al., *The spatial distribution of albedo particles at altitudes of 500 Km*, Geomag. Aeronomy, 25, 4, 462-466, 1985

[102] Barwick S.W. et al., *Cosmic reentrant electron albedo: HEAT balloon measurements*, Journ. Geoph. Res., 103, a3, 4817-4823, 1998

[103] Wenzel K.P. et al., *Splash albedo protons between 4 and 315 MeV at high and low geomagnetic latitude*, Journ. Geoph. Res., 80, 25, 3580-3584, 1975

[104] Gangnes A.V. et al., Phys. Rev., 75, 1, 57, 1949

[105] Cummings et al., *New evidence of geomagnetically trapped ACR*, Geaph. Res. Lett., 20, 2003-2006, 1993

[106] Singer S.F., *Radiation belt and trapped cosmic ray albedo*, Phys. Rev., 77, 729, 1950

[107] Winckler J.R. et al., Phys. Rev., 79, 656, 1950

[108] Winckler J.R. et al., *Geomagnetic and albedo studies with a Cerenkov detector at* 40^o *geomagnetic latitude*, Phys. Rev., 93, 596, 1954

[109] Voronov S.A. et al., *Magnetic scintillate spectrometer of electrons*, Pribory i Technika Experimenta, 2, 35, 1986 (in Russian)

[110] Voronov S.A. et al., *High energy electrons and positrons in the Earth's radiation belt*, Geomag. Aeronomy, 27, 3, 424-426, 1986

[111] Voronov S.A. et al., *Spectra of albedo electrons and positrons with energies greather than* $20MeV$, Cosmic Research, 33, 3, 300-302, 1995

[112] Voronov S.A. et al., *Nature of high energy electrons in the Earth's radiation belt*, Cosmic Research, 33, 5, 497-499,1995

[113] Pugacheva G.I. et al.,*On the natural energetic positron population in the Earth's inner radiation belt*, Journ. Atm. Solar Terr. Phys., 59, 3, 363-369, 1997

[114] Moskalenko I.V. et al., *Production and propagation of cosmic ray positrons and electrons*, ApJ, 493, 694-707, 1998

[115] Protheroe R.J., ApJ, 254, 391, 1982

[116] Daniel R.R. et al., *Cosmic ray produced electrons and gamma rays in the atmosphere*, Rev. Geoph. Space Phys., 12, 2, 233-258, 1974

[117] Galper A.M. et al, *Discovery of high energy electrons in the radiation belt by devices with gas cherenkov counters*, NIM A, 248, p. 238., 1986

[118] Ahlen S. et al., NIM A, 350, 351, 1994

[119] Webber W.R. et al., ApJ, 390, 96, 1992

[120] Mitsui T. et al., Phys. Lett. B 389, 169, 1996

[121] Ellison J. et al., Phys. Lett. B 214, 403, 1988

[122] Viertel G.M. et al., NIM A, 419, 295, 1998

[123] Alvisi D. et al., NIM A, 437, 212, 1999

[124] Baranvourt D. et al., *The AMS01 Aerogel Threshold Cerenkov Counter*, NIM A, 465, 306, 2001

[125] Alcaraz J. et al., *A new silicon microstrip tracker in space*, Nuovo Cimento, 112A, 11, 1325-1344, 1999

[126] Suter H., *Space Shuttle flight parameters for the STS-91 mission*, AMS Internal Note, 1999

[127] Innocente V. et al., *Geane*, Cern program library W5013-E, 1991

[128] Brun R. et al., *Geant3*, Cern DD/EE/84-1 Revised 1987

[129] Blobel V., *Unfolding methods in high energy physics*, Proc. 1984 Cern School of Comput., 85-09,88-127, 1985

[130] D'Agostini G., *A multidimensional unfolding method based on the Bayes theorem*, NIM A, 362, 487, 1995

[131] *AMS experiment home page, [http://ams.cern.ch/]*, CERN, Switzerland, 1997

[132] Alcaraz J. et al., *Protons in near Earth orbit*, Phys. Lett. B472, 215-235, 2000

[133] Alcaraz J. et al., *Leptons in near Earth orbit*, Phys. Lett. B484, 10-22, 2000

[134] Alcaraz J. et al., *Cosmic protons*, Phys. Lett. B490, 27-35, 2000

[135] Alcaraz J. et al., *The AMS on ISS Part I*, Phys. Reports, vol. 366/6, 331-404, 2002

[136] DST monitoring home page [http://swdcdb.kugi.kyoto-u.ac.jp/]

[137] Baker P. et al., *Strong electron acceleration in the Earth's magnetosphere*, Adv. Space Res., 21, 609, 1998

[138] Sullivan J.D., *Geometrical factor and directional response of single and multi-element particle telescope*, NIM A, 95, 5-11, 1971

[139] Tylka A.J. *A review of cosmic ray albedo studies*, Code 7652, Naval Res. Lab, http://gamma.nrl.navy.mil/glast/shared/May00/Albedo_Report.pdf

[140] Lowes F.J., *An estimate of the errors of the IGRF field 1945-2000*, Earth Planets Space, 52, 1207-1211, 2000

[141] Galper A.M. et al, *Electrons with energy exceeding 10Mev in the Earth's radiation belt* , in Radiation Belts: models and standards, Geoph. Monogr, 1997, Lemaire, Heynderickx, Baker editors, 1997

[142] Mikhailov V.V., *MARYA-2 data*, unpublished, private communication, 2002

[143] Derome L. et al, *Origin of the high energy proton component below the geomagnetic cutoff in near orbit*, Phys. Lett. B 489, 1-8, 2000

[144] Derome L. et al, *Origin of leptons in near orbit*, astro-ph/0103474, 2001.

[145] Lipari P., *The fluxes of sub-cutoff particles detected by AMS, the cosmic ray albedo and the atmospheric neutrinos*, Astrop. Phys. 14, 153, 2000

[146] Zuccon P., *MonteCarlo simulation of the interactions of CR with atmosphere*, PhD Thesis, Univ. of Perugia, Italy, 2002

[147] Lencheck A.M. et al., *Effect of finite gyroradii of geomagnetically trapped protons*, Journ. Geoph. Res., 67, 4073-4075, 1962

[148] Dragt A.J., *Solar cycle modulation of the radiation belt proton flux*, Journ. Geoph. Res., 76, 2313-2344, 1971

[149] Clafin E.S., *A study of equatorial inner belt protons from 2 to 200 MeV*, Journ. Geoph. Res., 79, 959, 1974

[150] Walt M., *The physical mechanisms of the inner Van Allen Belt*, Fund. Cosmic Phys., 2, 1, 1976

[151] Walt M., *Introduction to geomagnetically trapped radiation*, Cambridge Univ. Press 1994

[152] Jentsch V. et al., *An analytic study of the energy and pitch angle distribution of inner zone proton* , Journ. Geoph. Res., 85, 1-8, 1980

[153] Pugacheva G. I. et al., *Hydrogen and helium isotope inner radiation belts in the Earth's magnetospgere*, Ann. Geoph, 16, 931-939, 1998

[154] Pugacheva G. I. et al., *On synchrotron radiation energy losses of trapped magnetospheric electrons*, Journ. Atm. Sol. Terr. Phys., 60, 1159-1162, 1998

[155] Theodoridis G.C. et al., *Acceleration of trapped electrons and protons trough bimodal diffusion in the Earth's radiation belts*, Journ. Geoph. Res., 74, 1238, 1969

[156] Spjeldvik W.,N., *Equilibrium structure of equatorially mirroring radiation belt protons* , Journ. Geoph. Res., 82, 2801, 1977

[157] Fiandrini E. et al., *Leptons with* $E > 200MeV$ *trapped in the Earth's magnetic field*, Journ. Geoph. Res., 107, A6, 10129, 2002

[158] Fiandrini E. et al., *Leptons with* $E > 200MeV$ *trapped in the SAA*, submitted to Journ. Geoph. Res.